

EFFECTIVE CHARGES IN NUCLEI IN THE VICINITY OF ^{100}Sn

ANDREAS EKSTRÖM



LUND UNIVERSITY

Department of Physics, 2009

EFFECTIVE CHARGES IN NUCLEI IN THE VICINITY OF ^{100}Sn

ANDREAS EKSTRÖM



LUND
UNIVERSITY

DEPARTMENT OF PHYSICS
2009

Effective Charges in Nuclei in the Vicinity of ^{100}Sn
Thesis for the Degree of Doctor of Philosophy

Division of Nuclear Physics
Department of Physics
Lund University
Box 118
SE-221 00 Lund
Sweden

LUNFD6/(NFFR-1031)1-125/(2009)
ISBN 978-91-628-7991-4

Typeset by the author using L^AT_EX 3.1415926-1.40.9
Printed in 2009 by Tryckeriet i E-huset, Lund, Sweden

THESIS FOR THE DEGREE OF DOCTOR OF PHILOSOPHY

EFFECTIVE CHARGES IN NUCLEI IN THE VICINITY OF ^{100}Sn

ANDREAS EKSTRÖM

DIVISION OF NUCLEAR PHYSICS
DEPARTMENT OF PHYSICS
LUND UNIVERSITY
SWEDEN

FACULTY OPPONENT: DR. RODERICK M. CLARK
NUCLEAR SCIENCE DIVISION
LAWRENCE BERKELEY NATIONAL LABORATORY
BERKELEY, CA 94720-8101, USA

ACADEMIC DISSERTATION WHICH, BY THE PERMISSION OF THE FACULTY OF SCIENCE AT LUND UNIVERSITY, WILL BE PUBLICLY DEFENDED ON FRIDAY THE 12TH OF FEBRUARY 2010, AT 10.15 IN LECTURE HALL B AT THE DEPARTMENT OF PHYSICS, SÖLVEGATAN 14A, LUND.

Organization LUND UNIVERSITY Department of Physics Box 118 SE-221 00 Lund Sweden		Document name DOCTORAL DISSERTATION	
		Date of issue December 16, 2009	
Author(s) Andreas Ekström		Sponsoring organization	
Title and subtitle Effective Charges in Nuclei in the Vicinity of 100Sn			
Abstract <p>The shell structure of atomic nuclei far from the line of beta-stability and the properties of the nucleon-nucleon interaction in exotic isotopes are not well known. The development of radioactive ion beams (RIBs) puts certain unexplored regions of the nuclear chart within reach of detailed experimental investigations.</p> <p>The low-energy nuclear structure of the unstable isotopes 106,108,110Sn, 100,102,104Cd, and 106,108In have been studied using sub-barrier Coulomb excitation of postaccelerated RIBs. The experiments were carried out at the REX-ISOLDE facility at CERN. The deduced transition probabilities - B(E2) values - provide a detailed benchmark of modern models of the nucleon-nucleon interaction.</p> <p>The B(E2) values between the 0+ ground states and the first excited 2+ states in the Sn and Cd isotopes were compared with shell-model calculations. These are based on effective interactions derived from renormalized multi-meson and QCD-based nucleon-nucleon potentials. In order to reproduce the experimental results in the calculations, the neutron effective charge requires a renormalization. The observed effect is most prominent in the light Sn isotopes.</p> <p>The static quadrupole moments - Q(2+) values - of the first excited 2+ states in the 102Cd and 104Cd isotopes were measured using the reorientation effect in Coulomb excitation. In this approach, the B(E2) and Q(2+) values of each isotope are correlated. Therefore, the collected data were analyzed using the maximum likelihood method. In this way, the two-dimensional probability distributions could be determined. In turn, this enables a detailed comparison with theoretical models. Here, the results were interpreted using the shell-model.</p> <p>The observed gamma-ray de-excitation patterns in 106,108In were also interpreted in the shell-model. The excited states in 108In were further analyzed in terms of their proton-neutron multiplet character.</p>			
Key words: Coulomb excitation, reorientation effect, radioactive ion beams, shell-model calculations			
Classification system and/or index terms (if any):			
Supplementary bibliographical information:		Language English	
ISSN and key title:		ISBN 978-91-628-7991-4	
Recipient's notes		Number of pages 184	Price
		Security classification	

Distribution by (name and address) A. Ekström, Department of Physics, Box 118, 221 00 Lund, Sweden
 I, the undersigned, being the copyright owner of the abstract of the above-mentioned dissertation, hereby grant to all reference sources permission to publish and disseminate the abstract of the above-mentioned dissertation.

Signature _____

Date December 16, 2009

LIST OF PUBLICATIONS

This thesis is based on the following peer-reviewed publications and submitted manuscripts.

PAPER I: **Sub-Barrier Coulomb Excitation of ^{110}Sn and Its Implications for the ^{100}Sn Shell Closure**

Physical Review Letters **98**, 172501 (2007).

J. Cederkäll, A. Ekström, C. Fahlander, A. M. Hurst, M. Hjorth-Jensen, F. Ames, A. Banu, P. A. Butler, T. Davinson, U. Datta Pramanik, J. Eberth, S. Franchoo, G. Georgiev, M. Górska, D. Habs, M. Huyse, O. Ivanov, J. Iwanicki, O. Kester, U. Koster, B. A. Marsh, O. Niedermaier, T. Nilsson, P. Reiter, H. Scheit, D. Schwalm, T. Sieber, G. Sletten, I. Stefanescu, J. Van de Walle, P. Van Duppen, N. Warr, D. Weisshaar, and F. Wenander

PAPER II: **$0_{\text{gs}}^+ \rightarrow 2_1^+$ Transition Strengths in ^{106}Sn and ^{108}Sn**

Physical Review Letters **101**, 012502 (2008).

A. Ekström, J. Cederkäll, C. Fahlander, M. Hjorth-Jensen, F. Ames, P. A. Butler, T. Davinson, J. Eberth, F. Fincke, A. Gorgen, M. Górska, D. Habs, A. M. Hurst, M. Huyse, O. Ivanov, J. Iwanicki, O. Kester, U. Koster, B. A. Marsh, J. Mierzejewski, P. Reiter, H. Scheit, D. Schwalm, S. Siem, G. Sletten, I. Stefanescu, G. M. Tveten, J. Van de Walle, P. Van Duppen, D. Voulot, N. Warr, D. Weisshaar, F. Wenander, and M. Zielińska

PAPER III: **Electric quadrupole moments of the 2_1^+ states in $^{100,102,104}\text{Cd}$**

Physical Review C **80**, 054302 (2009).

A. Ekström, J. Cederkäll, D. D. DiJulio, C. Fahlander, M. Hjorth-Jensen, A. Blazhev, B. Bruyneel, P. A. Butler, T. Davinson, J. Eberth, C. Fransen, K. Geibel, H. Hess, O. Ivanov, J. Iwanicki, O. Kester, J. Kownacki, U. Köster, B. A. Marsh, P. Reiter, M. Scheck, B. Siebeck, S. Siem, I. Stefanescu, H. K. Toft, G. M. Tveten, J. Van de Walle, D. Voulot, N. Warr, D. Weisshaar, F. Wenander, K. Wrzosek, and M. Zielińska

PAPER IV: **Coulomb excitation of the odd-odd Isotopes ^{106,108}In**
submitted to European Physical Journal A
A. Ekström, J. Cederkäll, D. D. DiJulio, C. Fahlander, M.
Hjorth-Jensen, A. Blazhev, B. Bruyneel, P. A. Butler, T.
Davinson, J. Eberth, C. Fransen, K. Geibel, H. Hess, O.
Ivanov, J. Iwanicki, O. Kester, J. Kownacki, U. Köster, B. A.
Marsh, P. Reiter, M. Scheck, B. Siebeck, S. Siem, I. Stefanescu,
H. K. Toft, G. M. Tveten, J. Van de Walle, D. Voulot, N. Warr,
D. Weisshaar, F. Wenander, K. Wrzosek, and M. Zielińska

PAPER V: **Determination of the isomeric fraction in a postaccelerated radioactive ion beam using the coupled decay-chain equations**
Accepted for publication in Nuclear Instruments and Methods
in Physics Research Section A.
A. Ekström, J. Cederkäll, D. D. DiJulio, C. Fahlander, and J.
Van de Walle

The papers are reprinted with the permission of the copyright holders:

American Physical Society
Research Road
Box 9000, Ridge
NY 11961-9000

Elsevier B.V.
Radarweg 29
1043 NX Amsterdam
The Netherlands

The cooperation of the copyright holders is gratefully acknowledged.

Publications not included in the thesis

Coulomb Excitation of ^{110}Sn using REX-ISOLDE

Physica Scripta **T125**, 190 (2006).

Proceedings of the International Conference on Finite Fermionic Systems: Nilsson Model 50 Years.

A. Ekström, J. Cederkäll, A. Hurst, C. Fahlander, A. Banu, P. Butler, J. Eberth, M. Gorska, D. Habs, M. Huyse, O. Kester, O. Niedermaier, T. Nilsson, M. Pantea, H. Scheit, D. Schwalm, G. Sletten, D. P. Ushasi, P. van Duppen, N. Warr, D. Weisshaar and the IS418 REX-ISOLDE ISOLDE collaborations

Measurement of the sign of the spectroscopic quadrupole moment for the 2_1^+ state in ^{70}Se : No evidence for oblate shape

Physical Review Letters **98**, 072501 (2007).

A.M. Hurst, P.A. Butler, D.G. Jenkins, P. Delahaye, F. Wenander, F. Ames, C.J. Barton, T. Behrens, A. Burger, J. Cederkäll, E. Clement, T. Czosnyka, T. Davinson, G. de Angelis, J. Eberth, A. Ekström, S. Franchoo, G. Georgiev, A. Gorgen, R.D. Herzberg, M. Huyse, O. Ivanov, J. Iwanicki, G.D. Jones, P. Kent, U. Koster, T. Kroll, R. Krucken, A.C. Larsen, M. Nespolo, M. Pantea, E.S. Paul, M. Petri, H. Scheit, T. Sieber, S. Siem, J.F. Smith, A. Steer, I. Stefanescu, N.U.H. Syed, J. de Walle, J. Van de Walle, P. Van Duppen, R. Wadsworth, N. Warr, D. Weisshaar, and M. Zielinska

Coulomb Excitation of Neutron-Rich Zn Isotopes: First Observation of the 2_1^+ State in ^{80}Zn

Physical Review Letters **99**, 142501 (2007).

J. Van de Walle, F. Aksouh, F. Ames, T. Behrens, V. Bildstein, A. Blazhev, J. Cederkall, E. Clement, T. E. Cocolios, T. Davinson, P. Delahaye, J. Eberth, A. Ekström, D. V. Fedorov, V. N. Fedosseev, L. M. Fraile, S. Franchoo, R. Gernhauser, G. Georgiev, D. Habs, K. Heyde, G. Huber, M. Huyse, F. Ibrahim, O. Ivanov, J. Iwanicki, J. Jolie, O. Kester, U. Koster, T. Kroll, R. Krucken, M. Lauer, A. F. Lisetskiy, R. Lutter, B. A. Marsh, P. Mayet, O. Niedermaier, T. Nilsson, M. Pantea, O. Perru, R. Raabe, P. Reiter, M. Sawicka, H. Scheit, G. Schrieder, D. Schwalm, M. D. Seliverstov, T. Sieber, G. Sletten, N. Smirnova, M. Stanoiu, I. Stefanescu, J.-C. Thomas, J. J. Valiente-Dobon, P. Van Duppen, D. Verney, D. Voulot, N. Warr, D. Weisshaar, F. Wenander, B. H. Wolf, and M. Zielinska

Coulomb excitation of neutron rich $^{138,140,142}\text{Xe}$ at REX-ISOLDE

European Physics Journal - Special Topics **150**, 127 (2007).

Proceedings of the 7th International Conference on Radioactive Nuclear Beams.

T. Kroll, T. Behrens, R. Krucken, V. Bildstein, R. Gernhauser, P. Maierbeck, I. Stefanescu, O. Ivanov, J. Van de Walle, N. Warr, P.A. Butler, J. Cederkäll, P. Delahaye, L.M. Fraile, G. Georgiev, U. Koster, T. Sieber, D. Voulot, F. Wenander, P.E. Kent, A. Ekström, K.H. Speidel, J. Leske, S. Schielke, D. Habs, R. Lutter, P. Thirolf, H. Scheit, and T. Davinson

Measurement of the sign of the spectroscopic quadrupole moment for the 2_1^+ state in ^{70}Se : No evidence for oblate shape

AIP Conference Proceedings **1012**, 296 (2008).

Proceedings of Frontiers in nuclear structure, astrophysics, and reactions - FINUSTAR 2.

A. Ekström, J. Cederkäll, C. Fahlander, M. Hjorth-Jensen, F. Ames, P.A. Butler, P.A. Butler, T. Davinson, J. Eberth, G. Georgiev, A. Gorgen, M. Gorska, D. Habs, M. Huyse, O. Ivanov, J. Iwanicki, O. Kester, U. Koster, B.A. Marsh, P. Reiter, H. Scheit, D. Schwalm, S. Siem, I. Stefanescu, G.M. Tveten, J. Van de Walle, P. Van Duppen, D. Voulot, N. Warr, D. Weisshaar, F. Wenander, and M. Zielinska

Coulomb excitation of the N=50 nucleus ^{80}Zn

AIP Conference Proceedings **1012**, 291 (2008).

Proceedings of Frontiers in nuclear structure, astrophysics, and reactions - FINUSTAR 2.

J. Van de Walle, F. Aksouh, F. Ames, T. Behrens, V. Bildstein, A. Blazhev, J. Cederkäll, E. Clement, T. E. Cocolios, T. Davinson, P. Delahaye, J. Eberth, A. Ekström, D. V. Fedorov, V. N. Fedosseev, L. M. Fraile, S. Franchoo, R. Gernhauser, G. Georgiev, D. Habs, K. Heyde, G. Huber, M. Huyse, F. Ibrahim, O. Ivanov, J. Iwanicki, J. Jolie, O. Kester, U. Koster, T. Kroll, R. Krucken, M. Lauer, A. F. Lisetskiy, R. Lutter, B. A. Marsh, P. Mayet, O. Niedermaier, T. Nilsson, M. Pan tea, O. Perru, R. Raabe, P. Reiter, M. Sawicka, H. Scheit, G. Schrieder, D. Schwalm, M. D. Seliverstov, T. Sieber, G. Sletten, N. Smirnova, M. Stanoiu, I. Stefanescu, J.-C. Thomas, J. J. Valiente-Dobon, P. Van Duppen, D. Verney, D. Voulot, N. Warr, D. Weisshaar, F. Wenander, B. H. Wolf, and M. Zielinska

Quadrupole collectivity of neutron-rich nuclei around ^{132}Sn

AIP Conference Proceedings **1012**, 84 (2008).

Proceedings of Frontiers in nuclear structure, astrophysics, and reactions - FINUSTAR 2.

T. Kroll, T. Behrens, R. Krucken, V. Bildstein, T. Faestermann, R. Gernhauser, M. Mahgoub, P. Maierbeck, A. Munch, W. Weinzierl, F. Ames, D. Habs, O. Kester, R. Lutter, T. Morgan, M. Pasini, K. Rudolph, P. Thirolf, J. Diriken, M. Huyse, O. Ivanov, P. Mayet, N. Patronis, I. Stefanescu, J. Van de Walle, P. Van Duppen, O. Niedermaier, H. Scheit, D. Schwalm, J. Eberth, F. Finke, D. Martin, P. Reiter, A. Scherillo, M. Seidlitz, N. Warr, D. Weisshaar, J. Iwanicki, P. Butler, J. Cederkäll, E. Clement, P. Delahaye, L.M. Fraile, G. Georgiev, U. Koster, T. Sieber, D. Voulot, F. Wenander, S. Franchoo, A. Hurst, A. Ekström, P.E. Kent, K.H. Speidel, J. Leske, S. Schielke, A. Jungclaus, V. Modamio, J. Walker, L. Coquard, M. Pantea, N. Pietralla, T. Davinson, and S. Nardelli

Interplay between single-particle and collective effects in the odd-A Cu isotopes beyond N=40

Physical Review Letters **100**, 112502 (2008).

I. Stefanescu, G. Georgiev, D. L. Balabanski, N. Blasi, A. Blazhev, N. Bree, J. Cederkäll, T. E. Cocolios, T. Davinson, J. Diriken, J. Eberth, A. Ekström, D. Fedorov, V. N. Fedosseev, L. M. Fraile, S. Franchoo, K. Gladnishki, M. Huyse, O. Ivanov, V. Ivanov, J. Iwanicki, J. Jolie, T. Konstantinopoulos, Th. Krll, R. Krcken, U. Kster, A. Lagoyannis, G. Lo Bianco, P. Maierbeck, B. A. Marsh, P. Napiorkowski, N. Patronis, D. Pauwels, G. Rainovski, P. Reiter, K. Riisager, M. Seliverstov, G. Sletten, J. Van de Walle, P. Van Duppen, D. Voulot, N. Warr, F. Wenander, and K. Wrzosek

Enhanced strength of the $2_1^+ \rightarrow 0_{\text{gs}}^+$ transition in ^{114}Sn studied via Coulomb excitation in inverse kinematics

Physical Review C **78**, 031303(R) (2008).

P. Doornenbal, P. Reiter, H. Grawe, H. J. Wollersheim, P. Bednarczyk, L. Caceres, J. Cederkäll, A. Ekström, J. Gerl, M. Górska, A. Jhingan, I. Kojouharov, R. Kumar, W. Prokopowicz, H. Schaffner, and R. P. Singh

Low-energy Coulomb excitation of neutron-rich zinc isotopes

Physical Review C **79**, 014309 (2008).

J. Van de Walle, F. Aksouh, T. Behrens, V. Bildstein, A. Blazhev, J. Cederkäll, E. Cément, T. E. Cocolios, T. Davinson, P. Delahaye, J. Eberth, A. Ekström, D. V. Fedorov, V. N. Fedosseev, L. M. Fraile, S. Franchoo, R. Gernhauser, G. Georgiev, D. Habs, K. Heyde, G. Huber, M. Huyse, F. Ibrahim, O. Ivanov, J. Iwanicki, J. Jolie, O. Kester, U. Koster, T. Kroll, R. Krcken, M. Lauer, A. F. Lisetskiy, R. Lutter, B. A. Marsh, P. Mayet, O. Niedermaier, M. Pantea, R. Raabe, P. Reiter, M. Sawicka, H. Scheit, G. Schrieder, D. Schwalm, M. D. Seliverstov, T. Sieber, G. Sletten, N. Smirnova, M. Stanoiu, I. Stefanescu, J.-C. Thomas, J. J. Valiente-Dobń, P. Van Duppen, D. Verney, D. Voulot, N. Warr, D. Weisshaar, F. Wenander, B. H. Wolf, and M. Zielinska

AUTHOR'S CONTRIBUTION

- **Paper I:** I participated in the experiment and analyzed the data. I took part in writing the published article.
- **Paper II:** I participated in the experiment, carried out the data analysis, and did the shell-model investigation. I also prepared and wrote the published article.
- **Paper III:** I participated in the experiment, carried out the data analysis, and did the shell-model investigation. I also prepared and wrote the published article.
- **Paper IV:** I participated in the experiment, carried out the data analysis, and did the shell-model investigation. I also prepared and wrote the submitted manuscript.
- **Paper V:** I implemented the method, wrote the χ^2 -analysis software, and carried out the GEANT4 simulations. I also prepared and wrote the published article.

The MED-to-ROOT format-conversion software and the offline event-builder were written as part of the thesis work. The renormalization of the nucleon-nucleon interaction, perturbative construction of the effective interaction, as well as the shell-model calculations were carried out using computer codes that were developed by the theoretical nuclear physics group at Oslo University.

I also participated in other experiments at ISOLDE CERN, GSI Darmstadt, and INFN Legnaro.

CONTENTS

1	Introduction	1
2	Experimental method	7
2.1	RIB production at ISOLDE	8
2.1.1	Isotope selection and postacceleration	9
2.1.2	Isobaric contamination from surface ionization	10
2.2	The MINIBALL Ge-detector array	12
2.2.1	γ -ray energy and efficiency calibration	12
2.3	The double-sided silicon-strip detector	14
2.3.1	Energy and position calibration	15
2.4	The data acquisition and event building	16
2.4.1	Detector signals	16
2.4.2	Particle- γ ray coincidence	16
2.4.3	Other signals	17
2.4.4	Computational environment	18
2.4.5	Physical event structure	18
2.5	Semiclassical Coulomb excitation	21
2.5.1	The excitation probability	22
2.5.2	Application to experiments	26
2.5.3	Quantal effects, conversion and atomic electrons	32
3	Data analysis and results	33
3.1	Particle data	33
3.1.1	The two-particle (2p) and one-particle (1p) events	34
3.2	Particle γ -ray coincidence	35
3.3	Doppler correction	39
3.3.1	Doppler correction without particle identification	40
3.4	Measured γ -ray yields	42
3.5	Beam composition analysis	54
3.5.1	Isobaric purity of the Sn and Cd RIBs	54
3.5.2	Correlation between laser power and beam purity	55
3.5.3	A coupled decay-chain analysis of the beam content	56
3.6	Extraction of the nuclear moments	64
3.6.1	$^{106,108,110}\text{Sn}$	64
3.6.2	$^{100,102,104}\text{Cd}$	66
3.7	Observed γ -ray transitions in $^{106,108}\text{In}$	75

4	Theoretical interpretation	79
4.1	Shell-model calculations	79
4.1.1	Single-particle energies	82
4.1.2	Effective charges	84
4.2	The effective two-body interaction	85
4.3	Renormalization of the free NN-interaction	87
4.3.1	The CD-Bonn and N3LO potentials	89
4.4	Shell-model interpretation of the Sn isotopes	91
4.5	Generalized seniority in the Sn isotopes	94
4.6	Shell-model interpretation of the Cd isotopes	100
4.7	Shell-model calculations in $^{106,108}\text{In}$	104
5	Summary and outlook	107
6	Popularized summary in Swedish	109
	Acknowledgements	111
A	γ-ray transitions	113
A.1	Selection rules	113
A.2	Transition rates	114
A.3	Mixing ratios	115
B	Two-body kinematics	117
B.1	Transformation of the cross section	118
B.2	Relativistic transformation	119
	Bibliography	121
 Paper I		
Sub-Barrier Coulomb Excitation of ^{110}Sn and Its Implications for the ^{100}Sn Shell Closure		
 Paper II		
$0_{\text{gs}}^+ \rightarrow 2_1^+$ Transition Strengths in ^{106}Sn and ^{108}Sn		
 Paper III		
Electric quadrupole moments of the 2_1^+ states in $^{100,102,104}\text{Cd}$		
 Paper IV		
Coulomb excitation of the odd-odd Isotopes $^{106,108}\text{In}$		
 Paper V		
Determination of the isomeric fraction in a postaccelerated radioactive ion beam using the coupled decay-chain equations		

CHAPTER 1

INTRODUCTION

Research in fundamental nuclear physics is driven by the urge to understand the interaction between nucleons and from this describe all the properties of the atomic nucleus in a unified theory. Available nuclear models are in general very good at explaining and predicting experimental observations such as nuclear masses and binding energies, the degree of deformation, and regularities in the energy spectra. However, each model is usually limited to a certain domain of phenomena. For instance, the energy spectra of a deformed and rotating nucleus is well understood in the collective nuclear model of Bohr and Mottelson whereas other models must be employed for e.g. a quantitative description of alpha decay.

The nuclear shell-model is the most successful theoretical framework for understanding the atomic nucleus in terms of its constituent nucleons. In the shell-model, the nucleons are, to first order, moving independently in a static potential created by all the other nucleons. This view is motivated by the short-ranged nature of the strong nuclear force in combination with the fact that the nucleons are on average quite far apart due to the Pauli principle. The single-nucleon energy levels of the shell model are ordered in a certain way and bunched into groups referred to as major shells. This explains the experimental observation that nuclei with so-called magic proton or neutron numbers 2,8,20,28,50,82, and 126 are particularly stable. The primary mechanism responsible for this bunching of the single-particle orbits is the spin-orbit force [1]¹ acting between the nucleons. Experiments also show that several nuclear properties can be ascribed to the valence protons and/or neutrons residing in the orbits above completely filled major proton and neutron shells, see e.g. Ref. [2]. The filled major shells are referred to as the core and are treated as one entity in the shell-model. This greatly reduces the dimensionality of the many-body problem and thus enables a numerical solution.

¹It was introduced by M. Goeppert-Mayer and J. H. D. Jensen in 1949. For this, they shared the Nobel Prize in physics in 1963 together with E. P. Wigner.

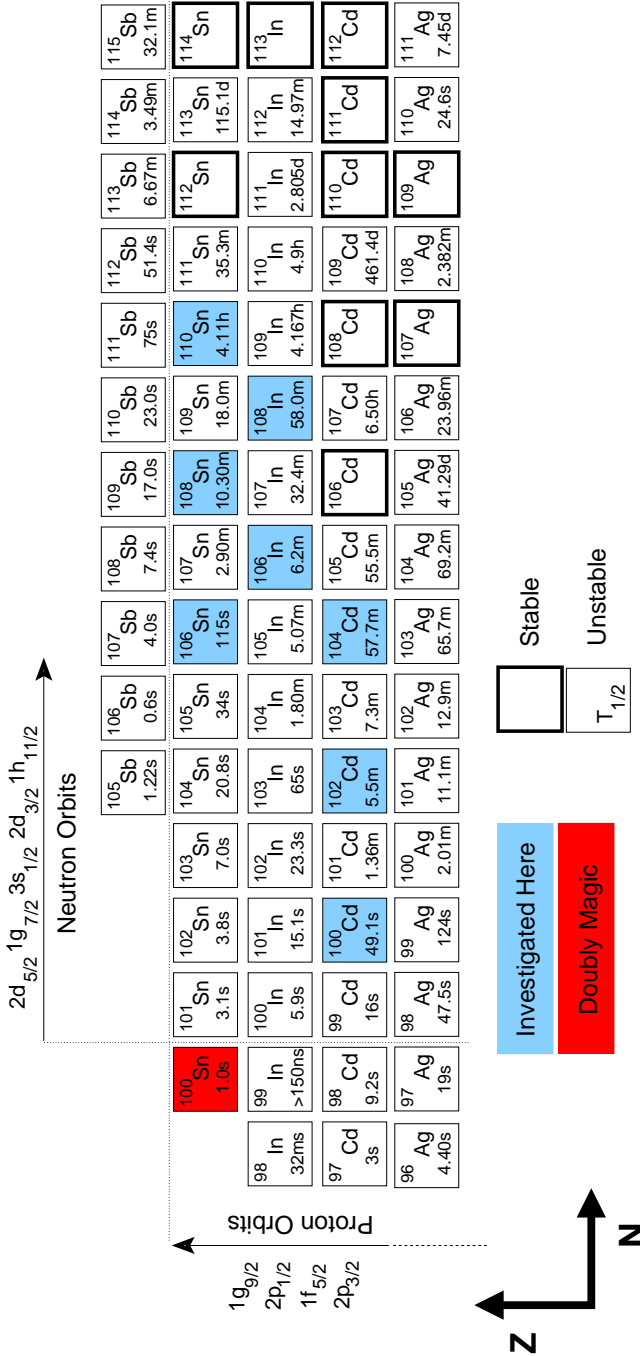


Figure 1.1: The nuclear chart in the region of ^{100}Sn and the isotopes that are investigated in this thesis. The proton and neutron single-particle orbits of relevance are indicated.

The many-body Schrödinger equation for A nucleons interacting via a two-body force $v(i, j)$ is given by

$$\left(\sum_{i=1}^A -\frac{\hbar}{2m} \nabla_i^2 + \sum_{i<j}^A v(i, j) \right) \Psi(1, 2, \dots, A) = E \Psi(1, 2, \dots, A) \quad (1.1)$$

where Ψ is the many-body wave function. In the shell-model approach one introduces a single-particle potential $U(i)$. This is the static one-body field created by the $A - 1$ nucleons in which the i th nucleon is moving. This is not given a priori. A common choice for $U(i)$, which is also implemented here, is the harmonic oscillator. In particular, it allows for separate analytical expressions for the center-of-mass motion and the relative single-particle motion. Equation 1.1 can be written

$$\left(\left[\sum_{i=1}^A -\frac{\hbar}{2m} \nabla_i^2 + U(i) \right] + \underbrace{\left[\sum_{i<j}^A v(i, j) - \sum_i^A U(i) \right]}_{V_R} \right) \Psi = E \Psi \quad (1.2)$$

where V_R is the residual interaction. There exists no unified description or method for deriving this from fundamental physical principles. Instead there are several different methods for approximating it. However, its documented weak strength enables a perturbative solution of the many-body Schrödinger equation. Experimentally, the nuclear wave functions, and thus the residual interaction, are probed by measuring the quantum mechanical observables.

So far, a vast majority of the experimental data comes from stable isotopes and nuclei in the vicinity of the line of β -stability. Current research in nuclear physics is geared towards exploring isotopes further from stability. Technical developments have opened up new regions of the nuclear chart for detailed experimental investigations. Studies of nuclei with more extreme proton-to-neutron ratios reveal or enhance various facets of the nuclear force. The most prominent feature is perhaps the appearance of new magic numbers due to the 'drift' of the single particle orbits. In addition, the nuclear structure of unstable isotopes is intimately connected with understanding nucleosynthesis in e.g. novae and supernovae.

This thesis presents an experimental study of electric-quadrupole transition probabilities² – $B(E2)$ values – between nuclear states in the unstable isotopes $^{106,108,110}\text{Sn}$, $^{100,102,104}\text{Cd}$, and $^{106,108}\text{In}$, see Fig. 1.1. The energies, spins, and parities of the excited states are rather well known in these nuclei. However, a transition probability is more sensitive to small variations in the structure of

²The transition probability is inversely proportional to the lifetime of the decaying state.

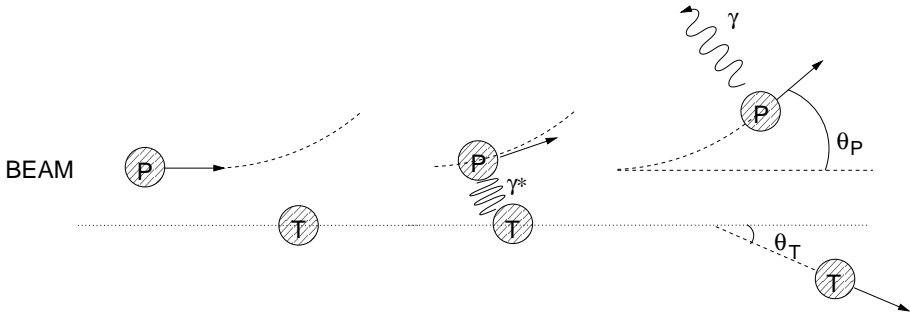


Figure 1.2: *Coulomb excitation is a nuclear scattering technique for measuring transition probabilities between nuclear states. In the collision between a projectile (P) and a target (T) nucleus, a nuclear excitation in the projectile (target) can be induced by the long-ranged electric force of the target (projectile). The populated state(s) subsequently de-excite via the emission of γ -rays and/or conversion electrons. The detection of these and the scattered particles provide a measure of the excitation cross section. In addition, for limited beam energies, the Coulomb barrier prevents the nuclei from contact. This removes any interference of the strong nuclear force in the excitation process.*

the nuclear wave function and therefore depends in detail on the properties of the residual interaction. Thus it provides a good benchmark for shell-model calculations. The experimental results presented here are interpreted by shell-model calculations based on residual interactions that are derived from QCD and multimeson-exchange nucleon-nucleon potentials. In particular, this thesis explores the neutron degree of freedom with respect to the ^{100}Sn nucleus in the light Sn and Cd isotopes. It is found that a renormalization of the neutron effective charge is required in order to understand the data.

The one-to-one proton-to-neutron ratio of the doubly-magic ^{100}Sn nucleus provides a unique opportunity to study the nucleon-nucleon interaction between protons and/or neutrons in identical single-particle orbits. Therefore the isotopes with one or two neutrons/protons more or less than ^{100}Sn are particularly interesting. However, ^{100}Sn is rather far from the line of β -stability, see Fig. 1.1, and presently it is not possible to produce the amounts required for an investigation of its excited states. However the evolution of the low-lying nuclear structure in Sn, Cd, and In, as a function of the neutron degree of freedom, is equally interesting. This allows for a systematic investigation of the observed regularities and its dependence on the number of nucleons outside the doubly-magic ^{100}Sn nucleus.

A transition probability can be expressed in terms of Weisskopf units (W.u.) [3]. In a certain sense, this unit reflects the number of particles that participate in the transition from one nuclear state to another. The $B(E2; 0_{\text{gs}}^+ \rightarrow 2_1^+)$ values that are measured in this work are of the order 10 W.u. and are thus collective in their nature³. From a simple shell-model perspective it is natural to assume that the transition probabilities in e.g. $^{106,108,110}\text{Sn}$ will decrease as one approaches ^{100}Sn . However, the transition strength could receive a sizable contribution from the nucleons in the ^{100}Sn core. Therefore, the physics case presented in this thesis primarily addresses whether or not the current understanding of the nucleon-nucleon interaction can reproduce the low-energy nuclear-structure of unstable nuclei in the vicinity of ^{100}Sn .

The transition probabilities were measured using Coulomb excitation, see Fig. 1.2. This is a well known experimental method [4, 5]. It depends only on the electromagnetic interaction and therefore enables a model-independent study of atomic nuclei. For the neutron-deficient even-mass Sn isotopes in particular, this method is the only option for measuring the $B(E2; 0_{\text{gs}}^+ \rightarrow 2_1^+)$ values. This is due to the higher lying nano-second isomeric 6_1^+ states present in these isotopes. These states hamper any lifetime measurements of the lower-lying 2_1^+ states if they are populated from above. It is virtually impossible to resolve the \sim ps lifetime of a 2_1^+ state from the decay curve of a \sim ns state. This issue is circumvented in Coulomb excitation since the 2_1^+ states are populated directly from the ground states.

The radioactive ion beams (RIB) were provided at the ISOLDE facility at CERN. This is one of few facilities in the world where it is possible to produce and postaccelerate unstable isotopes. Similar setups exist at e.g. TRIUMF in Canada, ORNL-HRIBF in USA, GANIL in France, and RIKEN in Japan but no other facility can produce the multitude of beams that ISOLDE does. Radioactive isotopes have been produced for 40 years at ISOLDE. It was only very recently that postacceleration became possible. This is essential for carrying out Coulomb excitation experiments since the excitation cross section in principle increases exponentially with the beam energy. RIB-based Coulomb excitation measurements enable a type of precision studies of exotic nuclei that have been successfully carried out in stable isotopes in the past.

³Highly collective excitations with transition probabilities > 100 W.u. are common in e.g. deformed rare-earth nuclei.

CHAPTER 2

EXPERIMENTAL METHOD

The postaccelerated radioactive ion beams (RIBs), partly consisting of the isotope under study, are bombarded onto the micrometer thick isotopically enriched secondary target. This is placed inside a vacuum chamber with a diameter of 184 mm. The Rutherford scattered projectile and target nuclei are detected by a circular Double-Sided Silicon Strip Detector (DSSSD) positioned 3 cm downstream of the target. The chamber is surrounded by the 24 Ge-crystals of the MINIBALL detector array. In the collisions between the projectile and the target nuclei there is a probability that the electromagnetic field of the projectile (target) induces a nuclear transition $|i\rangle \rightarrow |f\rangle$ in the target (projectile), where $|i\rangle$ and $|f\rangle$ represent the initial and final states. The probability for populating one or several excited states in the projectile and the target nuclei is given by the Coulomb excitation cross sections σ^{proj} and σ^{targ} . The Coulomb excitation cross section depends on the mass and proton numbers of the participating nuclei, the scattering angle of the particles in the center of mass frame of reference, the beam energy, and the structure of the wave functions of the initial and final nuclear states. The latter dependence provides a method to probe the nuclear wave function in terms of the transition probabilities between the populated states and the ground state of the nucleus. In the experiments that are presented here, the projectile excitation cross sections are determined using the following relation

$$\sigma^{\text{proj}} = \sigma^{\text{targ}} \cdot \frac{N_{\gamma}^{\text{proj}}}{N_{\gamma}^{\text{targ}}} \cdot \frac{\varepsilon_{\gamma}^{\text{targ}}}{\varepsilon_{\gamma}^{\text{proj}}} \cdot \frac{1}{\mathcal{P}} \cdot W \quad (2.1)$$

where N_{γ} represents the detected γ -ray yields from the de-excitation of the populated states in the projectile and target nuclei. The absolute normalization of the experimental data is provided by the known target excitation cross section. The remaining quantities on the right hand side are the γ -ray detection efficiencies ε_{γ} of the MINIBALL array, the isotopic purity \mathcal{P} of the RIB, and a correction, W , reflecting the differences in the form of the angular distributions of the γ -rays emitted from the scattered projectile and target nuclei. Every factor in Eq. 2.1 will be explained in detail below.

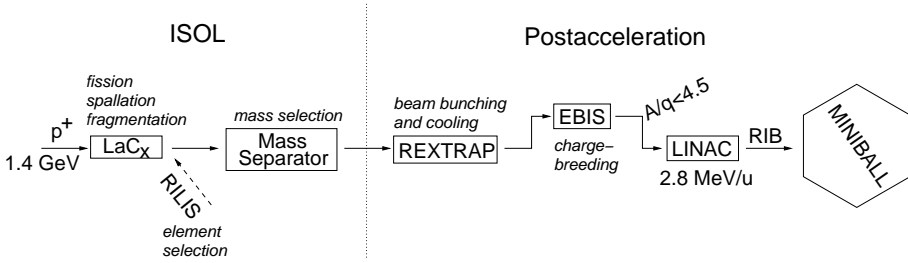


Figure 2.1: RIB production at ISOLDE together with an illustration of the postacceleration stage. The low energy ISOL-beam is trapped, charge bred, and postaccelerated to a final energy of 2.8 MeV/u.

Target	Isotope	Yield (ions/ μC)
70.4g $\text{LaC}_2\text{-C}$	^{110}Sn	$2.5 \cdot 10^8$
70.4g $\text{LaC}_2\text{-C}$	^{110}In	$2.5 \cdot 10^7$
70.4g $\text{LaC}_2\text{-C}$	$^{110}\text{In}^m$	$1\text{-}2 \cdot 10^7$
70.4g $\text{LaC}_2\text{-C}$	^{108}In	$5.5 \cdot 10^6$
70.4g $\text{LaC}_2\text{-C}$	^{106}In	$3.0 \cdot 10^6$
69.7g $\text{LaC}_2\text{-C}$	^{104}Cd	$2.0 \cdot 10^7$
69.7g $\text{LaC}_2\text{-C}$	^{102}Cd	$8.0 \cdot 10^5$
69.7g $\text{LaC}_2\text{-C}$	^{100}Cd	$8.5 \cdot 10^3$

Table 2.1: The primary target yields, when measured, are given in the standard unit of number of ions per μC . This can be transformed to the number of released ions per second by multiplying with the average proton beam current. If every other pulse of $3 \cdot 10^{13}$ protons is used the proton DC current is $2\mu\text{A}$.

2.1 RIB production at ISOLDE

A wide range of exotic isotopes are available at the ISOLDE facility. The unstable isotopes are produced using the Isotope Separator OnLine (ISOL) technique. The implementation of this method at ISOLDE is schematically illustrated in Fig. 2.1. A pulse of maximum $3.2 \cdot 10^{13}$ protons with an energy of 1.4 GeV is delivered every 1.2 seconds by the Proton Synchrotron Booster (PSB) of the CERN accelerator complex. These impinge on a thick primary target. For the present cases the target material consisted of $\text{LaC}_2\text{-C}$, i.e. lanthanum carbide. The choice of material is governed by the production cross section of the isotope under study. As a result of the high energy proton bombardment, a wide range of both stable and radioactive species form from the fission, fragmentation, and spallation reactions taking place in the target.

The produced isotopes diffuse through the target material and effuse into a transfer line leading to a hot ionizer cavity. The production and release of a certain isotope from the primary target material depends in an intricate way on the combination of the production cross section, the proton beam current, the type of target material, the target heating¹, and the chemical properties of the particular isotope etc. The measured primary-target production yields are given in Tab. 2.1. A list of the produced and postaccelerated RIBs used in the experiments presented here is given in Tab. 2.2.

RIB	Energy (MeV/u)	Intensity (ions/sec)	Purity(%)
¹¹⁰ Sn	2.82	$\sim 10^6$	90.0 ± 1.4
¹⁰⁸ Sn	2.82	$\sim 10^6$	59.0 ± 2.7
¹⁰⁶ Sn	2.83	$\sim 10^5$	29.2 ± 4.2
¹⁰⁴ Cd	2.87	$\sim 10^5$	99.0 ± 0.1
¹⁰² Cd	2.87	$\sim 10^5$	97.0 ± 0.3
¹⁰⁰ Cd	2.87	$\sim 10^3$	100.0 ± 10.0

Table 2.2: *The intensity of the postaccelerated beam is given in the third column. The purity \mathcal{P} refers to how much of the corresponding isotope that was present in the beam. The remaining fraction of the beam consisted of the surface ionized indium isobar.*

2.1.1 Isotope selection and postacceleration

The element of interest is singly ionized in the thin transfer line connecting the primary target and the ionizer cavity. The atoms are ionized by three laser beams with specific wavelengths [6] provided by the Resonance Ionization Laser Ion Source (RILIS) [7]. The 1^+ ions are subsequently extracted by the applied 60 kV electric field. Only the ⁵⁰Sn or the ⁴⁸Cd elements are selected using the RILIS. However, the postaccelerated RIBs also contains a certain fraction of the surface ionized [8] ⁴⁹In isobar, see Sec. 2.1.2. The indium component of the ^{100,102,104}Cd beams was suppressed using volatility-based selective trapping in the transfer line, see Sec. 2.1.2. The element(s) extracted from the cavity are isotopically separated using one of the two mass separators [9, 10] of the facility, i.e. the High Resolution Separator (HRS) or the General Purpose Separator (GPS). The design criteria of the mass-separation resolution ($\Delta M/M$) is 2400 and 5000 for the GPS and HRS, respectively. The ^{100,102,104}Cd beams are separated by the HRS while the GPS is employed for the remaining beams.

The low energy and singly-charged RIB is bunched and cooled in a Penning-type trap (REX-TRAP) using side-band cooling [11]. After a typical cycle time of 20 ms the cooled ion bunch is transferred to the Electron Beam Ion

¹The target was heated to 1800°-2000° depending on the run.

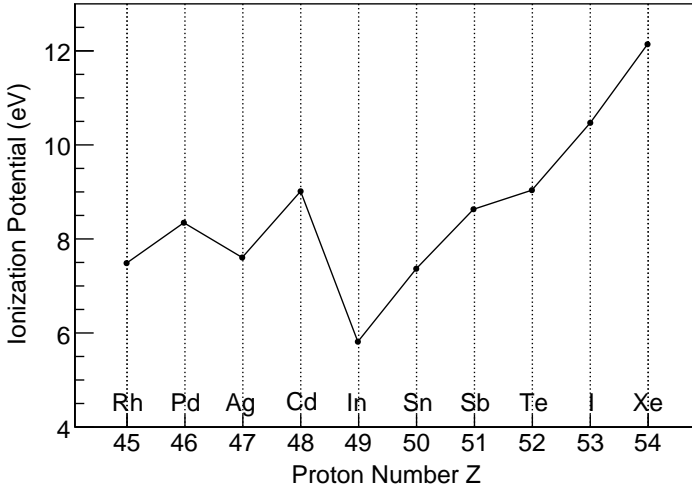


Figure 2.2: *Atomic ionization potentials for neutral atoms in the vicinity of $_{50}\text{Sn}$. The data are taken from Ref. [15].*

Source [12] (EBIS) of the facility for charge breeding. A 4.5 keV focused electron beam induces a stepwise stripping of the atomic electrons. The breeding time increases with the mass of the isotopes and the desired final charge state, e.g. to reach $^{108}\text{Sn}^{26+}$ requires 67 ms. The possibility of tuning the mass-to-charge ratio A/q in the EBIS extends the mass range of the ion beams that can be postaccelerated. The REX-LINAC [13] has an acceptance limit of $A/q < 4.5$. The temporal form and duration of the postaccelerated ions are governed by the release profile of the EBIS. The duration of the beam pulse delivered at the experimental setup is $\sim 500\mu\text{s}$. For the present cases, the final energy of the postaccelerated isotopes range between 2.82-2.87 MeV/u depending on the measurement, see Tab. 2.2. After the last bending magnet, which measures the final beam energy, the beam profile is typically 4 mm in diameter. The beam is focused onto the center of the target foil using a set of quadrupole magnets. The position of the beam is also monitored in a Parallel Plate Avalanche Counter (PPAC) [14] placed ~ 10 cm downstream of target chamber.

2.1.2 Isobaric contamination from surface ionization

The element $_{49}\text{In}$ has a low ionization potential compared to neighboring elements, see Fig. 2.2, and is singly ionized by surface ionization on the heated

walls of the cavity and the Tungsten transfer line². The reason for heating the transfer line and the ionization cavity, despite the apparent drawbacks of increased surface ionization, is the increased ionization efficiency of the RILIS [7].

Determination of the isobaric contamination

As mentioned, the projectile excitations cross sections are normalized with respect to the purity \mathcal{P} of the RIBs, see Eq. 2.1. Therefore, the beam composition is monitored during the experiments. The laser beams of the RILIS system can be temporarily blocked by a metallic plate. This mode of operation is referred to as 'laser off'. Without laser ionization, the postaccelerated Sn and Cd RIBs consist of only the ^{49}In isobar. On the other hand, during a 'laser on' period the mass-separated RILIS-ionized element is present. The ratio between the detected beam intensities in a laser off period and a laser on period of equal duration provides a measure of the beam purity \mathcal{P} , at that moment. The beam composition is monitored in this way by switching to laser on/off mode for one hour every three hours, approximately. The durations of consecutive laser on and laser off periods are governed by the PS signal which indicates the arrival of a new supercycle of protons from the PSB. The PS operates at a repetition period of 1.2 seconds times the number of proton pulses per supercycle. The length of this varies between 14-42 pulses depending on the measurement. The RIB composition can be monitored continuously throughout an entire experiment. However, this would reduce the intensity of the RIB. Instead, a time-averaged measure of \mathcal{P} is obtained by interpolating the periodical laser on/off measurements, see Sec. 3.5.1. During the ^{110}Sn measurement, the laser status, i.e. on or off, was not registered in the data acquisition system nor the data stream, see Sec. 2.4.3. Instead the RILIS was periodically blocked while the beam current was measured online using a Faraday cup that was located just before the secondary target.

Suppression of the isobaric contamination: thermochromatography

In the $^{100,102,104}\text{Cd}$ measurements the ^{49}In isobaric contamination is suppressed with a factor of ~ 100 , see Tab. 2.2, using a volatility based selection technique called isothermal vacuum chromatography [16, 17]. This method is implemented with a temperature controlled quartz-glass transfer tube³ placed in the primary target. In short, ^{48}Cd , with a normal boiling temperature of 767°C , is relatively more volatile than ^{49}In , that has a normal boiling temperature of 2080°C . The higher volatility of the group 12 elements (Zn,Cd,Hg) originates in a $d^{10}s^2$ atomic sub-shell closure that weakens the metallic bonding. The temperature of the quartz glass transfer tube is set such that the less volatile ^{49}In isotopes condense on its surface. Thus hindering any further propagation

²The probability of surface ionization is described by the Langmuir-Saha equation [8]. This depends on the ionization potential of the element, the temperature and work function of the surface

³melting point 1600°

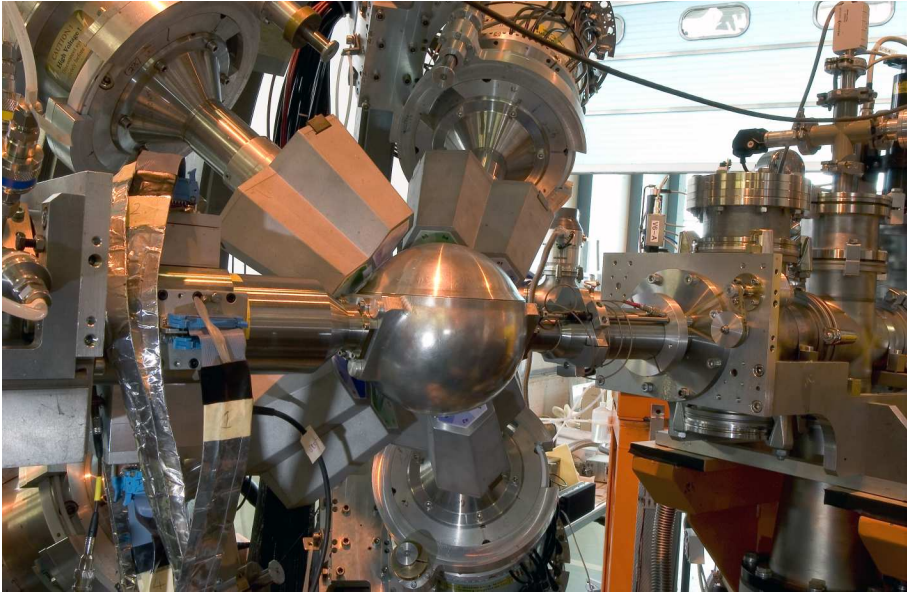


Figure 2.3: *A photograph of the MINIBALL Ge-detector array. Four of the eight triple-clusters and the spherical target chamber are visible.*

down the RIB production chain. This technique cannot be implemented for the Sn beams since the normal boiling temperature of ${}_{50}\text{Sn}$ is 2602°C .

2.2 The MINIBALL Ge-detector array

The MINIBALL Ge-detector array [18] consists of 24 high-purity Ge-crystals, see Fig. 2.3. A triple-cluster, consisting of three Ge-crystals, is connected to one liquid nitrogen cryostat and mounted on a movable mechanical frame. The eight triple-clusters are arranged in a spherical configuration at a distance of 125 mm from the secondary target. Each crystal is electrically divided into six segments which results in a total granularity of $8 \cdot 6 \cdot 3 = 144$ individual detection volumes in the MINIBALL array. The high granularity increases the angular resolution of the detected γ -rays to a level sufficient for Doppler correction, see Sec. 3.3. A depletion voltage of 2.5-4.5 kV, depending on the detector, is applied to each crystal through a central core electrode. The sum of the energies deposited in the segments are read from the core signal. The energy resolution at a γ -ray energy of 1 MeV is 2.9 keV.

Energy (keV)	Intensity (%)
121.8	28.58(6)
244.7	7.583(19)
344.3	26.5(4)
778.9	12.942(19)
964.1	14.605(21)
1085.9	10.207(21)
1112.1	13.644(21)
1408.0	21.005(24)

Table 2.3: The energy and intensity of the γ -rays following β -decay of ^{152}Eu that are used for the efficiency calibration of the MINIBALL array. Intensity values are taken from [19].

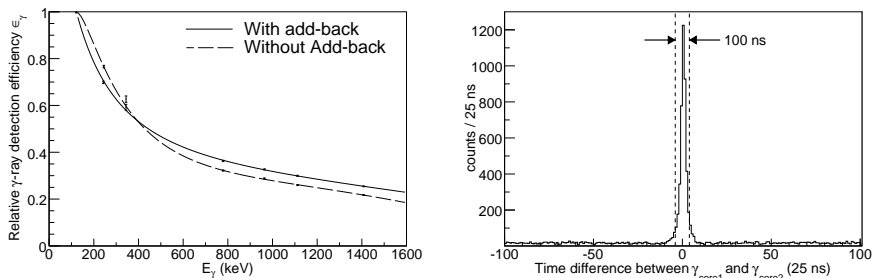


Figure 2.4: (Left) The relative γ -ray detection efficiency of the MINIBALL array as obtained from a ^{152}Eu calibration. (Right) The time-difference between two γ -rays detected in two different cores of the same triple-cluster. The deduced γ -ray addback gate of 100 ns is indicated.

2.2.1 γ -ray energy and efficiency calibration

The MINIBALL detector system is calibrated with respect to energy and detection efficiency using a well-known calibration source consisting of the β -unstable isotope ^{152}Eu . This is mounted in the secondary target position. According to Eq. 2.1 only the relative photopeak efficiencies ϵ_γ are needed in the analysis. These are obtained by comparing the detected γ -ray yields of the transitions listed in Tab. 2.3 with the known intensities.⁴ The energy dependence of ϵ_γ is fitted to the following function

$$\ln(\epsilon_\gamma) = \sum_{i=0}^4 A_i (\ln(E_\gamma))^i \quad (2.2)$$

⁴The absolute detection efficiency is $\sim 6\%$ at $E_\gamma = 1$ MeV.

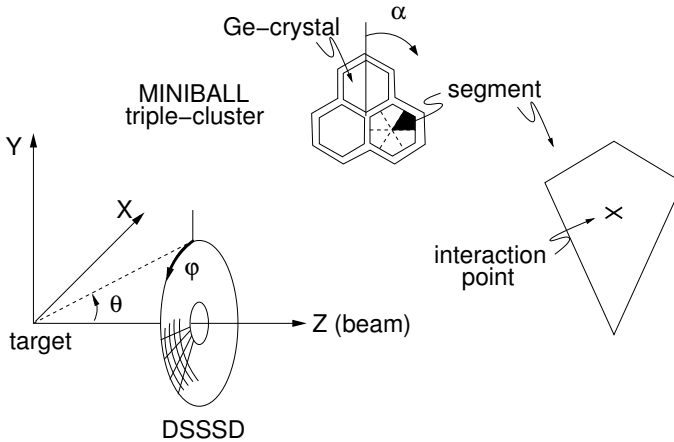


Figure 2.5: *The geometry and coordinate definition of the experimental setup. The triple-cluster can be rotated an angle α around its symmetry axis. Therefore, the position of each core is given by the angle α and the position of the center of the triple-cluster. Regarding the segments, these are identified with the polar coordinates (θ, φ) . The coordinate for each pixel of the DSSSD is defined from the same polar coordinate system.*

where A_i are the fitted parameters. The γ -ray detection efficiency is improved by an add-back algorithm. This is implemented in the following way. If two γ -rays are detected within 100 ns of each other in different Ge-crystals of the same triple-cluster their intensities are added, see Fig. 2.4. The segment signal with the highest energy is selected as the primary interaction point. Figure 2.4 shows the relative efficiency curve with and without add-back. The add-back algorithm increases the detection efficiency with $\sim 10\%$ at 1 MeV. The position of each segment is given by the polar coordinates (θ, φ) with respect to a right-handed coordinate system oriented such that the positive z -axis coincides with direction of the incoming beam, see Fig. 2.5. The interaction point of the detected γ -rays is defined as the geometrical center of gravity of the polygon-shaped front face of the segment crystal, see Fig. 2.5.

2.3 The double-sided silicon-strip detector

The scattered beam and target particles are detected by a circular Double Sided Silicon Strip Detector (DSSSD) [20]. The Si wafer thickness is $480 \mu\text{m}$ and the active area of the detector is 90.7% of the total area. A drawing and a photograph of the detector is shown in Fig. 2.6. It consists of four quadrants. These are treated individually in the data acquisition system and thus operates as independent particle detectors. The front side of the detector consists of 16

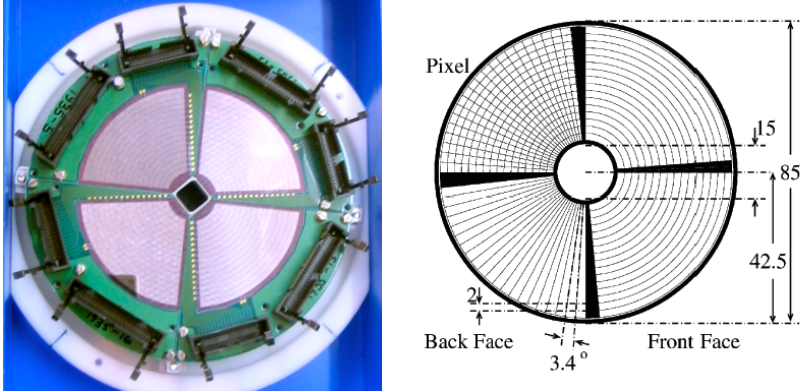


Figure 2.6: (left) A photograph of the DSSSD detector. (right) A schematic drawing showing the front/back segmentation. (Taken from Ref. [20])

annular strips of 1.9 mm width and 2 mm pitch. The back side consists of 24 radial sectors at 3.4° pitch. The combined segmentation of the front and back sides provides a total of $4 \cdot 12 \cdot 24 = 1152$ pixels. However, the 24 signals from the radial sectors on the back side are coupled into pairs in the electronic setup.

2.3.1 Energy and position calibration

For the $^{106,108}\text{Sn}$ and $^{106,108}\text{In}$ experiments the distance from the DSSSD to the secondary target is deduced from the hit-pattern of a triple- α source in the target position. For each strip, the ratio between the number of detected particles and the number of expected particles depends on the solid angle coverage of the detector. In turn, this depends on the known geometry of the DSSSD and the distance to the triple- α source. The detection efficiency is assumed to be equal for all strips in this analysis. Indeed, no effects related to a varying detection efficiency is observed in the detected particle intensities. The distance 30.0 ± 0.6 mm gives the best fit to the data. This distance is in accordance with the distance measured in the target chamber for that experimental campaign. For the other runs, a distance of 32.5 mm is measured directly from the setup.

The DSSSD is energy-calibrated in the offline analysis using the known kinematics of each run, see Sec. 3.1 and Appendix B. The energy calibration is required for the Doppler correction and indirectly for the integration of the Coulomb excitation cross section, see Sec. 2.5.2. The energy loss of the scattered beam and target particles as they traverse the $\sim 2 \mu\text{m}$ thick target foil is calculated using the SRIM computer code [21]. For example, the integrated

energy loss of a 300 MeV ^{106}Sn projectile as it passes a 2.25 μm thick ^{58}Ni target foil is 91 MeV.

2.4 The data acquisition and event building

A complete overview of the electronic setup for the data acquisition system is given in Ref. [22].

2.4.1 Detector signals

The pre-amplified signals from the strips of the DSSSD are further amplified by the Edinburgh/RAL 109 shaping amplifiers which also produce a time signal using a constant fraction discriminator. The energy signals of each quadrant are sent to a dedicated analogue peak sensing CAEN V785 ADC [23] and the time signals of each quadrant are sent to a dedicated V775 TDC [23]. It should be noted that the front strip time signals were not read out in the ^{110}Sn experiment. A summary of the ADC/TDC readout of the DSSSD is given in Tab. 2.4. For each quadrant, the OR of the time signals from the front and the back strips generate a ~ 15 ns wide logic 1 signal, which indicates the presence of an event in the corresponding DSSSD quadrant.

The six segment signals and the one core signal of each Ge-crystal are read out by two XIA Digital Gamma Finder (DGF-4C) modules [24]. Each DGF module has four input channels. The core signal is sent to channel 0 on the first module and the six segment signals are sent to remaining channels of the two modules. The time-stamping of the DGF modules is synchronized by a common 40 MHz clock. Furthermore, the readout of the DGF modules are synchronized by a BUSY-SYNCH loop. Whenever a DGF started a run the BUSY output is set to logic one. All the BUSY outputs are OR'ed in a fan-in/fan-out module and the output of this is sent back to the SYNCH-input of each module. In this way all the DGF modules have a common acquisition start and stop. The core signal triggers a 800 ns wide γ -gate which is joined with the particle signals in a coincidence unit.

2.4.2 Particle- γ ray coincidence

The DSSSD 15 ns logic 1 signal from each quadrant is gated in a coincidence (AND) unit with the DGF γ -gate. It should be noted that the particle signal is delayed 800 ns in order to compensate for the processing time of the DGFs. The coincidence unit generates a particle- γ coincidence trigger if any of the DSSSD quadrants give a front signal within the 800 ns wide γ -gate. The DSSSD event signal is split into three identical copies. One is sent to the coincidence unit, the second is sent directly to the trigger box where it is downscaled a factor

Experiment	DSSSD strips	TDC/ADC channels
^{110}Sn	Front annular 0-15	ADC 0-15 No TDC readout
	Back radial 0-11	ADC 16-27 TDC 0-11
$^{106,108}\text{Sn}$ In and Cd	Front annular 0-15	ADC 0-15 TDC 0-7
	Back radial 0-11	ADC 16-27 TDC 16-27

Table 2.4: *The layout of the hardware cabling of the ADC/TDC readout. The annular strips 0-15 of the front side of the DSSSD are numbered according to outer strip \rightarrow inner strip. The radial strips of the back side are numbered in the clockwise direction as seen from the incoming beam.*

2^n , and the third goes directly to a scaler that is read out every second⁵. The downsampled signal produces a particle- γ trigger for every detected 2^n th particle. The downscale factor is set to $2^6 = 64$ in all the experiments. This procedure saves bandwidth and reduces the size of the particle data outside the 800 ns coincidence window. The OR of the four outputs from the coincidence unit, one per DSSSD quadrant, generates the ADC gate and the TDC stop. Furthermore, the time stamping of the particles are synchronized with the γ -rays using four DGFs, one for each quadrant of the DSSSD.

2.4.3 Other signals

The typical EBIS breeding times for the current beams are 60-70 ms. The EBIS signal triggers a 800 μs long 'on-window' during which the data acquisition system is active. In this way the data acquisition system is synchronized with the operation of the EBIS and the REX-linac. The end marker of the on-window triggers the 800 μs off-window during which the data buffers of the ADC/TDC modules are read out again, in order to be empty for the next particle bunch. The EBIS signal is timestamped in a dedicated DGF. The impact of a proton pulse on the primary target (T1) and the start of a new proton supercycle (PS) are also timestamped in a DGF module.

Laser flag

The laser beams from the RILIS are used to extract the isobaric contamination of the RIB, see Sec. 2.1.2. For the $^{106,108}\text{Sn}$, $^{106,108}\text{In}$, and $^{100,102,104}\text{Cd}$ measurements the laser status, i.e. on or off, and the laser power of the RILIS laser are written to the data. The laser status is recorded in bit number 9 of

⁵This provides an average rate of the detected number of particles.

the pattern unit box and a measure of the laser power is sent to channel 29 in the ADC of DSSSD quadrant 1.

2.4.4 Computational environment

The data analysis described in Ch. 3 is carried out within the C++ based object-oriented ROOT [25] framework. During the experiments the data are stored in the MBS Event Data (MED) format [26]. The conversion software (mbs2root) from MED to ROOT was written as a part of the thesis work. The program is based on the MED-I/O libraries by R. Lutter. The MED data file contains a stream of event buffers that differ in format depending on the type of module that is read out.

- The buffer data from the XIA DGF-4C module data are written in the MARABOU MBS 10,2X format [26, 27]. The most significant information contained in these data buffers are
 - DGF Channel (0...3)
 - Energy value
 - Timestamp
 - Module number:
 - * 1-48: γ -ray data
 - * 49: DSSSD Quadrant 1 particle timestamp (ch 0)
 - * 50: DSSSD Quadrant 2 particle timestamp (ch 0)
 - * 51: DSSSD Quadrant 3 particle timestamp (ch 0)
 - * 52: DSSSD Quadrant 4 particle timestamp (ch 0)
 - * 53: EBIS timestamp (DGF Channel 0), T1 timestamp (DGF Channel 1), PS timestamp (DGF Channel 2)
- The data from the CAEN V7X5 ADC/TDC modules are written in the MARABOU MBS 10,4X format [26, 27]. Each buffer may contain up to 32 events. Each event contains
 - Module serial number
 - Channel: strip number according to Tab. 2.4
 - 12 bit Energy data (if ADC module)
 - 12 bit Time data (if TDC module)

This information is converted into ROOT format. At this point, no physical events are constructed.

2.4.5 Physical event structure

The construction of a physical event is dictated by the reconstruction of the physical particles. These are constructed from two coincident front and back strip events within each quadrant using the CAEN TDC time data. However, the lack of TDC front strip data in the ^{110}Sn experiment implies that a particle can be reconstructed only from the MED data buffers with a quadrant-multiplicity of one. For the other experiments the TDC front strip data is available, and a 90 ns coincidence gate between the front-back strip events is established. This increases the number of constructed particles with 80% compared to the ^{110}Sn experiment. Furthermore, 20% and 13% of the double-hits in adjacent front- or back-strips, respectively, are found to be coincident within 60 ns. These events are combined and the position of the particle is assigned to the strip with the highest energy. The particle time is set according to the corresponding DGF timestamp data. The γ -rays detected within $4\mu\text{s}$ of a physical particle are assigned to the particle event. A given γ -ray is maximally assigned to one event.

Two different types of particle events can occur. Due to the two-body character of the scattering process the projectile and target nuclei from a physical event should be detected in coincidence in opposite quadrants, see Fig. 2.7. This defines the two-particle (2p) event type. Particle identification is determined from the angular dependence of the detected energy, see Sec. 3.1 and Fig. 3.2. Depending on the details of the kinematics, one of the particles may scatter outside of the angular range of the DSSSD. Also, the CAEN modules of the DSSSD have a deadtime of about $10\mu\text{s}$. This implies that there are 1p events present also in the 2p angular interval. The missing particle is reconstructed from the energy and angle of the detected one.

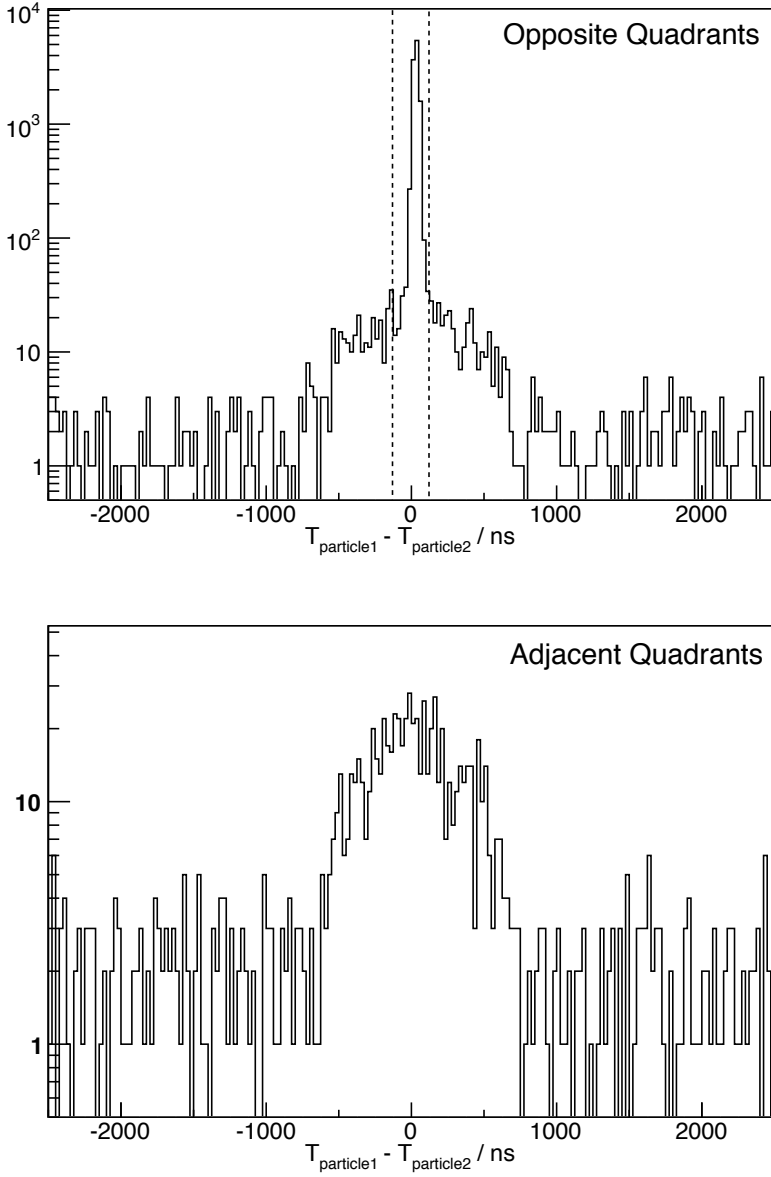


Figure 2.7: The time difference between two particles detected in (top) opposite quadrants or (bottom) adjacent quadrants of the DSSSD.

2.5 Semiclassical Coulomb excitation

In the semiclassical description of Coulomb excitation the relative motion of the projectile and target particles are described by hyperbolic orbits while the probability for finding either particle in an excited state after the collision is described by quantum mechanical perturbation theory. The applicability of this approach requires that the de Broglie wavelength λ is small compared to the dimensions of the classical orbits. This condition is fulfilled for large values of the Sommerfeld parameter η defined as

$$\eta = \frac{b}{2\lambda} = \frac{Z_p Z_t e^2}{\hbar v} \quad (2.3)$$

where v is the relative velocity of the particles at infinity, b is the distance of closest approach in a head-on collision⁶, and Z_p and Z_t are the proton numbers of the projectile and target nuclei. For the present experiments $\eta > 100$.

The onset of nuclear forces is expected to drop exponentially with the distance between the nuclear surfaces [5]. The projectile energy in the laboratory below which the strong nuclear force can be safely disregarded is given by [5]

$$E_{\text{safe}} = 1.44 \frac{A_p + A_t}{A_t} \frac{Z_p \cdot Z_t}{1.25(A_p^{1/3} + A_t^{1/3}) + 5} \text{MeV} \quad (2.4)$$

which corresponds to an internuclear surface-separation of 5 fm in a head-on collision. Furthermore, the transfer of energy, $\Delta E_{i \rightarrow f}$, and angular momentum, $\Delta \ell_{i \rightarrow f}$, in the Coulomb excitation induced transition between the nuclear states i and f must be small enough to not perturb the classical hyperbolic orbits of the particles, i.e

$$\Delta E_{i \rightarrow f}/E \ll 1 \text{ and } \Delta \ell_{i \rightarrow f}/\ell \ll 1 \quad (2.5)$$

where E is the center of mass energy and ℓ is the total angular momentum $\ell \approx m_0 v a = \hbar \eta$, where m_0 is the reduced mass of the particles. The inequalities in Eq. 2.5 hold for all the states that were populated in the present experiments. The probability for an excitation from the ground state i to the final state f can be estimated from the adiabaticity parameter defined as

$$\xi_{i \rightarrow f} = \frac{E_f}{\hbar} \tau = \frac{E_f}{\hbar} \frac{a}{v} \quad (2.6)$$

where the collision time τ is estimated from a/v . It should be noted that the probability for Coulomb excitation tends to zero exponentially for $\xi_{i \rightarrow f} \gtrsim 1$. The differential cross section for Coulomb excitation from the initial state i to the final state f is given by

$$\left. \frac{d\sigma}{d\Omega} \right|_{i \rightarrow f} = \frac{d\sigma}{d\Omega_R} P_{i \rightarrow f}(\theta) \quad (2.7)$$

⁶Half the distance of closest approach $a = b/2$ is given by $a = 0.719990(1 + A_p/A_t)Z_p Z_t/E_{p,\text{MeV}}^{\text{lab}}$ fm.

where the subscript R denotes the Rutherford cross section⁷ and P is the $i \rightarrow f$ excitation probability at the center of mass scattering angle θ .

The number of detected γ -rays N_γ from the $f \rightarrow i$ de-excitation of the projectiles per second can be estimated from

$$N_\gamma = 6.022 \cdot I_{\text{beam}} \frac{d_{\text{mg/cm}^2} \sigma_{\text{mb}}}{A_{\text{targ}}} \varepsilon_\gamma^{\text{absolute}} \times 10^{-7} \text{ s}^{-1} \quad (2.8)$$

where d is the thickness of the target foil in mg/cm^2 , A is the mass number of the target, σ is the cross section in mb, I_{beam} is the beam intensity in particles per second, and $\varepsilon_\gamma^{\text{absolute}}$ is the absolute γ -ray detection efficiency.

2.5.1 The excitation probability

The excitation probability $P_{i \rightarrow f}$ from the state $i = |I_i M_i\rangle$ to the state $f = |I_f M_f\rangle$ is given by the squared sum of the excitation amplitudes $a_{i \rightarrow f}$

$$P_{i \rightarrow f} = \frac{1}{2I_i + 1} \sum_{M_i M_f} |a_{i \rightarrow f}|^2 \quad (2.9)$$

where I and M are denote the spins and magnetic substates, respectively. If the excitation amplitude is small, it can be estimated from time-dependent perturbation theory. The magnitude of $a_{i \rightarrow f}$ depends on the strength of the electromagnetic interaction $V(\mathbf{r})$. This can be estimated from the action

$$\langle f | V(\mathbf{r}) | i \rangle \tau \quad (2.10)$$

evaluated at the distance of closest approach b and for a collision time $\tau = b/2v$. Thus, the strength of the electromagnetic interaction with the nucleus is characterized by

$$\chi = \frac{\langle f | V(b) | i \rangle b}{2\hbar v} \quad (2.11)$$

A multipole expansion of the electric field leads to a strength parameter for projectile excitation for each multipole order λ

$$\chi_{i \rightarrow f}^{(\lambda)} = \frac{\sqrt{16\pi}(\lambda - 1)!}{(2\lambda + 1)!!} \frac{Z_t e}{\hbar v} \frac{\langle I_i || E_\lambda || I_f \rangle}{a^\lambda \sqrt{2I_i + 1}} \quad (2.12)$$

The absolute square of this measures the λ -pole excitation probability for center a center of mass scattering angle $\theta = \pi$ and $\xi = 0$. Following a detailed discussion in Ref. [5] it is clear that the amplitudes $a_{i \rightarrow f}$ are very small for most cases and therefore a perturbative treatment of $a_{i \rightarrow f}$ is in general valid. For the present cases $\chi_{0 \rightarrow 2}^{\lambda=2} \lesssim 0.5$. To second order, the excitation amplitude is given by

$$a_{i \rightarrow f} = a_{i \rightarrow f}^{(1)} + a_{i \rightarrow f}^{(2)} \quad (2.13)$$

⁷ $\frac{d\sigma}{d\Omega_R} = \frac{1}{4} a^2 \sin^{-4} \frac{\theta}{2}$, where θ is the center of mass scattering angle

In the following, the discussion specified to the case of electric excitations⁸. Magnetic excitations are suppressed with a factor $(v/c)^2$ apart from any difference in the nuclear matrix element [5]. The electric multipole operator is given by

$$E(\lambda\mu) = \int \rho(\mathbf{r}) r^\lambda Y_{\lambda\mu}(\hat{\mathbf{r}}) d\tau \quad (2.14)$$

where the integration is performed over the charge density of the nucleus, $\lambda = 0, 1, 2, 3, \dots$, and $\mu = -\lambda, -\lambda + 1, \dots, \lambda$. The charge distribution ρ is defined in a coordinate system with origo in the center of mass of the projectile nucleus.

The first order expression for projectile electric excitation is given by

$$\begin{aligned} a_{I_i M_i \rightarrow I_f M_f}^{(1)} &= \frac{1}{i\hbar} \int_{-\infty}^{+\infty} dt \langle I_f M_f | V(t) | I_i M_i \rangle e^{\frac{i}{\hbar}(E_f - E_i)t} \\ &= \frac{4\pi Z_t e}{i\hbar v} \sum_{\lambda\mu} \frac{1}{a^\lambda} \frac{(\lambda-1)!}{(2\lambda+1)!!} \sqrt{\frac{2\lambda+1}{\pi}} (-1)^{I_i - M_i} \times \\ &\quad \begin{pmatrix} I_i & \lambda & I_f \\ -M_i & \mu & M_f \end{pmatrix} \langle I_i || E\lambda || I_f \rangle R_{\lambda\mu}(\theta, \xi) \end{aligned} \quad (2.15)$$

where $R_{\mu\nu}$ contains the integral over the hyperbolic orbit and θ is the center of mass scattering angle. The $R_{\mu\nu}$ function is treated in detail and evaluated numerically in Ref. [5].

The second order term is given by

$$\begin{aligned} a_{I_i M_i \rightarrow I_f M_f}^{(2)} &= \sum_z \left(\frac{-i}{\hbar} \right)^2 \int_{-\infty}^{+\infty} dt \langle I_f M_f | V(t) | I_z M_z \rangle e^{\frac{i}{\hbar}(E_f - E_z)t} \times \\ &\quad \int_{-\infty}^t dt' \langle I_z M_z | V(t') | I_i M_i \rangle e^{\frac{i}{\hbar}(E_z - E_i)t'} = \\ &= -\frac{1}{2} \sum_{\lambda\lambda'\mu\mu' I_z M_z} \sqrt{(2I_i+1)(2I_z+1)(2\lambda+1)(2\lambda'+1)} \times \\ &\quad (-1)^{I_i - M_i + I_z - M_z} \begin{pmatrix} I_i & \lambda & I_z \\ -M_i & \mu & M_z \end{pmatrix} \begin{pmatrix} I_z & \lambda' & I_f \\ -M_z & \mu' & M_f \end{pmatrix} \times \\ &\quad \chi_{i \rightarrow z}^{(\lambda)} \chi_{z \rightarrow f}^{(\lambda')} \times \{ R_{\lambda\mu}(\theta, \xi_{i \rightarrow z}) R_{\lambda'\mu'}(\theta, \xi_{z \rightarrow f}) + \\ &\quad \frac{i}{\pi} \mathcal{P} \int_{-\infty}^{+\infty} \frac{d\xi}{\xi} R_{\lambda\mu}(\theta, \xi_{i \rightarrow z} + \xi) R_{\lambda'\mu'}(\theta, \xi_{z \rightarrow f} - \xi) \} \end{aligned} \quad (2.16)$$

where $\xi = \xi_{i \rightarrow z} + \xi_{z \rightarrow f}$ and \mathcal{P} denotes the Cauchy principal value of the improper integral. In the above expression the summation runs over all inter-

⁸The magnetic excitation amplitudes are obtained in a similar fashion using instead the magnetic multipole operator $M(\lambda\mu) = \frac{-i}{c(\lambda+1)} \int \mathbf{j}(\mathbf{r}) r^\lambda (-i\mathbf{r} \times \nabla) Y_{\lambda\mu}(\hat{\mathbf{r}}) d\tau$

mediate states z , including i and f . The excitation probability to second order is given by the sum

$$P_{i \rightarrow f} = P_{i \rightarrow f}^{(1)} + P_{i \rightarrow f}^{(1,2)} + P_{i \rightarrow f}^{(2)} \quad (2.17)$$

where the superscripts indicate the order in the perturbative expansion and $P^{(1,2)}$ is the interference term. This term plays an important role in the evaluation of the Coulomb excitation cross sections that are presented here, in particular for the $^{100,102,104}\text{Cd}$ experiments. This is discussed further below. The excitation probabilities at each order are given by

$$P_{i \rightarrow f}^{(1)} = \sum_{\lambda} |\chi_{i \rightarrow f}^{(\lambda)}|^2 R_{\lambda}^2(\theta, \xi_{i \rightarrow f}) \quad (2.18)$$

$$\begin{aligned} P_{i \rightarrow f}^{(1,2)} = & \sum_{\lambda \lambda' \lambda'' I_z} \sqrt{(2I_z + 1)(2\lambda + 1)(2\lambda' + 1)(2\lambda'' + 1)} (-1)^{I_i + I_f} \times \\ & \left\{ \begin{array}{ccc} \lambda & \lambda' & \lambda'' \\ I_z & I_f & I_i \end{array} \right\} \chi_{i \rightarrow f}^{(\lambda)} \chi_{i \rightarrow z}^{(\lambda')} \chi_{z \rightarrow f}^{(\lambda'')} \times \\ & \sum_{\mu} R_{\lambda \mu}^*(\theta, \xi_{i \rightarrow f}) G_{(\lambda' \lambda'') \lambda \mu}(\theta, \xi_{i \rightarrow z}, \xi_{z \rightarrow f}) \end{aligned} \quad (2.19)$$

$$\begin{aligned} P_{i \rightarrow f}^{(2)} = & \frac{1}{4} \sum_{\substack{\lambda_1 \lambda'_1 \lambda_2 \lambda'_2 \\ I_z I_{z'} k}} \sqrt{(2I_z + 1)(2I_{z'} + 1)(2\lambda_1 + 1)(2\lambda'_1 + 1)(2\lambda_2 + 1)(2\lambda'_2 + 1)} \times \\ & (2k + 1) \left\{ \begin{array}{ccc} \lambda_1 & \lambda_2 & k \\ I_f & I_i & I_z \end{array} \right\} \left\{ \begin{array}{ccc} \lambda'_1 & \lambda'_2 & k \\ I_f & I_i & I_{z'} \end{array} \right\} \chi_{i \rightarrow z}^{(\lambda_1)} \chi_{z \rightarrow f}^{(\lambda_2)} \chi_{i \rightarrow z'}^{(\lambda'_1)} \chi_{z' \rightarrow f}^{(\lambda'_2)} \times \\ & \sum_{\kappa} \left[R_{(\lambda_1 \lambda_2) k \kappa}^* R_{(\lambda'_1 \lambda'_2) k \kappa} + G_{(\lambda_1 \lambda_2) k \kappa}^* G_{(\lambda'_1 \lambda'_2) k \kappa} \right] \end{aligned} \quad (2.20)$$

where for the interference and the second-order terms, two new spherical tensors that couple the $\lambda + \lambda'$ excitations have been defined according to

$$R_{(\lambda \lambda') k \kappa}(\theta, \xi_{i \rightarrow z}, \xi_{z \rightarrow f}) = \sum_{\mu \mu'} (-1)^{\kappa} \left(\begin{array}{ccc} \lambda & \lambda' & k \\ \mu & \mu' & -\kappa \end{array} \right) R_{\lambda \mu}(\theta, \xi_{i \rightarrow z}) R_{\lambda' \mu'}(\theta, \xi_{z \rightarrow f}) \quad (2.21)$$

and

$$G_{(\lambda \lambda') k \kappa}(\theta, \xi_{i \rightarrow z}, \xi_{z \rightarrow f}) = \sum_{\mu \mu'} (-1)^{\kappa} \left(\begin{array}{ccc} \lambda & \lambda' & k \\ \mu & \mu' & -\kappa \end{array} \right) G_{\mu \mu'}^{\lambda \lambda'}(\theta, \xi_{i \rightarrow z}, \xi_{z \rightarrow f}) \quad (2.22)$$

where

$$G_{\mu \mu'}^{\lambda \lambda'}(\theta, \xi, \xi') = \frac{1}{\pi} \mathcal{P} \int_{-\infty}^{+\infty} \frac{dq}{q} R_{\lambda \mu}(\theta, \xi + q) R_{\lambda' \mu'}(\theta, \xi' - q) \quad (2.23)$$

These expressions are evaluated numerically in e.g Refs. [4, 5, 28]. The $R_{\lambda\mu}$, $R_{(\lambda\lambda')k\kappa}$, and $G_{\mu\mu'}^{\lambda\lambda'}$ differ slightly in their ξ dependence. The $R_{\lambda\mu}$ of the first order term vanish exponentially with ξ [4], e.g. for large excitation energies. The $R_{(\lambda\lambda')k\kappa}$ is proportional to the product of the first order integrals and therefore also vanish exponentially with ξ . The $G_{\mu\mu'}^{\lambda\lambda'}$ functions vanish exponentially for large values of $|\xi_{i \rightarrow z} + \xi_{z \rightarrow f}|$, i.e. for a double excitation of a high energy state. However, if a low lying state is excited through an intermediate state of high energy, i.e. $\xi_{z \rightarrow f} \approx -\xi_{i \rightarrow z}$ the G function only vanish with $1/\xi$. In, general, this leads to a non-negligible impact of the higher lying states on the excitation cross section of the low-lying states. For the cases presented here, this effect is $\lesssim 1 - 2\%$ and taken into account.

As mentioned, the expressions presented above for the Coulomb excitation probability includes the intermediate states $|z\rangle$. For a case with several excited states, such as in the $^{106,108}\text{In}$ experiments, it is impractical to carry out the coupled summations. It is more convenient to diagonalize the coupled differential equations that describe the time evolution of the excitation amplitudes. The effects of the higher lying and excluded states are then included as a perturbation via a polarization potential, see Ref.[5]. This is the approach implemented in this thesis. The coupled equations were solved using the computer codes CLX [29] or GOSIA [30], see Sec. 3.6. In brief, the time evolution of the nuclear state vector $|\Psi(t)\rangle = \sum_n a_n(t)|n\rangle \exp(-iE_n t/\hbar)$ of the projectile is described by the Schrödinger equation

$$i\hbar \frac{d}{dt} \left(\sum_n a_n(t) |n\rangle \exp(-iE_n t/\hbar) \right) = V(t) \left(\sum_n a_n(t) |n\rangle \exp(-iE_n t/\hbar) \right) \quad (2.24)$$

Multiplying from the left with state $\langle m|$ gives a differential equation for $a_m(t)$

$$i\hbar \frac{d}{dt} a_m(t) = \sum_n a_m(t) \langle m|V(t)|n\rangle \exp(i(E_m - E_n)t/\hbar) \quad (2.25)$$

The initial conditions for this coupled set of equations are $a_n(t = -\infty) = \delta_{0n}$, i.e. the nucleus is initially in its ground state. After the collision, the excitation amplitudes are given by $|a_n(t = +\infty)|^2$.

Definition of the static and dynamic moments

The two main quantities that are measured in a Coulomb excitation experiment are the static quadrupole moment and the reduced transition probability.

1. The electric/magnetic transition probability between the states $|i\rangle$ and $|f\rangle$ is defined as

$$B(\mathcal{O}\lambda, I_i \rightarrow I_f) \equiv \frac{1}{2I_i + 1} |\langle i||\mathcal{O}\lambda||f\rangle|^2 \quad (2.26)$$

where $\mathcal{O}\lambda$ represents the electric/magnetic λ -pole operator.

2. The spectroscopic electric quadrupole moment for the state $|f\rangle$ is defined as

$$Q(I_f) \equiv \sqrt{\frac{16\pi}{5}} \begin{pmatrix} I_f & 2 & I_f \\ -I_f & 0 & I_f \end{pmatrix} \langle I_f || E2 || I_f \rangle = \sqrt{\frac{16\pi}{5}} \sqrt{\frac{I_f(2I_f-1)}{(I_f+1)(2I_f+1)(2I_f+3)}} \langle I_f || E2 || I_f \rangle \quad (2.27)$$

Note that a spin 0 and spin $\frac{1}{2}$ state does not possess a spectroscopic moment even if the intrinsic moment is non-zero. For the M1 operator, the magnetic dipole moment is defined as

$$\mu(I_f) \equiv \sqrt{\frac{4\pi}{3}} \sqrt{\frac{I_f}{(I_f+1)(2I_f+1)}} \langle I_f || M1 || I_f \rangle \quad (2.28)$$

2.5.2 Application to experiments

The Coulomb excitation cross section σ depends strongly on the projectile energy, the energy of the excited state, and on the product $Z_p Z_t$. This is exemplified in a set of calculations based on the projectile excitation of ^{108}Sn , see Fig. 2.8. The transition probability was set to the value determined in the analysis presented in Ch. 3. The differential cross section was integrated over the projectile scattering angles covered by the DSSSD, if nothing else is stated in the figure. It should be pointed out that in the data analysis the differential cross sections are also integrated over the thickness of the target foil. As is apparent from the panels in the figure, the projectile excitation cross section increases with the beam energy and the Z of the target. However, the increasing Coulomb barrier between the projectile and the heavier targets requires an equivalent increase in beam energy in order to exploit the larger Z value of target. Clearly, for the beam energy available at the REX-ISOLDE facility, the optimal projectile cross section for the ^{108}Sn case occurs for targets in the vicinity of ^{58}Ni .

The second order effects: double excitation and reorientation

The projectile and target isotopes in the experiments presented here are mostly even-even with a 0^+ ground state and a first excited 2^+ state. The next observed higher lying state is either a 2^+ or a 4^+ state. The second order effects occurring in Coulomb excitation are conveniently discussed if only one intermediate state $|z\rangle$ is included in Eqs.2.19-2.20. In the following a $0_{\text{gs}}^+ \rightarrow 2_1^+$ excitation in the presence of a second higher lying 2_2^+ state is discussed. A double excitation and the reorientation effect are schematically drawn in Fig. 2.9 In the case of a direct excitation $0_{\text{gs}}^+ \rightarrow 2_1^+$, the integrated Coulomb excitation cross

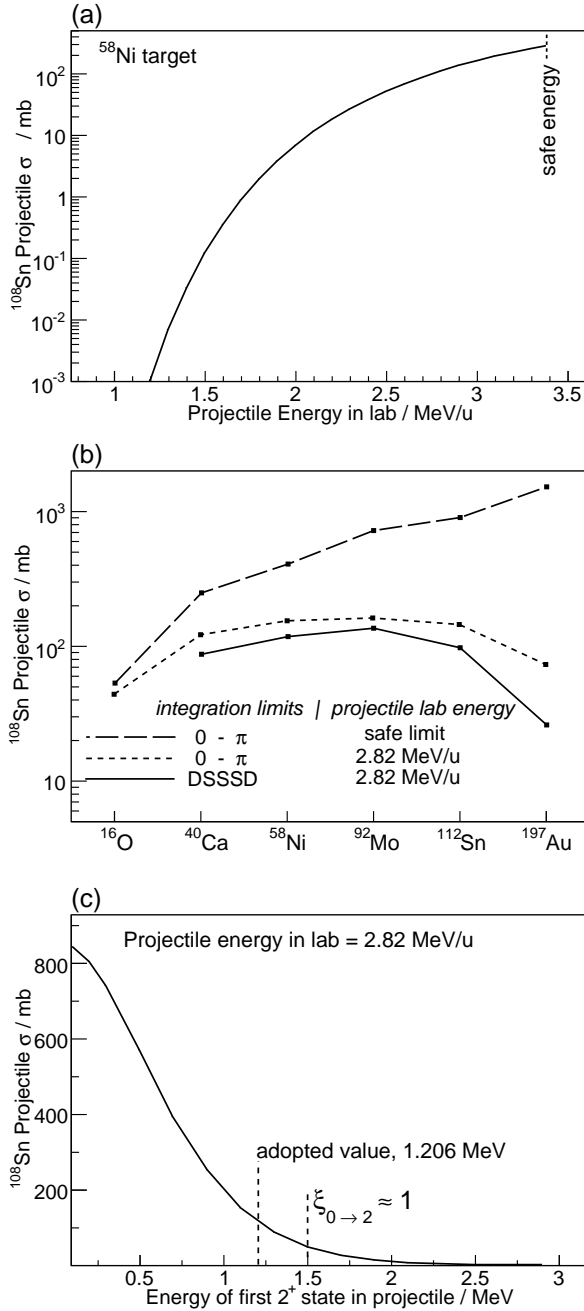


Figure 2.8: The ^{108}Sn projectile Coulomb excitation cross section vs (a) the projectile energy in the laboratory frame of reference (b) different targets (c) the energy of the 2_1^+ state. In the calculations, the value of $\langle 0_{\text{gs}}^+ || E2 || 2_1^+ \rangle$ was set according to the results from the data analysis, see Ch. 3.

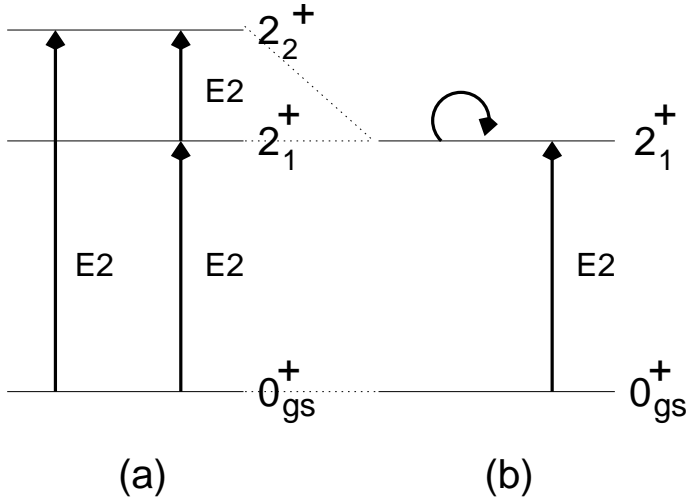


Figure 2.9: Two of the fundamental effects due to an intermediate state. (a) Double excitation: the $0_{\text{gs}}^+ \rightarrow 2_2^+$ excitation can proceed directly or through an intermediate state, which in the figure is the 2_1^+ state. (b) Reorientation effect: in a sense, this can be considered as a double-excitation where the 2_1^+ and 2_2^+ states in panel (a) coincide. This is indicated with a circular arrow. The strength of the reorientation effect is reflected in the $Q(2_1^+)$ value.

section for the projectile and target nucleus is to first order directly proportional to the corresponding $B(E2)$ value. The upper limit of the $P^{(1)}$ excitation probability is reached for $\theta = \pi$ and $\xi = 0$, hence $P_{0 \rightarrow 2_1}^{(1)} \leq |\chi_{0 \rightarrow 2_1}^{(2)}|^2$. The excitation from the ground state to the 2_2^+ state can proceed with a direct E2 transition or as a double excitation via the 2_1^+ state. The probability for the latter transition is given by the sum of the interference term $P_{0 \rightarrow 2_2}^{(1,2)} \propto \chi_{0 \rightarrow 2_2}^{(2)} \chi_{0 \rightarrow 2_1}^{(2)} \chi_{2_1 \rightarrow 2_2}^{(2)}$ and the second order term $P_{0 \rightarrow 2_2}^{(2)} \propto |\chi_{0 \rightarrow 2_1}^{(2)}|^2 |\chi_{2_1 \rightarrow 2_2}^{(2)}|^2$. However, the latter term is small compared to the former. The probability of a double-excitation depends on the E2-coupling between the states, the center of mass scattering angle as well as energy of both of the excited states through the adiabaticity parameters $\xi_{0 \rightarrow 2_2}$, $\xi_{0 \rightarrow 2_1}$, and $\xi_{2_1 \rightarrow 2_2}$. If instead the higher lying 2_2^+ state has spin and parity 4^+ , the first order and the interference excitation probabilities practically vanish since the E4 transition is orders of magnitude weaker than the E2 transition [31]. In this case, only the second order excitation probability $P_{0 \rightarrow 4}^{(2)} \propto |\chi_{0 \rightarrow 2_1}^{(2)}|^2 |\chi_{2_1 \rightarrow 4}^{(2)}|^2$ remains. This term is in principle proportional to the square of two first order probabilities and is the first sizable contribution to the cross section of a $0_{\text{gs}}^+ \rightarrow 4_1^+$ excitation via an intermediate 2_1^+ state.

The reorientation effect arises from the interference term $P^{(1,2)}$ and introduces a dependence of the static moment in the cross section. Indeed, if $2_2^+ = 2_1^+$, and higher the order corrections are neglected, then the expression for the excitation probability, Eq. 2.17, can be written

$$\begin{aligned}
 P_{0 \rightarrow 2} &= P_{0 \rightarrow 2}^{(1)} + P_{0 \rightarrow 2}^{(1,2)} = |\chi_{0 \rightarrow 2}^{(2)}|^2 R_2^2(\theta, \xi_{0 \rightarrow 2}) + \\
 &25 \left\{ \begin{array}{ccc} 2 & 2 & 2 \\ 2 & 2 & 0 \end{array} \right\} \chi_{0 \rightarrow 2}^{(2)} \chi_{0 \rightarrow 2}^{(2)} \chi_{2 \rightarrow 2}^{(2)} \sum_{\mu} R_{2\mu}^*(\theta, \xi_{0 \rightarrow 2}) G_{(22)2\mu}(\theta, \xi_{0 \rightarrow 2}, \xi_{2 \rightarrow 2}) = \\
 &= |\chi_{0 \rightarrow 2}^{(2)}|^2 R_2^2 \left(1 + \chi_{2 \rightarrow 2}^{(2)} \cdot 5 \cdot \frac{\sum_{\mu} R_{2\mu}^* G_{(22)2\mu}}{R_2^2} \right) = \\
 &= |\chi_{0 \rightarrow 2}^{(2)}|^2 R_2^2 \left(1 + \left[\frac{\sqrt{16\pi}}{15} \frac{Z_t e}{\hbar v} \frac{\langle 2^+ || E2 || 2^+ \rangle}{a^2 \sqrt{5}} \right] 5 \cdot \frac{\sum_{\mu} R_{2\mu}^* G_{(22)2\mu}}{R_2^2} \right) = \\
 &= |\chi_{0 \rightarrow 2}^{(2)}|^2 R_2^2 \left(1 + \left[\sqrt{\frac{7}{90}} \frac{Z_t e}{a^2 \hbar v} Q(2^+) \right] 5 \cdot \frac{\sum_{\mu} R_{2\mu}^* G_{(22)2\mu}}{R_2^2} \right) = \\
 &= 206.19045 \cdot \frac{A_{\text{proj}} E_{\text{beam, MeV}}^3}{Z_{\text{targ}}^2 Z_{\text{proj}}^4 (1 + A_{\text{proj}}/A_{\text{targ}})^4} \cdot B(E2; 0^+ \rightarrow 2^+)_{e^2 b^2 R_2^2} \\
 &\left(1 + 8.47465 \cdot \frac{A_{\text{proj}}^{1/2} E_{\text{beam, MeV}}^{3/2}}{Z_{\text{targ}} Z_{\text{proj}}^2 (1 + A_{\text{proj}}/A_{\text{targ}})^2} Q(2^+)_{\text{proj, eb}} 5 \cdot \frac{\sum_{\mu} R_{2\mu}^* G_{(22)2\mu}}{R_2^2} \right) \quad (2.29)
 \end{aligned}$$

Evidently the $B(E2)$ value and the $Q(2^+)$ value, including the sign, of the projectile nucleus can be determined from two independent cross section measurements. This approach is pursued in the study of $^{102,104}\text{Cd}$. However, the full coupled-channels theory of Coulomb excitation is used in the data analysis. Still, the expression in Eq. 2.29 gives an estimate of the contribution from the static moment to the excitation probability. For the case of a ^{104}Cd projectile with an energy of 2.87 MeV/u scattered against a ^{64}Zn target, the expression in Eq. 2.29 becomes

$$\begin{aligned}
 P_{0 \rightarrow 2} &= 206.19 \cdot \frac{104 \cdot 299^3}{30^2 \cdot 48^4 \cdot 2.6^4} \cdot B(E2 \uparrow) \cdot R_2^2 \\
 &\left(1 + 8.47 \cdot \frac{104^{1/2} \cdot 299^{3/2}}{30 \cdot 48^2 \cdot 2.6^2} Q(2_1^+) 5 \frac{\sum_{\mu} R_{2\mu}^* G_{(22)2\mu}}{R_2^2} \right) = \quad (2.30) \\
 &= 2.63 B(E2 \uparrow) \cdot R_2^2 \left(1 + 0.96 Q(2_1^+) \cdot 5 \frac{\sum_{\mu} R_{2\mu}^* G_{(22)2\mu}}{R_2^2} \right)
 \end{aligned}$$

In this case, the adiabaticity parameter is $\xi \approx 0.4$, and for a center of mass scattering angle $\theta = 100^\circ$ the orbital integrals R and G are according to Ref. [5] $R_2^2 \approx 0.18$ and $5 \frac{\sum_{\mu} R_{2\mu}^* G_{(22)2\mu}}{R_2^2} \approx 0.4$, thus

$$P_{0 \rightarrow 2} \approx 0.47 B(E2 \uparrow) \cdot (1 + Q(2_1^+) 0.38) \quad (2.31)$$

The numerical values for the transition probability and the quadrupole moment as deduced from the data analysis are e.g. $B(E2; 0^+ \rightarrow 2^+) = 0.35e^2b^2$ and $Q(2) = -0.23$, see Paper III. This leads to an excitation probability

$$P_{0 \rightarrow 2} \approx 0.16 \cdot (0.91) = 0.15 \quad (2.32)$$

In conclusion, for the present case the effects of the static quadrupole moment on the excitation probability is in the order of $\sim 10\%$. Therefore, a $\sim 1\%$ precision is required for the measured cross section in order to extract a static moment with $\sim 10\%$ precision. A computational multiple Coulomb excitation calculation, which includes an integration over the target thickness and the projectile scattering angles, gives $P_{0 \rightarrow 2} = 0.12$ for the current case. The differential Coulomb excitation cross section is shown in Fig. 2.10.

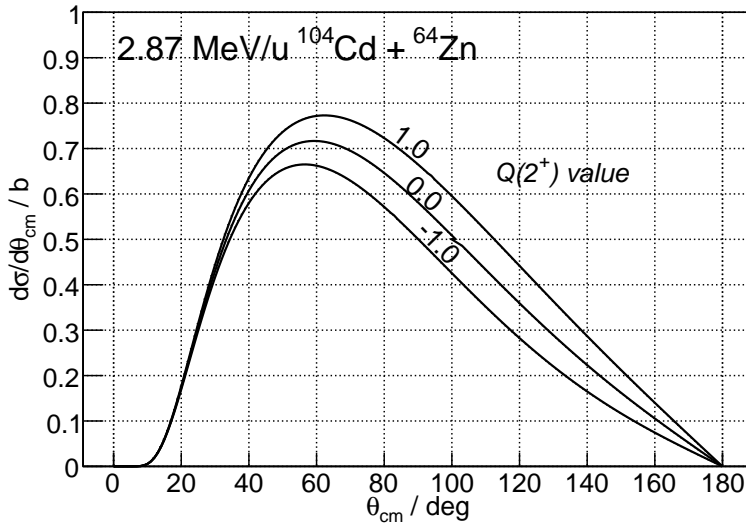


Figure 2.10: The differential Coulomb excitation cross section for 2.87 MeV/u $^{104}\text{Cd} + ^{64}\text{Zn}$ with $Q(2^+) = \{-1.0, 0.0, 1.0\}$ eb as indicated on the respective curve.

Angular distribution of de-excitation γ -rays

The states populated in Coulomb excitation are generally left with an unequal distribution with respect to the magnetic sub-states. Therefore, the de-excitation γ -rays are not emitted isotropically. The probability of observing a γ -ray in the solid angle element $d\Omega_\gamma$ while the nucleus is observed in $d\Omega_p$, is given by a differential cross section $d^2\sigma/(d\Omega_\gamma d\Omega_p)$. The explicit expressions

are given in Ref. [5]. Furthermore, the γ -rays are emitted in flight. Therefore, the angular distribution of the detected γ -rays will be shifted in the direction of motion of the nucleus. The angular distribution in the laboratory frame W_γ is calculated for each case using the computer code GOSIA [30]. The differential cross section for γ -ray emission is integrated over the energy loss of the particles in the target foil and the particle detection angles used in the analysis, see Fig. 2.11. As can be noted from the figure, the symmetric form of the

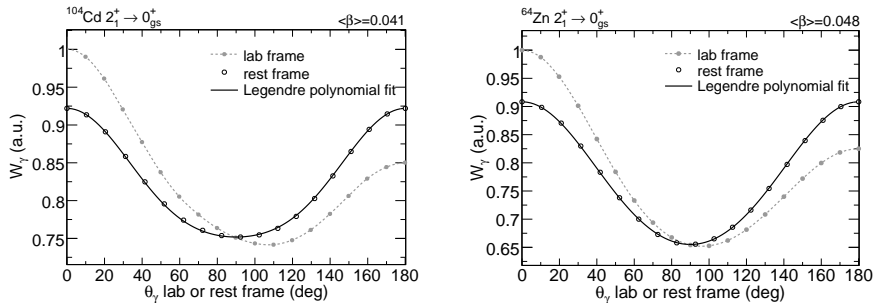


Figure 2.11: *The angular distribution of the emitted γ -rays in the $^{104}\text{Cd}+^{64}\text{Zn}$ experiment. The average velocity $\langle\beta\rangle$ used in the transformation from the laboratory frame to the rest frame is indicated in the upper right corner.*

angular distributions are retained if the calculated values are transformed to the rest frame of the emitting nucleus, see Appendix B. However, due to the integration over particle scattering angles, an average recoil velocity $\langle\beta\rangle$ must be introduced in the transformation.

The measured Coulomb excitation cross sections are corrected for the differences in the angular distributions of the detected γ -rays emitted by the projectile and target nuclei. The angular distribution correction factor W is defined as

$$W = \frac{w_\gamma^{\text{targ}}}{w_\gamma^{\text{proj}}} \quad (2.33)$$

where the angular distribution coefficient w_γ is obtained from the normalized integral of the angular distribution W_γ in the laboratory frame of reference. The integration limits are set according to the θ -coverage of the MINIBALL array. This is quite large, typically $30^\circ - 75^\circ$ and $100^\circ - 155^\circ$. Therefore, the correction factors W , see Tab. 2.5, are relatively small. For the same reason, the correction factors become rather insensitive to the integration over the projectile scattering angles.

Experiment	W
$^{110}\text{Sn}+^{58}\text{Ni}$	1.0084
$^{108}\text{Sn}+^{58}\text{Ni}$	0.9951
$^{106}\text{Sn}+^{58}\text{Ni}$	1.0068
$^{104}\text{Cd}+^{64}\text{Zn}$	0.9870
$^{104}\text{Cd}+^{109}\text{Ag}(311\text{ keV})$	1.0227
$^{104}\text{Cd}+^{109}\text{Ag}(415\text{ keV})$	1.0177
$^{102}\text{Cd}+^{64}\text{Zn}$	0.9958
$^{102}\text{Cd}+^{109}\text{Ag}(311\text{ keV})$	1.0294
$^{102}\text{Cd}+^{109}\text{Ag}(415\text{ keV})$	1.0251
$^{100}\text{Cd}+^{109}\text{Ag}(311\text{ keV})$	1.0396
$^{100}\text{Cd}+^{109}\text{Ag}(415\text{ keV})$	1.0362

Table 2.5: *The angular distribution correction factors $W = w_{\gamma}^{\text{targ}}/w_{\gamma}^{\text{proj}}$ for the experiments.*

2.5.3 Quantal effects, conversion and atomic electrons

The semiclassical derivation of the Coulomb excitation cross section is valid for $\eta \gg 1$, see Eq. 2.3. A fully quantum-mechanical derivation is given in Ref. [5] and discussed with respect to second order effects in Ref. [32]. The quantal correction C_{QM} to the semiclassical results decrease with increasing η and the corrected cross section σ can be written as

$$\sigma(\eta, \theta, \xi) = \sigma_{\text{classic}}(\theta, \xi) - \frac{1}{\eta^2} C_{QM}(\xi) \quad (2.34)$$

where C_{QM} is of order unity [5]. Most of the quantal corrections can be included by a proper symmetrization of the classical parameters η , ξ , and a see Refs. [4, 5]. This approximately accounts for the distortion of the classical hyperbolic trajectory caused by the energy transfer from the excitation process.

The excited states are not de-excited solely by the emission of γ -rays but also via internal conversion. This effect is accounted for in the analysis by using the internal conversion coefficients $\alpha(\lambda)$ of Ref. [33]. This effect is increasingly important for low energy γ -ray transitions and large proton numbers Z .

The postaccelerated isotopes are not completely stripped of their atomic electrons, but rather in a charge state $\sim +25$. The target isotopes are clearly surrounded by atomic electrons. The combined effect of the atomic electrons is reduction of the center of mass energy. This energy shift δE can be estimated from the Thomas-Fermi potential of atoms [5]. For the cases presented in this work, δE is less than 0.3% of the initial beam energy. This gives an effect on the cross sections that is smaller than 0.8%.

CHAPTER 3

DATA ANALYSIS AND RESULTS

The analysis of the particle and γ -ray part of the data consists of four sequential reductions that enable a statistically significant extraction of the detected γ -ray yields. The data reduction steps are:

- Particle- γ coincidence cut.
- Particle-Particle coincidence cut.
- Particle identification.
- Doppler correction of the detected γ -ray energy.

Each reduction is explained and demonstrated below.

3.1 Particle data

A typical scatter plot of the detected particles is shown in Fig. 3.1. Three observations can be made from this figure. Firstly, the angular dependence of the Rutherford cross section is clearly visible. Secondly, the beam is well centered. Thirdly, the innermost strip of the left quadrant is broken for the particular case that is shown. For the cases where an annular strip of the DSSSD is broken this is taken into account by correcting the integrated cross sections for the projectile and target nuclei accordingly. It should be noted that the data from the innermost annular strips are not used in the analysis of the Sn experiments. The case of one or several broken radial strips are handled in a similar fashion. Nevertheless, any broken strips, radial or annular, reduces the overall detection efficiency. Apart from the $^{100,102,104}\text{Cd}+^{109}\text{Ag}$ experiments the particle kinematics are always inverse, i.e. $A_{\text{proj}} > A_{\text{targ}}$. The detected particle energy versus scattering angle in the $^{110}\text{Sn}+^{58}\text{Ni}$ experiment is shown in Fig. 3.2. The effects due to the energy loss of the particles as they traverse the target foil is shown in Fig. 3.3 for the case of 2.82 MeV/u ^{110}Sn projectiles on a 2.0 mg/cm² thick ^{58}Ni target foil. The kinematics and the energy loss are calculated using Eqs. B.5- B.6 and the computer code SRIM [21]. The energy loss and the finite width of incoming beam adds a broadening of the kinematical branches. This is apparent from a set of Monte Carlo simulations of the detected particles as a function of the beam width and the target thickness, see Fig. 3.4.

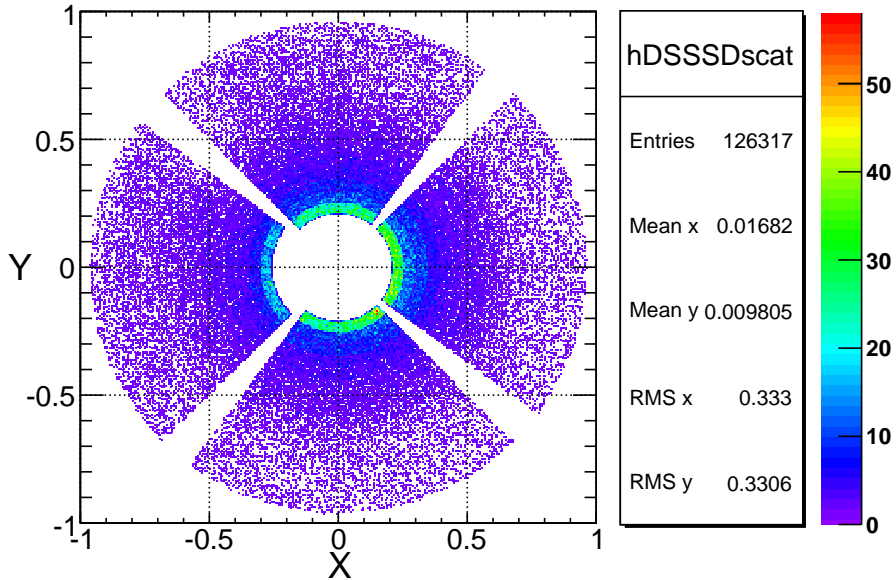


Figure 3.1: Particle hit pattern as detected by the DSSSD in the $^{104}\text{Cd} + ^{64}\text{Zn}$ experiment. See the text for details.

3.1.1 The two-particle (2p) and one-particle (1p) events

The two-particle (2p) event is defined in Sec. 2.4.5. This type of event is confined to a certain interval of the detected scattering angles, see Fig. 3.5. In the experiments with inverse kinematics, the 2p cut removes the projectile and target events below a certain annular strip of the DSSSD. In detail, the projectiles that scatter with a small angle in the laboratory system are detected with a higher energy. The accompanying target receives the remaining energy and is scattered with a large angle in the laboratory frame. Therefore, for the 2p events, the upper angular coverage of the DSSSD limits the detection of the high energy projectiles. Similarly, the detection of targets with high energy and small scattering angles are limited by the lower energy threshold of the DSSSD. The 2p-cut is applied to the data from the experiments with inverse kinematics for two reasons. Firstly, it improves the signal-to-background ratio of the particle- γ coincidences, see Fig. 3.6. This is due to the removal of the large fraction of coincidences at low angles and the fact that the condition of a second particle in the opposite quadrant reflects the two-body scattering process. Secondly, it is advantageous to remove the small angle events since the kinematical branches in this region merge. It should be pointed out that the majority of the projectile excitation cross section resides in the 2p angular region.

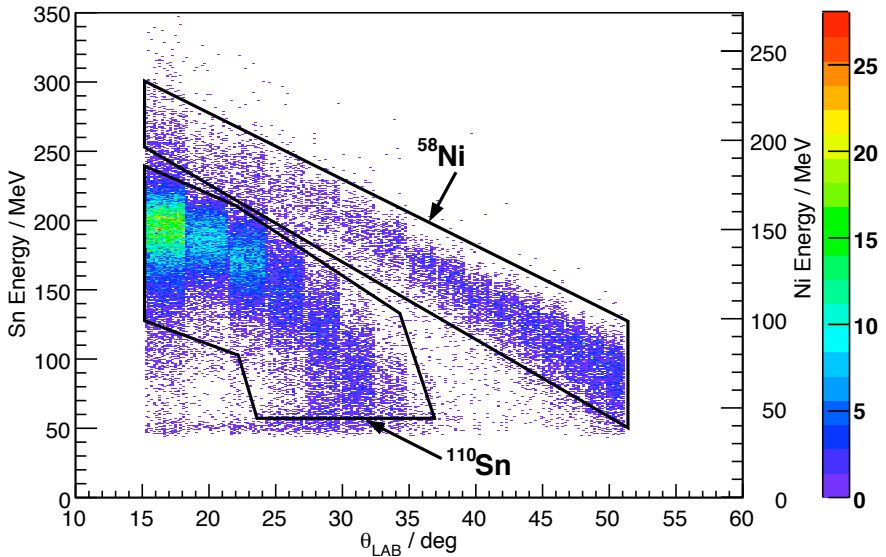


Figure 3.2: The two panels show the energy versus scattering angles for the detected particles in the $^{110}\text{Sn} + ^{58}\text{Ni}$ experiment.

The 1p event data is just as complete as the 2p event data apart from the larger fraction of random particle events, see Fig. 3.6. The undetected particles in the 1p data set are reconstructed event-by-event using the energy and angle of the detected particle. For the reconstruction of the energy it is assumed that the particle scattering took place in the center of the target.

3.2 Particle γ -ray coincidence

The prompt particle- γ coincidences are selected in the corresponding time-difference spectrum, see Fig. 3.6. This cut is set separately for each quadrant of the DSSSD and is typically 75-125 ns wide. The prompt coincidence peak is more prominent in the 2p subset of the data due to the particle-particle cut. This singles out the physically relevant events from the background very efficiently. A random background subtraction is only carried out for the $^{106,108}\text{In}$ γ -ray spectra where several weak γ -ray transitions are observed.

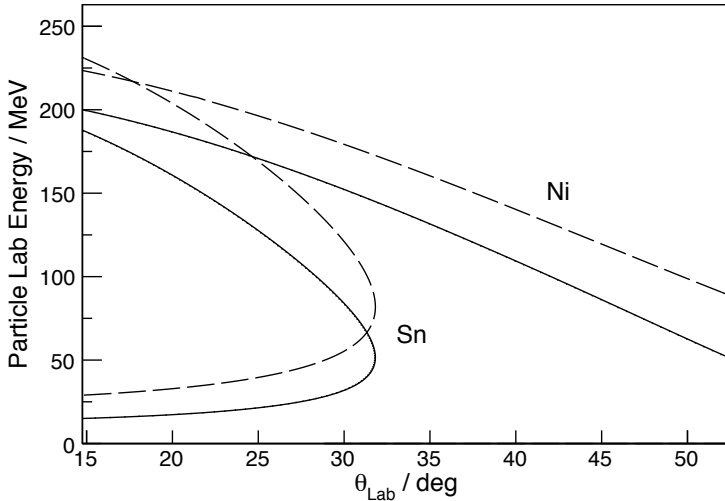


Figure 3.3: Calculated energy vs. scattering angle for $2.82 \text{ MeV/u } ^{110}\text{Sn}$ projectiles scattered against a 2.0 mg/cm^2 thick ^{58}Ni target foil. For the dashed curve it is assumed that the particles scatter in the center of the target. The solid curves include the energy loss from traveling through the remaining half of the target. It is interesting to note that one of the effects of the energy loss is that it further separates the two kinematical branches.

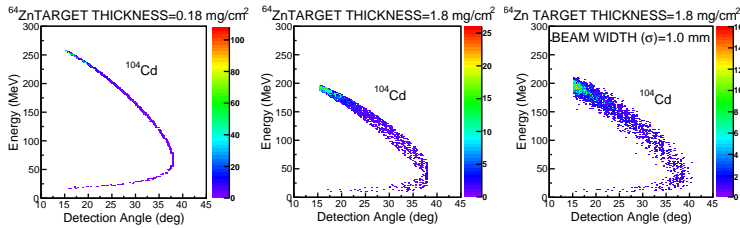


Figure 3.4: The panels show the results from a Monte Carlo simulation of the particle energy versus scattering angle as detected by the DSSSD. In the simulation, $2.87 \text{ MeV/u } ^{104}\text{Cd}$ projectiles are scattered against a 1.8 mg/cm^2 thick ^{64}Zn target foil. Starting from the left panel, the target thickness is 0.18 mg/cm^2 . In the middle panel the thickness is 1.8 mg/cm^2 . In the right panel, the beam spot is distributed according to a Gaussian with a standard deviation of 1 mm . This corresponds to an effective beam spot diameter of 4 mm .

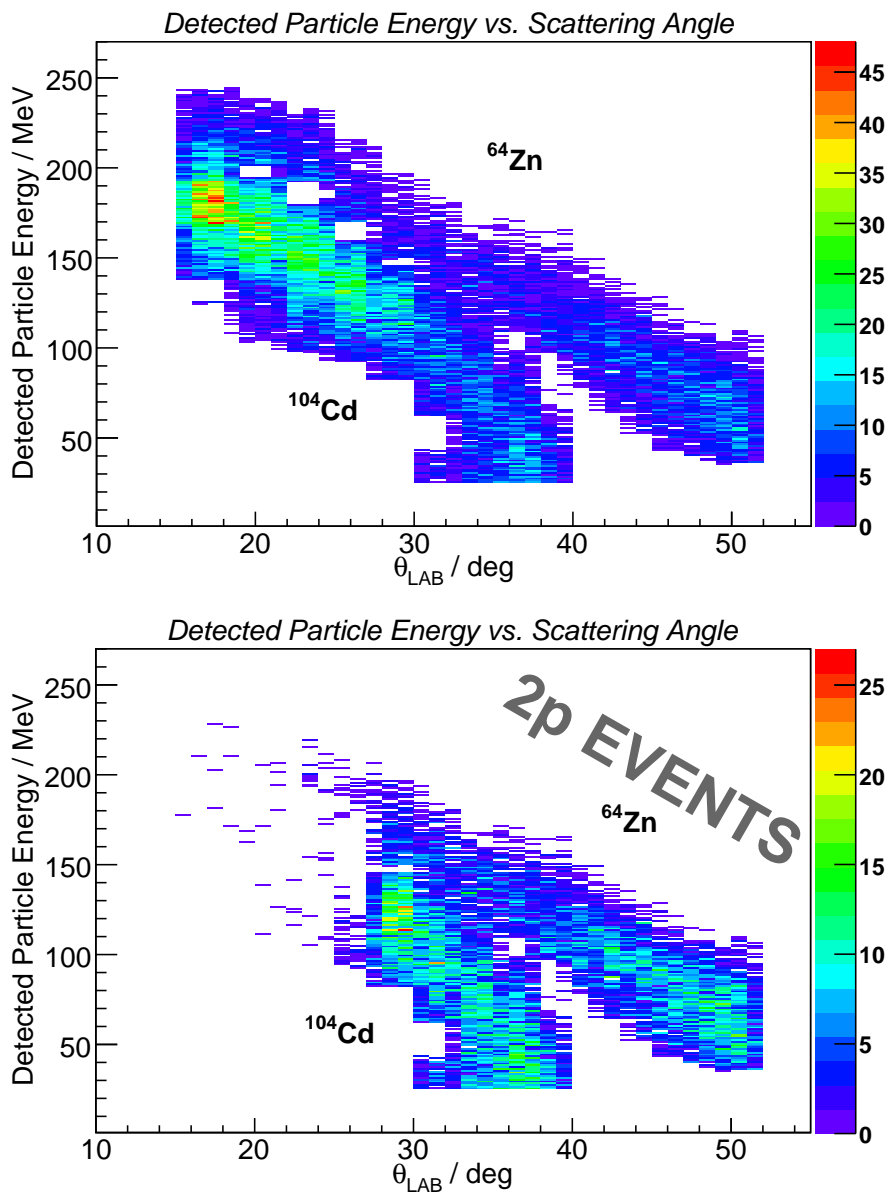


Figure 3.5: In the $^{104}\text{Cd}+^{64}\text{Zn}$ measurement the events below 27° are removed by the 2p cut.

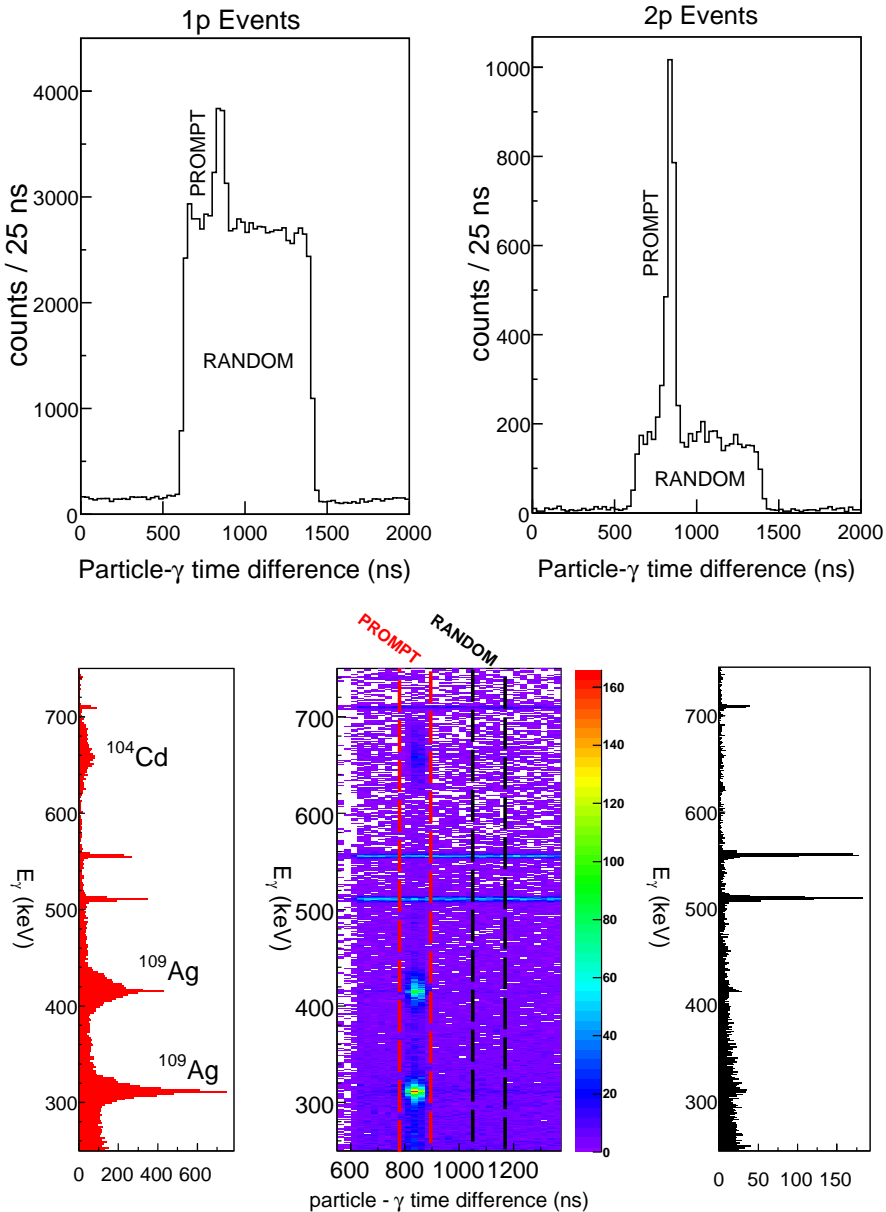


Figure 3.6: (Top) Particle γ -ray time-difference spectrum from the $^{102}\text{Cd}+^{64}\text{Zn}$ experiment. The spectra for the 1p and 2p events are shown separately. To the left and right of the random coincidences are the down-scaled events. The physical significance of the 2p events is reflected in the enhanced prompt coincidence peak. (Bottom) The two-dimensional distribution of the γ -ray energy versus the particle- γ time difference. The projections to the left and right show the γ -ray energy for prompt and random particle- γ time difference cuts.

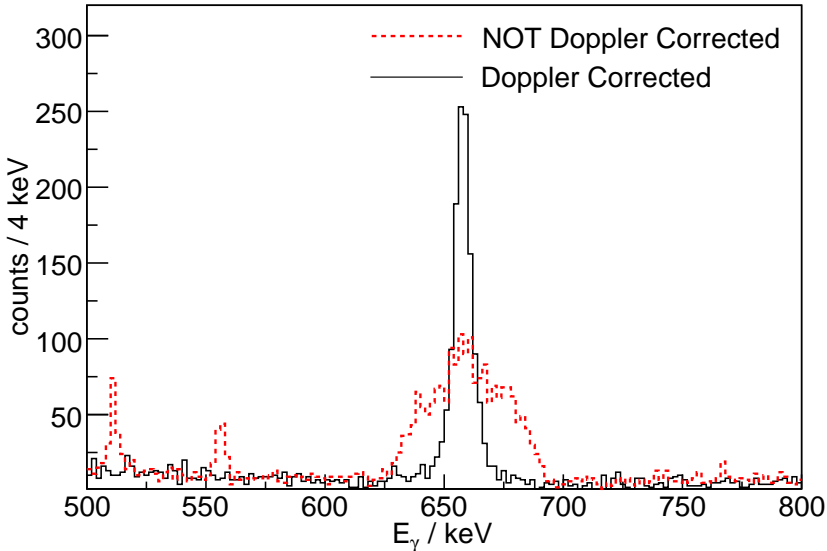


Figure 3.7: *Doppler Corrected gamma-ray energy spectrum. The prompt particle- γ gate is imposed. This spectrum is based on the $^{104}\text{Cd}+^{64}\text{Zn}$ data.*

3.3 Doppler correction

Due to the relativistic Doppler shift the energy E_{γ}^{LAB} of the detected γ -ray is different from its energy E_{γ}^{REST} in the rest frame of the nucleus it is emitted from. Furthermore, the Doppler shift depends on the emission angle $\theta_{p\gamma}$ of the γ -ray with respect to the direction of motion of the nucleus. Therefore the shifted peak will also be broadened. The angle $\theta_{p\gamma}$ is related to the detection angles θ_{γ} and φ_{γ} of the γ -ray and the detection angles θ_p and φ_p of the nucleus as

$$\cos \theta_{p\gamma}^{\text{LAB}} = \sin \theta_p \sin \theta_{\gamma} \cos(\varphi_p - \varphi_{\gamma}) + \cos \theta_p \cos \theta_{\gamma} \quad (3.1)$$

The detected γ -ray energy is related to the rest-frame γ -ray energy as

$$E_{\gamma}^{\text{REST}} = E_{\gamma}^{\text{LAB}} \cdot \gamma(1 - \beta \cdot \cos(\theta_{p\gamma}^{\text{LAB}})) \quad (3.2)$$

where the relativistic parameters are given by $\beta = v/c$ and $\gamma = 1/\sqrt{1 - \beta^2}$. The detection angles of the γ -ray are determined from the center of gravity of the segments of the MINIBALL detectors, see Fig. 2.5. The positions of the MINIBALL clusters are read from the holding-frame. These values are subsequently fine tuned in the software by rotating each of the triple-clusters, with the relative segment positions fixed according to the construction of the triple-cluster, until a minimum FWHM of the Doppler corrected γ -ray peak is

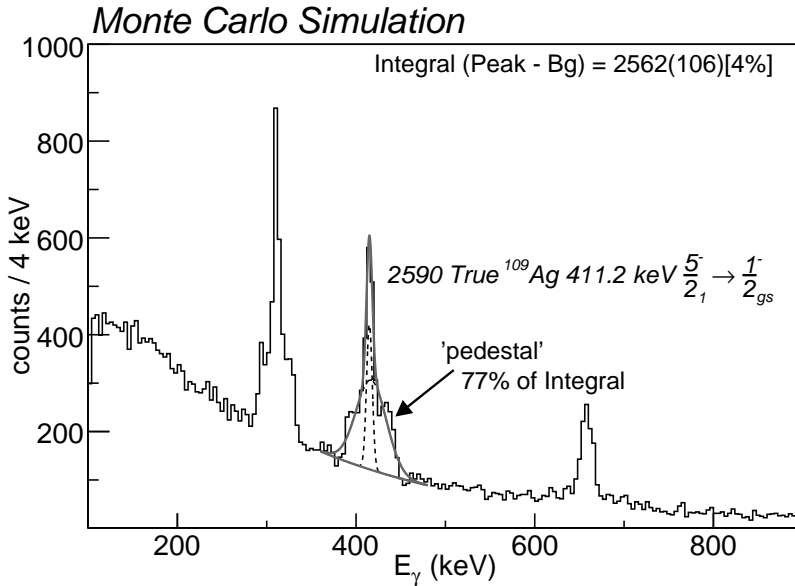


Figure 3.8: *Monte Carlo simulation of a Doppler corrected gamma-ray peak based on incomplete particle identification. The 'pedestal' refers to the broader structure that is present in the base region of the 411.2 keV γ -ray peak. See the text for details.*

obtained. On average, a combined adjustment of the angular position comparable to the size of a triple cluster is required. The scattering angles of the particles are determined from the randomized detection positions in the annular strips of the DSSSD. For the present cases, a difference of 100 MeV in the kinetic energy of the emitting nucleus has an effect of 1% on the Doppler shifted energy of the detected γ -ray. The lifetime of the excited states are ~ 10 ps implying that the de-excitation γ -ray is emitted a few μm downstream of the target. The induced perturbation of the origin of the coordinate system is neglected since the MINIBALL and the DSSSD detectors are positioned 12.5 cm and 3.0 cm from the secondary target, respectively. The detected intensity of the γ -rays is also transformed to the rest frame of the emitting nucleus, see Appendix. B.2. This has a 0.9% effect on the Doppler corrected γ -ray yields.

3.3.1 Doppler correction without particle identification

In the $^{100,102,104}\text{Cd} + ^{109}\text{Ag}$ experiment it is not possible to uniquely identify the detected particles due to the almost identical masses of the projectiles and targets. This removes the possibility to uniquely correlate the detected γ -rays with the projectile and target nuclei. In turn, this affects the performance

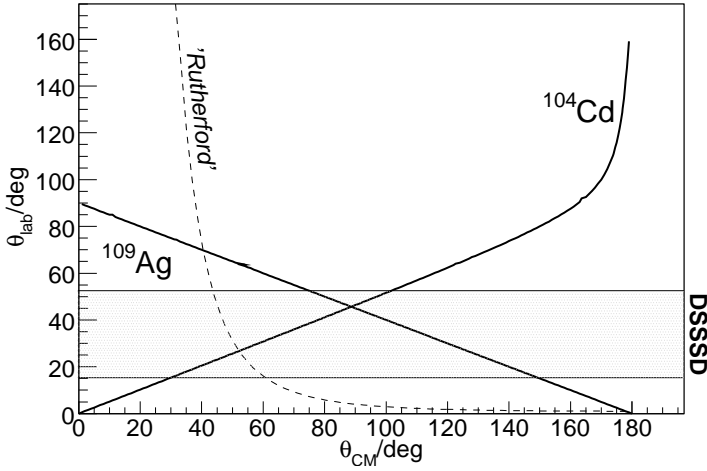


Figure 3.9: *Laboratory versus center of mass scattering angles for a ^{104}Cd projectile and a ^{109}Ag target. The gray region corresponds to the angular coverage of the DSSSD. The shape of the Rutherford cross section is included for comparison.*

of the Doppler correction which is realized as a broad structure surrounding the base of the corrected γ -ray peak, see Figs. 3.14 and 3.16. Here, this is referred to as the 'pedestal' or 'base' of the peak. The magnitude of this compared to the integral of the peak depends on the probability of an erroneous particle- γ combination. In the following, the Doppler correction of the ^{109}Ag $(\frac{5}{2})_1^- \rightarrow (\frac{1}{2})_{\text{gs}}^-$ transition in the $^{104}\text{Cd}+^{109}\text{Ag}$ experiment is examined in detail using a Monte Carlo simulation. However, the discussion applies equally well to the $(\frac{3}{2})_1^- \rightarrow (\frac{1}{2})_{\text{gs}}^-$ transition or the $2_1^+ \rightarrow 0_{\text{gs}}^+$ transition of the Cd projectile. The following effects are taken into account in the simulation code; the energy loss of the particles as they traversed the target foil, the angular distributions of the emitted γ -rays, the MINIBALL detection efficiency, the geometry of the DSSSD, a beam spot with a Gaussian distribution with a standard deviation of 1 mm. Applying the Doppler correction to the simulated data under the assumption that all the detected particles are Cd gives the result shown in Fig. 3.8. This is in agreement with the result of the Doppler correction of the experimental data, see e.g. Fig. 3.14. Firstly, according to the Rutherford cross section, 97% of the detected particles are in fact Cd. This is illustrated in Fig. 3.9. However, the number of detected de-excitation γ -rays from the target depends on the Coulomb excitation cross section. Indeed, folding the Coulomb excitation probability $P(\theta)$ onto the Rutherford cross section shows that 76% of the target γ -rays are registered in coincidence with a projectile. Thus, 24%

of the target γ -rays are correctly assigned, which displays the fact that the detected target particles, which have large center of mass scattering angles and correspond to 3% of the total number of detected particles, carry a large fraction of the Coulomb excitation cross section. Consequently, the Doppler correction of the target γ -rays improve if it is based on the reconstructed particles. In this reconstruction it is assumed that all detected particles are projectiles. This is clearly seen in the data, see the bottom panels in Figs. 3.14 and 3.16. The target γ -ray yield remains unchanged within one standard deviation irrespective of the employed Doppler correction method. Returning to the experimental data, the integrated pedestal of the γ -ray peak corresponds to 78(4)% of the total γ -ray yield. The Doppler corrected peaks are fitted with a double-Gaussian function. This assumption is verified by testing the fit-routine on the Monte Carlo generated pedestal which returns a pedestal-fraction of 77(5)%.

3.4 Measured γ -ray yields

The following pages contain a summary of all the Doppler corrected γ -ray energy spectra. The extracted yields are listed in Tabs. 3.1- 3.2. The cuts explained in the preceding sections have been applied to the data.

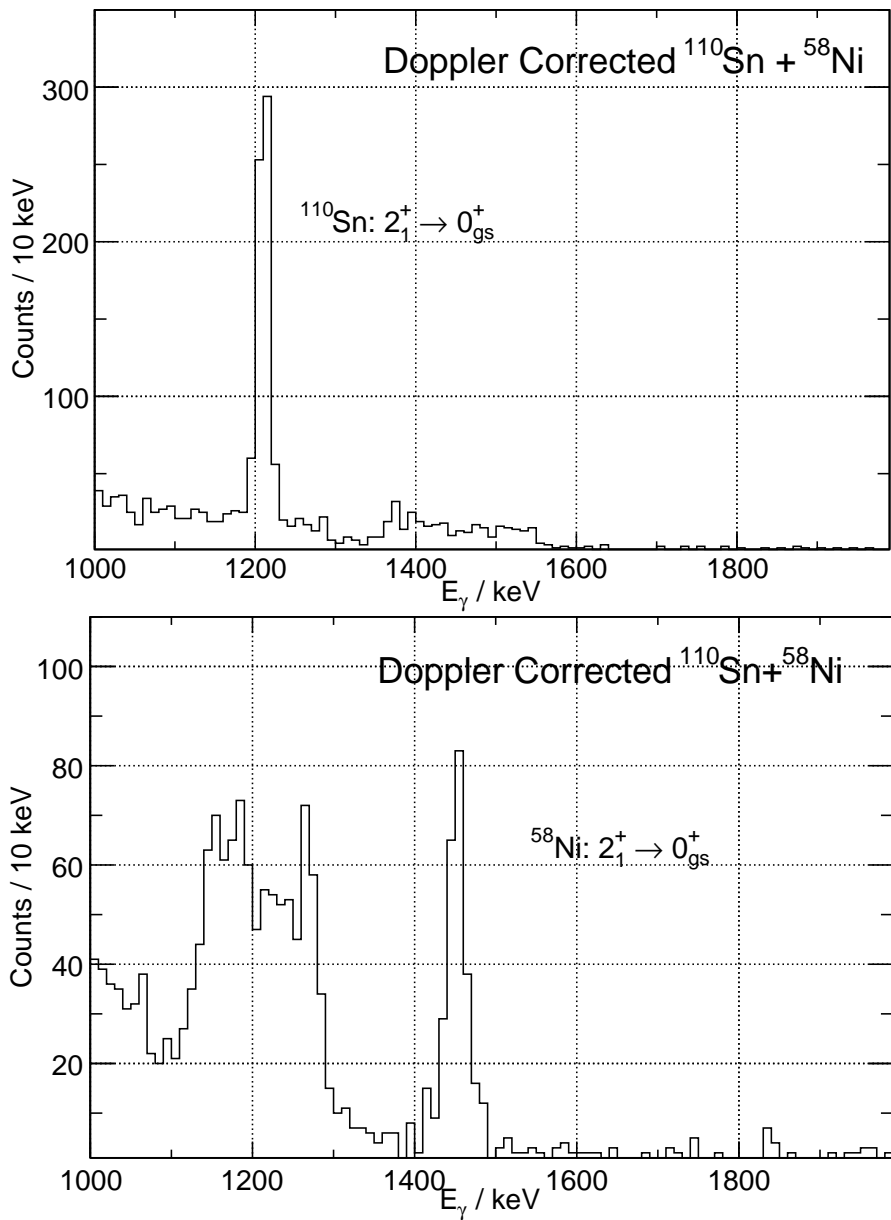


Figure 3.10: **projectile** 2.82 MeV/u ^{110}Sn **target** 2.0 mg/cm² thick ^{58}Ni

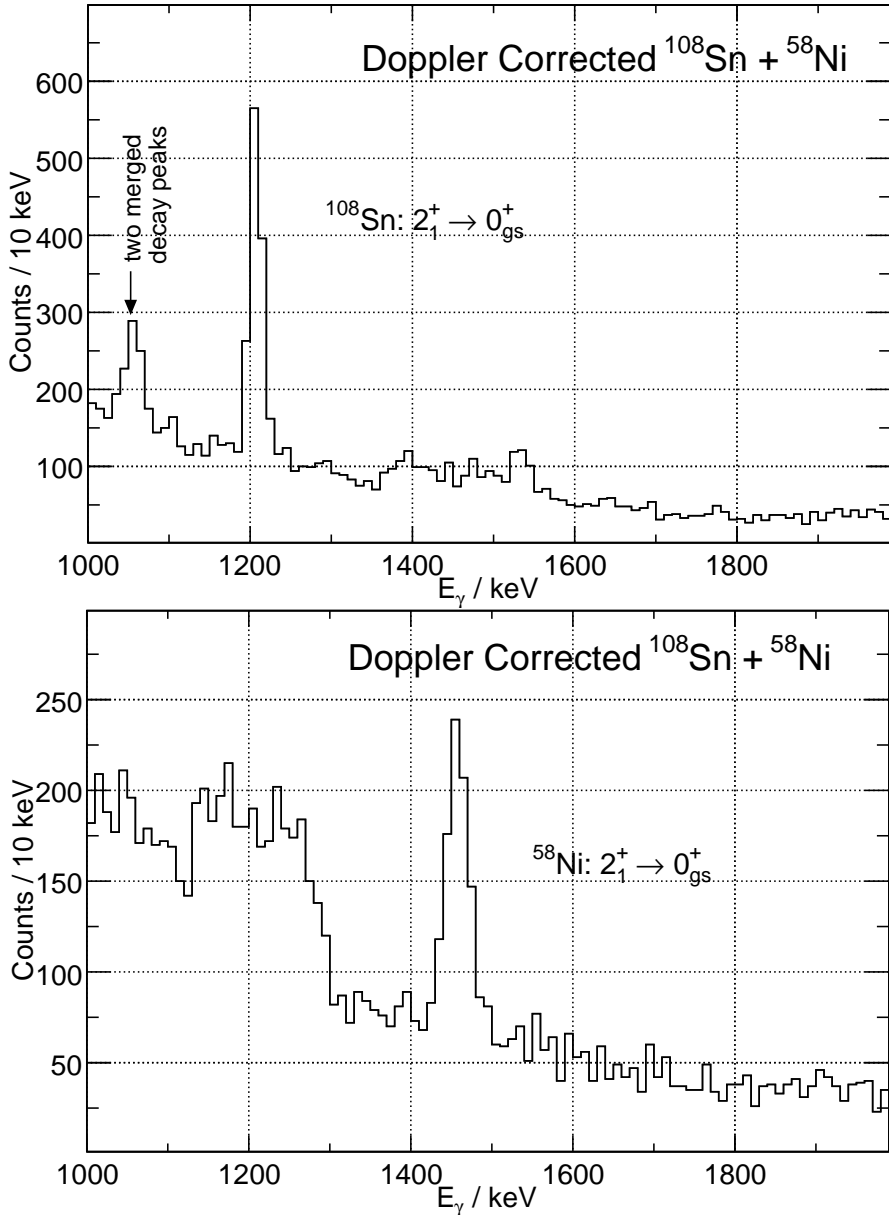


Figure 3.11: **projectile** 2.82 MeV/u ^{108}Sn **target** 2.0 mg/cm^2 thick ^{58}Ni

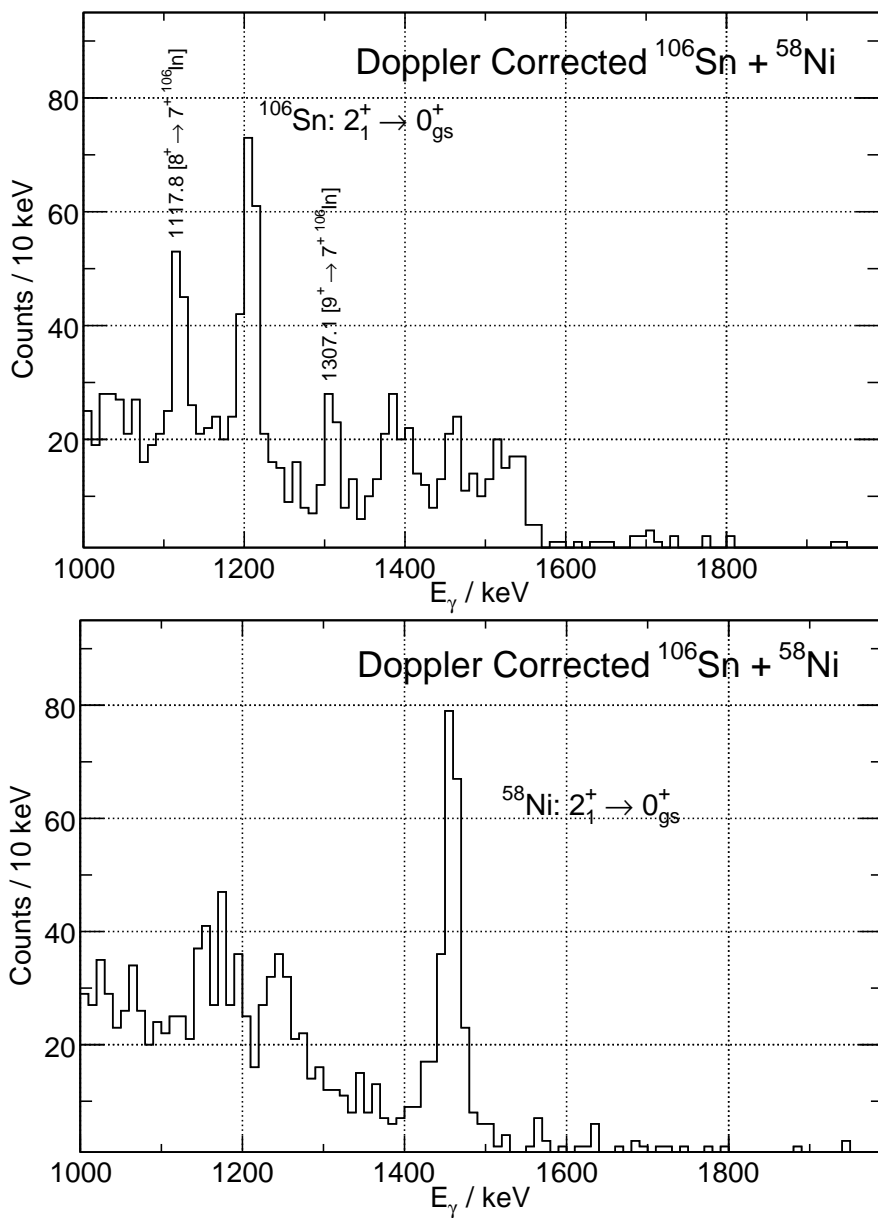


Figure 3.12: *projectile* 2.83 MeV/u ^{106}Sn *target* 2.0 mg/cm² thick ^{58}Ni

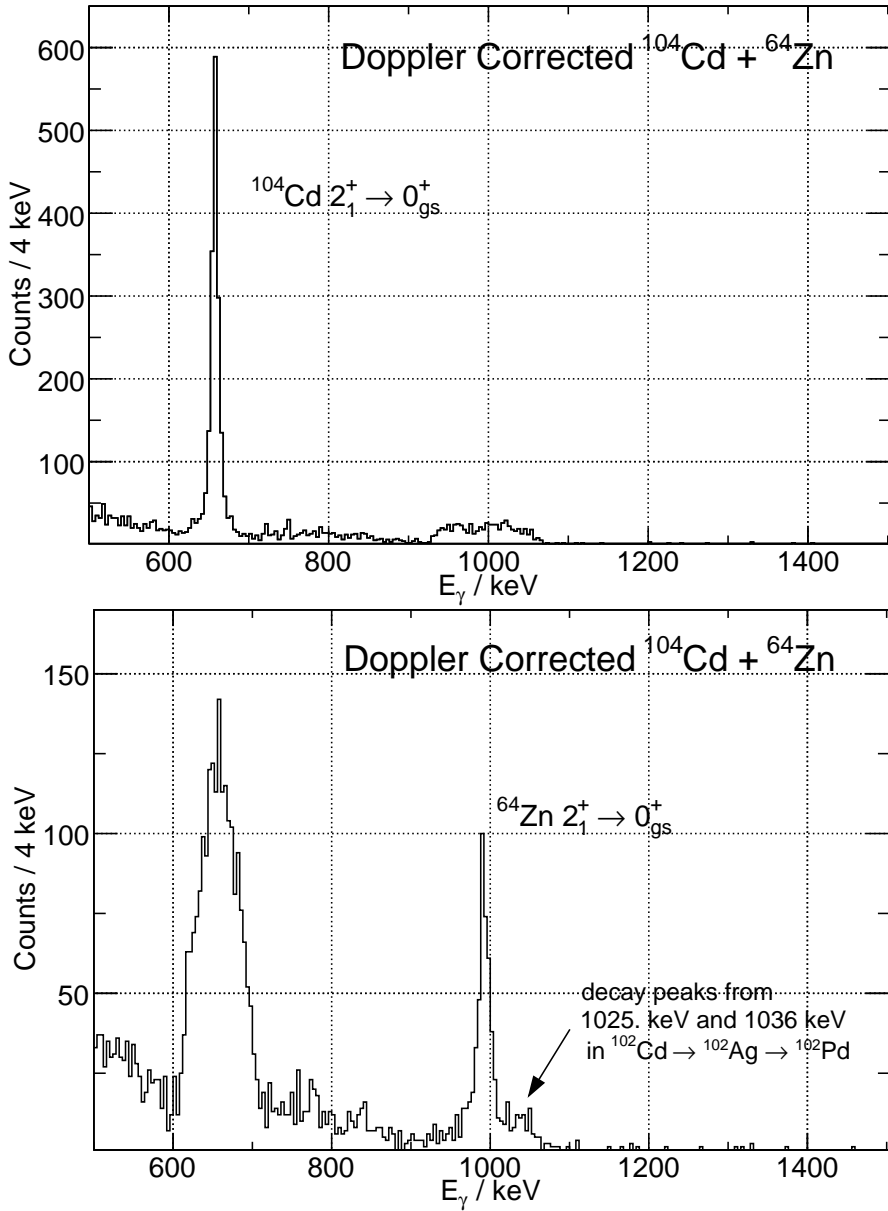


Figure 3.13: *projectile* 2.87 MeV/u ^{104}Cd *target* 1.8 mg/cm² thick ^{64}Zn

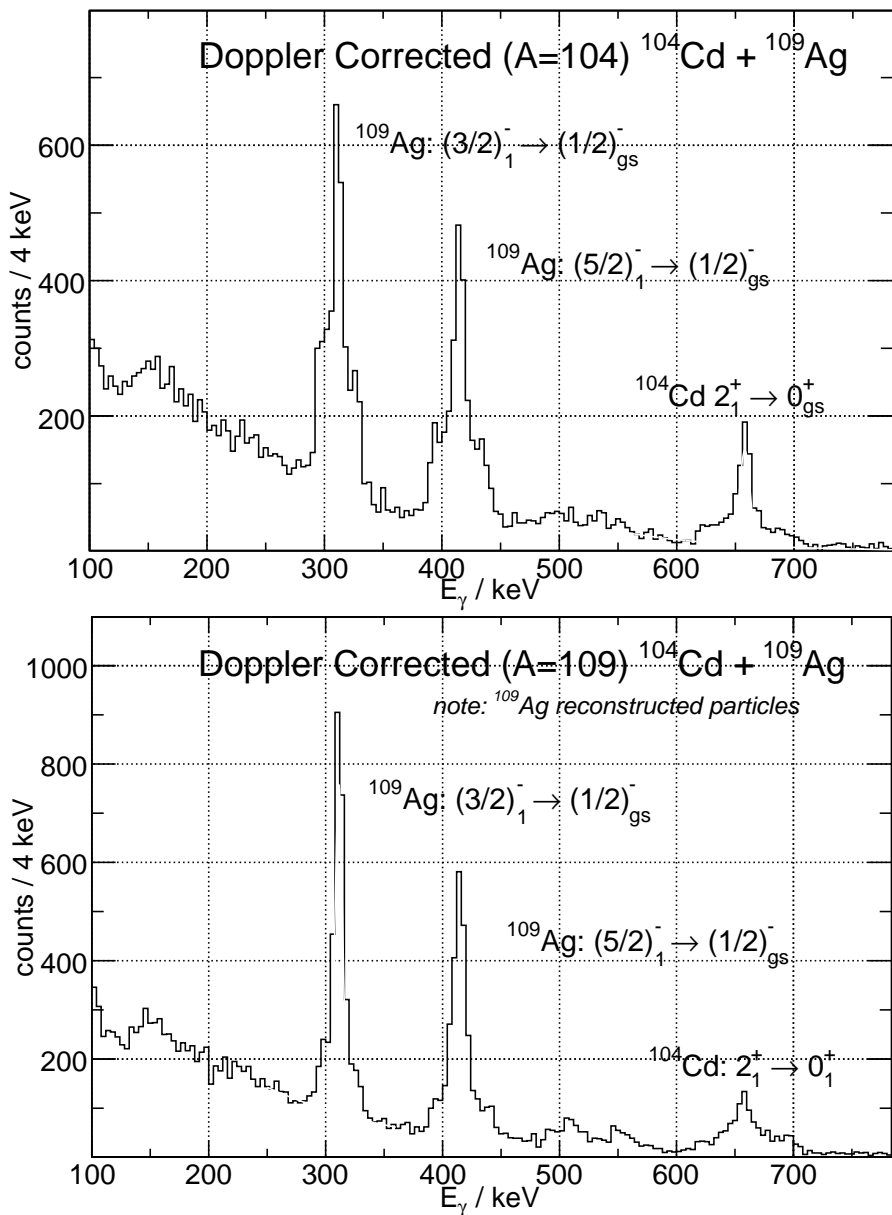


Figure 3.14: **projectile** 2.87 MeV/u ^{104}Cd **target** 1.9 mg/cm² thick ^{109}Ag

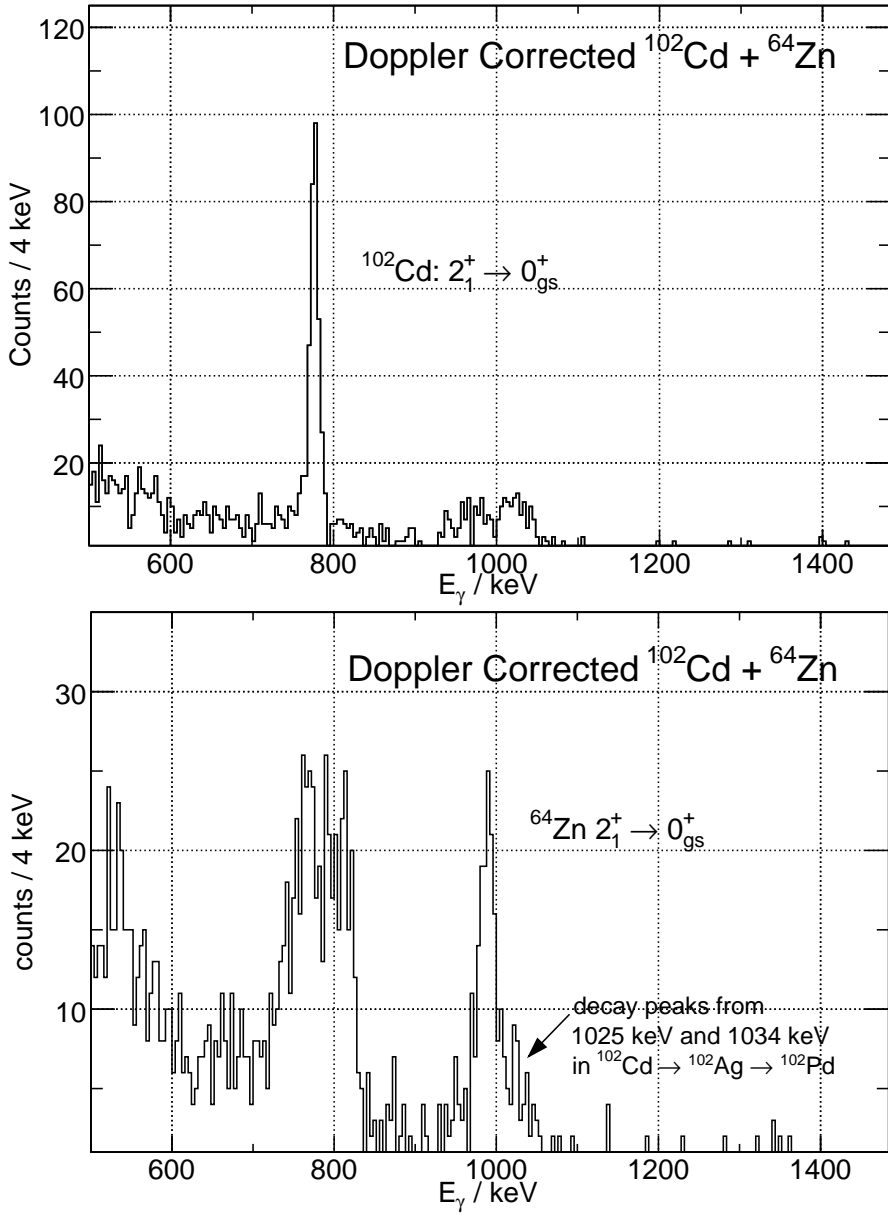


Figure 3.15: *projectile* 2.87 MeV/u ^{102}Cd *target* 1.8 mg/cm² thick ^{64}Zn

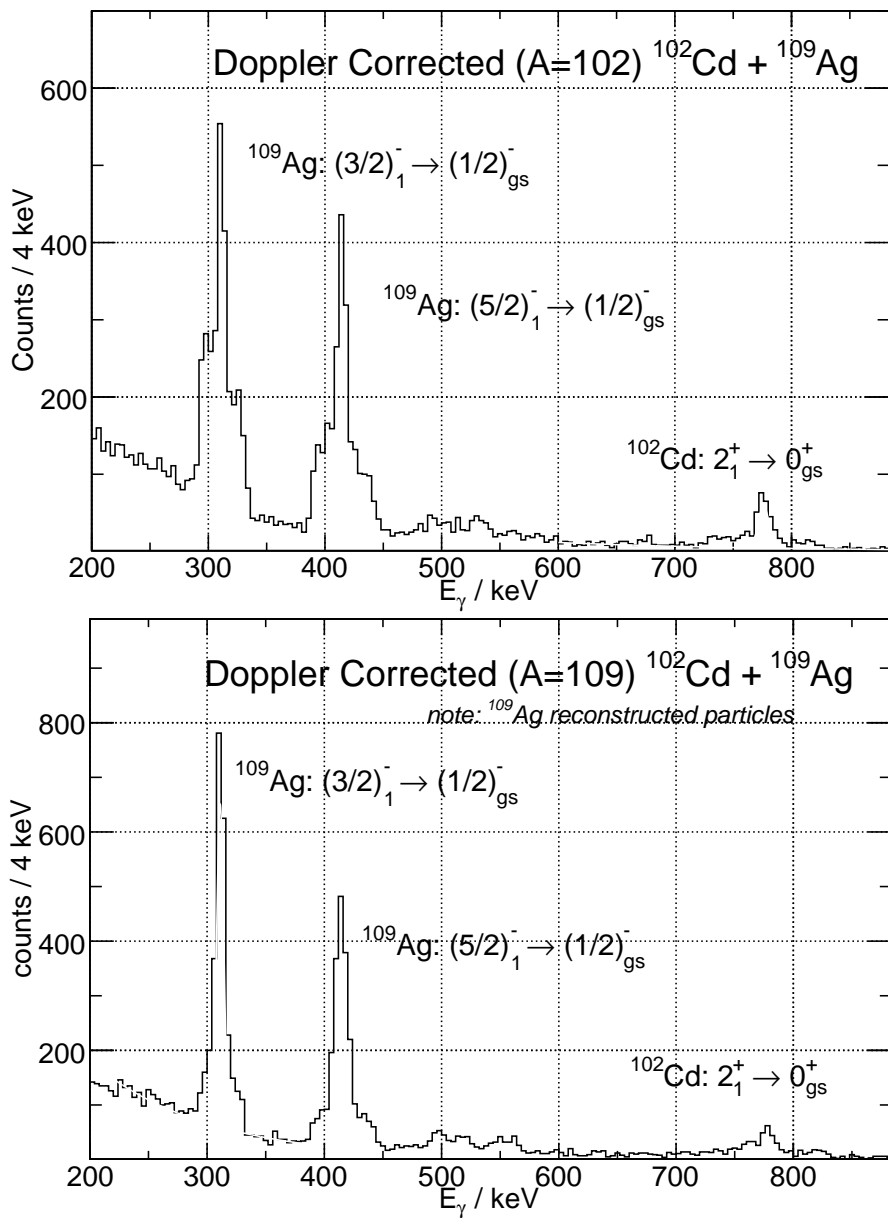


Figure 3.16: **projectile** 2.87 MeV/u ^{102}Cd **target** 1.9 mg/cm² thick ^{109}Ag

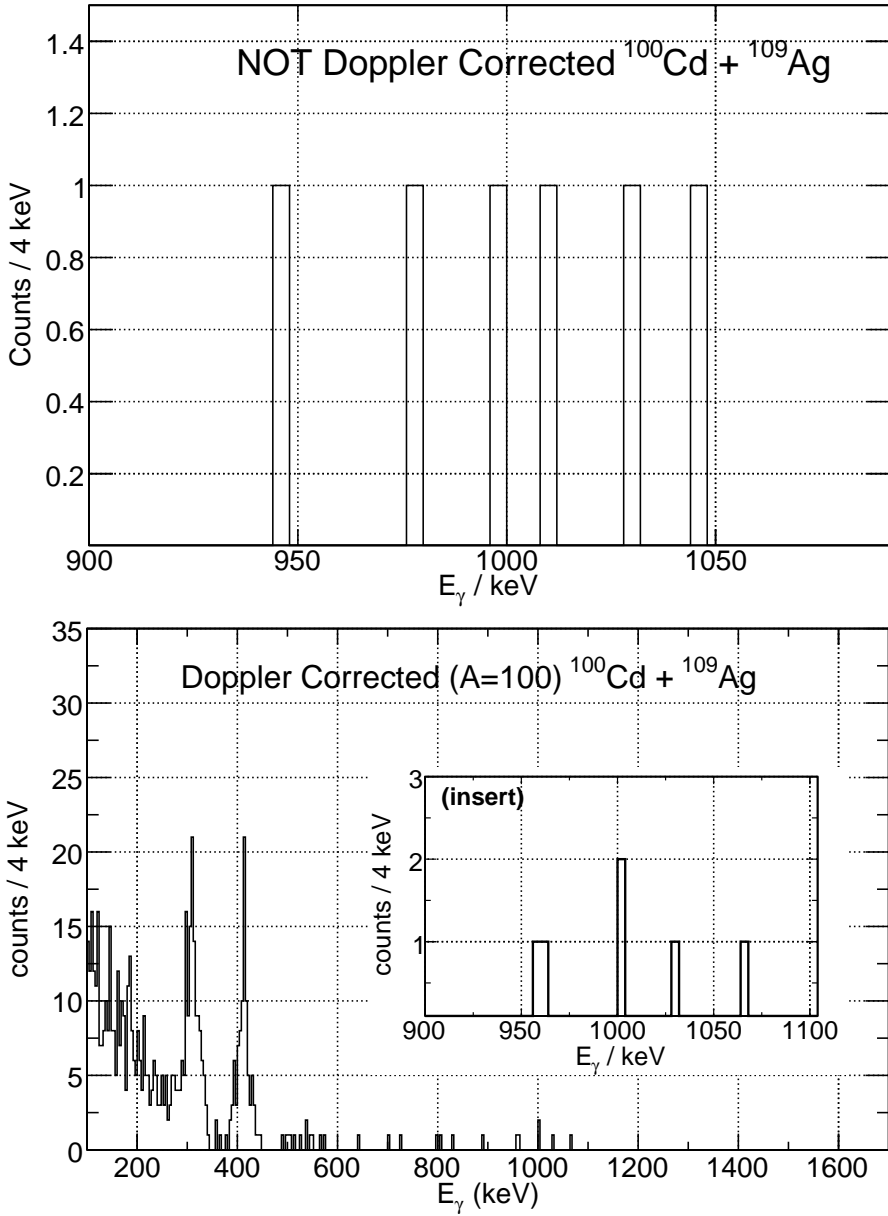


Figure 3.17: *projectile* 2.87 MeV/u ^{100}Cd *target* 1.9 mg/cm^2 thick ^{109}Ag

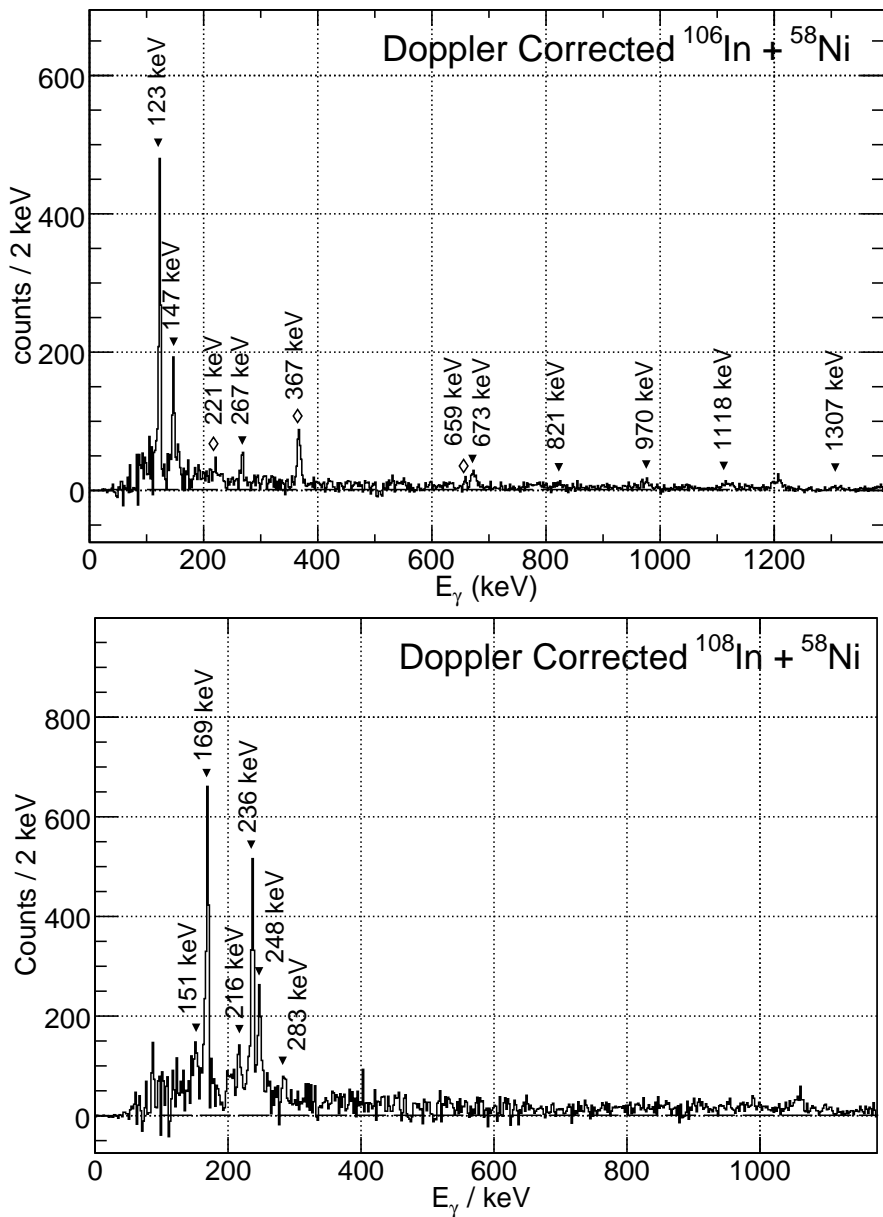


Figure 3.18: *projectile* (top panel) $2.83 \text{ MeV/u } ^{106}\text{In}$ (bottom panel) $2.82 \text{ } ^{108}\text{In}$ *target* 2.0 mg/cm^2 thick ^{58}Ni

Table 3.1: *The observed γ -ray yields from the Sn and Cd experiments.*

Measurement	E_γ / keV	Transition	γ -ray yield
Fig. 3.10 $^{110}\text{Sn} + ^{58}\text{Ni}$			
	1212	$^{110}\text{Sn}: 2_1^+ \rightarrow 0_{\text{gs}}^+$	579(24)
	1454	$^{58}\text{Ni}: 2_1^+ \rightarrow 0_{\text{gs}}^+$	237(15)
Fig. 3.11 $^{108}\text{Sn} + ^{58}\text{Ni}$			
	1206	$^{108}\text{Sn}: 2_1^+ \rightarrow 0_{\text{gs}}^+$	994(38)
	1454	$^{58}\text{Ni}: 2_1^+ \rightarrow 0_{\text{gs}}^+$	577(34)
Fig. 3.12 $^{106}\text{Sn} + ^{58}\text{Ni}$			
	1208	$^{106}\text{Sn}: 2_1^+ \rightarrow 0_{\text{gs}}^+$	133(14)
	1454	$^{58}\text{Ni}: 2_1^+ \rightarrow 0_{\text{gs}}^+$	207(15)
Fig. 3.13 $^{104}\text{Cd} + ^{64}\text{Zn}$			
	658	$^{104}\text{Cd}: 2_1^+ \rightarrow 0_{\text{gs}}^+$	1487(59)
	992	$^{64}\text{Zn}: 2_1^+ \rightarrow 0_{\text{gs}}^+$	471(28)
Fig. 3.14 $^{104}\text{Cd} + ^{109}\text{Ag}$			
	658	$^{104}\text{Cd}: 2_1^+ \rightarrow 0_{\text{gs}}^+$	1028(47)
	311	$^{109}\text{Ag}: \frac{3}{2}1^- \rightarrow \frac{1}{2}2_{\text{gs}}^-$	2753(95)
	415	$^{109}\text{Ag}: \frac{5}{2}1^- \rightarrow \frac{1}{2}2_{\text{gs}}^-$	2289(84)
Fig. 3.15 $^{102}\text{Cd} + ^{64}\text{Zn}$			
	777	$^{102}\text{Cd}: 2_1^+ \rightarrow 0_{\text{gs}}^+$	308(28)
	992	$^{64}\text{Zn}: 2_1^+ \rightarrow 0_{\text{gs}}^+$	156(23)
Fig. 3.16 $^{102}\text{Cd} + ^{109}\text{Ag}$			
	777	$^{102}\text{Cd}: 2_1^+ \rightarrow 0_{\text{gs}}^+$	486(34)
	311	$^{109}\text{Ag}: \frac{3}{2}1^- \rightarrow \frac{1}{2}2_{\text{gs}}^-$	2249(83)
	415	$^{109}\text{Ag}: \frac{5}{2}1^- \rightarrow \frac{1}{2}2_{\text{gs}}^-$	1985(65)
Fig. 3.17 $^{100}\text{Cd} + ^{109}\text{Ag}$			
	1004	$^{100}\text{Cd}: 2_1^+ \rightarrow 0_{\text{gs}}^+$	$\leq 6.0(24)$
	311	$^{109}\text{Ag}: \frac{3}{2}1^- \rightarrow \frac{1}{2}2_{\text{gs}}^-$	101(17)
	415	$^{109}\text{Ag}: \frac{5}{2}1^- \rightarrow \frac{1}{2}2_{\text{gs}}^-$	75(14)

Table 3.2: The observed γ -ray yields from the In experiments. The transition energy E_γ corresponds to the adopted value unless the transition is observed in this work for the first time, in which case the value of E_γ is given with an uncertainty. The 151 keV doublet in ^{108}In is resolved using known branching ratios.

Measurement	E_γ / keV	Transition	γ -ray yield
Fig. 3.18			
$^{108}\text{In} + ^{58}\text{Ni}$			
	1454	$^{58}\text{Ni}: 2^+ \rightarrow 0^+_{\text{gs}}$	565(35)
	151	$^{108}\text{In}: 7^+ \rightarrow 7^+_{\text{gs}}$	377(66)
	169	$^{108}\text{In}: 3^+ \rightarrow 2^+$	1536(64)
	248	$^{108}\text{In}: (5)^+ \rightarrow 7^+_{\text{gs}}$	631(50)
	151	$^{108}\text{In}: (5)^+ \rightarrow (6, 7, 8)$	79(14)
	236	$^{108}\text{In}: 3^+ \rightarrow 2^+$	1106(67)
	283	$^{108}\text{In}: 4^+ \rightarrow 3^+$	192(60)
	216	$^{108}\text{In}: 4^+ \rightarrow 3^+$	150(50)
Fig. 3.18			
$^{106}\text{In} + ^{106}\text{In}$			
	1454	$^{58}\text{Ni}: 2^+_1 \rightarrow 0^+_{\text{gs}}$	194(25)
	123	$^{106}\text{In}: (6^+7^+8^+9^+) \rightarrow 7^+_{\text{gs}}$	897(41)
	147	$^{106}\text{In}: (7^+) \rightarrow 7^+_{\text{gs}}$	566(61)
	123	$^{106}\text{In}: (2)^+ \rightarrow (2)^+$	897(41)
	367.1(2)	$^{106}\text{In}: (6^+) \rightarrow 7^+_{\text{gs}}$	321(29)
	221.1(14)	$^{106}\text{In}: (6^+) \rightarrow (7^+)$	38(14)
	267	$^{106}\text{In}: 6 \rightarrow (6^+7^+8^+9^+)$	105(21)
	821	$^{106}\text{In}: (8^+) \rightarrow 7^+_{\text{gs}}$	59(16)
	673	$^{106}\text{In}: (8^+) \rightarrow (7^+)$	128(24)
	1118	$^{106}\text{In}: (8^+) \rightarrow 7^+_{\text{gs}}$	66(23)
	970	$^{106}\text{In}: (8^+) \rightarrow (7^+)$	81(21)
	1307	$^{106}\text{In}: (9)^+ \rightarrow 7^+_{\text{gs}}$	40(12)
	658.7(4)	$^{106}\text{In}: \text{not placed}$	42(11)

3.5 Beam composition analysis

The beam purity \mathcal{P} is sampled for one hour every three hours during each experiment using a laser based method referred to as laser on/off, see Sec. 2.1.2. A time-averaged value \mathcal{P} , that is representative for an entire experiment, is deduced from the $\mathcal{P}_{\text{on/off}}$ samples. The precision and consistency of the laser-based measure of \mathcal{P} is carefully investigated using two complementary methods. These are applied to the ^{108}Sn experiment.

3.5.1 Isobaric purity of the Sn and Cd RIBs

The beam purity $\mathcal{P}_{\text{on/off}}$ is deduced from each laser on/off run data by observing the differences in the total number of particles N detected in the DSSSD during the laser on and the laser off periods

$$\mathcal{P}_{\text{on/off}} = \frac{N_{\text{on}} - N_{\text{off}}}{N_{\text{on}}} \quad (3.3)$$

The uncertainty of $\mathcal{P}_{\text{on/off}}$ is given from the Poisson statistics of the detected particles. The \mathcal{P} value for an entire experiment is obtained using the intensity of the Coulomb excited In isobar. The number of de-excitation γ -rays $N_{\gamma}(\text{In})$ following the population of excited states in the isobaric contaminant is proportional to the number of indium particles scattered against the target, i.e.

$$N_{\gamma}(\text{In})_{\text{off}} = N(\text{In})_{\text{off}} \cdot \tilde{\sigma} \quad (3.4)$$

where $\tilde{\sigma}$ is a measure of the corresponding Coulomb excitation cross section. Irrespective of its actual value, it remains constant for a given experiment. Therefore, the total number of incident contaminant particles is proportional to the number of detected Coulomb excitation γ -rays

$$N_{\gamma}(\text{In})_{\text{tot}} = N(\text{In})_{\text{tot}} \cdot \tilde{\sigma} \quad (3.5)$$

which leads to

$$N(\text{In})_{\text{tot}} = \frac{N_{\gamma}(\text{In})_{\text{tot}} \cdot N(\text{In})_{\text{off}}}{N_{\gamma}(\text{In})_{\text{off}}} \quad (3.6)$$

and the final value for \mathcal{P} is obtained from

$$\mathcal{P} = 1 - \frac{N_{\gamma}(\text{In})_{\text{tot}} \cdot N(\text{In})_{\text{off}}}{N_{\gamma}(\text{In})_{\text{off}} N(\text{Sn+In})_{\text{tot}}} \quad (3.7)$$

As mentioned, during the $^{110}\text{Sn} + ^{58}\text{Ni}$ experiment, there are no laser data stored for offline use. Instead the isobaric contamination is deduced using the on/off method in combination with a Faraday cup that measures the beam current just before the ^{58}Ni target. The result is consistent with the analysis of the implantation γ -ray spectroscopy carried out at the primary target. For the $^{106,108}\text{Sn}$ experiments the procedure outlined above lead to the values listed

Experiment	\mathcal{P} /%
$^{110}\text{Sn}+^{58}\text{Ni}$	90.0(14)
$^{108}\text{Sn}+^{58}\text{Ni}$	59.0(27)
$^{106}\text{Sn}+^{58}\text{Ni}$	29.2(42)
$^{104}\text{Cd}+^{64}\text{Zn}$	99.6(1)
$^{104}\text{Cd}+^{109}\text{Ag}$	99.2(1)
$^{102}\text{Cd}+^{64}\text{Zn}$	97.3(3)
$^{102}\text{Cd}+^{109}\text{Ag}$	99.6(1)
$^{100}\text{Cd}+^{109}\text{Ag}$	100.0(100)

Table 3.3: *The time-averaged beam purity \mathcal{P} with respect to the Sn and Cd content for each RIB.*

in Tab. 3.3. However, for the $^{100,102,104}\text{Cd}$ experiments it is not possible to detect any Coulomb excitation of the In contaminant in the Cd beams due to the suppression of this isotope, see Sec. 2.1.2. Therefore the quoted values are the ones obtained from the average of the laser on/off measurements. Also, the purity for the ^{100}Cd is according to the scattered number of particles during the laser-off runs consistently zero. A statistical uncertainty of 10%, with added margins, is assigned based on the maximum uncertainty found in the table.

3.5.2 Correlation between laser power and beam purity

It is interesting to study the correlation between the injected laser power and the number of detected Sn particles. This offers a check of the laser on/off procedure outlined in the previous section. For the $^{108}\text{Sn}+^{58}\text{Ni}$ experiment the offline data contains a measure of the injected laser power. Also, the RIB contains a sizable amount of indium. Therefore, this experiment is suitable for further studies of this type. During the laser on/off periods, the number of scattered Sn particles $N(\text{Sn})$ is given by

$$N(\text{Sn})_{\text{on}} = N(\text{Sn}+\text{In})_{\text{on}} - N(\text{In})_{\text{off}} \quad (3.8)$$

The assumption that $N(\text{In})_{\text{on}} = N(\text{In})_{\text{off}}$ for consecutive on and off periods is reasonable since the fluctuations in the ionization efficiency occurs on a larger time scale. Furthermore, $N(\text{Sn})_{\text{on}}$ is correlated¹ with the laser power L_P injected in the ionization cavity. This is quantified by e.g. the Pearson product-moment correlation coefficient

$$\mathcal{C}(\langle N(\text{Sn}) \rangle_T, \langle L_P \rangle_T) = \frac{n \sum_i x_i y_i - \sum_i x_i \sum_i y_i}{\sqrt{n \sum_i x_i^2 - (\sum_i x_i)^2} \sqrt{n \sum_i y_i^2 - (\sum_i y_i)^2}} \quad (3.9)$$

¹Correlation does not imply causality. However, for this study the causality is inferred from the technical and physical knowledge of the RILIS.

where $y_i = \langle N(\text{Sn}) \rangle_{T,i}$ and $x_i = \langle L_P \rangle_{T,i}$. Note that the number of detected particles in the on/off periods are averaged over a time period T . However, see Tab. 3.4, the deduced values of the correlation coefficient is rather independent of the length of the time interval T . The linear fit between the detected number of Sn ions and the injected laser power for the time average with the largest correlation coefficient is shown in Fig. 3.19. For completeness, the correlation

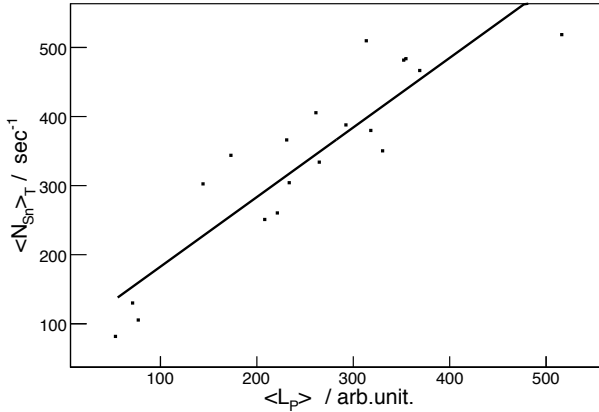


Figure 3.19: Time-averaged values of scattered ^{108}Sn versus laser power. The straight line is the linear fit to the data.

T (min)	\mathcal{C}
10	0.86
20	0.87
30	0.85
40	0.90
50	0.86

Table 3.4: \mathcal{C} for various time intervals T . The optimal T is marked with bold font.

coefficient between the contaminant and the laser power $\mathcal{C}(\langle N(\text{In}) \rangle_T, \langle L_P \rangle_T)$ is 0.38. This value indicates, as expected, that there exists no correlation between the laser power and the surface ionized component of the beam. The correlation between the laser power and the number of Sn particles scattered into the DSSSD offers an alternative measure of \mathcal{P} since the laser power is continuously stored during this experiment. The number of scattered ^{108}Sn nuclei is deduced from the linear fit in Fig. 3.19. and the corresponding value of \mathcal{P} is

$$\mathcal{P}^{\mathcal{C}} = 0.58 \pm 0.01 \quad (3.10)$$

This value is consistent with the \mathcal{P} -value deduced from the extrapolated $\mathcal{P}_{\text{on/off}}$ -value. It is not possible to correlate the laser power with the number of scattered ^{106}Sn particles. One reason for this could be a drift in the position of the laser beams during that experiment.

3.5.3 A coupled decay-chain analysis of the beam content

A third approach to verify the consistency of the deduced isobaric contamination is given by the detected number of γ -rays from the decay of the RIB

components. This method is completely independent of the laser based methods discussed above. Here, it is applied to the ^{108}Sn experiment. In detail, the beam composition is reflected in the total number of detected γ -rays coming from the transitions following the decay of each component of the beam, see Fig. 3.20. The indium fraction of the beam consists of two species, namely indium in the ground state and indium with the first excited and isomeric state populated. The ratio of these two quantities depends on the targetry of the experiment. For the $^{108}\text{In}^{gs} + ^{108}\text{In}^m + ^{108}\text{Sn}$ beam, where *gs* means the 7^+ ground state and *m* means the first meta-stable 2^+ state, it is possible to find a set of decay γ -rays that can be used to identify the various parts of the beam, see Tab. 3.5. The magnitudes of the components of the beam can be written as

$$\mathcal{P} \cdot ^A\text{Sn} + \mathcal{Q} \cdot ^A\text{In} + \mathcal{R} \cdot ^A\text{In}^m \quad (3.11)$$

where $\mathcal{P}, \mathcal{Q}, \mathcal{R}$ varies between zero and one such that $\mathcal{P} + \mathcal{Q} + \mathcal{R} = 1$. The

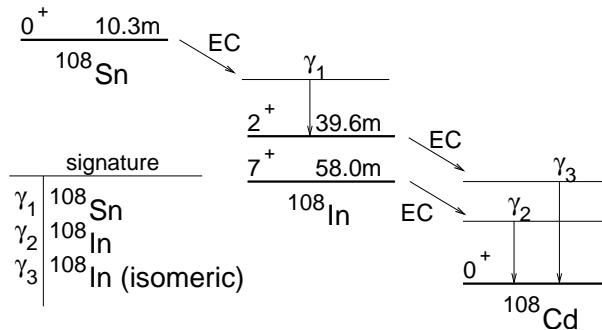


Figure 3.20: Schematic illustration of the decay-chain of the components of the RIB in the ^{108}Sn experiment.

Table 3.5: The γ -rays following the decay chain $^{108}\text{Sn} \rightarrow ^{108}\text{In} \rightarrow ^{108}\text{Cd}$ that are used as signatures of the beam components. The γ -ray intensities I_γ [34] are normalized to the decay of the parent nucleus.

No.	Decay- E_γ / keV	I_γ /%	Observed Yield	Parent
1	272.75	45.5(6)	6801282(6229)	^{108}Sn
2	396.43	64.3(6)	9788686(5212)	^{108}Sn
3	669.11	22.6(4)	2383319(3667)	^{108}Sn
4	730.87	9.3(10)	467648(2737)	^{108}In
5	1032.92	35(3)	1017867(2096)	^{108}In
6	1056.79	29(3)	1309156(2076)	^{108}In
7	1529.72	7.3(4)	802648(1596)	$^{108}\text{In}^m$

data presented in Table 3.5 are collected over the entire duration of the experiment. This data is modeled by the coupled decay-chain equations

$$\begin{aligned} \frac{d}{dt}\text{Sn}(t) &= -\lambda_{\text{Sn}} \cdot \text{Sn}(t) + \mathcal{P}\mathcal{F}(t) \\ \frac{d}{dt}\text{In}^m(t) &= +\lambda_{\text{Sn}} \cdot \text{Sn}(t) - \lambda_{\text{In}^m} \cdot \text{In}^m(t) + (1 - \mathcal{P})\alpha\mathcal{F}(t) \\ \frac{d}{dt}\text{In}^{gs}(t) &= -\lambda_{\text{In}^{gs}} \cdot \text{In}^{gs}(t) + (1 - \mathcal{P})(1 - \alpha)\mathcal{F}(t) \end{aligned} \quad (3.12)$$

where a measure of the time-dependent incoming beam flux $\mathcal{F}(t)$ is given by the number of detected particles in the DSSSD, see Fig. 3.21, and the isomeric ratio α is defined as $\alpha \equiv \mathcal{R}/(\mathcal{Q} + \mathcal{R})$. Neither the chemical nor the heating properties

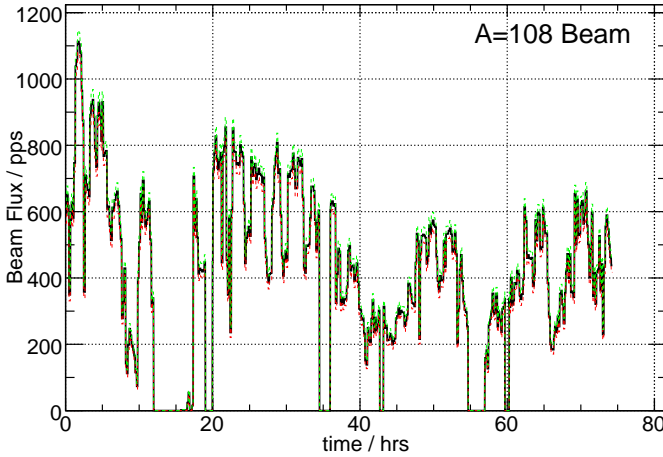


Figure 3.21: *The detected number of particles during the experiment provides a measure of the fluctuations of the beam flux. The dashed red and green curves indicate the uncertainty of the beam flux as estimated from Poisson statistics. Clearly, the periods of no-beam are included in the beam flux curve. See the text for more details.*

of the primary target varied during the experiment such that it affected the isomeric ratio. This justifies the assumption of keeping α time-independent. Furthermore, the time-dependence of the Sn-fraction $\mathcal{P}(t)$ is removed by using the time-average $\langle \mathcal{P} \rangle$ according to;

$$\langle \mathcal{P} \rangle = \frac{\int \mathcal{P}(t)\mathcal{F}(t) dt}{\int \mathcal{F}(t) dt} \quad (3.13)$$

This is identical to the \mathcal{P} introduced in the preceding sections. The decay-equations are solved numerically for given values of \mathcal{P} and α using a fourth order Runge-Kutta routine with the initial conditions

$$\text{Sn}(t = 0) = \text{In}^m(t = 0) = \text{In}(t = 0) = 0. \quad (3.14)$$

The overall normalization constant of the total number of deposited particles and emitted γ -rays is removed by forming ratios R_i according to

$$\frac{Y_\gamma(\text{In}^{gs})}{Y_\gamma(\text{Sn})}, \frac{Y_\gamma(\text{In}^m)}{Y_\gamma(\text{Sn})}, \frac{Y_\gamma(\text{In}^m)}{Y_\gamma(\text{In}^{gs})} \quad (3.15)$$

The simulated ratios are compared to the experimental ratios using a χ^2 -type penalty function defined as

$$X^2/\nu = \frac{1}{\nu} \sum_{i=1} \left(\frac{R_i^{exp} - R_i^{calc}}{\sigma_i} \right)^2 \quad (3.16)$$

This function is denoted with X^2 to emphasize the sample nature of it. The number of degrees of freedom ν is given by the number of ratios minus the number of parameters, α and \mathcal{P} , of the model. The uncertainties of the detection efficiency, the γ -ray branching ratios, and the integrated γ -ray yields are carried over to the final uncertainty σ_i using Gaussian error propagation. The strength of the decay-chain method is twofold. Firstly, the methods provides an offline-tool for extracting the isomeric fraction of the $A = 108$ RIB. Secondly, the X^2 -statistic is sensitive to both α and \mathcal{P} and therefore provides a consistency check of the laser on/off method.

The MINIBALL detection efficiency of a Rutherford scattered source

The γ -rays from the $\text{Sn} \rightarrow \text{In}^m \rightarrow \text{Cd}$ and $\text{In}^{gs} \rightarrow \text{Cd}$ decay-chain are emitted from particles implanted in either the target chamber, the downstream beam dump, or somewhere in the beam pipes connecting these regions. However, the γ -rays are detected by the MINIBALL detector array that is positioned around the target chamber. Therefore, the γ -ray detection efficiency for this type of Rutherford scattered source is determined from an internal calibration using the γ -rays that are emitted from the $\text{In}^{gs} \rightarrow \text{Cd}$ part of the decay-chain. The resulting relative efficiency is fitted with an exponential function. The result is shown as a blue dashed line in Fig. 3.22. From this, one can note that the low-energy γ -rays are attenuated more compared to the high energy ones. Intuitively, this originates in the increased amount of material that the emitted γ -rays must penetrate before reaching any of the MINIBALL triple-clusters. Furthermore, the attenuation increases with the distance from the center of the target chamber, i.e. it reaches a maximum for γ -rays emitted from the beam dump. However, given the uncertainties in the efficiency curve from the internal calibration, this hypothesis is verified using a GEANT4 simulation². The implementation of the GEANT4 physics-processes is verified by simulating the detection of γ -rays from a ^{152}Eu source in the target position, see Fig. 3.23 In the simulation, a 2.82 MeV/u ^{108}In beam is scattered against a 2.0 mg/cm²

²The GEANT4 implementation of the MINIBALL triple-clusters is provided by H. Boie et al., Heidelberg.

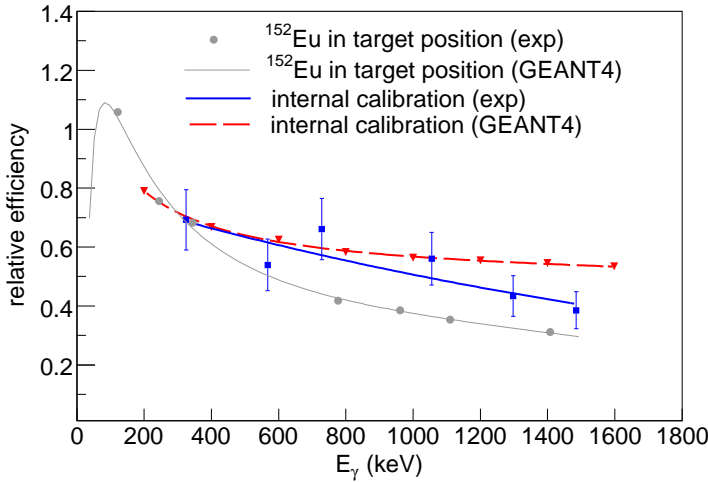


Figure 3.22: *Simulated and experimental relative efficiency curves. The simulated relative detection efficiency of a centered γ -ray source is in excellent agreement with the experimentally obtained efficiency curve*

thick ^{58}Ni target. The width of 95% of the beam is 4.0 mm and follows a Gaussian distribution and the transverse emittance is $0.3 \cdot \pi \text{mm} \cdot \text{mrad}$ normalized at 3.0 MeV/u according to simulations and measurements [35]. The resulting absolute detection efficiency for a γ -ray that is emitted from the beam dump is in the order of 0.02%. This is 500 times less than the detection efficiency of a γ -ray that is emitted in the target chamber, see Fig. 3.24. Note that the detection efficiency of the γ -rays coming from the beam dump increases with increasing energy of the emitted γ -ray. This is the origin of the rather flat efficiency curve of the internal calibration. The number of particles implanted in the beam dump is ~ 1000 times the number of particles implanted inside and in the vicinity of the target chamber. Therefore, the internal efficiency curve can be understood from the properly weighted linear combination of the two efficiency curves in Fig. 3.24. That is, 0.1% of the beam is implanted in the vicinity of the target chamber and therefore 0.1% of the total efficiency curve of the scattered beam comes from the target chamber efficiency curve and likewise for the fraction of the beam that is implanted in the beam dump. In this model, the particles that are stopped in the beam pipes between the chamber and the beam dump are neglected. Indeed, the fit of the linear combination of the simulated efficiency curves to the internal calibration curve is improved if the weight of the component due to the target chamber is shifted from 0.1% to 0.2%. This shift is included in the red curve in Fig. 3.22.

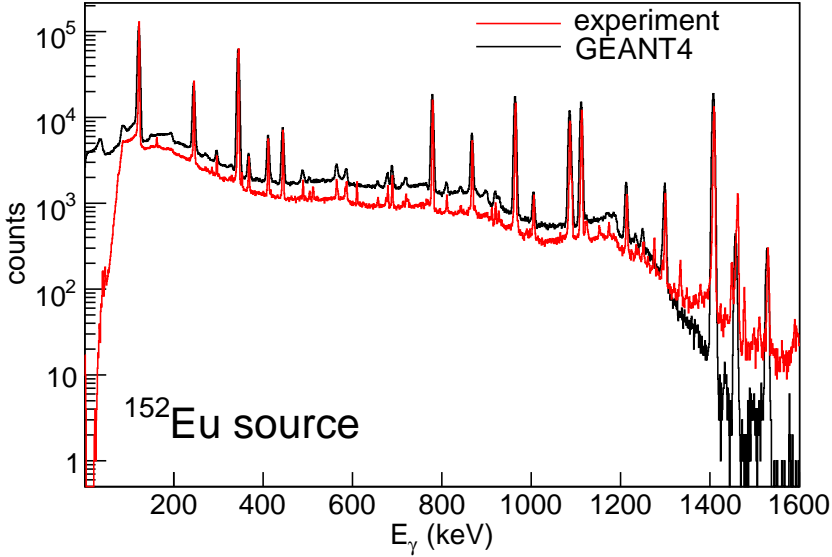


Figure 3.23: Simulated and experimental γ -ray energy spectrum of a ^{152}Eu source in the target position.

X^2 -analysis of the beam composition

The coupled differential equations in Eq. 3.12 are integrated over the entire duration of the experiment. The integration routine takes into account the time periods when the data acquisition system is switched off. The results based on the internal calibration efficiency and the γ -ray data summarized in Tab. 3.5 gives the X^2 surface in Fig. 3.25(a). The minimum X^2_{min} value is 0.82 and defines the point of optimal α and \mathcal{P} values that best fit the observed γ -ray yields. This minimum extends over a certain region. The $X^2_{min} + 1$ contour defines the region of one standard deviation. The projection of this area onto the respective axis delimits the \mathcal{R} and \mathcal{P} values that within one standard deviation fits best with the observed data. The numerical values are $50 \lesssim \mathcal{P} \lesssim 80\%$ and $0\% \lesssim \mathcal{R} \lesssim 30\%$. The \mathcal{P} interval is clearly consistent with the value $59 \pm 2.7\%$ that is obtained with the laser on/off method. The isomeric fraction is further constrained if the laser based measure is used in conjunction with the decay-chain result, see Fig. 3.25. This implies that equal amounts of isomeric and ground state ^{108}In are produced in the primary target.

An important systematic effect that contributes to the width of the $X^2_{min} + 1$ contour comes from the precision of the γ -ray branching ratios in Tab. 3.5. Indeed, if only one γ -ray transition per beam component is included in the X^2 -

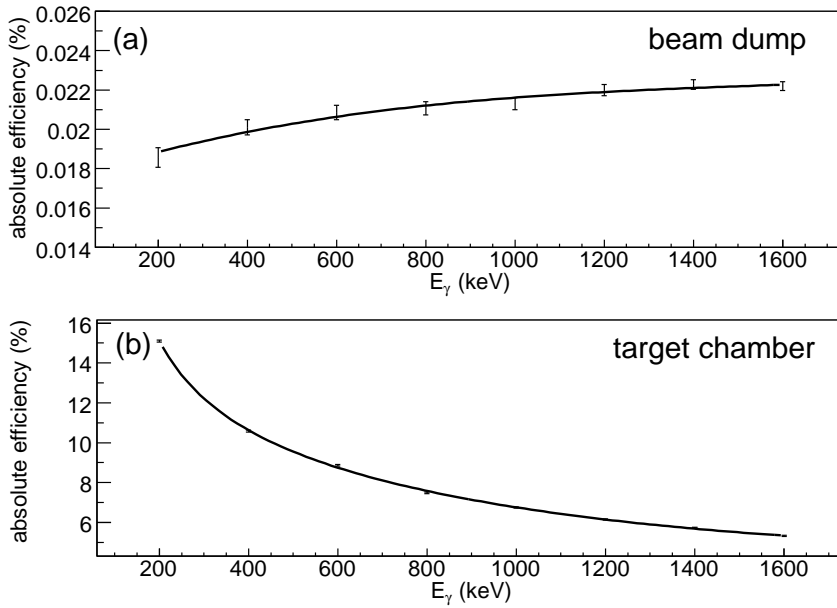


Figure 3.24: *Simulated absolute γ -ray detection efficiencies of the MINI-BALL detectors. The particle source is distributed in (a) the target chamber and (b) in the beam dump. The error bars come from the statistical uncertainty of the integration of the simulated γ -ray peaks.*

sum the resulting X^2 -surface becomes more narrow, see Fig. 3.25(b). However, the choice of transitions introduces a bias in the final result. In order to avoid this, the model should be based on as many γ -ray transitions as possible.

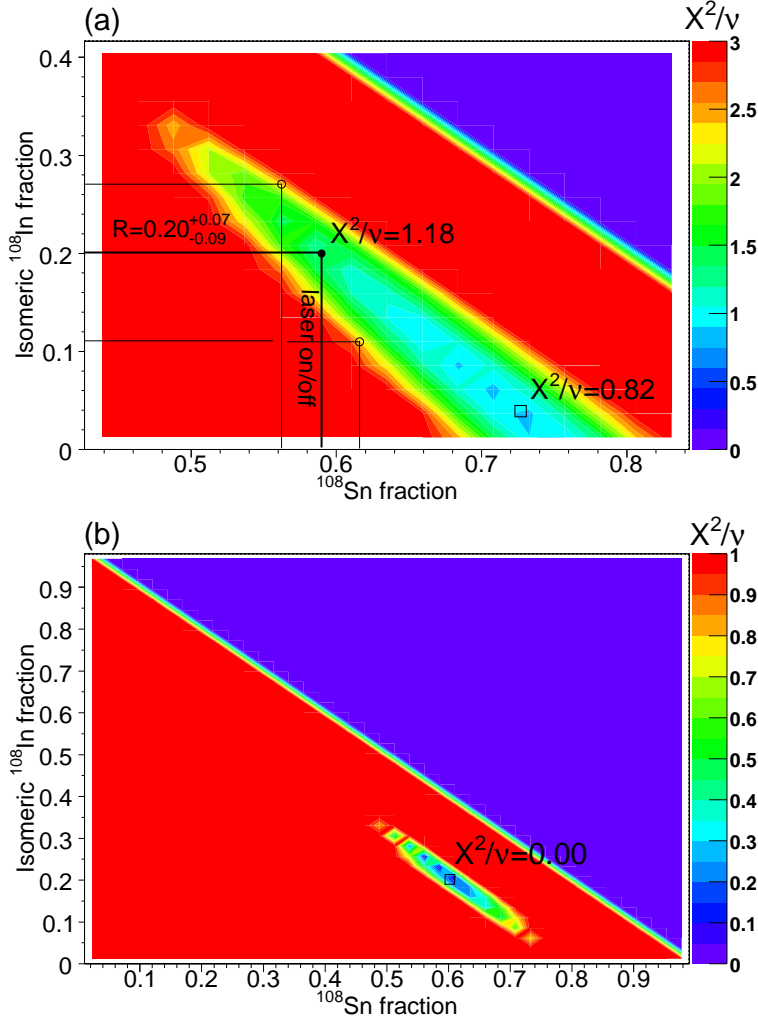


Figure 3.25: (a) The X^2/ν distribution in the $R - P$ plane based on the γ -ray efficiency curve obtained from the internal calibration and the γ -ray yields listed in Tab. 3.5. The isomeric fraction of the indium component of the beam is extracted using the P value based on the laser on/off measurements. (b) The X^2/ν distribution based on transitions No. 3, 5, and 7 in Tab. 3.5. With three data points and two parameters in the model, the number of degrees of freedom for this case is $\nu = 1$. Note the narrow minimum obtained in this calculation compared to the one presented in panel (a).

3.6 Extraction of the nuclear moments

In the Sn and Cd experiments only the first excited 2_1^+ states are populated. The cross sections mainly depend on the $B(E2; 0_{\text{gs}}^+ \rightarrow 2_1^+)$ value and the $Q(2_1^+)$ value, see Sec. 2.5 and Eq. 2.29 in particular.

The $^{106,108,110}\text{Sn}$ experiments are analyzed with the computer code GOSIA [30]. The excitation-algorithms of the program are based on the semi-classical coupled channels theory [4, 5] which is presented briefly in Sec. 2.5.1. The code can also simulate the observed γ -ray yields for a given set of matrix elements and any experimental setup, i.e. it can incorporate the effects of the particle and γ -ray detector geometries, the target thickness, the angular distribution of the γ -rays, the internal conversion coefficients, the branching ratios, the mixing ratios etc. However, the main functionality of GOSIA is its capability of fitting a large but limited set of transition matrix elements to the experimentally observed γ -ray yields. This is done in a χ^2 analysis where the coordinates of the matrix elements in the parameter space are iteratively updated using a modified steepest descent algorithm. For a reasonable ratio of the number of free parameters to the number of data points, the program will converge to a set of matrix elements that best reproduce the observed γ -ray yields. For the Sn-isotopes a $Q(2_1^+) = 0.0$ eb is used in accordance with theoretical calculations and experimental results from heavier stable Sn isotopes [36].

The projectile and target γ -ray yields from the $^{100,102,104}\text{Cd}$ experiments are analyzed using the computer code CLX [29]. This code is identical to GOSIA apart from missing the χ^2 -minimization algorithm and the possibility of including the geometry of the γ -ray detectors.

The γ -ray yields observed in the $^{106,108}\text{In}$ experiments are compared to a GOSIA-simulation based on shell-model matrix elements. This enables a study of the proton-neutron multiplet structure in ^{108}In , see Sec. 4.7.

3.6.1 $^{106,108,110}\text{Sn}$

The level schemes of the $^{106,108,110}\text{Sn}$ projectiles and the ^{58}Ni target are shown in Fig. 3.26. The absolute normalization of the extracted $B(E2)$ values is provided by the known target matrix elements, see Tab. 3.6. Therefore a version of the GOSIA code, called GOSIA2 [30], which can handle the simultaneous excitation of the target and the projectile is employed. The static quadrupole moment $Q(2_1^+)$ in ^{58}Ni has a $\sim 7\%$ effect on the extracted $B(E2)$ values in the Sn isotopes. The remaining target matrix-elements have an additional effect of 0.5% on the result. The differential cross sections of the projectiles and targets are integrated by GOSIA2 over the 2p angular range in the center of mass frame, see Fig. 3.27. The resulting $B(E2)$ values for $^{106,108,110}\text{Sn}$ provided by GOSIA2 are given in Tab. 3.7. The 4_1^+ and 2_2^+ states in the Sn isotopes,

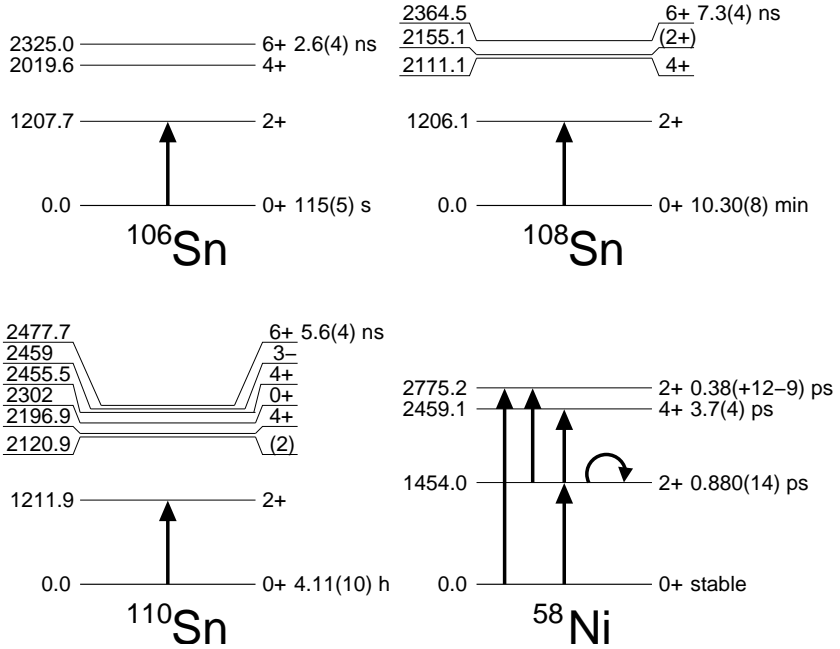


Figure 3.26: The low-lying levels in $^{106,108,110}\text{Sn}$ and ^{58}Ni . The diagonal and non-diagonal transition matrix elements of relevance to the analysis are indicated with arrows. The previously known half-lives are included.

Table 3.6: The level index, spin, parity, level energy, and reduced matrix elements $\langle i || E2 || j \rangle = M_{ij}$ for ^{58}Ni . The adopted values of the matrix elements are from Ref. [37]. The matrix elements and level energies are given in units of eb and MeV, respectively.

Level	I^π	Energy	1	2	3	4
1	0 ⁺	0.0	0.0	0.266(4)	0.0	0.014(4)
2	2 ⁺	1.454		-0.132(79)	0.367(20)	0.306(50)
3	4 ⁺	2.459			0.0	0.0
4	2 ⁺	2.775				0.0

although the 2_2^+ state is not experimentally observed in ^{106}Sn , couple via the E2 operator to the 2_1^+ state. Based on the corresponding matrix elements in ^{112}Sn it is concluded that the influence on the $B(E2; 0_{\text{gs}}^+ \rightarrow 2_1^+)$ values is negligible. The $B(E2)$ values presented here are corroborated by intermediate energy Coulomb excitation measurements [38, 39], see Fig. 3.28. The transition probabilities in the neutron-deficient Sn isotopes do not decrease as rapidly as

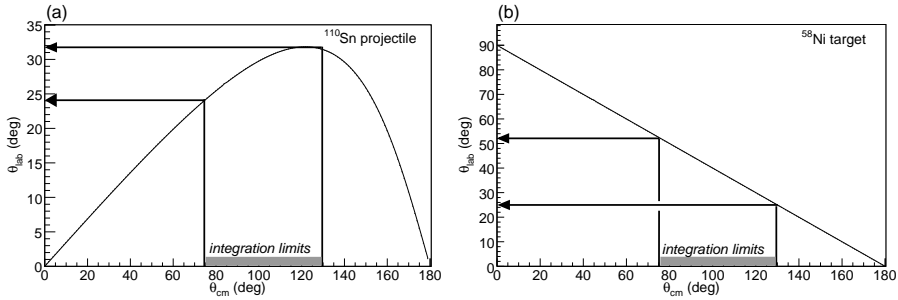


Figure 3.27: The panels show the $2p$ angular range for the $^{110}\text{Sn}+^{58}\text{Ni}$ experiment. The integration limits in the center of mass frame is indicated for (a) the scattered projectile nuclei and (b) the scattered target nuclei.

Table 3.7: The $B(E2; 0_{\text{gs}}^+)$ values in $^{106,108,110}\text{Sn}$ extracted using GOSIA2.

Isotope	$B(E2; 0_{\text{gs}}^+ \rightarrow 2_1^+)$	$\langle 0_{\text{gs}}^+ E2 2_1^+ \rangle$
^{110}Sn	0.220(22)	0.470(23)
^{108}Sn	0.222(19)	0.471(20)
^{106}Sn	0.195(39)	0.442(45)

expected from theoretical predictions. The significant discrepancy between experiment and theory appears already in the stable ^{114}Sn isotope. This was recently remeasured using intermediate energy Coulomb excitation [40]. The adopted value [41] is 3% larger, but with a considerable uncertainty. For the heavier Sn isotopes there are no significant deviations from theory. In Secs. 4.4 and 4.5, the neutron-deficient Sn isotopes are investigated in a set of large-scale shell-model calculations and discussed from a generalized seniority perspective.

3.6.2 $^{100,102,104}\text{Cd}$

For each measurement with the Cd isotopes, the projectile excitation cross section is deduced using Eq. 2.1. The target excitation cross sections are calculated from the known matrix elements, see Tabs. 3.8-3.9. The known level schemes, for both the targets and the projectiles, are shown in Fig. 3.29. It is pointed out in the discussion of Eq. 2.29 that a determination of both the $B(E2)$ and the $Q(2_1^+)$ values using Coulomb excitation requires e.g. at least two independent measurements of the cross section. This condition is fulfilled in the $^{102,104}\text{Cd}$ experiments since both isotopes are Coulomb excited against a ^{109}Ag target as well as a ^{64}Zn target. Furthermore, for the measurements rela-

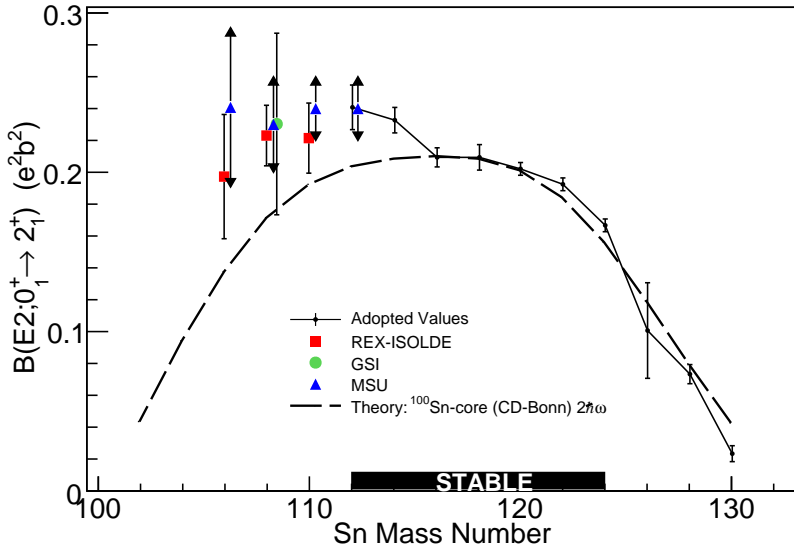


Figure 3.28: Experimental $B(E2 \uparrow)$ values in the even-mass Sn isotopes. The red squares indicate the values deduced in this work. The shell-model calculation is from Ref. [38]. The GSI value is from Ref. [38] and the MSU values are from Ref. [39].

Table 3.8: The level index, spin, parity, level energy, and reduced matrix elements $\langle i || E2 || j \rangle = M_{ij}$ for ^{64}Zn . The data are taken from Refs. [41, 42, 43, 37]. The matrix elements and level energies are given in units of eb and MeV respectively.

Level	I^π	Energy	1	2	3
1	0^+	0	0.0	0.400(19)	0.043(2)
2	2^+	0.991		-0.420(79)	0.545(28)
3	2^+	1.799			0.0

tive to the ^{64}Zn target, it is possible to extract the projectile cross section also for small scattering angles in the center of mass frame, i.e. the events detected in the two or three innermost annular strips of the DSSSD. The kinematics of the measurements with the ^{109}Ag target are such that it is not possible to determine if a detected particle is a projectile or a target. Therefore the low- θ_{cm} events cannot be distinguished from the large- θ_{cm} events. The three indepen-

Table 3.9: *The level index, spin, parity, level energy, and reduced matrix elements $\langle i||E2||j\rangle = M_{ij}$ for ^{109}Ag . The data are taken from Refs. [37, 44, 45]. The matrix elements and level energies are given in units of eb and MeV, respectively.*

Level	I^π	Energy	1	2	3	4	5	6
1	$\frac{1}{2}^-$	0.0	0.0	0.0	0.0	0.67(3)	0.80(3)	0.04(1)
2	$\frac{7}{2}^+$	0.088		0.0	3.05(2)	0.0	0.0	0.0
3	$\frac{9}{2}^+$	0.133			0.0	0.0	0.0	0.0
4	$\frac{3}{2}^-$	0.311				-0.91(39)	0.22(11)	0.0
5	$\frac{5}{2}^-$	0.415					-0.42(42)	0.0
6	$\frac{3}{2}^-$	0.702						0.0

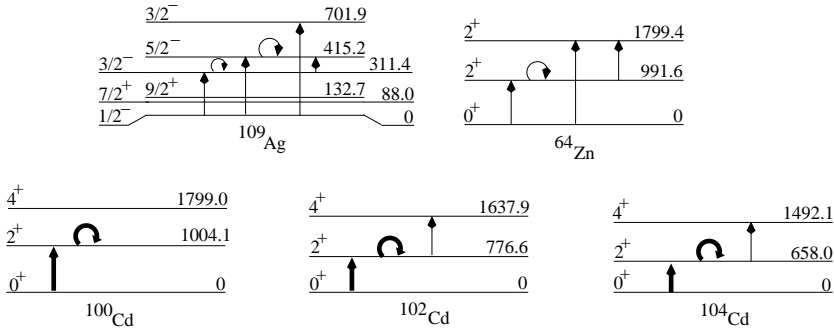


Figure 3.29: *The low-lying levels in $^{100,102,104}\text{Sn}$, ^{64}Zn , and ^{109}Ag . The diagonal and non-diagonal transition matrix elements of relevance to the analysis are indicated with arrows. The ones that are bold were fitted in this analysis.*

dent measurements of the projectile $0^+_{\text{gs}} \rightarrow 2^+_1$ excitation cross section in ^{102}Cd and ^{104}Cd are denoted $[\text{Ag}]$, $[\text{Zn}]$, and $[\text{Zn}(\text{small-}\theta_{\text{cm}})]$. The excitation cross section measurement for the ^{100}Cd isotope is lower and the intensity of the RIB was on the verge of what is sufficient for a successful experiment. Therefore this isotope was Coulomb excited against the ^{109}Ag target only. An upper limit of 6.0(24) projectile excitation events is extracted from counting all detected projectile γ -rays within $E_\gamma = 1004 \pm 100$ keV. This energy interval is given by the extreme values of the Doppler shifted energy. The complete list of deduced cross section can be found in Tab. 3.10. Several comments are in order. As mentioned, both the reorientation effect and the E2-coupling between the first excited 2^+ and the higher lying states are second order effects. Therefore, the

Table 3.10: *The Coulomb excitation cross sections of $^{100,102,104}\text{Cd}$ measured in this work. The second column indicates which target isotope that was used.*

Projectile	Target	Projectile σ_{E2} / mb
^{104}Cd	^{64}Zn	307(39)
	^{109}Ag	1013(61)
^{102}Cd	^{64}Zn	202(43)
	^{109}Ag	596(48)
^{100}Cd	^{109}Ag	201(64)

influence of the latter effect on the former is investigated. The lifetime of the 4_1^+ states in $^{102,104}\text{Cd}$ has been measured in fusion-evaporation based plunger experiments, see Refs. [46, 47, 48]. The adopted lifetimes for these states are > 5.6 ps and < 4.2 ps for ^{102}Cd and ^{104}Cd , respectively [37]. This is equivalent to reduced matrix elements $\langle 2_1^+ || E2 || 4_1^+ \rangle < 0.44$ eb and > 0.54 eb. This means that the influence of the 4_1^+ state on the $0_{\text{gs}}^+ \rightarrow 2_1^+$ excitation cross section is less than 0.4%. The low-lying states in the Cd isotopes can be explained from a vibrational structure. Therefore, one can expect a second 2^+ state at approximately twice the energy of the first excited 2^+ state. However, this two-phonon state has not been observed in the $^{100,102,104}\text{Cd}$ isotopes. Nevertheless, the effect of the 2_2^+ state on the excitation cross section can be inferred from the $\langle 2_1^+ || E2 || 2_2^+ \rangle = 0.497$ eb and $\langle 0_{\text{gs}}^+ || E2 || 2_2^+ \rangle = 0.190$ eb matrix elements in ^{106}Cd [49]. From this, it is concluded that virtual quadrupole excitations via the higher lying 2_2^+ state have a $\sim 2\%$ impact on the projectile excitation cross sections in the $^{100,102,104}\text{Cd}$ isotopes. This corresponds to a ~ 0.05 eb change in the static quadrupole moment. Thus, the effects of a higher lying 2_2^+ state are not included in this analysis.

A likelihood-based combination of several cross sections

As mentioned, the simultaneous extraction of the $Q(2_1^+)$ and $B(E2)$ values in the $^{102,104}\text{Cd}$ -isotopes requires an expanded analysis of the measured cross sections. The experimental uncertainties confine the range of possible $B(E2; 0_{\text{gs}}^+ \rightarrow 2_1^+)$ values and $Q(2_1^+)$ values to a 'one-sigma' band in the $B(E2) - Q(2_1^+)$ plane, see Fig. 3.30. The one-sigma bands extracted from each of the $^{102,104}\text{Cd}$ cross section measurements and the single one-sigma band extracted from the ^{100}Cd cross section relative to the ^{109}Ag target are shown in Paper III. Clearly, for ^{100}Cd , a definite $B(E2)$ value and $Q(2_1^+)$ value cannot be determined without any auxiliary data such as another cross section or the value of the lifetime of the 2_1^+ state. However, from the proximity of ^{100}Cd to the spherical ^{100}Sn core it is reasonable to assume that $Q(2_1^+) = 0.0$ eb. This leads to an upper limit

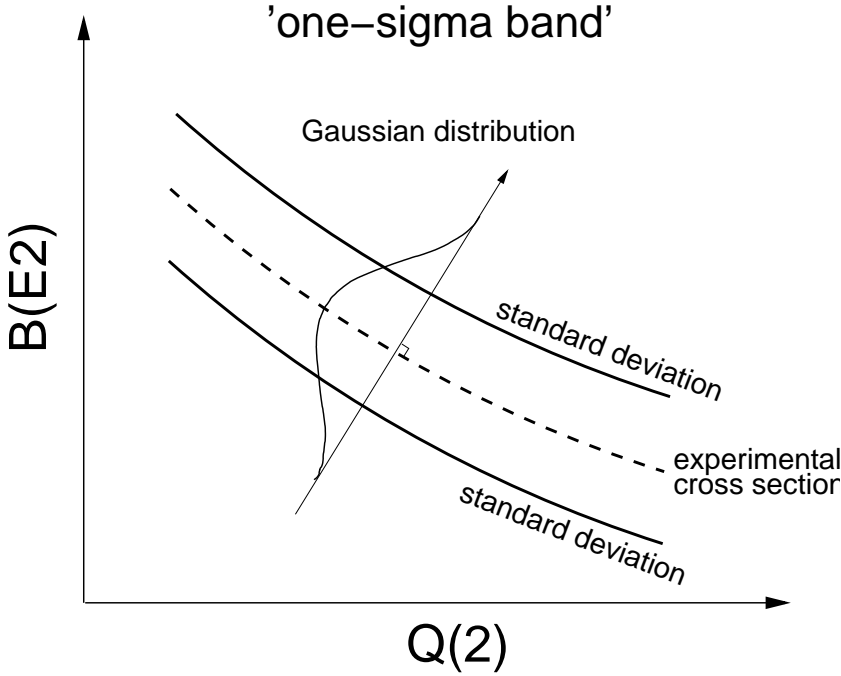


Figure 3.30: The 'one-sigma' band of $B(E2)$ and $Q(2_1^+)$ values that reproduce the experimentally determined cross section withing one sigma.

of $B(E2) < 0.28 \text{ e}^2\text{b}^2$. On the other hand, from the $^{102,104}\text{Cd}$ measurements it is possible to extract the most probable pair of the $B(E2)$ and $Q(2_1^+)$ values. The coordinates, called (B, Q) for short, for each measurement are assigned a statistical weight that reflects their distance from the measured cross section. In the numerical analysis, this weight is approximated with a Gaussian probability distribution P_k directed along the gradient of the cross-section contour curve, see Fig. 3.30. For ^{102}Cd and ^{104}Cd , the three cross sections are combined into a two-dimensional likelihood distribution according to

$$\mathcal{L}(B, Q) = \prod_{\text{measurements}} P_k(B, Q) \quad (3.17)$$

This function is evaluated for $B \in [0, 1] \text{ e}^2\text{b}^2$ and $Q \in [-2, 2] \text{ eb}$, which represents physically reasonable values compared to the heavier Cd isotopes. The normalized likelihood function is calculated on a 200×200 grid. This generates the likelihood surfaces in Fig. 3.31. The $B(E2)$ and $Q(2_1^+)$ values with the maximum likelihood are assigned as the final values. Furthermore, the one-sigma boundary of the likelihood distribution is defined as the contour curve $\mathcal{L}(B, Q) = 0.682$, in accordance with the one-sigma probability mass of a Gaus-

Table 3.11: The $B(E2; 0_{\text{gs}}^+ \rightarrow 2_1^+)/e^2b^2$ and $Q(2_1^+)/eb$ values in $^{100,102,104}\text{Cd}$.

Isotope	$B(E2; 0_{\text{gs}}^+ \rightarrow 2_1^+)$	$Q(2_1^+)$	$\langle 0_{\text{gs}}^+ E2 2_1^+ \rangle$	$\langle 2_1^+ E2 2_1^+ \rangle$
^{104}Cd	0.33(2)	0.06(15)	0.57(2)	0.08(20)
^{102}Cd	0.28(3)	0.22(19)	0.53(3)	0.29(25)
^{100}Cd	≤ 0.28	0.0	≤ 0.53	0.0

sian distribution. The two-dimensional projection of the one-sigma surface for each isotope is shown in the panels of Fig. 3.32. One can note that the likelihood surface for ^{102}Cd does not fall off as rapidly as it does for ^{104}Cd . This is primarily due to the lower statistical precision in the cross section deduced from the ^{102}Cd measurements. The probability distributions in Fig. 3.32 clearly display the correlation between the dynamic and static quadrupole moments measured in Coulomb excitation. The upper and lower uncertainties of the $B(E2)$ or $Q(2_1^+)$ values that are extracted from the point of maximum likelihood are defined as the distances along the lines of the corresponding constant $Q(2_1^+)$ or $B(E2)$ value to the intersections with the border of the one-sigma contour. If instead the full one-sigma contour is projected onto the respective axis and taken as the final uncertainty it would contain a correlation component leading to an over-estimation of the error. The resulting $B(E2)$ and $Q(2_1^+)$ values in $^{100,102,104}\text{Cd}$ are listed in Tab. 3.11. These values are plotted in Fig. 3.33 together with the known values in the heavier even-mass Cd isotopes and a shell-model prediction, see Sec. 4.6. In contrast to the light Sn isotopes, the $B(E2)$ values in $^{100,102,104}\text{Cd}$, see Fig. 3.33(a) exhibit a smooth and decreasing trend as the proton drip-line is approached. This is in agreement with the shell-model prediction presented in this figure. The amount of experimental data on the neutron rich side is scarce but indicates a slightly steeper decrease of the $B(E2)$ values. The $B(E2)$ value in ^{104}Cd has previously been measured two times using lifetime-based techniques. Muller et al. [48] report a $B(E2; 0_{\text{gs}}^+ \rightarrow 2_1^+) = 0.367^{+0.182}_{-0.092} e^2b^2$. The precision of this value is $\sim 40\%$ and is clearly in agreement with the value presented here. Boelaert et al. [46] report a very precise value, $B(E2; 0_{\text{gs}}^+ \rightarrow 2_1^+) = 0.389(13) e^2b^2$. This transition probability is 2% larger than in ^{106}Cd . Such an increase is not observed here. The $B(E2)$ value for ^{102}Cd in Tab. 3.11 is in agreement with the results from previously published lifetime measurements [46, 47]. The statistically very precise lifetimes of the 2_1^+ states in $^{102,104}\text{Cd}$ are also used in conjunction with the probability distributions in Fig. 3.32 to obtain the corresponding $Q(2_1^+)$ values, see Sec. 4.6. There, the results are also interpreted in the shell-model.

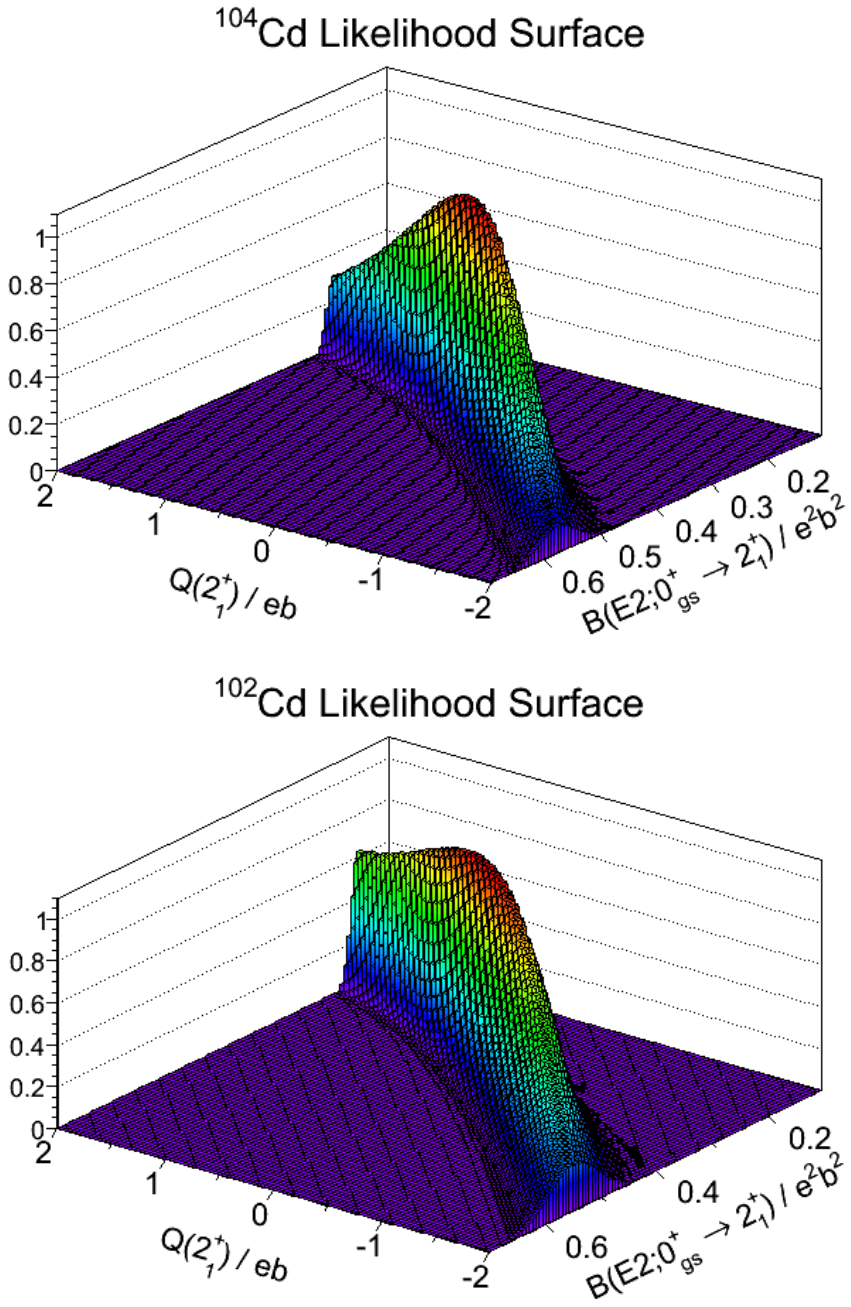


Figure 3.31: The likelihood surfaces of the $B(E2)$ and $Q(2_1^+)$ values in $^{102,104}\text{Cd}$.

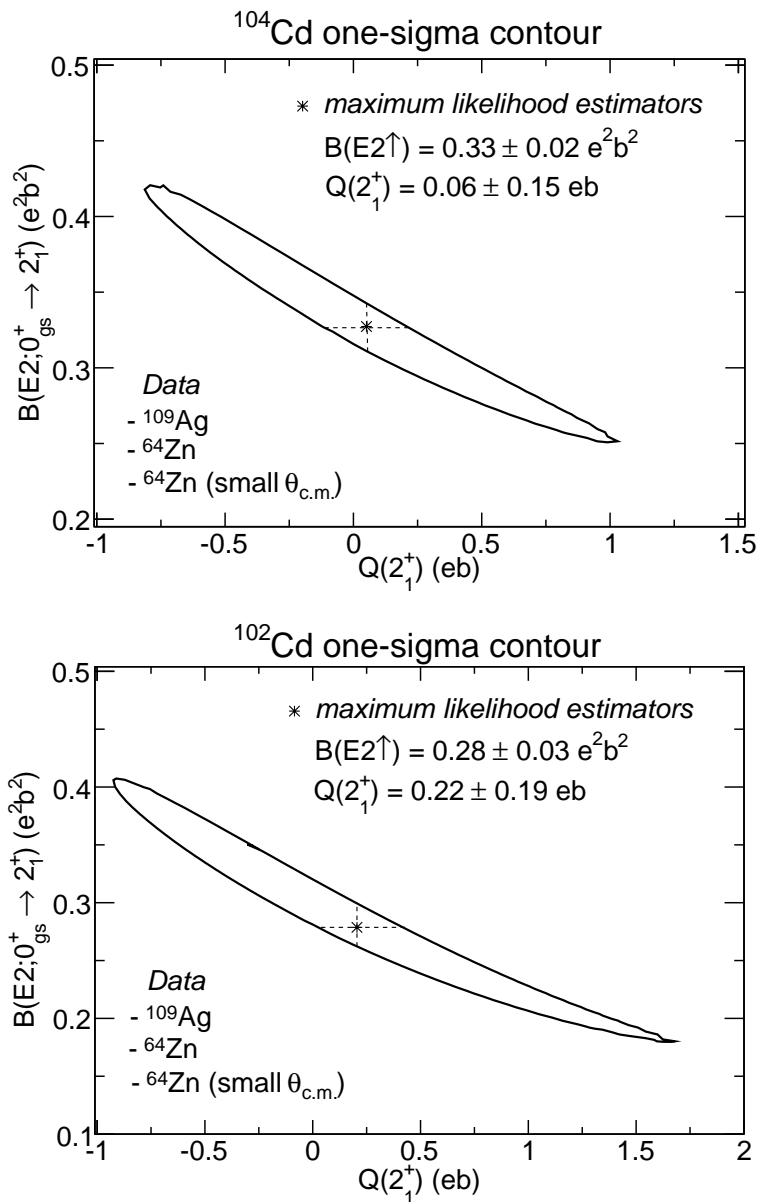


Figure 3.32: The final one-sigma contours in the $B(E2) - Q(2_1^+)$ plane. The maximum likelihood estimators for the electric quadrupole moments are indicated

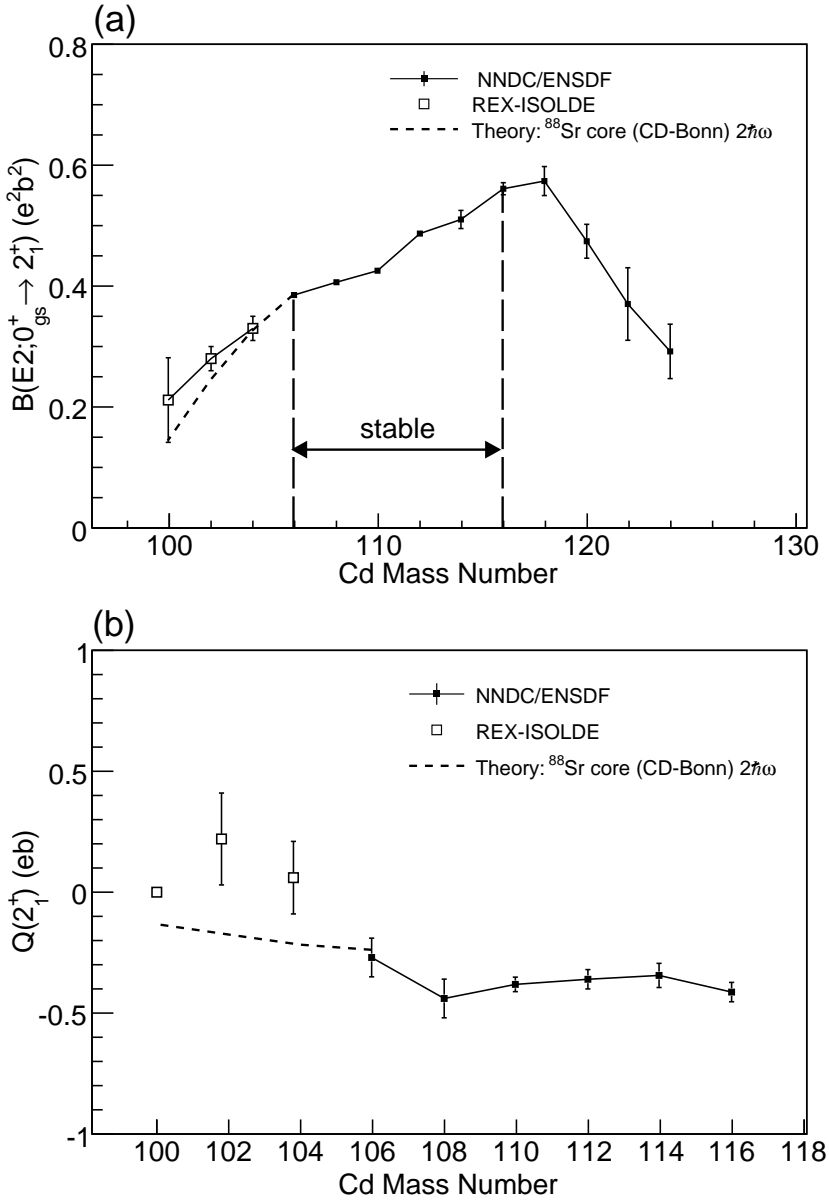


Figure 3.33: Experimental and theoretical $B(E2)$ and $Q(2^+_1)$ values in the even-mass Cd isotopes.

Transition	E_i (keV)	E_f (keV)	Lifetime τ_m (ps)	B(E2) (Wu)
$7^+ \rightarrow 7_{\text{gs}}^+$	150.8	0.0	$4 \leq \tau_m \lesssim 2000$	< 196
$6^+, (7)^+ \rightarrow 7_{\text{gs}}^+$	247.7	0.0	$15 \leq \tau_m \lesssim 2000$	< 222
$6^+, (7)^+ \rightarrow (6, 7, 8)$	247.7	96.9	$15 \leq \tau_m \lesssim 2000$	< 93

Table 3.12: Observed γ -ray transitions in ^{108}In and the deduced limits on the transition probabilities where possible.

3.7 Observed γ -ray transitions in $^{106,108}\text{In}$

The observed γ -ray transitions in $^{106,108}\text{In}$, see Tab. 3.2, are placed in the known level schemes of these isotopes, see Fig. 3.34. The assignments are based on the energies of the transitions. The excited states of $^{106,108}\text{In}$ have previously only been investigated in decay studies, see e.g. Ref. [50], and reaction experiments [51, 52, 53]. In Coulomb excitation the population of the excited states is governed by the reduced matrix elements with respect to the initial state. Therefore a different population pattern might be explored using this technique as compared to the ones previously employed. Indeed, three previously unknown γ -ray transitions at 221.1(14), 367.1(2) and 658.7(4) keV are detected in ^{106}In . Regarding the first two of these, the low probability for multiple Coulomb excitation favors a direct excitation from the 7_{gs}^+ state to a $(5^+, 6^+, 7^+, 8^+, 9^+)$ state at 367.1(2) keV. However, according to the shell-model calculations, see Sec. 4.7, this state is tentatively assigned with a spin and parity 6^+ . Regarding the 221.1(14) keV γ -ray, this is placed as an 9(3)% decay-branch from the 367 keV state to the (7^+) state at 147.2 keV. This further strengthens the existence of a state at 367 keV. The weak 658.7 keV transition could not be placed. It should be pointed out that the low statistics of the collected γ -ray yields exclude a reliable $\gamma - \gamma$ coincidence analysis. It is therefore stressed that the placement of the observed 367 keV transition in ^{106}In is based on the observed energy sums. The 151 keV γ -ray yield in ^{108}In is a doublet, i.e. this yield is the sum of the $(5)^+ \rightarrow (6, 7, 8)$ and $7^+ \rightarrow 7_{\text{gs}}^+$ transitions. This doublet is separated using the previously known branching ratio and the observed γ -ray yield of the 248 keV transition $(5)^+ \rightarrow 7_{\text{gs}}^{+3}$. A γ -ray transition doublet at 123 keV is observed also in ^{106}In . The yield is the sum of the $(2)^+ \rightarrow (2)^+$ and $(6^+, 7^+, 8^+, 9^+) \rightarrow 7_{\text{gs}}^+$ transitions. However, the lack of known branching ratios for this case removes the possibility of a separation similar to that of ^{108}In .

The GOSIA analysis of the γ -ray yields from ^{106}In and ^{108}In is hampered by the lack of existing spectroscopic data such as branching ratios and mixing ratios. Nevertheless, the χ^2 -minimization converged for the ^{108}In case. The determined $B(E2)$ values are given in Tab. 3.12. The upper limit of the $B(E2)$

³Branching ratios of the $(5)^+$ state at 247.7 keV. $E_\gamma = 151$ keV ($I_\gamma = 8.8(13)\%$) and $E_\gamma = 248$ keV ($I_\gamma = 91.2(63)\%$)

values provide a lower limit on the lifetime. Furthermore, the γ -ray yields are extracted from peaks that are sensitive to and improved by the Doppler correction. This means the γ -rays are emitted from the nuclei in flight. Therefore, an upper limit on the lifetime is given by the known flight time from the ^{58}Ni target to the DSSSD, i.e. ~ 2 ns.

In Sec. 4.7, the observed de-excitation patterns in $^{106,108}\text{In}$ are interpreted using the shell-model. A set of E2 and M1 reduced matrix elements are calculated and used to simulate the strengths of the corresponding γ -ray transitions. From the comparison with the experimental data a more detailed investigation of the structure of the excited states is carried out. In particular, the excited states of ^{108}In are analyzed with respect to their $\pi^{-1} \otimes \nu$ multiplet structure.

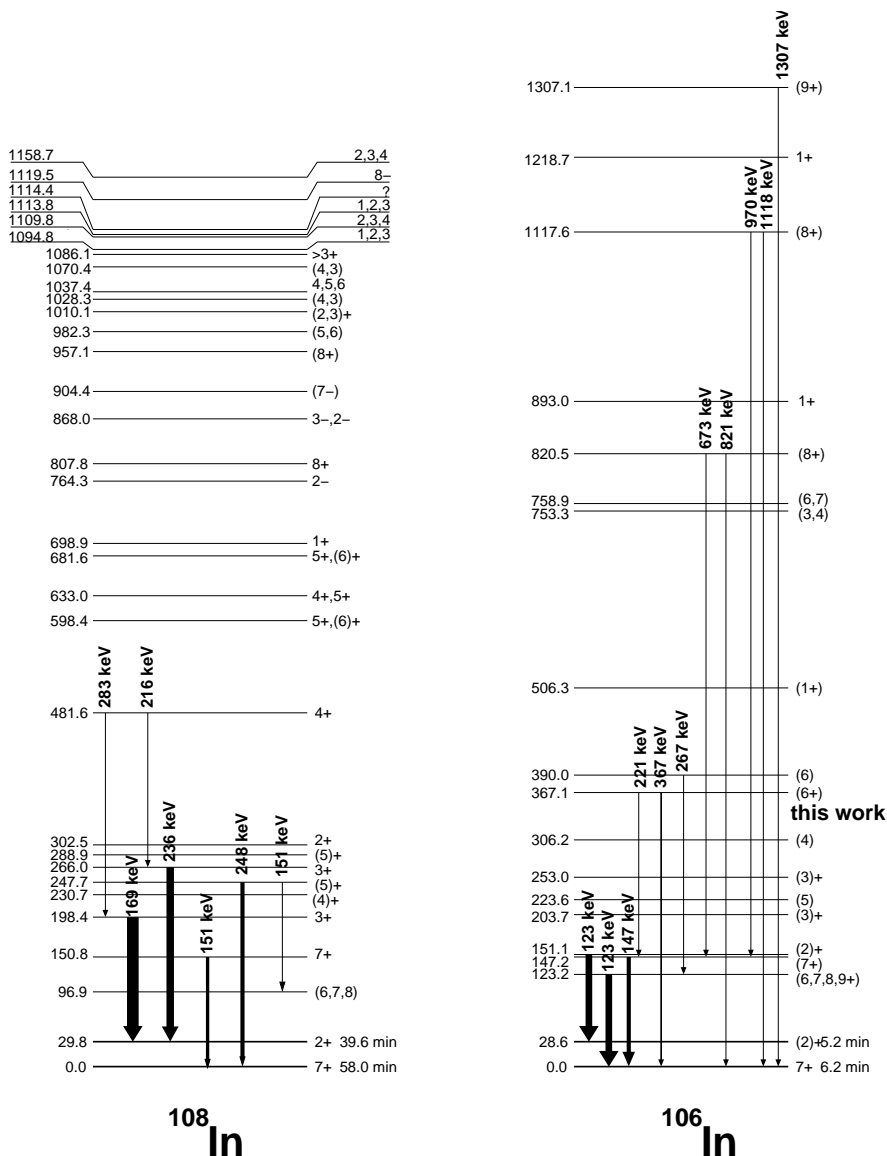


Figure 3.34: The observed excitation patterns in $^{106,108}\text{In}$. The thickness of the lines indicate the intensity of the observed γ -ray transitions.

CHAPTER 4

THEORETICAL INTERPRETATION

The shell-model studies of $^{106,108,110}\text{Sn}$, $^{100,102,104}\text{Cd}$, and $^{106,108}\text{In}$ carried out in this thesis are based on realistic two-body effective interactions derived from the G-matrix renormalized free nucleon-nucleon potentials CD-Bonn [54, 55] or N3LO [56, 57]. The G-matrix renormalization and the subsequent many-body perturbative expansion [58] of the nucleon-nucleon interaction as well as the large-scale shell-model calculations [59] are carried out using the computational codes provided by the theoretical nuclear physics group at Oslo University. The underlying theory is discussed in Secs. 4.1-4.3. The results and interpretations of the shell-model calculations in the Sn and the Cd isotopes are presented in Secs. 4.4 and 4.6. The generalized seniority scheme and its application to the Sn isotopes is described in Sec. 4.5. The shell-model calculations of the In isotopes and the proton-neutron multiplet interpretation of the excited states in ^{108}In are presented in Sec. 4.7.

4.1 Shell-model calculations

The key ingredient in the many-body Schrödinger equation Eq. 1.1 is the residual interaction V_R between two nucleons that are moving in the static one-body field of the nucleus. The single-particle orbits of the shell-model are schematically shown in Fig. 4.1. As mentioned in the introduction, the shell-model approach to the nuclear many-body problem is based on the weak strength of V_R . This enables a perturbative solution of the Schrödinger equation. The interaction energy of two nucleons that scatter from the shell-model states a and b into the states c and d is given by the two-body matrix element (TBME) $\langle ab|V_R|cd\rangle_{JT}$ where J is the coupled angular momentum and T is the isospin. The details of the construction of V_R for the present cases are presented in Sec. 4.2. A perturbative approach implies that the Schrödinger equation can be solved in the unperturbed single-particle basis $|\Phi_i\rangle$. In this work, this is constructed from Slater determinants [60] of harmonic oscillator wave functions. The oscillator energy is given by $\hbar\omega = 45A^{-1/3} - 25A^{-2/3}$, where A is the mass number of the nucleus. The Slater determinants represent multi-particle configurations. However, the two-body interaction in a multi-particle configu-

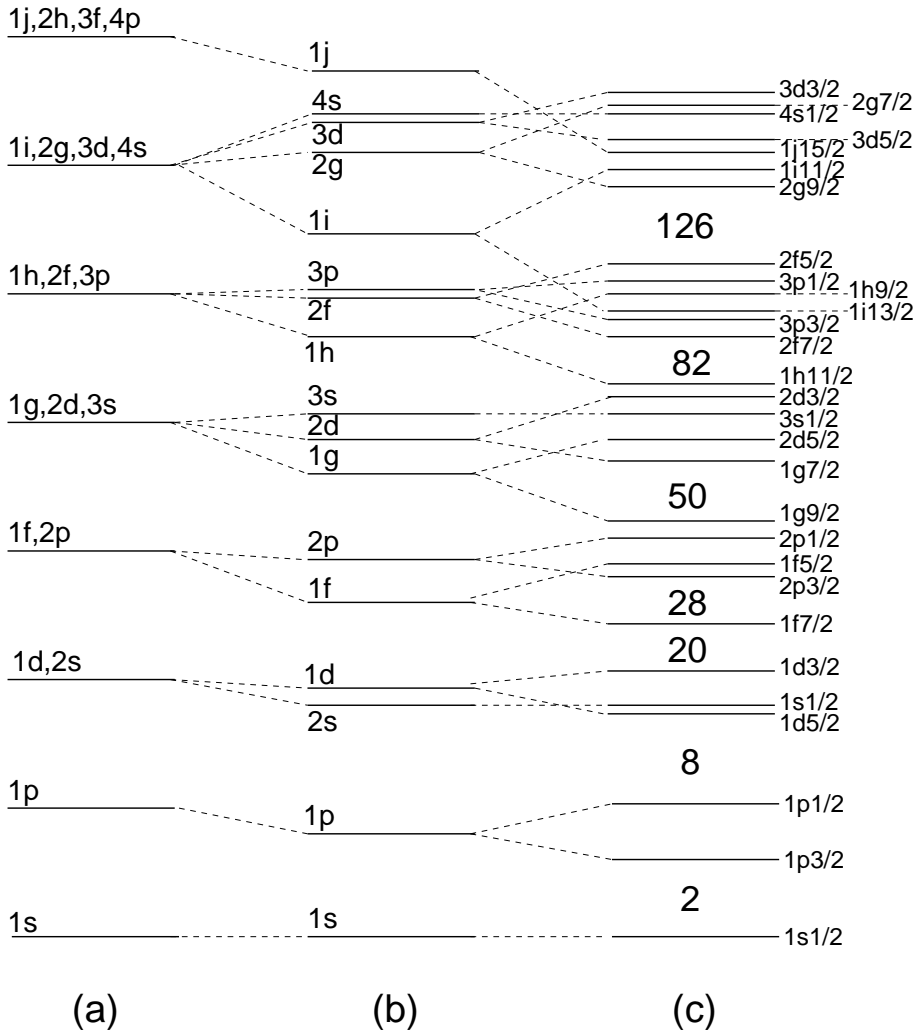


Figure 4.1: The proton and neutron energy levels in (a) the harmonic oscillator potential (b) the harmonic oscillator potential without the ℓ -degeneracy (c) the harmonic oscillator without the ℓ -degeneracy but with the inclusion of a spin-orbit coupling. Notice how the single-particle orbits are bunched such that energy-gaps occur at the proton and neutron numbers 2, 8, 20, 28, 50, 82, 126. These are sometimes referred to as 'magic numbers'.

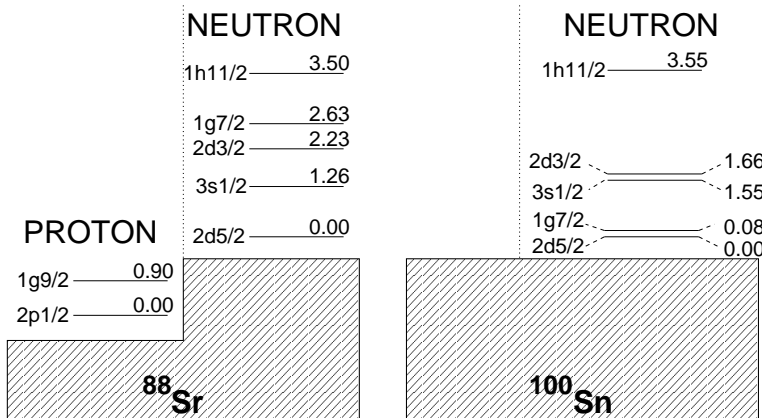


Figure 4.2: Schematic illustration of the ^{88}Sr and ^{100}Sn shell-model cores used in the calculations here. The energies, in MeV, of the single-particle orbits of the proton and neutron model spaces are indicated. The ^{88}Sr core is used in the shell-model calculations of the Cd and In isotopes while the ^{100}Sn core is used for the calculations in the Sn isotopic chain.

ration can be expressed as a linear combination of matrix elements of two-body configurations [60]. In addition to the perturbative treatment of the residual interaction, the Hilbert space of the A -body problem is truncated. The dimensionality of the single-particle basis grows combinatorially with the number of protons (n_π) and neutrons (n_ν) as

$$\begin{pmatrix} N_\pi \\ n_\pi \end{pmatrix} \begin{pmatrix} N_\nu \\ n_\nu \end{pmatrix} \quad (4.1)$$

where N_π and N_ν are total proton and neutron degeneracies of the considered single-particle orbits. Therefore, the equations are solved in a subspace referred to as the model space \mathcal{M} . Two different model spaces are used in the calculations presented here, see Fig. 4.2. The lower-energy orbits are referred to as the core. The introduction of a model space requires the concept of an effective interaction V_{eff} . Indeed, the exclusion of certain nuclear configurations $|\Phi_i\rangle$ implies that if the model-space wave functions $|\Psi_i^{\mathcal{M}}\rangle = \sum_{i \in \mathcal{M}} |\Phi_i\rangle$ are to reproduce the true energies E_i of the nuclear states, a similarity transformed Hamiltonian H_{eff} must be constructed such that

$$H_{\text{eff}}|\Psi_i^{\mathcal{M}}\rangle = E_i|\Psi_i^{\mathcal{M}}\rangle \quad (4.2)$$

The choice of model space is dictated by the configurations that are essential for the construction of the low-lying excited states. The major shells offer a natural limit of the model space boundaries. The dominating components of the wave functions are the ones of the valence particles, i.e. the nucleons in

the model space. The energy required for a particle to scatter across the gap between two major shells is much larger than the energy splitting between two single-particle states in the model space. The effective interaction should be constructed so that it captures the dominating correlations between the nucleons inside and outside the model space. Early examples that show the strengths and validate the applicability of this approach includes e.g. Refs. [61, 62]. In the current work, the effective interactions for the model spaces in Fig. 4.2 are derived using many-body perturbation theory [58], see Sec. 4.2.

Even with an effective interaction in place, solving the many-body Schrödinger equation poses a computationally challenging problem. It is evident that the dimensionalities of the model-space single-particle basis for the present cases ($\sim 10^7$) grow beyond the limits for an exact diagonalization. The memory requirements alone prevent this. Instead, a numerical method called the Lanczos algorithm [63] is used to extract the lowest eigenvalues and the corresponding eigenvectors. The numerical computation of the results presented here are carried out on the computational clusters Milleotto, at the LUNARC facility in Lund, and on Neolith, at the National Supercomputer Centre in Linköping.

4.1.1 Single-particle energies

The single-particle energies (SPEs) serve as the second input to the shell-model calculation. They are given relative to the specific core that is used, i.e. for the present cases either ^{100}Sn or ^{88}Sr . However, the single-particle energies can drift as the effective interaction is switched on and the nucleon number is varied. This can affect the outcome of the calculations. Naturally, care must be taken such that the magicity of the chosen core remains for the isotopes studied in the calculation. The drift of the SPEs can be partially absorbed by tuning the TBMEs of the effective interaction. In such cases, the tuning is done such that the shell-model calculations reproduce the spectroscopy of a selected set of nuclei in the vicinity of the employed core. This phenomenological approach is widely used although it is not implemented here. It has several apparent advantages but one drawback is that it obscures the bottom-up approach in understanding the nucleon-nucleon interaction.

The proton and neutron SPEs relative to the ^{88}Sr core, see Fig. 4.2, are known from experiments. The neutron structure of the stable ^{89}Sr nucleus is known from $\text{Sr}^{88}(d, p)^{89}\text{Sr}$ reactions [64, 65]. The first excited state in the $1\pi + ^{88}\text{Sr}$ system, i.e. the ^{89}Y nucleus, is a $\frac{9}{2}^+$ state at 909 keV and originates from the promotion of a proton from the $2p_{1/2}$ orbit to the $1g_{9/2}$ orbit, see Ref. [66] and references therein. These proton and neutron SPEs have previously been used together with realistic effective interactions in shell-model studies of e.g. the neutron-rich $^{92-100}\text{Zr}$ isotopes [67] and the ^{102}In isotope [68].

The ^{100}Sn core is unstable but still suitable as shell-model core, see Ref. [69]

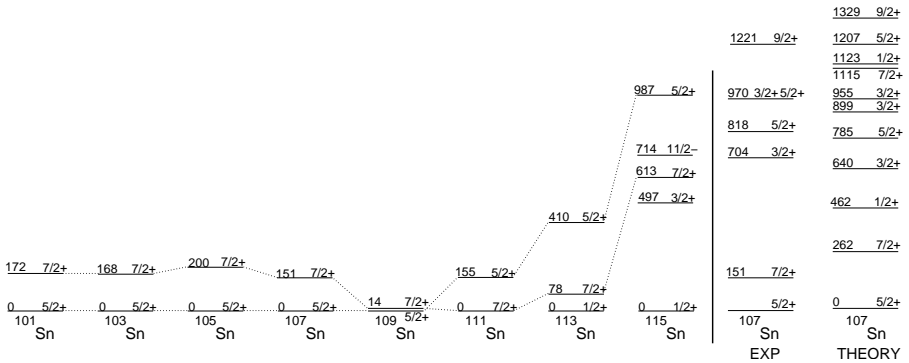


Figure 4.3: The lowest lying $\frac{5}{2}^+$ and $\frac{7}{2}^+$ states in the odd mass isotopes $^{101-115}\text{Sn}$. In the extreme single-particle picture the $2d_{5/2}1g_{7/2}$ neutron orbits are filled at ^{114}Sn . The right part of the figure shows the result from a shell-model calculation of ^{107}Sn using the ^{100}Sn core, the SPEs from Fig. 4.2, and the N3LO-based effective interaction.

and references therein. Very little is known regarding the neutron SPEs in the major shell above ^{100}Sn . The $2d_{5/2} - 1g_{7/2}$ single-neutron energy difference was recently measured to 171.7(6) keV in decay studies of ^{101}Sn [70]. The corresponding energy difference in ^{103}Sn is known from a fusion-evaporation experiment [71]. For the present shell-model studies, a set of neutron SPEs, see Fig. 4.2, are adopted according to Ref. [38]. These reproduce the low-lying spectroscopy of the even-mass $^{102-130}\text{Sn}$ isotopes. The $(\frac{5}{2})_1^+$ and $(\frac{7}{2})_1^+$ states in the light Sn isotopes are estimated to be $\sim 80\%$ of single-particle character [72]. The $(\frac{3}{2})_1^+$ and $(\frac{1}{2})_1^+$ states are more mixed. This allows one to approximately follow the single-particle energy drift of the $1g_{7/2}$ and $2d_{5/2}$ orbits in the light Sn isotopes, see Fig. 4.3. This indicates that the $2d_{5/2}$ and $1g_{7/2}$ orbits are nearly degenerate in the light Sn isotopes. Less can be said about the location of the $3s_{1/2}$, $2d_{3/2}$, and $1h_{11/2}$ orbits. The SPEs used in this region are tuned to reproduce the low-lying spectra of the odd-mass isotopes. Since the results also depend on the choice of effective interaction, various values can be found in the literature, see Ref. [72] for a partial compilation. It can be noted that the energy of the $3s_{1/2}$ orbit ranges between 1.6-2.5 MeV. Similarly the $2d_{5/2}$ and $1h_{11/2}$ SPEs range between 1.6-3.2 and 2.4-3.55 MeV, respectively. The neutron single-hole states relative to the ^{132}Sn core are known from β^- and γ -ray spectroscopy of ^{131}In [73]. The heavy $^{120-130}\text{Sn}$ isotopes have been investigated relative to the ^{132}Sn core using a realistic neutron-hole effective interaction [74]. The results are in agreement with the experimental $B(E2; 0_{\text{gs}}^+ \rightarrow 2_1^+)$ values for the heavy Sn isotopes.

The drift of the single-particle energies is exemplified in the difference between

the single-neutron energies relative to the ^{88}Sr core and the ^{100}Sn core. The underlying mechanism is to a large extent the monopole part of the nuclear tensor force [75] between nucleons in nearly identical orbits. This phenomenon dates back to the microscopic origin of the onset of deformation as explained by Federman and Pittel [76, 77]. The most striking difference in the neutron single-particle energies of the ^{88}Sr core as compared to the ^{100}Sn core is the location of the neutron orbits $1g_{7/2}$ and $2d_{5/2}$. In the transition from ^{88}Sr to ^{100}Sn the protons gradually fill the $1g_{9/2}$ orbit. The tensor force is attractive when acting between one nucleon in the $j' = \ell' + \frac{1}{2}$ orbit and the other in the $j = \ell - \frac{1}{2}$ orbit. Likewise, it is repulsive between nucleons in $j' = \ell' \pm \frac{1}{2}$ and $j = \ell \pm \frac{1}{2}$ orbits. Furthermore, the monopole tensor force is twice as strong between unlike nucleons [75]. Therefore the neutron $1g_{7/2}$ orbit is lowered relative to $2d_{5/2}$ as the proton $1g_{9/2}$ is filled. It should be noted that this effect, although in different orbits, is suggested as responsible for the weakening of the $N = 28$ shell closure [78].

4.1.2 Effective charges

The electromagnetic quadrupole transition probability between two shell-model wave functions $|\Psi_i^{\mathcal{M}}\rangle$ are readily calculated as the overlap integral

$$\langle \Psi_i^{\mathcal{M}} || E2_{\text{eff}} || \Psi_j^{\mathcal{M}} \rangle \quad (4.3)$$

where an effective $E2$ transition operator $E2_{\text{eff}}$ is introduced on the same grounds as the effective interaction i.e. that the transition probabilities calculated using model-space wave functions should give the same result as when using the true wave functions $|\Psi\rangle$. The renormalization of the $E2$ operator is given by an effective charge e_{eff} for the protons and the neutrons separately. These retain their physical values $e^{\nu} = 0.0$ e and $e^{\pi} = 1.0$ e if the Hilbert space is not truncated. The concept of effective charges is physically relevant. It is well-known that the same effective charges can be used for similar transitions in different nuclei in the same shell or model space [3]. Physically, the effective charge arises from the contributions of core excited particles that participate in the transition between two states in the model space. In the collective model of Bohr and Mottelson [79, 80] the effective charge is interpreted as a polarization of the core by the valence nucleons. The core becomes deformed by the non-spherical field generated by the valence nucleons and consequently acquires a quadrupole moment. In this picture, the effective charge minus the bare charge of the nucleon is called the polarization charge e_{pol} . In the isospin formalism¹ the polarization charge is decomposed into an isovector $e_{\text{pol}}^{(1)}$ and an isoscalar $e_{\text{pol}}^{(0)}$ component according to

$$e_{\text{pol}} = e_{\text{pol}}^{(0)} + e_{\text{pol}}^{(1)} \cdot 2t_z \quad (4.4)$$

¹The proton-neutron formalism is used otherwise throughout the presentation here.

where t_z is the projection of the isospin quantum number. The effective proton and neutron charges can therefore be written as

$$\begin{aligned} e_{\text{eff}}^{\pi} &= 1 + e_{\text{pol}}^{(0)} - e_{\text{pol}}^{(1)} \\ e_{\text{eff}}^{\nu} &= e_{\text{pol}}^{(0)} + e_{\text{pol}}^{(1)} \end{aligned} \quad (4.5)$$

In this work, the need for a renormalization of the neutron effective $E2$ charge is observed, in particular for the light Sn isotopes, see Secs. 4.4-4.6. It should be pointed out that the j -dependence of the effective charge is neglected in the calculations presented here. This could come to play an important role in tracing the origin of the observed renormalization effects.

4.2 The effective two-body interaction

There exists various approaches in obtaining an effective two-body interaction for use within the model-space. In the empirical approach the two-body matrix elements (TBME), of a rather small model space, is extracted from the experimentally observed energy spectra in several nuclei, see e.g. Ref [61]. This method circumvents the need for explicitly defining the effective interaction in order to understand the regularities in the observed spectra. However, little insight is gained about the microscopic features of the interaction. A second approach is to define the interaction from observed properties and symmetries of nuclei. This leads to e.g. the (modified) surface delta interaction [81] which essentially captures the short-ranged nature of the nucleon-nucleon interaction. A second exampled is the quadrupole-quadrupole interaction [82] which can be used to describe the quadrupole deformation of nuclei.

The starting point of the many-body perturbative construction of the effective interaction is the renormalized free nucleon-nucleon interaction. Indeed, the singular nature of the free nucleon-force, see Fig. 4.4, requires renormalization before treating it perturbatively. The G -matrix technique is employed for this purpose, see Sec. 4.3. The Hilbert space of single-particle basis states is divided into a model space \mathcal{M} and a remaining part. The corresponding projection operators P and Q onto the respective spaces are defined as

$$P = \sum_{i \in \mathcal{M}} |\Phi_i\rangle\langle\Phi_i| \quad Q = \sum_{i \notin \mathcal{M}} |\Phi_i\rangle\langle\Phi_i| \quad (4.6)$$

Therefore, the model-space component of the true wave function $|\Psi\rangle$ is given by $P|\Psi\rangle$. There exists a mapping from the model-space wave function to the true wave function, i.e. $|\Psi\rangle = \Omega|\Psi^{\mathcal{M}}\rangle$ where Ω is defined as the wave operator, see Ref. [58]. Furthermore, the true wave function can be written as

$$|\Psi\rangle = |\Psi_{\mathcal{M}}\rangle + \sum_{i \notin \mathcal{M}} \frac{|\Phi_i\rangle\langle\Phi_i|V_R|\Psi\rangle}{E - \varepsilon_i} \quad (4.7)$$

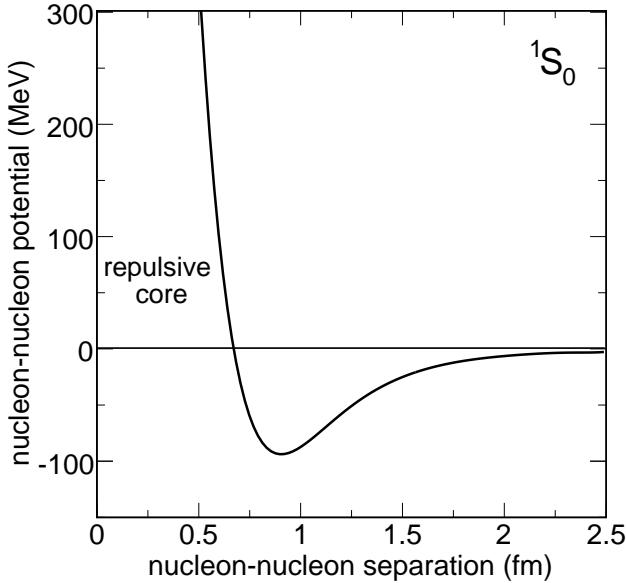


Figure 4.4: The 1S_0 (Russell-Saunders notation) inter-nucleon potential as a function of nucleon-nucleon separation. The singular nature of the free nucleon interaction is here manifested as a repulsive core.

where V_R is the residual interaction, and E and ε_i are the energy eigenvalues of $|\Psi\rangle$ and $|\Phi_i\rangle$, respectively. This can be written more compactly in operator form

$$\Omega(E) = 1 + \frac{Q}{E - H^{(0)}} V_R \Omega(E) \quad (4.8)$$

where $H^{(0)}$ is the Hamiltonian of the unperturbed one-body field and the energy dependence has been emphasized. According to e.g. Ref. [58], the effective model-space interaction is given by $V_{\text{eff}} = V_R \Omega(E)$. Iterating this with the above expression gives

$$V_{\text{eff}} = V_R + V_R \frac{Q}{E - H^{(0)}} V_R + V_R \frac{Q}{E - H^{(0)}} V_R \frac{Q}{E - H^{(0)}} V_R + \dots \quad (4.9)$$

This expansion contains the unknown energy E of the true wave function.² The expansion can be transformed into one containing only the unperturbed energy E_v of the valence nucleons relative to the core and a corresponding model-space

²i.e. it is a Brillouin-Wigner expansion

Hamiltonian $H_v^{(0)}$ [58]³

$$V_{\text{eff}} = V_R + V_R \frac{Q}{E_v - H_v^{(0)}} V_R + V_R \frac{Q}{E_v - H_v^{(0)}} V_R \frac{Q}{E_v - H_v^{(0)}} V_R + \dots \quad (4.10)$$

In this work, the valence nucleon energies are degenerate and the expansion is truncated at third order. Furthermore, the excitation energy of the intermediate particle-hole interactions are limited to $5\hbar\omega$. The expansion in Eq. 4.10 introduces the correlations between the valence particles and the core as well as with the unoccupied states at higher energy. The order-by-order effects of Eq. 4.10 on the excited states in ^{108}Sn and the $B(E2; 0_{\text{gs}}^+ \rightarrow 2_1^+)$ values are shown in Fig. 4.5. A detailed list of which interaction diagrams that are taken into account at each order is given in Ref. [58]. The first order term corresponds to the 'bare' interaction as given by the G -matrix. This includes only the particle-particle interactions. The important intermediate core-excited states occur first at second order. The well-known 3p-1h core-polarization interaction is one of them. This describes the interaction of two valence particles via the intermediate creation of a particle-hole excitation of the core. The corresponding interaction diagram is included in the bottom of the second-order calculation in Fig. 4.5. In this figure it is also noted that the excited spectrum of ^{108}Sn does not change much when adding the third-order correlations. However, from detailed investigations [83] it has been observed that in some cases the third-order diagrams tend to cancel the second-order contributions. It should also be pointed out that the expansion does not exhibit any general order-by-order convergence. In Fig. 4.5 one of the third-order diagrams has been included. This particular example can be interpreted as a renormalization of the particle-hole propagator of the second-order core-polarization.

4.3 Renormalization of the free NN-interaction

From measurement of the phase shifts in nucleon-nucleon scattering experiments it is evident that the free nucleon-nucleon interaction V_{NN} has a strong repulsive character at very short distances, see Fig. 4.4. Since the uncorrelated nucleon wave functions $|\psi\rangle$ are non-zero for small nucleon-nucleon separations, the interaction matrix elements $\langle\psi|V_{NN}|\psi\rangle$ are very large in this region. The G -matrix [84, 85] introduces a correlation such that the matrix elements are limited and become suitable for a perturbative expansion. In a diagram interpretation the G -matrix corresponds to summing up the particle-particle ladder-diagrams. The G -matrix is obtained from the solution to the Bethe-Salpeter equation

$$G(\omega) = V_{NN} + V_{NN} \frac{Q_F}{\omega - H^{(0)}} G(\omega) \quad (4.11)$$

³i.e. a Rayleigh-Schrödinger expansion

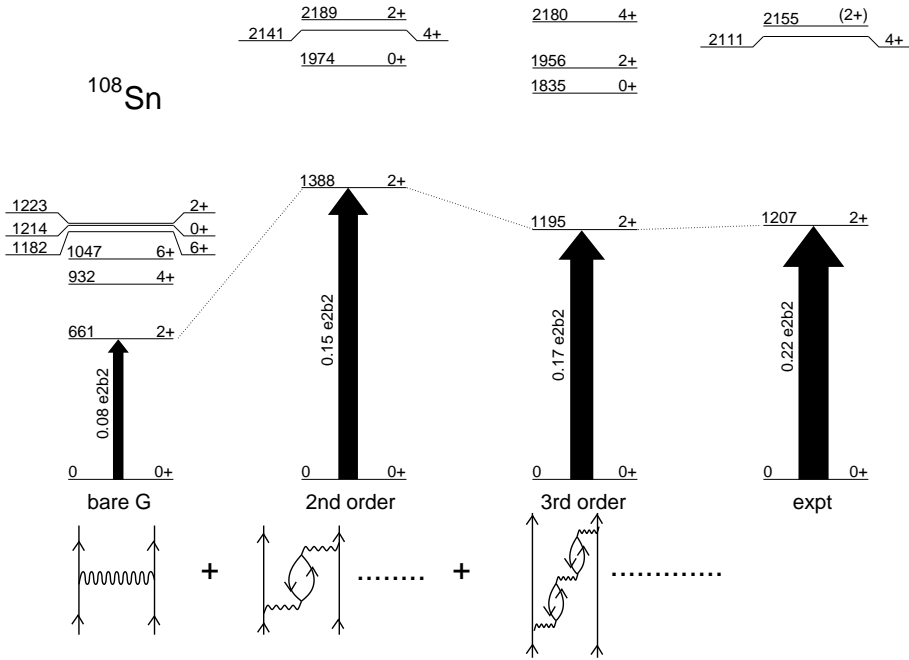


Figure 4.5: The low-lying states in ^{108}Sn calculated from the $N3\text{LO}$ nucleon-nucleon potential. The different segments show the effects of successively adding the first, second, and third order terms in Eq. 4.10. At first order, only the bare interaction, i.e. the G -matrix, is included. At second order, the well-known core-polarization term appears. This has a large impact on the calculated spectrum as well as the transition probability and clearly shows that intermediate core-excited states are needed in the interaction. See the text for further details.

where \mathcal{Q}_F is the Pauli operator that controls the summation of states in G such that particles below the Fermi energy only scatter into states above it. The starting energy ω represents the effects of the nuclear medium on the interaction. It is demonstrated in Ref. [58] that the final two-body matrix elements of the effective interaction and energy eigenvalues are relatively insensitive to the choice of starting energies. Many of the details regarding the solution of Eq. 4.11 are given in e.g. Refs. [58, 3]. For the present cases, the G -matrix methods are employed using the computational codes provided by the Oslo group.

4.3.1 The CD-Bonn and N3LO potentials

The phase shifts from nucleon-nucleon scattering experiments with laboratory energies ≤ 350 MeV and $\ell \leq 6$ have been fitted to a wide range of different nucleon-nucleon potentials, see e.g. Ref. [86]. Here, the two recent momentum-space nucleon-nucleon interaction models CD-Bonn [54, 55] and N3LO [56, 57] are used as input to the G -matrix. These models reproduce the measured on-shell phase shifts equally well. However, the off-shell behavior and in particular the physical interpretation of the N3LO potential differ from the CD-Bonn potential. CD-Bonn is based on a multiboson-exchange while the N3LO interaction stems from the fundamental symmetries of quantum chromodynamics (QCD). In addition, only pions are included as mediators of the nuclear force.

The idea of massive-particle exchange as responsible for the nucleon-nucleon interaction was introduced by Yukawa in the 1930s. The meson-field $\varphi(r)$ solution to the Klein-Gordon equation is given by the well-known ‘Yukawa potential’

$$\varphi(r) = \frac{g}{4\pi} \frac{e^{-mr}}{r} \quad (4.12)$$

The effective range of the interaction can be estimated from the mass m of the force-mediating particle. In this picture the intermediate region ($1 \text{ fm} \lesssim r \lesssim 2 \text{ fm}$) of the nucleon-nucleon interaction is described by two-pion exchange, while one-pion exchange dominates in the longer range ($r \gtrsim 2 \text{ fm}$). In the CD-Bonn potential, several additional bosons, including the fictitious σ -boson, are included in order to reproduce the experimentally determined phase shifts. It is the most elaborate boson-exchange model ever constructed. The effective interaction in the shell-model calculations of the Cd and In isotopes is derived from a version of the CD-Bonn potential described in Ref. [54]. For the Sn calculations the CD-Bonn potential of Ref. [55] is used. The latter and more recent version is based on an extended and more sophisticated description of the charge-dependence of V_{NN} . The charge-symmetry breaking (CSB) in V_{NN} , i.e. the fact that the proton-proton force is not equal to the neutron-neutron force, originates in the proton-neutron mass difference [87]. The neutron-to-proton mass ratio is 1.0014 and the absolute difference is 1.2933 MeV. It is experimentally verified that e.g. in the 1S_0 partial wave the neutron-neutron force is slightly more attractive than the proton-proton force, disregarding electromagnetic effects [87]. The charge independence breaking (CIB) in V_{NN} , i.e. the fact that the proton-neutron force is not equal to the force between like nucleons, originates primarily from the pion mass-splitting [88]. The effects of CSB and CIB can be studied by e.g. comparing the energies of analogue states in mirror nuclei and isobaric mass triplets, respectively. It was concluded in Ref. [89] that CSB and CIB play an equally important role as the Coulomb potential. All effective interactions employed here include CSB and CIB.

It is now also realized that spontaneously broken chiral symmetry [90] is crucial

for an accurate description of nuclei. This is exploited in the N3LO nucleon-nucleon interaction [57, 56]. The chiral (left-right handed) symmetry group of the up-down quark sector of the QCD Lagrangian is broken by the non-zero and non-equal quark masses. If the physical solutions to the nucleon-nucleon Lagrangian were chiral invariant, which is not seen experimentally [90], there would e.g. have existed opposite parity and equal-mass nucleons and pions. The N3LO Lagrangian is an effective field theory (EFT) [91] in the sense that it includes only pions and nucleons. The quark-gluon degrees of freedom are integrated out. Weinberg showed [92] that it is possible to construct a systematic expansion, known as a chiral perturbation, of the free nucleon-nucleon interaction in terms of $(Q/\Lambda)^\nu$, where Q is the pion momentum transfer, Λ is ~ 1 GeV, and $\nu = 1, 2, 3, \dots$. For the chiral expansion to converge, Q must be smaller than Λ . The number of terms in the expansion to order ν is finite. Presently, $\nu = 4$ is the highest-order chiral EFT nucleon-nucleon Lagrangian constructed. Three-nucleon forces are present at order $\nu \geq 3$, but not included in the present N3LO interaction. The N3LO interaction contains $N_{par} = 29$ parameters whereas CD-Bonn has 38. At $\nu = 4$ the χ^2/N_{par} of the fit to neutron-proton scattering data is 1.1. The corresponding value for CD-Bonn is 1.02. The χ^2/N_{par} for $NNLO$ ($\nu = 3$) and NLO ($\nu = 2$) are 10.1 and 36.2 [57, 93], respectively. This indicates a rapid convergence with increasing ν . There are two arguments that make chiral EFT models appealing. First of all, it stems from the underlying QCD making it the most fundamental approach as of today, and secondly, many-body interactions come out systematically with increasing chiral order ν .

In the shell-model calculations of the even-mass Sn isotopes, two effective interactions are derived. One based on CD-Bonn and the other on N3LO. No real difference could be observed in the final results. The difference between different nucleon-nucleon potentials primarily appears in the off-shell momenta, i.e. inelastic in scattering-matrix elements. The off-shell effects are certainly present in the nuclear many-body problem as the intermediate states of nucleon excitations violate energy conservation for a short period of time. The implications for nuclear structure calculations are predominantly in the bulk properties of nuclei such as binding energies. There exists an important connection between the tensor force of the free nucleon-nucleon potential and the central potential it generates in the nuclear medium. Namely, the G -matrix can approximately be decomposed as $V_{central} + V_{tensor}$ [86]. In addition, all nuclear interaction models reproduce very similar on-shell G -matrix elements. Therefore, a weak (strong) central force implies a strong (weak) tensor force. The strength of the tensor force is reflected in the magnitude P_D of the D -state⁴ component of the deuteron wave function. The presence of this is essential for the nucleon-nucleon interaction to reproduce the electric quadrupole and magnetic dipole moments of the deuteron. For N3LO, P_D is 4.51% whereas

⁴angular momentum $L = 2$

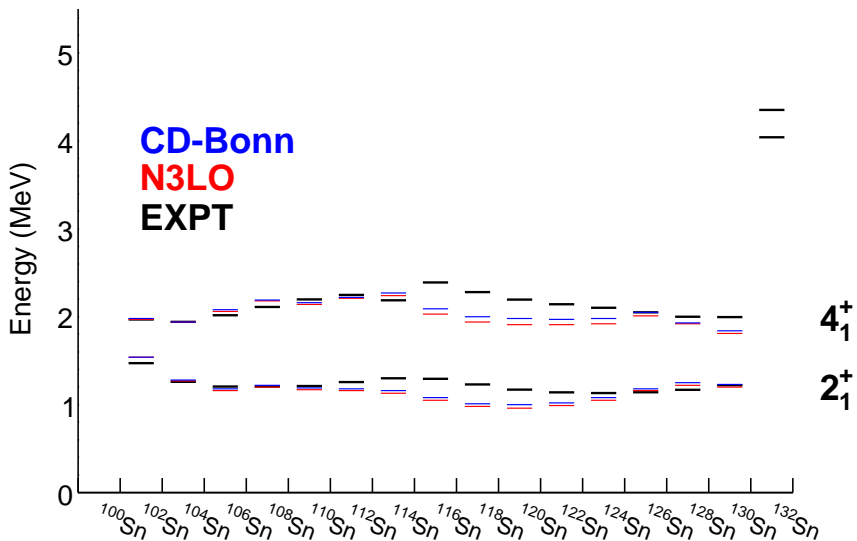


Figure 4.6: Energies of the first excited 2^+ and 4^+ states in the even-mass Sn isotopes. The shell-model calculation based on the N3LO interaction gives ~ 30 keV lower excitation energies than the one with the CD-Bonn interaction. Both shell-model calculations give energies lower than the experimental values. However, the overall agreement is good.

for CD-Bonn 4.85%. Thus, it is reasonable that they generate very similar shell-model results.

4.4 Shell-model interpretation of the Sn isotopes

The shell-model calculations reproduce the approximate constancy of the energy spacing between the 2_1^+ and 0_{gs}^+ states in the even-mass Sn isotopes, see Fig. 4.6. This feature can be explained in the generalized seniority scheme, see Sec. 4.5. On the neutron-rich side, the high excitation energy 4.04 MeV of the 2_1^+ state in ^{132}Sn , measured in β^- -decay studies of ^{132}In produced in fission [94], is a first indication of a strong $Z = 50$ $N = 82$ shell-closure. This is further strengthened by the decreasing $B(E2)$ values as one approaches the isotope ^{132}Sn , see Fig. 4.7. The experimental information regarding the excited spectrum in the neutron-deficient Sn isotopes is more scarce. For instance, the 2_1^+ energy in ^{100}Sn is not known. From Hartree-Fock calculations [95] it is predicted to be of $4.3 - 5.2$ MeV, depending on the parametrization of the Skyrme interaction. Empirical estimates based on observations in the lighter doubly-

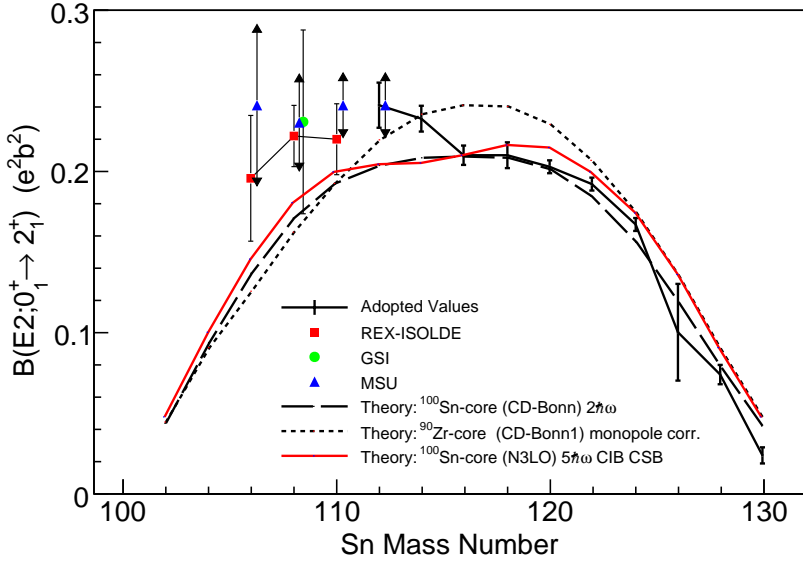


Figure 4.7: The red squares represent the $B(E2)$ values obtained in this work. The red curve is a shell-model calculation based on the renormalized $N3LO$ nucleon-nucleon potential. This is tailored to the neutron model-space above the ^{100}Sn core, see Fig. 4.2, using third order perturbation theory with inclusion of the intermediate excitations $\leq 5\hbar\omega$. The shell-model calculations based on the $CD\text{-Bonn}$ nucleon-nucleon potential with $\leq 5\hbar\omega$ excitations is in principle identical, see Paper II, and therefore omitted in this figure. The neutron effective charge is set to $e_\nu^{\text{eff}} = 1.0 e$. The seniority truncated shell-model calculations outside the ^{90}Zr core with $e_\nu^{\text{eff}} = 0.5 e$ and $e_\pi^{\text{eff}} = 1.5 e$ is from Ref. [38].

magic nucleus ^{56}Ni leads to a somewhat lower excitation energy of 3 – 4 MeV. The $N = Z = 50$ shell-gap is estimated to be ~ 6.5 MeV in calculations and from indirect experimental observations [96, 97]. For instance, a 6.46(15) MeV strong ^{100}Sn shell-gap was inferred from a shell-model calculation by matching the excitation energy of the 12^+ core-excited isomeric state at 6.635 MeV in ^{98}Cd . Similarly, the excitation energies of the $J \geq \frac{25}{2}^+$ states in ^{101}In is sensitive to the energy of the neutron $1g_{9/2}$ orbit [68] and requires a neutron $N = 50$ shell-gap of 6.5 MeV.

The $B(E2)$ values in $^{106,108,110}\text{Sn}$ reported here, see Fig. 4.7, are significantly larger than the shell-model calculation predictions. Apparently, a sizable fraction of the $0_{\text{gs}}^+ \rightarrow 2_1^+$ excitation strength is not accounted for in the calcu-

lations. The neutron effective charge $e_{\nu}^{\text{eff}} = 1.0$ e gives the best fit of the $B(E2; 0_{\text{gs}}^+ \rightarrow 2_1^+)$ values in the mid-shell and neutron-rich Sn isotopes. The agreement on the neutron-deficient side is poor and indicates a strong renormalization of e_{ν}^{eff} . Indications for a renormalized neutron effective charge is apparent also from the experimental $B(E2; 6_1^+ \rightarrow 4_1^+)$ values in $^{102-110}\text{Sn}$, see Tab. 4.1. The consensus from several shell-model calculations is that a neu-

Table 4.1: $B(E2; 6_1^+ \rightarrow 4_1^+)$ in $^{102-112}\text{Sn}$. The value for ^{102}Sn is from Ref. [98], ^{104}Sn is from Ref. [99], and $^{106-112}\text{Sn}$ is from Ref. [100].

Isotope	$E(6_1^+)$ (MeV)	$E(4_1^+)$ (MeV)	$B(E2; 6_1^+ \rightarrow 4_1^+)$
^{102}Sn	2.017	1.969	$0.0116^{+0.0070}_{-0.0030}$
^{104}Sn	2.257	1.943	0.0113(17)
^{106}Sn	2.020	2.325	0.0074(15)
^{108}Sn	2.364	2.111	0.0068(4)
^{110}Sn	2.478	2.197	0.0055(6)
^{112}Sn	2.549	2.248	0.00157(6)

tron effective charge of 1.6-2.3 e outside ^{100}Sn is needed in order to reproduce the experimental values. The large variation in the neutron effective charge comes from variations in the estimated positions of the $\nu 2d_{5/2}$ and $3s_{1/2}$ single particle energies [98]. The significant discrepancy between the measured and calculated $B(E2)$ values in $^{106,108,110}\text{Sn}$ could be interpreted as a weakening of the $N = Z = 50$ shell-closure. In relation to this, it has also been observed [101] that the excitation energies of the first excited 2^+ and 4^+ states in the $N = Z + 2$ nucleus $^{110}_{54}\text{Xe}$ break the trend of increasing values as the $N = 50$ shell gap is approached.

The enhanced $B(E2)$ values can also be understood from nucleon-nucleon correlations across the ^{100}Sn gap that are not accounted for in the calculations. The doubly magic nucleus ^{56}Ni is located in a region of the nuclear chart that is similar to the one of ^{100}Sn . However, the $^{56-68}\text{Ni}$ isotopic chain is more accessible for experimental studies since it does not stretch as far from stability as the much longer $^{100-132}\text{Sn}$ isotopic chain. The ^{56}Ni nucleus is an ℓs -open core with respect to the $1f_{7/2} - 1f_{5/2}$ splitting. This is similar to the $1g_{9/2} - 1g_{7/2}$ splitting of the ^{100}Sn core, see Fig. 4.1. This allows for $1f_{7/2} - 2p_{3/2}$ and $1f_{7/2} - 1f_{5/2}$ couplings across the ^{56}Ni shell-gap. Indeed, the relatively large $B(E2)$ value in ^{56}Ni , see Fig. 4.8, is explained from the large coherent $1f_{7/2} - 2p_{3/2}$ and $1f_{7/2} - 1f_{5/2}$ components in the wave function of its 2_1^+ state [102]. It should be pointed out that the neutron-magicity of the ^{68}Ni nucleus is debated [103]. The $B(E2)$ value is lower than in ^{58}Ni , but it is argued that this is due to the neutron-character of the 2_1^+ state in ^{68}Ni and that the $B(E2; 0_{\text{gs}}^+ \rightarrow 2_1^+)$ only exhausts a fraction of the low-lying $B(E2)$ strength. In addition, another typical indication of a sub-shell closure, the measured two-neutron separation

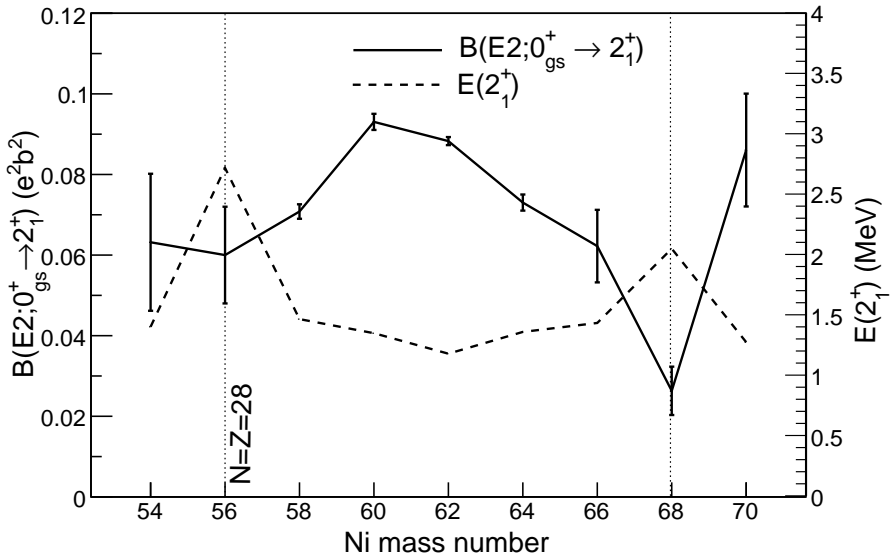


Figure 4.8: Experimental $E(2_1^+)$ and $B(E2; 0_{gs}^+ \rightarrow 2_1^+)$ values in the even-mass $^{56-68}\text{Ni}$ isotopes. The data is taken from Refs. [41].

energy, does not peak for ^{68}Ni compared to ^{66}Ni and ^{70}Ni .

In conclusion, on similar grounds as in ^{56}Ni , one might explain the enhanced $B(E2)$ values in the neutron-deficient Sn isotopes as coming from core-excited $1g_{9/2} - 2d_{5/2}$ and $1g_{9/2} - 1g_{7/2}$ components of the 2_1^+ wave function. The magnitude depends in part on the strength of the ^{100}Sn shell-closure. Indeed, it is shown in paper II that the $B(E2)$ values in the light Sn isotopes are directly proportional to the ^{100}Sn shell-gap.

4.5 Generalized seniority in the Sn isotopes

A convenient method, which also have practical implications, for classifying j^n configurations of n identical nucleons in an orbit with total angular momentum j is offered by the seniority scheme⁵. The seniority quantum number ν was first introduced for LS -coupled electron-configurations in 1943 by G. Racah [104]. In 1953 it was introduced for jj -coupled nuclear states, see e.g. references in [60]. It is based on the notion of pairs coupled to a total angular momentum $J = 0$. The quantum number ν is equal to the number of unpaired nucleons.

⁵For j^n configurations with protons and neutrons in the same j -orbit, the seniority quantum number does not play an equally important role [60].

For instance, for a j^2 configuration in the $J = 0$ state there is complete pairing, thus $\nu = 0$, whereas in the $J = 2, 4, \dots, 2j - 1$ states there are no $J = 0$ pairs, thus $\nu = 2$. The pair-creation operator is defined in second quantization as [60]

$$S_j^+ = \sqrt{\frac{2j+1}{2}} A^+(j^2 J = 0, M = 0) = \frac{1}{2} \sum (-1)^{j-m} a_{jm}^+ a_{j,-m}^- \quad (4.13)$$

Similarly, the pair-annihilation operator is defined as $S_j^- = (S_j^+)^{\dagger}$. Therefore, a state with seniority ν in the j^{ν} configuration can be defined as

$$S_j^- |j^{\nu}, \nu, J, M\rangle = 0 \quad (4.14)$$

It should be noted that for e.g. the $(\frac{9}{2})^4$ configuration there are e.g. two $\nu = 4$ states with $J = 4$. Therefore, for a unique classification of these states an additional quantum number α must be introduced. Note that for two such orthogonal j^{ν} states, the application of S_j^+ preserves the orthogonality of the seniority basis [60]. Also, in $j < \frac{9}{2}$, any two-body interaction is diagonal in the seniority scheme. Therefore, in order to investigate the seniority properties of the nuclear interaction ($j \geq \frac{9}{2}$) n configurations must be investigated, e.g. $(1h_{11/2})^2$ proton configurations in $Z > 64$ and $N = 82$ nuclei [60]. In all cases, the two-body effective interaction between identical nucleons in j^n configurations is diagonal in the seniority scheme [60]. The usefulness of seniority primarily lies in the several closed expressions for matrix elements of one-body and two-body operators [60]. For the present case, the one of most interest is the seniority relation for an electric quadrupole transition between states with a seniority difference of 2, e.g. a $J = 2^+$ state and a $J = 0^+$ state

$$\begin{aligned} \langle j^n \nu \alpha J || E2 || j^n \nu - 2, \alpha' J' \rangle = \\ \sqrt{\frac{(n - \nu + 2)(2j + 3 - n - \nu)}{2(2j + 3 - 2\nu)}} \langle j^{\nu} \nu \alpha J || E2 || j^{\nu} \nu - 2, \alpha' J' \rangle \end{aligned} \quad (4.15)$$

The coefficient on the right hand side is symmetric between n and $2j + 1 - n$. Therefore, the $B(E2)$ values between states in the j^n -configuration with a seniority difference of two units follow a symmetric trend. It also turns out that level spacings in the j^n configurations are independent of n . Note that the above considerations apply to even as well as odd nuclei. Turning the attention to the even-mass Sn isotopes, the energies of the first 2^+ states, and to some extent the $B(E2)$ values, exhibit the aforementioned features. However, the wave function basis consists of several j -orbits. Conceptually, the seniority model of a single- j orbit can be expanded to the case of several j -orbits. The *generalized* seniority pair-creation operator can be written as

$$S^+ = \sum_j \alpha_j S_j^+ \quad (4.16)$$

where j runs over the j -orbits included in the construction of the state. For the semi-magic Sn isotopes this implies the neutron $1g_{7/2}, 2d_{5/2}, 2d_{3/2}, 1s_{1/2}, 1h_{11/2}$

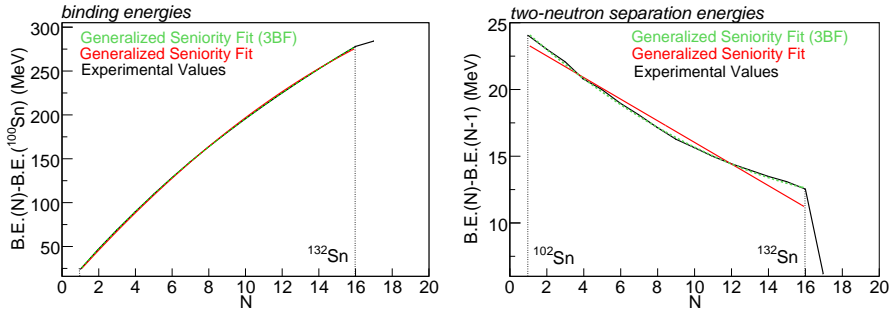


Figure 4.9: *Experimental binding energies and two-neutron separation energies in the even-mass Sn isotopes relative to the ^{100}Sn core. The red curve indicates the generalized seniority prediction using two-body forces while the green dashed curve is the generalized seniority prediction with the inclusion of effective three-body forces. See the text for details.*

orbits. The creation and annihilation operators of the seniority model generates the $SU(2)$ group known as quasi-spin. Also, if all α_j coefficients in Eq. 4.16 are equal this group structure remains. However, in generalized seniority the α_j coefficients are not equal. Therefore, the closed expressions of the seniority model do not carry over to the generalized seniority model by default. However, several seniority-like features emerge in the generalized seniority scheme if certain conditions of the nuclear Hamiltonian are fulfilled. Starting from the vacuum $|0\rangle$, i.e. the magic-core, the addition of N generalized-seniority pairs of nucleons is given by the state

$$(S^+)^N |0\rangle \quad (4.17)$$

where the number of nucleons is $n = 2N$. The states in Eq. 4.17 are taken to be the lowest energy states, i.e. the analogies of the $J = 0$ and $\nu = 0$ states of seniority. It turns out that these states are the eigenstates for a Hamiltonian H that contain only one-body terms and a two-body interaction if the following commutation relations are fulfilled [60]

1. $[H, S^+] = V_0 S^+$
2. $[[H, S^+], S^+] = W(S^+)^2$

where V_0 and W are numerical coefficients. Note that in the generalized seniority scheme the coefficients α_j are independent of N and do not change as the major shell is being filled. It is shown in Ref. [60] that higher order expressions such as $H(S^+)^4|0\rangle$ yield no further conditions on H . Thus, the eigenvalue of $H(S^+)^N|0\rangle$ for any N is given by

$$H(S^+)^N|0\rangle = (NV_0 + \frac{1}{2}N(N-1)W)(S^+)^N|0\rangle \quad (4.18)$$

In turn, the binding energies of even semi-magic nuclei are given by

$$\text{B.E.}(n = 2N) = \text{B.E.}(n = N = 0) + NV_0 + \frac{1}{2}N(N-1)W \quad (4.19)$$

Therefore, the two-nucleon separation energies are given by a linear expression

$$\text{B.E.}(N) - \text{B.E.}(N-1) = V_0 + (N-1)W \quad (4.20)$$

It should be pointed out that if the lowest eigenvalues of the Hamiltonian H are given by Eq. 4.18 it does not follow that the lowest eigenstates are given by Eq. 4.17 [105]. The binding energies and the two-neutron separation energies $\text{B.E.}(N) - \text{B.E.}(N-1)$ for the even-mass Sn isotopes are shown in Fig. 4.9. In this figure, the binding energies for $^{102-132}\text{Sn}$ are fitted to Eq. 4.19. The extracted values of V_0 and W are subsequently used to estimate the two-neutron separation energies. The experimental two-neutron separation energies in the even-mass Sn isotopes are not linear with respect to the particle number. It is shown in Ref. [60] that the inclusion of three-body terms in the effective interaction gives rise to an additional cubic term in Eq. 4.19. This gives a quadratic term in Eq. 4.20. The effect is small, but the fit to the two-neutron separation energies improves, see the green curve in Fig. 4.9. Note also that there are no hints of any $1g_{7/2}2d_{5/2} - 1s_{1/2}2d_{3/2}$ sub-shell closure in the experimental two-neutron separation energies. In the generalized seniority scheme the smoothness of the two-neutron separation energies originates in the constancy of α_j and their independence of N [60].

There is only one $J = 0$ state that can be assigned with generalized seniority zero. This is taken to be the ground state in the even-mass Sn isotopes. In a similar fashion it is possible to create only one state with generalized seniority two which is the analogue of a $\nu = 2$ state in the ordinary seniority scheme. In the even-mass Sn isotopes this can be taken as the first excited 2^+ state. According to Ref. [60] a pair of identical nucleons with $J = 2$ is created by the operator

$$D_M^+ = A^+(jj'J = 2, M) = \frac{1}{\sqrt{1 + \delta_{jj'}}} \sum_{mm'} (jmj'm' | jj'2M) a_{jm}^+ a_{j'm'}^+ \quad (4.21)$$

In the generalized seniority model the lowest $J = 2$ state is a mixture of D_M^+ components created in the major shell of single particle orbits. Therefore the lowest eigenstate is given by

$$D_M^+ = \sum_{j \leq j'} \beta_{jj'} D_M^+(jj') \quad (4.22)$$

For instance, the energy of the first excited 2^+ state in ^{102}Sn is given by

$$H D_M^+ |0\rangle = V_2 D_M^+ |0\rangle \quad (4.23)$$

This imposes some constraints on the choice of Hamiltonian. To be of any practical interest the Hamiltonian should also have eigenstates given by

$$(S^+)^{N-1}D_M^+|0\rangle \quad (4.24)$$

It is shown in Ref. [60] that for this to be an eigenstate of a Hamiltonian H containing only one-body and two-body terms the following must be fulfilled

$$[[H, S^+], D_M^+] = \lambda S^+ D_M^+ \quad (4.25)$$

Furthermore, it can be shown [60] that $\lambda = W$. From this it follows that the eigenstates in Eq. 4.24 have eigenvalues $E^{(2)}$ which are independent of N . That is, according to the generalized seniority scheme the energy spacings between the $J = 0$ ground states and the first excited $J = 2$ states in the even-mass Sn isotopes are independent of the number of neutrons outside the ^{100}Sn core. This is approximately true, as can be seen in Fig. 4.6. The expression 'approximately true' should be compared to the energy variation of the low-lying states in the odd-mass Sn isotopes, where a difference in 10 neutrons shift the excited states with an energy of ~ 1.0 MeV. It can be shown [60] that for a $(S^+)^N a_{jm}^+|0\rangle$ state to be an eigenstate of the shell-model Hamiltonian all the α_j coefficients must be equal. This reduces the generalized seniority scheme to the quasi-spin scheme which is a generator of the $SU(2)$ algebra and in this description the level spacing in even-mass as well as odd-mass semi-magic nuclei is independent of the nucleon number. Therefore, looking at the experimental data, it is not possible to assign the excited states in the odd-mass nuclei with a generalized seniority quantum number equal to one.

In contrast to single j -orbit seniority, no clear predication can be made regarding shape or symmetry of the reduced transition probabilities as a function of particle number. For the actual case of an E2 transition between the generalized seniority zero $J = 0$ ground state and the seniority two $J = 2$ state the following overlap should be calculated

$$\langle 0|D_M^-(S^-)^{N-1}Q(S^+)^N|0\rangle \quad (4.26)$$

where Q is a single-nucleon operator defined such that when it acts on the seniority zero ground state $(S^+)^N|0\rangle$ it is transformed into a state proportional to $(S^+)^{N-1}D_M^+|0\rangle$ with seniority two. Thus, the action of the quadrupole operator in generalized seniority is given by [60]

$$Q_M(S^+)^N|0\rangle = N(S^+)^{N-1}D_M^+|0\rangle \quad (4.27)$$

This gives for the transition matrix element in Eq. 4.26

$$\langle 0|D^-(S^-)^{N-1}Q(S^+)^N|0\rangle = N \cdot \langle 0|D(S^-)^{N-1}(S^+)^{N-1}D'^+|0\rangle \quad (4.28)$$

where the index M on the D and Q operators has been dropped. Furthermore it is noted that the operator Q might not exhaust the full transition strength.

Therefore the $J = 2$ creation operator is denoted with a prime and might not be equal to D^+ . This expression does not give any general prediction due to its intricate normalization. Consider a generalized seniority model in a space consisting of the two orbits j and j' . The transition matrix element becomes

$$\begin{aligned} \langle 0|D^-(S^-)^{N-1}Q(S^+)^N|0\rangle &= N \cdot \langle 0|D^-(S^-)^{N-1}(S^+)^{N-1}D'^+|0\rangle = \\ N \cdot \langle 0|(aD_j^- + bD_{j'}^-)(\alpha S_j^- + \beta S_{j'}^-)^{N-1}(\alpha S_j^+ + \beta S_{j'}^+)^{N-1}(cD_j^+ + dD_{j'}^+)|0\rangle \end{aligned} \quad (4.29)$$

The normalization of this matrix element is not trivial. To see this, one can look at the normalization of the ground and first excited states. The normalization constants of a single j -orbit pair state with seniority $\nu = 0$ or $\nu = 2$ are given by [60]

$$\begin{aligned} (\nu = 0) : \quad \langle 0|(S_j^-)^N(S_j^+)^N|0\rangle &= \frac{N! \left(\frac{2j+1}{2}\right)!}{\left(\frac{2j+1}{2} - n\right)!} \\ (\nu = 2) : \quad \langle 0|D_j^-(S_j^-)^{N-1}(S_j^+)^{N-1}D_j^+|0\rangle &= \frac{(N-1)! \left(\frac{2j-3}{2}\right)!}{\left(\frac{2j-1}{2} - n\right)!} \end{aligned} \quad (4.30)$$

Therefore, Eq. 4.29 will be normalized by an expression which depends explicitly on the values of a, b, c, d, α , and β . The conclusion is that in a generalized seniority model the $B(E2; 0_{\text{gs}}^+ \rightarrow 2_1^+)$ values of the even-mass Sn isotopes does not necessarily follow any simple expression depending on the nucleon number, such as a parabola. In this respect, the experimental $B(E2)$ values presented here do not indicate the presence of any seniority violating components in the nuclear Hamiltonian. Still, it is interesting to note that the shell-model calculations predict a close to symmetric and 'seniority-like' parabola for the $B(E2)$ values. The generalized-seniority content or correlation in the shell-model wave functions $|\text{SM}^A\text{Sn}(0^+)\nu = 0\rangle$ and $|\text{SM}^A\text{Sn}(2^+)\nu = 2\rangle$ can be estimated from the squared overlaps with respect to the generalized seniority states, see Eqs. 4.17 and 4.24.

$$\begin{aligned} |\langle \text{SM}^A\text{Sn}(0^+)\nu = 0 | (S^+)^{N=\frac{A-100}{2}} | 0 \rangle|^2 \\ |\langle \text{SM}^A\text{Sn}(2^+)\nu = 2 | (S^+)^{N=\frac{A-100}{2}-1} D^+ | 0 \rangle|^2 \end{aligned} \quad (4.31)$$

Here, the expansion coefficients of the generalized seniority operators are fitted to reproduce the calculated amplitudes of the ground and excited states in ^{102}Sn , respectively. This pair-structure is then kept constant. The results for the N3LO-based effective interaction are given in Tab. 4.2. These are very similar to the results in Ref. [106] which are based on the Bonn B nucleon-nucleon interaction. Thus, as more particles are added, a truncation of the shell-model basis to a generalized seniority one and two basis does not capture the pairing correlations in the shell model wave functions obtained from using either the CD-Bonn or Bonn B realistic effective interactions.

Table 4.2: *Seniority zero and two overlaps for the ground and first excited states, respectively, in the even-mass $^{104-110}\text{Sn}$ isotopes. The values presented here come from a shell-model calculations based on the CD-Bonn interaction. The Bonn B interaction was used in Ref. [106]. The seniority content of the 2^+ is slightly larger when using the CD-Bonn interaction. However, on average both calculations give the same result to within $\sim 10\%$.*

J^π	^{104}Sn	^{106}Sn	^{108}Sn	^{110}Sn
0_{gs}^+	0.937	0.838	0.750	0.687
2_1^+	0.929	0.787	0.704	0.578
Ref. [106]				
0_{gs}^+	0.950	0.876	0.796	0.742
2_1^+	0.931	0.787	0.663	0.438

4.6 Shell-model interpretation of the Cd isotopes

The isotopes $^{100,102,104}\text{Cd}$ isotopes have a somewhat different structure than the Sn isotopes, see Fig. 4.10. The 4_1^+ , 6_1^+ , and 8_1^+ states in ^{98}Cd are pure $(\pi g_{9/2})^{-2}$ configurations [107]. A 12^+ core-excited isomeric state was reported in Ref. [96]. From this the ^{100}Sn shell gap was determined to 6.46(15) MeV. A proton effective charge $e_\pi^{\text{eff}} < 1.4$ e was inferred by matching a shell-model calculation to the experimental data. That calculation is based on the $\pi\nu(1g2d3s)$ model space above an inert ^{80}Zr core. A slightly larger proton effective charge of $1.45^{+0.20}_{-0.25}$ e was determined when reducing the proton-model space to $\pi(1g_{9/2}2p_{1/2})$. This proton model-space is used also in the shell-model calculations presented here. A G-matrix renormalized CD-Bonn [54] potential is tailored to the ^{88}Sr core shown in Fig. 4.2. With $e_\pi^{\text{eff}} = 1.6$ e the $B(E2; 0_{\text{gs}}^+ \rightarrow 2_1^+)$ value in ^{106}Cd is exactly reproduced, see Fig. 4.11. This is taken as the starting point for investigating the neutron effective charge in the $\nu(1g_{7/2}2d_{5/2}2d_{3/2}3s_{1/2}1h_{11/2})$ model space. The neutron degree of freedom in the light Cd isotopes is expected to be similar to the one in the light Sn isotopes. The excited spectrum in ^{100}Cd differ from the one in ^{98}Cd by the presence of states with a predominant neutron character. The isomeric 8_1^+ state as well as the 6_2^+ and 4_2^+ states have a $\pi 1g_{9/2}^{-2}$ configuration while the 4_1^+ and 6_1^+ states are 82% and 84% pure neutron configurations [108]. This indicates a weak coupling between the protons and neutrons in the light Cd isotopes. The theoretical $B(E2 \uparrow)$ and $Q(2_1^+)$ values

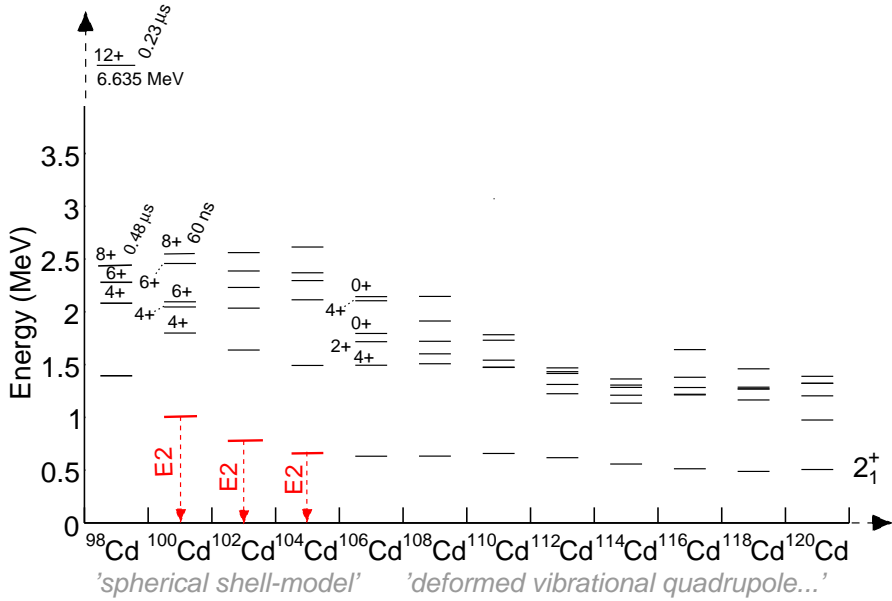


Figure 4.10: The low-energy excited spectrum in the even-mass $^{98-120}\text{Cd}$ isotopes. With $\gtrsim 10$ valence neutrons the Cd isotopes exhibit an excited spectrum typical to that of a deformed vibrator.

in $^{106-100}\text{Cd}$ in terms of the proton and neutron effective charges are given by

$$\begin{aligned}
 &^{106}\text{Cd} \\
 &\quad B(E2 \uparrow) = (0.1356 \cdot e_{\pi}^{\text{eff}} + 0.4026 \cdot e_{\nu}^{\text{eff}})^2 e^2 b^2 \\
 &\quad Q(2_1^+) = (-0.0529 \cdot e_{\pi}^{\text{eff}} - 0.1583 \cdot e_{\nu}^{\text{eff}}) \text{ eb} \\
 &^{104}\text{Cd} \\
 &\quad B(E2 \uparrow) = (0.1374 \cdot e_{\pi}^{\text{eff}} + 0.3474 \cdot e_{\nu}^{\text{eff}})^2 e^2 b^2 \\
 &\quad Q(2_1^+) = (-0.0530 \cdot e_{\pi}^{\text{eff}} - 0.1336 \cdot e_{\nu}^{\text{eff}}) \text{ eb} \\
 &^{102}\text{Cd} \\
 &\quad B(E2 \uparrow) = (0.1378 \cdot e_{\pi}^{\text{eff}} + 0.2713 \cdot e_{\nu}^{\text{eff}})^2 e^2 b^2 \\
 &\quad Q(2_1^+) = (-0.0514 \cdot e_{\pi}^{\text{eff}} - 0.0933 \cdot e_{\nu}^{\text{eff}}) \text{ eb} \\
 &^{100}\text{Cd} \\
 &\quad B(E2 \uparrow) = (0.1458 \cdot e_{\pi}^{\text{eff}} + 0.1450 \cdot e_{\nu}^{\text{eff}})^2 e^2 b^2 \\
 &\quad Q(2_1^+) = (-0.0531 \cdot e_{\pi}^{\text{eff}} - 0.0477 \cdot e_{\nu}^{\text{eff}}) \text{ eb}
 \end{aligned} \tag{4.32}$$

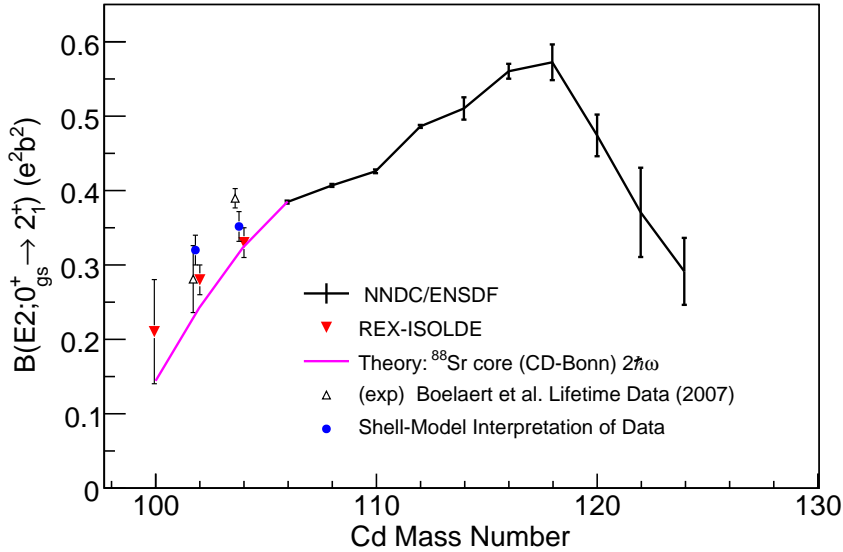


Figure 4.11: *Experimental and theoretical $B(E2)$ values in the even-mass Cd isotopes.*

In the above expressions, the proton components are nearly independent of the number of neutrons. This is a further indication of the weak proton-neutron coupling in the light Cd isotopes. The variation of e_ν^{eff} , while $e_\pi^{\text{eff}} = 1.6$ e is fixed, generates a trajectory in the $B(E2) - Q(2^+)$ planes of ^{102}Cd and ^{104}Cd , see Fig. 4.12. The best fit of e_ν^{eff} along each trajectory is given at the point of maximum likelihood. The likelihood reach 0.96 and 0.95 for the trajectories in the ^{104}Cd and ^{102}Cd cases, respectively. The neutron effective charges deduced in this way are $1.07 \pm 0.05e$ and $1.27 \pm 0.07e$ for ^{104}Cd and ^{102}Cd . In conclusion, this indicates a +25% e_ν^{eff} -renormalization when going from ^{106}Cd to ^{102}Cd . The similar need for a renormalized e_ν^{eff} is observed also in the light Sn isotopes. The $B(E2)$ values based on these effective charges are indicated with blue dots in Fig. 4.11. It is interesting to note that the effective-charge trajectories reproduce nearly the same $Q(2_1^+)$ values independently of the neutron as well as the proton effective charges, see Fig. 4.12. The $Q(2_1^+)$ values in the stable and even-mass $^{106-116}\text{Cd}$ isotopes have been known since long from reorientation measurements [109]. The shell-model calculation with $e_\pi^{\text{eff}} = 1.6$ e and $e_\nu^{\text{eff}} = 1.0$ e reproduces the experimental $Q(2_1^+)$ value in ^{106}Cd , see Fig. 4.13. Furthermore, the predicted trend of values for $^{100-106}\text{Cd}$ is in line with increasing sphericity as ^{98}Cd is approached. This also strengthens the assumption of setting $Q(2_1^+) = 0.0$ eb in the analysis of the ^{100}Cd data.

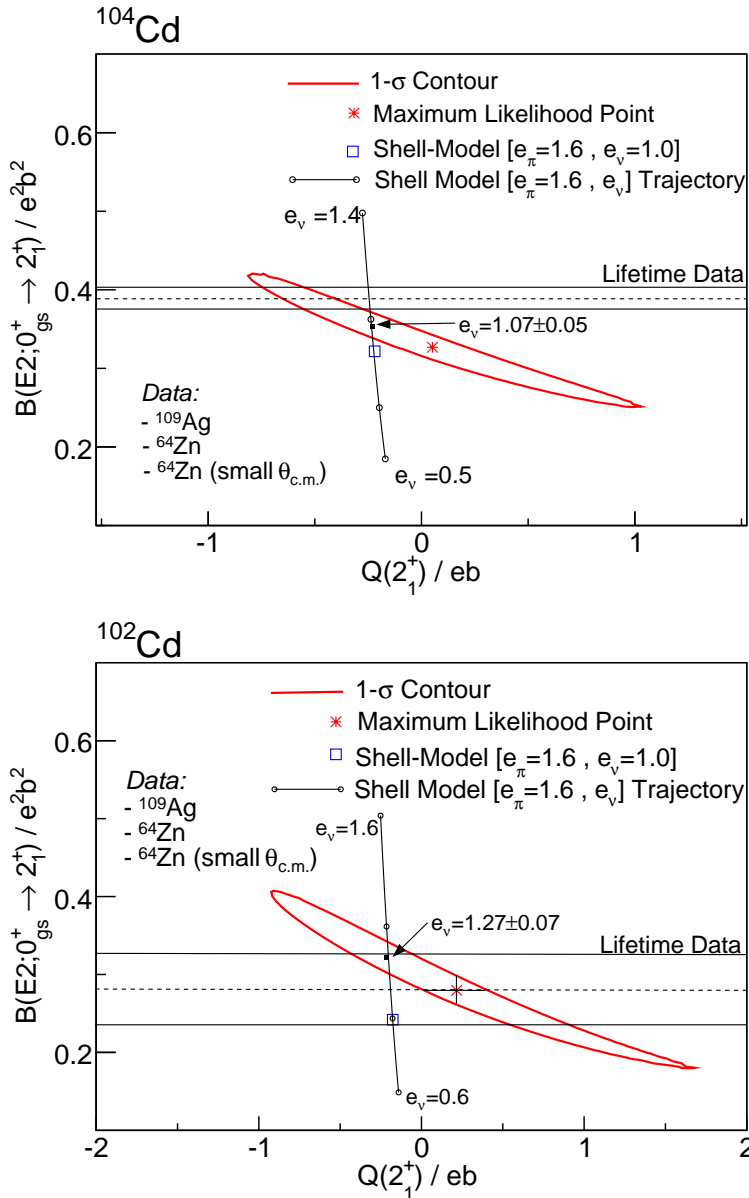


Figure 4.12: The experimental one-sigma contours in the (B, Q) planes of $^{102,104}\text{Cd}$. The effective charge trajectories as well as the results of the lifetime measurements of Ref. [46] are included.

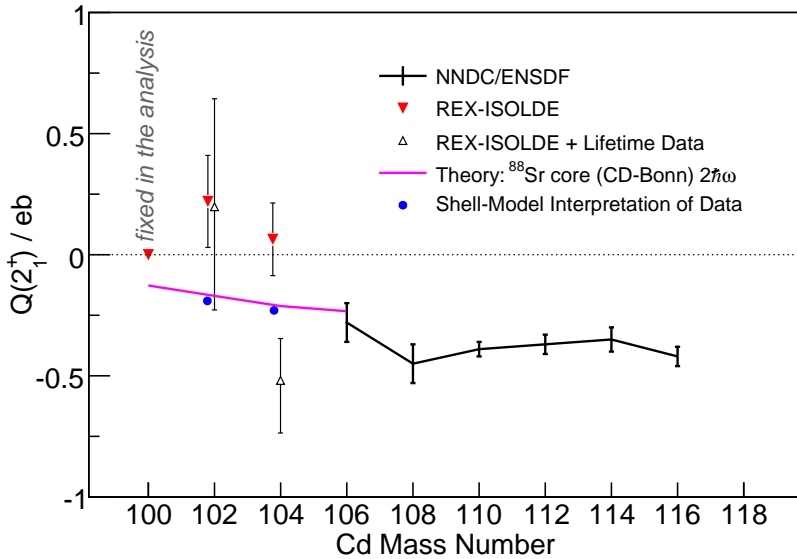


Figure 4.13: *Experimental and theoretical $Q(2_1^+)$ values in the even-mass Cd isotopes.*

The $Q(2_1^+)$ values in $^{102,104}\text{Cd}$ indicated with red triangles in Fig. 4.13 are deduced from the point of maximum likelihood in Fig. 4.12. The values are shifted upwards with respect to the theoretical prediction but the increasing trend remains. The $Q(2_1^+)$ values indicated with white triangles come from the combination of the 1σ -contours in the $B(E2) - Q(2_1^+)$ plane with the plunger-based lifetime measurements in Ref. [46]. The origin of the deviating $Q(2_1^+)$ value in ^{104}Cd is due to the large $B(E2)$ value of Ref. [46].

4.7 Shell-model calculations in $^{106,108}\text{In}$

^{101}In is the lightest indium isotope where excited states have been observed [110]. The first excited $\frac{13}{2}^+$ state most likely corresponds to a proton $1g_{9/2}$ hole coupled to the 2_1^+ state in ^{102}Sn . Similarly, the low-lying excited states in $^{106,108}\text{In}$ can be related to the neutron structure in $^{107,109}\text{Sn}$. The low-lying states in these nuclei are known from the β -decay of $^{107,109}\text{Sb}$. Both ^{107}Sn and ^{109}Sn have a $\frac{5}{2}^+$ ground state and a first excited $\frac{7}{2}^+$ state, see Fig. 4.3. The states are 80% pure in terms of the $1g_{7/2}$ and $2d_{5/2}$ neutron configurations [72]. The magnetic dipole moments of the 7^+ ground states in $^{106,108}\text{In}$ and the isomeric 2^+ state in ^{108}In indicate a dominating $\pi g_{9/2}^{-1} \otimes d_{5/2}$ configuration [111, 112, 113].

The configuration of the isomeric $(2)^+$ state in ^{106}In is less clear. However, most likely it belongs to the same multiplet. The coupling of a proton hole in the $1g_{9/2}$ orbit to a neutron quasi-particle in the $1g_{7/2}$ or $2d_{5/2}$ orbits generates the positive-parity spin sequences 1, 2, 3, 4, 5, 6, 7, 8 and 2, 3, 4, 5, 6, 7, respectively. These exhaust almost all the low-lying states in $^{106,108}\text{In}$. The $\pi^{-1} \otimes \nu$ multiplets in these isotopes have been investigated in a set of $(p,n\gamma)$ reaction experiments [51, 52]. The multiplet character of the excited states is identified from the measured angular distributions, branching ratios and γ -ray transition intensities. The result for ^{108}In is shown Fig. 4(a) in Paper IV and were compared to an interacting boson-fermion-fermion calculation reproduced in Fig. 4(b) in Paper IV. In this work, the excited states in $^{106,108}\text{In}$ are calculated in the shell-model, see Fig. 4.14. The effective interaction is again derived from a G-matrix renormalized CD-Bonn potential [54] and tailored to the ^{88}Sr core of Fig. 4.2. The agreement is rather good considering the odd-odd nature of these isotopes. Furthermore, the shell-model E2/M1 matrix elements⁶ qualitatively reproduce the observed γ -ray de-excitation patterns. In particular the observed coupling of the ground state to higher lying states in ^{106}In as compared to ^{108}In . Also, it should be noted that the coupled decay-pattern of the 283 keV, 216 keV, 169 keV, and 236 keV γ -ray transitions in ^{108}In appears also in the calculation. From a comparison between the simulated and the observed γ -ray de-excitation patterns some of the excited states in $^{106,108}\text{In}$ could be identified in the shell-model calculations. These are indicated with dashed lines in Fig. 4.14. The detailed reasoning is given in Paper IV. This encourages a further interpretation of the excited states in terms of their $\pi^{-1} \otimes \nu$ multiplet character.

An indirect measure of the M1 matrix elements between the excited states of ^{108}In are provided via the shell-model based simulation. Between $J \pm 1$ states of the same multiplet one can expect particularly large M1 matrix elements. Based on this principle, the shell-model identified states, and the known $\pi g_{9/2}^{-1} \otimes \nu d_{5/2}$ multiplet configuration of the 7^+ ground state and first excited 2^+ state in ^{108}In , one can trace out the remaining experimental states of this multiplet. The members of the $\pi g_{9/2}^{-1} \otimes \nu g_{7/2}$ multiplet are identified by starting from the only low-lying 1^+ state. A detailed discussion of how the states are assigned is found in Paper IV. The multiplets that result from this investigation are different from that of Ref. [51], see Fig. 4(c) in paper IV. The key reason is in the multiplet identification of the 3^+ states at 198 and 266 keV. Here, the latter is identified with a dominating $\pi g_{9/2}^{-1} \otimes \nu d_{5/2}$ configuration whereas in Ref. [51] it was identified as a $\pi g_{9/2}^{-1} \otimes \nu g_{7/2}$ configuration. The reverse holds for the 3^+ state at 198 keV. As a consequence, the $\pi g_{9/2}^{-1} \otimes \nu g_{7/2}$ and $\pi g_{9/2}^{-1} \otimes \nu d_{5/2}$ multiplets presented here overlap in energy. This could possibly be traced back to the nearly degenerate $\frac{5}{2}^+$ ground state and $\frac{7}{2}^+$ first excited state in ^{109}Sn .

⁶Effective charges $e_{\pi}^{\text{eff}} = 1.5$ e and $e_{\nu}^{\text{eff}} = 1.0$ and standard gyromagnetic ratios.

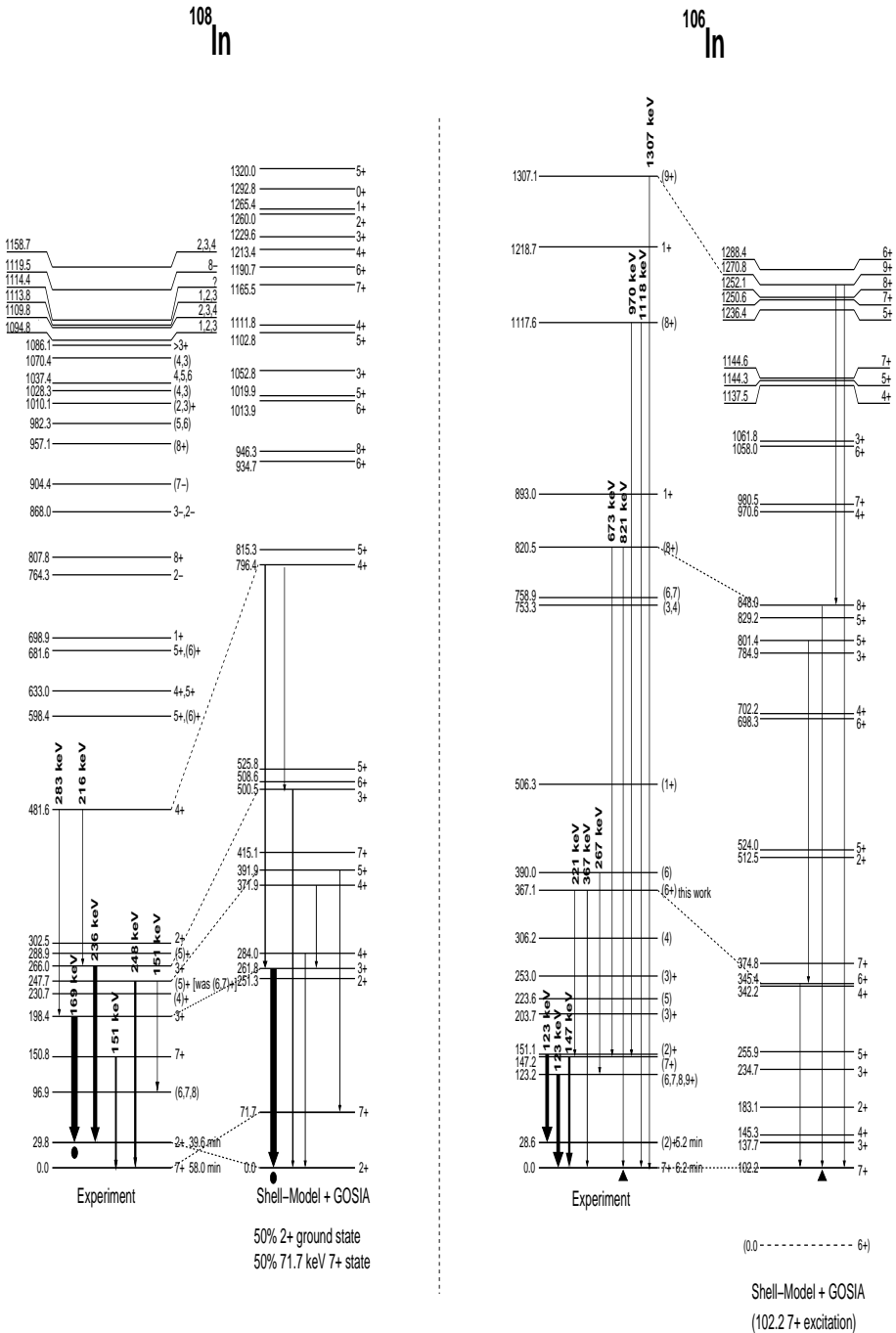


Figure 4.14: Comparison between experimentally observed γ -ray de-excitation pattern and the one simulated by GOSIA. The simulation is based on the transition matrix elements calculated in the shell-model.

CHAPTER 5

SUMMARY AND OUTLOOK

Three Coulomb excitation experiments with postaccelerated RIBs consisting of the light even-even Sn, Cd, or odd-odd In isotopes were carried out at the REX-ISOLDE facility at CERN. It was concluded that the measured $B(E2; 0_{\text{gs}}^+ \rightarrow 2_1^+)$ values in $^{106,108,110}\text{Sn}$ are significantly larger than what is obtained from shell-model calculations based on a G -matrix renormalized effective interaction outside the ^{100}Sn core. Theory predicts that the $B(E2)$ values in $^{102-130}\text{Sn}$ follow a close to symmetric parabola that peaks at mid-shell. This is in excellent agreement with the experimental $B(E2)$ values in the even mass $^{116-130}\text{Sn}$ isotopes. However, starting from ^{114}Sn , the $B(E2)$ values suddenly increase and stay almost constant in the isotopes down to ^{108}Sn . A decrease is observed in ^{106}Sn although this $B(E2)$ value is still larger than the theoretical prediction. From this it was concluded that the neutron effective charge shows strong renormalization effects in the light Sn isotopes.

For $^{102,104}\text{Cd}$ the $B(E2)$ and the $Q(2_1^+)$ values were deduced simultaneously by measuring the Coulomb excitation cross section for both isotopes relative to a ^{64}Zn target and a ^{109}Ag target. For ^{100}Cd a first upper limit on the $B(E2)$ value was extracted assuming a $Q(2_1^+) = 0.0$ eb value. The correlation between the $Q(2_1^+)$ and $B(E2; 0_{\text{gs}}^+ \rightarrow 2_1^+)$ values was extracted from the data using a likelihood function. The resulting 1σ -contours in the $B(E2) - Q(2_1^+)$ planes of ^{104}Cd and ^{102}Cd were used to benchmark the shell-model calculations. This analysis showed that the measured $B(E2)$ values in $^{102,104}\text{Cd}$ also require a renormalized neutron effective charge. However, the observed effect was not as apparent as in the Sn case. The first excited states in the light Cd isotopes are primarily built on configurations of neutrons above the ^{100}Sn core. Therefore, the observed renormalization effect could have the same origin as in the light Sn isotopes.

The detected γ -ray de-excitation patterns from $^{106,108}\text{In}$ were analyzed and fairly well reproduced in the shell-model. The excited states in ^{108}In were interpreted in terms of the $\pi g_{9/2}^{-1} \otimes \nu d_{5/2}$ and $\pi g_{9/2}^{-1} \otimes \nu g_{7/2}$ multiplets. The results differ from previously published works based on decay- and reaction-spectroscopy. For the present case the energy of the multiplets overlap. This could be explained from the coupling of a proton $1g_{9/2}$ hole to the nearly de-

generate $\frac{5}{2}^+$ ground state and first excited $\frac{7}{2}^+$ state in ^{109}Sn . Regarding ^{106}In , a (6^+) state at 367 keV was observed. The spin and parity assignment was based on a shell-model interpretation.

The $B(E2; 0_{\text{gs}}^+ \rightarrow 2_1^+)$ value in ^{104}Sn will be measured in intermediate energy Coulomb excitation at GSI in 2010. In the light odd-odd Sn isotopes, Coulomb excitation of the $\frac{5}{2}^+$ ground state to the first excited $\frac{1}{2}^+$ state can reveal information regarding the position and evolution of the $3s_{1/2}$ orbit. Experimental studies to this end was initiated at REX-ISOLDE earlier this year.

Further theoretical studies are required in order to understand the observed $0_{\text{gs}}^+ \rightarrow 2_1^+$ transition strengths in the light Sn and Cd isotopes. A shell-model calculation in a larger model-space that explicitly takes into account the proton and neutron orbits above *and* below the $N = Z = 50$ shell-gap could provide this. The reduced transition probabilities are also sensitive to the radial wave functions. Here, they were given by the harmonic oscillator. Therefore, calculations based on e.g. Woods-Saxon wave functions would provide an interesting and alternative approach. In addition, the j -dependence of the effective charges is also something that could be explored.

Effective interactions are continuously improved upon and the inclusion of effective three-body forces could be of importance for the present case. However, since this extension is not required for an accurate description in e.g. the heavier Sn isotopes, the core-excitation component of the transition strength deserves the immediate attention.

CHAPTER 6

POPULARIZED SUMMARY IN SWEDISH

En atomkärna består av protoner och neutroner, vilka gemensamt kallas för nukleoner, som är bundna av den starka kärnkraften¹. Forskning inom fundamental kärnfysik syftar till att kartlägga och förstå egenskaperna hos denna kraft och därigenom kunna förklara alla de olika fenomen som en atomkärna kan uppvisa t.ex. antagandet av olika icke-sfäriska former. Det är nu väl etablerat att kärnans egenskaper till mycket stor del beror på det exakta antalet protoner och neutroner samt förhållandet sinsemellan. För vissa proton- och neutron-tal kan kärnan bli instabil. Stabilitet uppnås genom emission av en eller flera heliumkärnor (alfa-sönderfall), alternativt omvandlas en proton till en neutron eller vice versa (beta-sönderfall). Större delen av den samlade kunskapen om atomkärnors struktur kommer från experimentella undersökningar av stabila sådana. Det är dock av stort intresse att studera även instabila kärnor eftersom en del egenskaper hos kärnkraften kommer till större uttryck i dessa. Sedan några år tillbaka är det möjligt att tillverka och accelerera *instabila* isotoper och därigenom studera dem i väl kontrollerade experiment. Det är i synnerhet denna tekniska utveckling som har möjliggjort den studie som presenteras här.

I denna avhandling redovisas resultaten samt analysen av tre experiment som genomförts på CERN. Studien syftar till att undersöka den mikroskopiska strukturen i lätta tenn och kadmium isotoper. Dessa har 50 respektive 48 protoner och därtill ungefär lika många neutroner beroende på isotop. De har en mikroskopisk struktur som lämpar sig mycket väl för detaljerade undersökningar av kärnkraften i instabila atomkärnor. Dessutom innebär det ungefärliga ett-till-ett förhållandet mellan proton- och neutron-talen att kraften mellan protoner och neutroner renodlas.

Experimenten som denna avhandling grundar sig på gick till som följer. En stråle bestående av någon av de instabila $^{106,108,110}\text{Sn}$ (tenn) eller $^{100,102,104}\text{Cd}$ (kadmium) isotoperna sköts genom en två mikrometer tunn folie bestående av

¹Namnet leder till något som man förknippar med kärnkraftverk. Vad som avses här är endast kraften mellan protoner och/eller neutroner i samma mening som t.ex. gravitationskraften mellan två massor.

t.ex. ^{58}Ni (nickel). Kollisionerna mellan kärnorna i strålen och de i folien medför en viss sannolikhet för att en väl definierad mängd energi överförs mellan dem. De blir exciterade. Väldigt kort därefter (ungefär 0.000000000001 sekunder) utsänds exakt samma mängd energi i form av en ljuspartikel, en s.k. foton. Det totala antalet detekterade fotoner speglar sannolikheten för excitation. Denna i sin tur beror på den mikroskopiska strukturen i just den typ av kärna som man studerar. Därför kan man t.ex. från jämförelser av excitationssannolikheten i olika kärnor gentemot teoretiska beräkningar sluta sig till hur den underliggande proton-neutron strukturen varierar. De experimentella resultat som presenteras i denna avhandling kan ej förklaras med modeller grundade på den nuvarande beskrivningen av kärnkraften mellan protoner och/eller neutroner.

ACKNOWLEDGMENTS

First and foremost I would like to express my sincere gratitude to my excellent supervisor, Doc. Joakim Cederkäll. Thank You(!) for all the advice, encouragement, and constructive criticism in all parts and aspects of the work. I truly appreciated the team spirit, and all the open-minded and solution-oriented discussions.

Thank you Prof. Claes Fahlander for always taking the time to discuss any topic, showing interest, and providing concise and to-the-point feedback and advice.

Thank you Prof. Morten Hjorth-Jensen for your generous hospitality and all the sushi over the years. I am also grateful for the lectures on nuclear interactions, for providing me with the computational codes you developed, and for patiently answering all my questions. I enjoyed every trip to Oslo!

Thank you Prof. Torgeir Engeland for providing me with the shell-model codes you developed, and for patiently answering all my questions.

Thank you Prof. Igal Talmi for inviting me to the Weizmann Institute of Science, for your hospitality, and for being an excellent host during my two weeks stay. It was a true privilege for me to get the opportunity to discuss seniority and other topics with you.

Thank you all present and former members of the Nuclear Structure Group and the division of nuclear physics for creating a pleasant working atmosphere.

I would also like to thank Kungl. Fysiografiska Sällskapet for the financial support which allowed me to spend four interesting summers at CERN.

APPENDIX A

γ -RAY TRANSITIONS

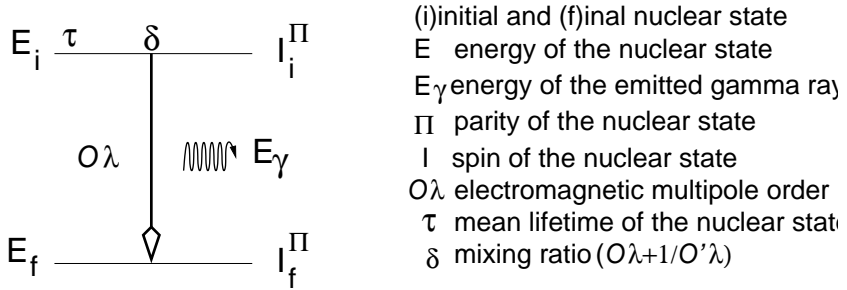


Figure A.1: *The observables related to a γ -ray transition and an explanation of the notation used here.*

A.1 Selection rules

The total angular momentum is conserved

$$I_i = I_f + \lambda \quad (\text{A.1})$$

This leads to the triangle condition:

$$|I_i - I_f| \leq \lambda \leq I_i + I_f \quad (\text{A.2})$$

with the addition that $\lambda \neq 0$, since monopole radiation solutions to the electrodynamic wave equation¹ vanish.

The parity Π_γ of the emitted radiation is given by

$$\Pi_\gamma(E\lambda) = (-1)^\lambda \quad \Pi_\gamma(M\lambda) = (-1)^{\lambda+1} \quad (\text{A.3})$$

The parity selection rule states that

$$\Pi_f \Pi_\gamma \Pi_i = +1 \quad (\text{A.4})$$

¹see e.g. Ref. [114]

A.2 Transition rates

The transition rate T for a transition $i \rightarrow f$ is given by

$$T(\mathcal{O}\lambda; I_i \rightarrow I_f) = \frac{8\pi(\lambda+1)}{\lambda[(2\lambda+1)!!!]^2} \frac{q^{2\lambda+1}}{\hbar} B(\mathcal{O}\lambda; I_i \rightarrow I_f) \quad (\text{A.5})$$

where the reduced transition probability is

$$B(\mathcal{O}\lambda; I_i \rightarrow I_f) = \frac{1}{2I_i + 1} |\langle I_f || \mathcal{O}\lambda || I_i \rangle|^2 \quad \text{unit } E\lambda : \text{e}^2 \text{b}^\lambda, \quad M\lambda : \text{n.m.}^2 \text{b}^{\lambda-1} \quad (\text{A.6})$$

and the wavenumber for a transition with energy $E_\gamma = E_i - E_f$ is

$$q = \frac{E_\gamma}{197.327 \text{ MeV} \cdot \text{fm}} \quad (\text{A.7})$$

The nuclear magneton, n.m., is given by

$$1 \text{ n.m.} = 0.105 \text{ e} \cdot \text{fm} \quad (\text{A.8})$$

Planck's constant and the square of the electric charge are given by

$$\hbar = 6.58211889 \times 10^{-22} \text{ MeV} \cdot \text{s}, \quad e^2 = 1.440 \text{ MeV} \cdot \text{fm} \quad (\text{A.9})$$

This gives expressions for numerical use, see Tab. A.1.

The mean lifetime τ of the decaying nuclear state is related to the transition rate via

$$\tau(\mathcal{O}\lambda; I_i \rightarrow I_f) = \frac{1}{T(\mathcal{O}\lambda; I_i \rightarrow I_f)} \quad (\text{A.10})$$

The width of a nuclear state is given by

$$\Gamma = \frac{\hbar}{\tau} = \frac{658 \text{ fs}}{\tau} \text{ meV} \quad (\text{A.11})$$

Note that the *total* width for the gamma decay of a nuclear state is given by the sum of the partial decay widths of each final state I_k

$$\Gamma_{TOT} = \sum_{\mathcal{O}\lambda, k} \Gamma(\mathcal{O}\lambda; I_i \rightarrow I_k) \quad (\text{A.12})$$

The branching ratio of each state, B_k , is defined from the partial decay widths Γ_k

$$B_k = \frac{\Gamma_k}{\Gamma_{TOT}} = \frac{\sum_{\mathcal{O}\lambda} \Gamma(\mathcal{O}\lambda; I_i \rightarrow I_k)}{\Gamma_{TOT}} \quad (\text{A.13})$$

The mean lifetime is related to the half-life of a nuclear state $T_{1/2}$ by

$$T_{1/2} = \tau \ln(2) \approx \tau \cdot 0.6931 \quad (\text{A.14})$$

$T(E1) = 1.587 \cdot 10^{17} E_{\gamma, MeV}^3 \cdot B(E1)_{e^2b}$	$B(E1)_{sp} = 6.446 \cdot 10^{-4} A^{2/3}$
$T(E2) = 1.223 \cdot 10^{13} E_{\gamma, MeV}^5 \cdot B(E2)_{e^2b^2}$	$B(E2)_{sp} = 5.940 \cdot 10^{-6} A^{4/3}$
$T(E3) = 5.698 \cdot 10^8 E_{\gamma, MeV}^7 \cdot B(E3)_{e^2b^3}$	$B(E3)_{sp} = 5.940 \cdot 10^{-8} A^2$
$T(E4) = 1.694 \cdot 10^4 E_{\gamma, MeV}^9 \cdot B(E4)_{e^2b^4}$	$B(E4)_{sp} = 6.285 \cdot 10^{-10} A^{8/3}$
$T(E5) = 3.451 \cdot 10^{-1} E_{\gamma, MeV}^{11} \cdot B(E5)_{e^2b^5}$	$B(E5)_{sp} = 6.928 \cdot 10^{-12} A^{10/3}$
$T(M1) = 1.779 \cdot 10^{13} E_{\gamma, MeV}^3 \cdot B(M1)_{n.m.^2}$	$B(M1)_{sp} = 1.790$
$T(M2) = 1.371 \cdot 10^9 E_{\gamma, MeV}^5 \cdot B(M2)_{n.m.^2b^1}$	$B(M2)_{sp} = 1.650 \cdot 10^{-2} A^{2/3}$
$T(M3) = 6.387 \cdot 10^4 E_{\gamma, MeV}^7 \cdot B(M3)_{n.m.^2b^2}$	$B(M3)_{sp} = 1.650 \cdot 10^{-4} A^{4/3}$
$T(M4) = 1.899 \cdot 10^0 E_{\gamma, MeV}^9 \cdot B(M4)_{n.m.^2b^3}$	$B(M4)_{sp} = 1.746 \cdot 10^{-6} A^2$
$T(M5) = 3.868 \cdot 10^{-5} E_{\gamma, MeV}^{11} \cdot B(M5)_{n.m.^2b^4}$	$B(M5)_{sp} = 1.924 \cdot 10^{-8} A^{8/3}$

Table A.1: *The transition rates T for $E1-E5$ and $M1-M5$ given in s^{-1} . The energies and transition probabilities should be expressed in units of MeV, e^2b^λ for electric transitions, and $n.m.^2b^{\lambda-1}$ for magnetic transitions. The right column gives the single-particle estimates, i.e. Weisskopf units, for a γ -ray transition in the downwards direction.*

A.3 Mixing ratios

Given the strong dependence of the transition rate on the multipole operator, usually no more than two multipole radiations are mixed. The mixing ratio δ is defined from

$$\delta^2(\mathcal{O}\lambda + 1/\mathcal{O}'\lambda) = \frac{\Gamma(\mathcal{O}\lambda + 1; I_i \rightarrow I_f)}{\Gamma(\mathcal{O}'\lambda; I_i \rightarrow I_f)} \quad (A.15)$$

with the two most common transition mixings being $E1 + M2$ and $E2 + M1$. The sign of δ depends on the adopted convention. The Condon-Shortley sign convention² for the angular part of the wavefunction, i.e.

$$Y_{\lambda\mu}(\hat{r})^* = (-1)^\mu Y_{\lambda, -\mu}(\hat{r}) \quad (A.16)$$

guarantees that the matrix elements of the electromagnetic transition operators are real. The most common mixing ratios are

$$\delta(E2/M1) = \pm \frac{1}{10} q\sqrt{3} \frac{\langle I_f || E2 || I_i \rangle}{\langle I_f || M1 || I_i \rangle} \quad (A.17)$$

$$\delta(M2/E1) = \pm \frac{1}{10} q\sqrt{3} \frac{\langle I_f || M2 || I_i \rangle}{\langle I_f || E1 || I_i \rangle} \quad (A.18)$$

²Condon E. U. and G. H. Shortley, The theory of atomic spectra (Cambridge University Press, 1953)

APPENDIX B

TWO-BODY KINEMATICS

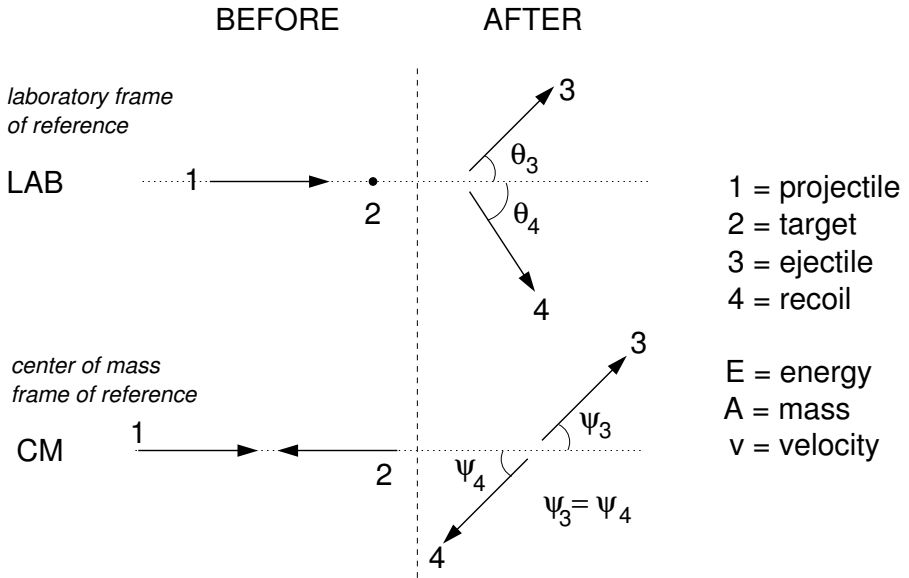


Figure B.1: *Explanation of the variables used below. The frame of reference is indicated with a superscript when needed.*

The particle kinematics of the cases presented in this thesis are non-relativistic, i.e. $\beta < 0.1$. The velocity (V) of CM in LAB is given by

$$V = \frac{m_1}{m_1 + m_2} v_1^{\text{LAB}} \quad (\text{B.1})$$

Velocities are additive in In non-relativistic kinematics, hence

$$v_1^{\text{CM}} = v_1^{\text{LAB}} - V, \quad v_2^{\text{CM}} = V \quad (\text{B.2})$$

The total energy in the LAB system is always greater than the total energy in the CM system.

$$E_{\text{TOT}}^{\text{LAB}} = \frac{A_1 + A_2}{A_2} E_{\text{TOT}}^{\text{CM}} (= E_1^{\text{LAB}}) \quad (\text{B.3})$$

The energy of the projectile/ejectile and target/recoil in CM is given by

$$E_{1,3}^{\text{CM}} = \frac{A_2}{A_1 + A_2} E_{\text{TOT}}^{\text{CM}}, \quad E_{2,4}^{\text{CM}} = \frac{A_1}{A_1 + A_2} E_{\text{TOT}}^{\text{CM}} \quad (\text{B.4})$$

The energy of the ejectile and recoil in the LAB system is given by

$$E_3^{\text{LAB}} = \left[\frac{A_1^2 + 2A_1A_2 \cos \psi + A_2^2}{(A_1 + A_2)^2} \right] E_{\text{TOT}}^{\text{LAB}} \quad (\text{B.5})$$

$$E_4^{\text{LAB}} = \left[\frac{2A_1A_2(1 - \cos \psi)}{(A_1 + A_2)^2} \right] E_{\text{TOT}}^{\text{LAB}} \quad (\text{B.6})$$

where $\psi = \psi_3 = \psi_4$. The CM and LAB angles of the ejectile and recoil are given by

$$\tan \theta_3 = \frac{\sin \psi}{\cos \psi + A_1/A_2} \quad (\text{B.7})$$

$$\tan \theta_4 = \frac{\sin \psi}{1 - \cos \psi} = \tan \left(\frac{\pi}{2} - \frac{\psi}{2} \right) \Rightarrow \theta_4 = \frac{\pi}{2} - \frac{\psi}{2} \quad (\text{B.8})$$

For $A_1 \geq A_2$, i.e. for *inverse kinematics* there exists a maximum value of the scattering angle θ_3 given by

$$\theta_3^{\text{MAX}} = \sin^{-1} \left(\frac{A_2}{A_1} \right) \quad (\text{B.9})$$

If $A_1 < A_2$ then $0 \leq \theta_3 \leq \pi$. Note that $0 \leq \theta_4 \leq \pi/2$, always. Also note that in inverse kinematics there exists two solutions to the $E_3^{\text{LAB}}(\theta_3)$ function, i.e. one in the forward direction in CM (high energy in LAB) and one in the backward direction in CM (low energy in LAB).

B.1 Transformation of the cross section

The differential cross section in the LAB system differs from the one in the CM system. However the cross sectional area is conserved

$$\frac{d\sigma}{d\Omega_{\text{CM}}} \frac{d\Omega_{\text{CM}}}{d\Omega_{\text{LAB}}} = \frac{d\sigma}{d\Omega_{\text{LAB}}} \quad (\text{B.10})$$

where the solid angle ratio is given by

$$\left| \frac{d\Omega_{\text{CM}}}{d\Omega_{\text{LAB}}} \right| = \frac{|2\pi \sin \psi d\psi|}{|2\pi \sin \theta d\theta|} = \frac{|d \cos \psi|}{|d \cos \theta|} \quad (\text{B.11})$$

According to Ref. [115], where a general Jacobian transformation method for both relativistic and non-relativistic kinematics is derived, the transformation between a fixed (F) and a moving (M) frame of reference is equal to

$$\frac{d\Omega_{\text{M}}}{d\Omega_{\text{F}}} = \frac{E^{\text{F}}}{E^{\text{M}}} \cos \delta \quad (\text{B.12})$$

where E is the kinetic energy of the particle in the respective frame and δ is the angle between momentum vectors describing the motion of the projectile as seen from the two different frames. For the special case of the fixed and moving frames being the LAB and the CM, respectively, the angle δ is zero, thus

$$\frac{d\Omega_{\text{CM}}}{d\Omega_{\text{LAB}}} = \frac{E^{\text{LAB}}}{E^{\text{CM}}} \quad (\text{B.13})$$

B.2 Relativistic transformation

If the γ -ray is emitted at an angle θ_γ in the rest frame of the nucleus, it is detected at an angle $\bar{\theta}_\gamma$ in the laboratory frame. These angles are related as

$$\cos \theta_\gamma = \frac{\cos \bar{\theta}_\gamma - \beta}{1 - \beta \cos \bar{\theta}_\gamma} \quad (\text{B.14})$$

or

$$\tan \left(\frac{1}{2} \theta_\gamma \right) = \sqrt{\frac{1 + \beta}{1 - \beta}} \tan \left(\frac{1}{2} \bar{\theta}_\gamma \right) \quad (\text{B.15})$$

The relativistic transformation of solid angles is given by

$$\left| \frac{d\Omega_{\text{CM}}}{d\Omega_{\text{LAB}}} \right| = \frac{|d \cos \theta_{p\gamma}^{\text{CM}}|}{|d \cos \theta_{p\gamma}^{\text{LAB}}|} = \frac{1}{\gamma^2 (1 - \beta \cos \theta_{p\gamma}^{\text{LAB}})^2} \quad (\text{B.16})$$

This in turn can be simplified to

$$\left| \frac{d\Omega_{\text{CM}}}{d\Omega_{\text{LAB}}} \right| = \left(\frac{E_\gamma^{\text{LAB}}}{E_\gamma^{\text{CM}}} \right)^2 = \frac{1}{\gamma^2 (1 - \beta \cos \theta_{p\gamma}^{\text{LAB}})^2} \quad (\text{B.17})$$

BIBLIOGRAPHY

- [1] M. G. Mayer, Phys. Rev. **75**, 1969 (1949).
- [2] M. G. Mayer, Phys. Rev. **78**, 16 (1950).
- [3] A. deShalit and H. Feshbach, *Theoretical Nuclear Physics I: Nuclear Structure* (John Wiley& Sons, inc., 1974).
- [4] K. Alder, A. Bohr, T. Huus, B. Mottelson, and A. Winther, Rev. Mod. Phys. **28**, 432 (1956).
- [5] K. Alder and A. Winther, *Electromagnetic Excitation* (North-Holland Publishing Company, 1975).
- [6] V. Fedosseev *et al.*, Nucl. Instr. and Meth. B **266**, 4378 (2008).
- [7] V. Mishin *et al.*, Nucl. Instr. and Meth. B **73**, 550 (1993).
- [8] B. Wolf, editor, *Ion Sources* (CRC Press. Inc., 1995).
- [9] E. Kugler *et al.*, Nucl. Instr. and Meth. B **70**, 41 (1992).
- [10] T. J. Giles *et al.*, Nucl. Instr. and Meth. B **204**, 497 (2003).
- [11] G. Savard *et al.*, Phys. Lett. A **158**, 247 (1991).
- [12] F. Wenander, Nucl. Phys. A **701**, 528 (2002).
- [13] O. Kester *et al.*, Nucl. Instr. and Meth. B **204**, 20 (2003).
- [14] J. Cub *et al.*, Nucl. Instr. and Meth. A **453**, 522 (2000).
- [15] D. R. Lide, editor, *Handbook of Chemistry and Physics*, 89th ed. (CRC Press. Inc., 2008-2009).
- [16] E. Bouquerel *et al.*, Eur. Phys. J. Special Topics **150**, 277 (2007).
- [17] U. Koster *et al.*, Nucl. Instr. and Meth. B **266**, 4229 (2008).
- [18] P. Reiter *et al.*, Nucl. Phys. A **701**, 209 (2002).
- [19] A. Artna-Cohen, Nucl. Data Sheets **79**, 1 (1996).
- [20] A. N. Ostrowski *et al.*, Nucl. Instr. and Meth. A **480**, 448 (2002).
- [21] J. F. Ziegler, Nucl. Instr. and Meth. B **219-220**, 1027 (2004).
- [22] N. Warr, Miniball electronics at cern.

- [23] CAEN, url <http://www.caen.it>.
- [24] XIA, *User's Manual Digital Gamma Finder (DGF)*, X-Ray Instrumentation Associates, 8450 Central Ave, Newark, CA. 94560 USA, 2004.
- [25] R. Brun and F. Rademakers, Nucl. Instr. and Meth. A **389**, 81 (1997).
- [26] T. M. Rudi Lutter, Med data structure, 2005.
- [27] R. Lutter and O. Schaile, Marabou - mbs and root based online/offline utility, <http://www.bl.physik.unimuenchen.de/marabou/html>.
- [28] K. Alder, F. Roesel, and R. Morf, Nucl. Phys. A **186**, 449 (1972).
- [29] H. Ower, computer program clx.
- [30] T. Czosnyka, D. Cline, and C. Wu, *Coulomb Excitation Data Analysis Code; GOSIA*, Nuclear Structure Research Laboratory, University of Rochester, 2009.
- [31] A. de Shalit and I. Talmi, *Nuclear Shell Theory* (Academic Press, New York and London, 1963).
- [32] U. Smilansky, Nucl. Phys. A **112**, 185 (1968).
- [33] T. Kiédi *et al.*, Nucl. Instr. and Meth. A **589**, 202 (2008).
- [34] J. Blachot, Nucl. Data Sheets **91**, 135 (2000).
- [35] D. Voulot, private communication.
- [36] R. Graetzer, S. M. Cohick, and J. X. Saladin, Phys. Rev. C **12**, 1462 (1975).
- [37] ENSDF, url <http://www.nndc.bnl.gov/ensdf/>.
- [38] A. Banu *et al.*, Phys. Rev. C **72**, 061305(R) (2005).
- [39] C. Vaman *et al.*, Phys. Rev. Lett. **99**, 162501 (2007).
- [40] P. Doornenbal *et al.*, Phys. Rev. C **78**, 031303(R) (2008).
- [41] S. Raman *et al.*, At. Data Nucl. Data Tables **78**, 1 (2001).
- [42] N. Stone, At. Data Nucl. Data Tables **90**, 75 (2005).
- [43] S. Salém-Vasconcelos *et al.*, Phys. Rev. C **38**, 2439 (1988).
- [44] P. Raghavan, Atom. Data Nucl. Data **42**, 189 (1989).
- [45] M. J. Throop *et al.*, Phys. Lett. B **41**, 585 (1972).
- [46] N. Boelaert *et al.*, Phys. Rev. C **75**, 054311 (2007).

- [47] K. P. Lieb *et al.*, Phys. Rev. C **63**, 054304 (2001).
- [48] G. A. Müller *et al.*, Phys. Rev. C **64**, 014305 (2001).
- [49] W. Milner *et al.*, Nucl. Phys. A **129**, 687 (1969).
- [50] H.-C. Hseuh and E. S. Macias, Phys. Rev. C **17**, 272 (1978).
- [51] A. Krasznahorkay *et al.*, Nucl. Phys. A **499**, 453 (1989).
- [52] J. Gulyas *et al.*, Nucl. Phys. A **506**, 196 (1990).
- [53] C. J. Chiara *et al.*, Phys. Rev. C **64**, 054314 (2001).
- [54] R. Machleidt *et al.*, Phys. Rev. C **53**, 1483(R) (1996).
- [55] R. Machleidt, Phys. Rev. C **63**, 024001 (2001).
- [56] D. R. Entem and R. Machleidt, Phys. Rev. C **66**, 014002 (2002).
- [57] D. R. Entem and R. Machleidt, Phys. Rev. C **68**, 041001 (2003).
- [58] M. Horth-Jensen, T. T.S. Kuo, and E. Osnes, Phys. Rep. **261**, 125 (1995).
- [59] T. Engeland, M. Hjorth-Jensen, and E. Osnes, Phys. Scr. **T56**, 58 (1995).
- [60] I. Talmi, *Simple Models of Complex Nuclei* (harwood academic publishers, 1993).
- [61] I. Talmi and I. Unna, Phys. Rev. Lett. **4**, 469 (1960).
- [62] T. Kuo and G. Brown, Nucl. Phys. A **85** (1966).
- [63] R. R. Whitehead, Nucl. Phys. A **182**, 290 (1972).
- [64] T. P. Cleary, Nucl. Phys. A **301**, 317 (1978).
- [65] A. Saganek *et al.*, J. Phys. G **10**, 549 (1984).
- [66] M. M. Stautberg *et al.*, Phys. Rev. **157**, 977 (1967).
- [67] A. Holt *et al.*, Phys. Rev. C **61**, 064318 (2000).
- [68] M. Lipoglavsek *et al.*, Phys. Rev. C **66**, 011302(R) (2002).
- [69] T. Engeland *et al.*, Phys. Rev. C **48**, 535(R) (1993).
- [70] D. Seweryniak *et al.*, Phys. Rev. Lett. **99**, 022504 (2007).
- [71] C. Fahlander *et al.*, Phys. Rev. C **63**, 021307 (2001).
- [72] J. J. Ressler *et al.*, Phys. Rev. C **65**, 044330 (2002).
- [73] B. Fogelberg and J. Blomqvist, Phys. Lett. B **137**, 20 (1984).

- [74] A. Holt *et al.*, Nucl. Phys. A **634**, 41 (1998).
- [75] T. Otsuka *et al.*, Phys. Rev. Lett. **95**, 232502 (2005).
- [76] P. Federman and S. Pittel, Phys. Lett. B **69** (1977).
- [77] P. Federman and S. Pittel, Phys. Rev. C **20**, 820 (1979).
- [78] L. Gaudefroy *et al.*, Phys. Rev. Lett. **97**, 092501 (2006).
- [79] A. Bohr and B. R. Mottelson, *Nuclear Structure Volume I* (W. A. Benjamin, 1969).
- [80] A. Bohr and B. R. Mottelson, *Nuclear Structure Volume II* (W. A. Benjamin, 1969).
- [81] A. Plastino *et al.*, Phys. Rev. **145**, 837 (1966).
- [82] P. Ring and P. Schuck, *The Nuclear Many-Body Problem* (Springer, 1980).
- [83] B. R. Barrett and M. W. Kirson, Nucl. Phys. A **148**, 145 (1970).
- [84] K. A. Brueckner, Phys. Rev. **97**, 1353 (1955).
- [85] H. A. Bethe *et al.*, Phys. Rev. **129**, 225 (1963).
- [86] R. Machleidt and G. Q. Li, Phys. Rep. , 5 (1994).
- [87] G. Q. Li and R. Machleidt, Phys. Rev. C **58**, 1393 (1998).
- [88] G. Q. Li and R. Machleidt, Phys. Rev. C **58**, 3153 (1998).
- [89] A. P. Zuker *et al.*, Phys. Rev. Lett. **89**, 142502 (2002).
- [90] A. M. Bernstein, Opening remarks at chiral dynamics 2006: Experimental tests of chiral symmetry breaking, arXiv:hep-ph/0707425v1.
- [91] S. Weinberg, Physica A **96** (1979).
- [92] S. Weinberg, Phys. Lett. B **251**, 288 (1990).
- [93] E. Epelbaum *et al.*, Eur. Phys. J. A **15**, 543 (2002).
- [94] A. Kerek *et al.*, Phys. Lett. B **44**, 252 (1973).
- [95] I. Hamamoto and H. Sagawa, Phys. Lett. B **394**, 1 (1997).
- [96] A. Blazhev *et al.*, Phys. Rev. C **69**, 064304 (2004).
- [97] H. Grawe and M. Lewitowicz, Nucl. Phys. A **693**, 116 (2001).
- [98] M. Lipoglavsek *et al.*, Phys. Lett. B **440** (1998).

- [99] M. Górska *et al.*, Phys. Rev. C **58**, 108 (1998).
- [100] W. Andrejtscheff *et al.*, Nucl. Phys. A **505**, 397 (1989).
- [101] M. Sandzelius *et al.*, Phys. Rev. Lett. **99**, 022501 (2007).
- [102] G. Kraus *et al.*, Phys. Rev. Lett. **73**, 1773 (1994).
- [103] K. Langanke *et al.*, Phys. Rev. C **67**, 044314 (2003).
- [104] G. Racah, Phys. Rev. **63**, 367 (1943).
- [105] I. Talmi, Nucl. Phys. A **172**, 1 (1971).
- [106] N. Sandulescu *et al.*, Phys. Rev. C **55**, 2708 (1997).
- [107] M. Górska *et al.*, Phys. Rev. Lett. **79**, 2415 (1997).
- [108] M. Górska *et al.*, Z. Phys. A **350**, 181 (1994).
- [109] M. T. Esat *et al.*, Nucl. Phys. A **274**, 237 (1976).
- [110] J. Cederkäll *et al.*, Phys. Rev. C **53**, 1955 (1996).
- [111] D. Vandeplasseche *et al.*, Phys. Rev. Lett. **57**, 2641 (1986).
- [112] J. Eberz *et al.*, Z. Phys. A **323**, 119 (1986).
- [113] J. Eberz *et al.*, Nucl. Phys. A **464**, 9 (1987).
- [114] P. J. Brussaard and P. W. M. Glaudemans, *Shell-Model Applications in Nuclear Spectroscopy* (North-Holland, 1977).
- [115] G. L. Catchen *et al.*, J. Chem. Phys. **69**, 1737 (1978).

I

SUB-BARRIER COULOMB EXCITATION OF ^{110}Sn AND ITS IMPLICATIONS FOR THE ^{100}Sn SHELL CLOSURE

PAPER I

Sub-Barrier Coulomb Excitation of ^{110}Sn and Its Implications for the ^{100}Sn Shell Closure

J. Cederkäll,^{1,2} A. Ekström,² C. Fahlander,² A. M. Hurst,³ M. Hjorth-Jensen,⁴ F. Ames,⁵ A. Banu,^{6,7} P. A. Butler,³ T. Davinson,⁸ U. Datta Pramanik,⁹ J. Eberth,¹⁰ S. Franchoo,¹¹ G. Georgiev,¹ M. Górski,⁶ D. Habs,¹² M. Huyse,¹³ O. Ivanov,¹³ J. Iwanicki,¹⁴ O. Kester,⁶ U. Köster,¹ B. A. Marsh,^{15,16} O. Niedermaier,¹⁷ T. Nilsson,¹⁸ P. Reiter,¹⁰ H. Scheit,¹⁷ D. Schwalm,¹⁷ T. Sieber,¹⁷ G. Sletten,¹⁹ I. Stefanescu,¹³ J. Van de Walle,¹³ P. Van Duppen,¹³ N. Warr,¹⁰ D. Weisshaar,¹⁰ and F. Wenander¹⁶

¹PH Department, CERN 1211, Geneva 23, Switzerland

²Physics Department, University of Lund, Sweden

³Oliver Lodge Laboratory, University of Liverpool, United Kingdom

⁴Physics Department and Center of Mathematics for Applications, University of Oslo, Norway

⁵TRIUMF, Vancouver, Canada

⁶Gesellschaft für Schwerionenforschung (GSI), Darmstadt, Germany

⁷Institute for Nuclear Physics, University of Mainz, Germany

⁸Department of Physics and Astronomy, University of Edinburgh, United Kingdom

⁹Saha Institute of Nuclear Physics, Kolkata 700064, India

¹⁰Institute of Nuclear Physics, University of Cologne, Germany

¹¹IPN Orsay, Orsay, France

¹²Physics Department, Ludwig-Maximilian University, Munich, Germany

¹³Instituut voor Kern- en Stralingsfysica, K.U. Leuven, Belgium

¹⁴Heavy Ion Laboratory, Warsaw University, Poland

¹⁵Department of Physics, University of Manchester, United Kingdom

¹⁶AB Department, CERN 1211, Geneva 23, Switzerland

¹⁷Max-Planck Institute of Nuclear Physics, Heidelberg, Germany

¹⁸Fundamental Physics, Chalmers University of Technology, Gothenburg, Sweden

¹⁹Physics Department, University of Copenhagen, Denmark

(Received 23 January 2007; published 27 April 2007)

The first excited 2^+ state of the unstable isotope ^{110}Sn has been studied in safe Coulomb excitation at 2.82 MeV/u using the MINIBALL array at the REX-ISOLDE post accelerator at CERN. This is the first measurement of the reduced transition probability of this state using this method for a neutron deficient Sn isotope. The strength of the approach lies in the excellent peak-to-background ratio that is achieved. The extracted reduced transition probability, $B(E2: 0^+ \rightarrow 2^+) = 0.220 \pm 0.022 e^2 b^2$, strengthens the observation of the evolution of the $B(E2)$ values of neutron deficient Sn isotopes that was observed recently in intermediate-energy Coulomb excitation of ^{108}Sn . It implies that the trend of these reduced transition probabilities in the even-even Sn isotopes is not symmetric with respect to the midshell mass number $A = 116$ as ^{100}Sn is approached.

DOI: 10.1103/PhysRevLett.98.172501

PACS numbers: 23.20.Js, 21.60.Cs, 25.70.De, 27.60.+j

Substantial interest has recently arisen in the shell structure of atomic nuclei with only a few nucleons outside the double shell closure at ^{100}Sn . As an example, a series of experiments aiming at isotopes in this region has been carried out using fusion-evaporation reactions in the recent past [1]. With the advent of radioactive ion beams these studies are now taken further using sub-barrier and intermediate-energy Coulomb excitation [2,3]. In this Letter we present the only sub-barrier or “safe” Coulomb excitation experiment in this region to date. The study of the reduced transition probability—the $B(E2)$ —of the first excited 2^+ state in an even-even nucleus gives a direct handle on the collectivity of that state. It can thus be used to measure systematic changes in the strengths of shell gaps. The general motivation for this kind of study goes back to our incomplete knowledge of the mechanisms that govern shell formation and their implications for the structure of

nuclei far from stability. It is well known that a strong spin-orbit force was introduced into the nuclear shell-model on Fermi’s suggestion by Goeppert Mayer [4] and independently by Haxel, Jensen, and Suess [4] to explain the observed shell gaps. However, these papers were substantially predated by the consideration of a nuclear spin-orbit force by Inglis [5] who noted that the relativistic Thomas term which arises as a consequence of the noncommutation of Lorentz transformations should act also in atomic nuclei. This term, given by the vector product of the velocity and acceleration of the bound nucleon, gives rise to nuclear LS coupling, a result which can be derived from the Dirac equation [6]. In this picture, the acceleration is proportional to the derivative of the potential experienced by the bound particle, a notion still used in mean-field approaches today. As a consequence, the splitting of the shell gaps becomes density dependent and may change with the

distribution of nucleons in the nucleus. Thus, already on a more fundamental level, changes in shell-gap structure could occur for exotic neutron-proton combinations. It should be added that the size of the Thomas term appeared too small to account for the splitting suggested by Goeppert Mayer and in a later paper Inglis conjectured an addition to spin-orbit partner splitting from meson exchange [7]. In a microscopic description of residual forces in the shell model, other considerations also become important. In particular, close to a self-conjugate shell closure correlations will arise between neutrons and protons that occupy orbits with the same quantum numbers. An example of this is so-called neutron-proton pairing [8]. Furthermore, as has been discussed by Otsuka *et al.* [9] one expects a particularly strong interaction between neutrons and protons occupying spin-orbit partner orbits. In this context, the so-called monopole drift of single-particle energies with respect to mass number becomes important [10]. A main motivation for a study of shell evolution is thus to see if the shell closures that are strong at stability remain so far from stability as the distribution of nucleons changes. This question is particularly interesting in the self-conjugate case. Coulomb excitation of radioactive beams at safe energies is a new and unique tool to address this topic.

The radioactive ^{110}Sn beam used in the experiment was produced by bombarding a 27 g/cm^2 LaC_x target at ISOLDE, CERN, with a 1.4 GeV proton beam from the PS booster. The Sn atoms, after having diffused through the heated target material and effused into an ionization cavity, were ionized by a three-step laser ionization scheme whereafter the beam was extracted and separated in the general purpose separator of the facility. This method provides a high degree of mass and element selectivity. Samples were collected with the laser beams switched on and off to identify the components of the beam. Collection of ^{110}Sn is possible as its half-life is 4.1 h . The γ rays emitted following β decay in the sample were measured offline using γ -spectroscopic methods. It was concluded that Sn ions were implanted only when the laser beams were switched on. Furthermore, surface ionized ^{110}In was identified as the main beam contaminant. A yield of 2.5×10^8 atoms/ μC of ^{110}Sn was established from this measurement. The yield of ionized contaminant ^{110}In was 1 order of magnitude smaller. The intensity of the post-accelerated beam was set to $\sim 10^6$ p/s on the secondary target. Because of the high production yield the beam current could be measured using pico-am meters with the lasers switched on and off, respectively. This was done at ten different occasions during the experiment in order to determine possible variations in beam composition. The measurements rendered a beam purity, consistent with the offline measurements, of $90.0 \pm 1.4\%$. Decay γ rays as well as Coulomb excitation γ rays from other contaminants than ^{110}In were searched for in the final data set but were not observed. As has been discussed previously [11] the REX-ISOLDE post accelerator relies on charge breed-

ing in an electron beam ion source (EBIS) as a first step. The charge breeder and the preceding beam cooling, accomplished by catching the ion bunch from the separator in a gas-filled Penning trap, set the repetition frequency of the beam. In this case the beam was charge bred to the 27^+ charge state over an EBIS confinement time of 98 ms . The extracted beam pulse had a duration of approximately $100\text{ }\mu\text{s}$ with a decaying exponential time profile. The beam was accelerated to 2.82 MeV/u in the REX-ISOLDE linac before hitting a 2 mg/cm^2 and 99.9% pure ^{58}Ni target. Because of the characteristic inverse kinematics of the experiment, beam and target particles emerge in a significantly forward-focused cone after scattering.

Coulomb excitation experiments at REX-ISOLDE use a setup that measures the energies and angles of emitted γ rays and scattered charged particles. The secondary target position is surrounded by a set of Ge detectors, in a close geometry, called the MINIBALL array [12]. The Ge detectors run independently using sampling ADCs with a common clock. The setup comprises 24 high-purity Ge crystals with a total of 144 segments. The typical photopeak efficiency is $\sim 10\%$ at 1.3 MeV . A circular double sided silicon strip detector (DSSSD) is located 30.6 mm downstream of the target. It registers the energy and angle of a scattered beam and/or target particle (see Fig. 1). To remedy possible dead-time effects the trigger for the particle detector included a raw particle trigger downscaled a factor of 2^6 , and a γ ray and charged particle coincidence trigger. The DSSSD comprises 16 annular (front face) and 24 radial (back face) strips. It is subdivided into four separate quadrants. The combined segmentation of the Ge detectors and the DSSSD makes it possible to reconstruct the kinematics of individual Coulomb excitation events for Doppler correction. At 2.82 MeV/u the incoming beam travels at $\beta \sim 8\%$ which results in a complete broadening of the raw γ -ray spectrum. The effect can be seen in Fig. 2.

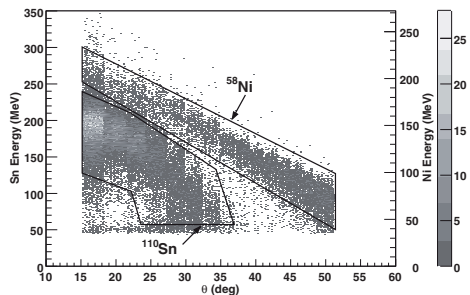


FIG. 1. Scattered beam and target particles as detected in the DSSSD. The upper branch corresponds to scattered ^{58}Ni and the lower branch to ^{110}Sn particles, respectively. The kinematical cuts used for the identification of beam and target particles are also indicated in the figure.

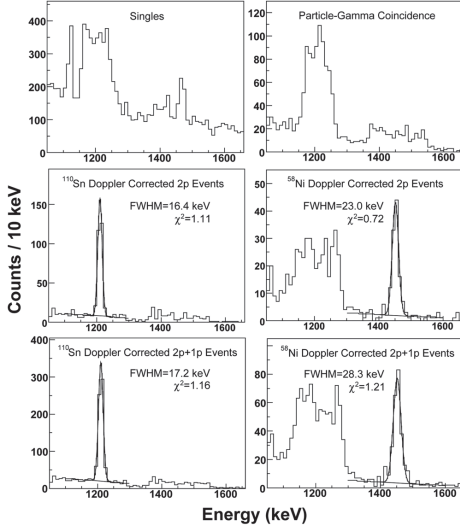


FIG. 2. Single and particle- γ coincidence γ -ray spectra before Doppler correction (top panels). Doppler-corrected γ -ray spectra for 2-particle γ -ray coincident events (central panel) and the corresponding Doppler-corrected γ -ray spectra for the sum of 2-particle and 1-particle reconstructed events for ^{110}Sn and ^{58}Ni (bottom panel). See text for detailed discussion.

In this experiment we selected the beam and target such that the kinematical difference in angle and energy of the two can be used for particle identification (Fig. 1). The scattered beam reaches its maximum scattering angle at $\sim 31.8^\circ$ and scattered target particles at $\sim 84.1^\circ$. All angles in this experiment correspond to safe collisions; i.e., there is no internuclear overlap. One can also note that the multiple-step excitation probability, or the probability to excite any other state than the first 2^+ , is negligible with this choice of kinematics. Two features of Fig. 1 can be commented on. First, the energy used for Doppler correction was calibrated using energy loss simulations and the known maximum scattering angle for ^{110}Sn . The main effect of this improved calibration is to reduce the half-width of the Doppler-corrected γ -ray peaks. Second, the broadening of the Sn and Ni branches in Fig. 1 is almost entirely caused by differences in emission angle due to the finite size of the beam spot. The two-body kinematics of the experiment was such that every Ni ion scattered within the angular range of the DSSSD is coincident with a beam particle scattered between 24° and 31.8° . Thus a substantial part of the data set contains 2-particle + γ -ray ($2p + \gamma$) coincidences. This is advantageous as it gives a direct correlation between the number of scattered ^{110}Sn ions, ^{58}Ni ions, and emitted γ rays. It also provides for Doppler correction for both particles using the energy detected in

the DSSSD. The Doppler-corrected spectra for these events are shown in the central panel of Fig. 2. A subset of events contains only 1-particle + γ -coincidences ($1p + \gamma$). These correspond either to the range for scattered beam below 24° or to events where only one hit could be uniquely reconstructed from the DSSSD. This is, e.g., due to noise or double hits. Note that in a true $2p$ event the particles come back to back in the c.m. system and are thus detected in opposite quadrants in the DSSSD and cannot cause double hits. Furthermore, two-body kinematics can be completely reconstructed by detecting one of the particles. As seen in Fig. 2 reconstruction leads to a slightly larger half-width. The intensities obtained in this fashion were used to extract the $B(E2)$ for the first 2^+ state in ^{110}Sn . The method relies on the fact that the $B(E2)$ for the first 2^+ state in ^{58}Ni is known. The cross section for exciting target and beam particles is proportional to the corresponding $B(E2)$. The angular distribution of the cross section was calculated for the relevant angular ranges using the code CLX [13]. Taking into account the beam purity, a small angular correction and the γ -ray detection efficiency, the $B(E2)$ for the first 2^+ state in ^{110}Sn was determined to be $B(E2) = 0.220 \pm 0.022 e^2 b^2$ (see Table I). The method and the proof-of-principle have been described in Refs. [14,15]. The new result (see Fig. 3) corroborates the published result from intermediate-energy Coulomb excitation of ^{108}Sn [2]. The two results imply that the first 2^+ states in the even-even neutron deficient Sn isotopes retain a relatively large part of collectivity compared to the neutron rich isotopes. These states have a constant energy of ~ 1200 keV which has been explained from the seniority scheme. We note that a recent safe Coulomb excitation measurement for ^{114}Sn at GSI has reduced the error bar of the $B(E2)$ for that 2^+ state to same range as for ^{116}Sn but that a shift towards a higher $B(E2)$ remains [16]. In the following, we compare the measured $B(E2)$ value in ^{110}Sn to the results of two large-scale shell-model calculations (see Ref. [2]). As a starting point, note that the $1d_{5/2}$ and $0g_{7/2}$ orbits are neutron valence orbits from ^{114}Sn towards ^{100}Sn . The main proton valence orbit is $0g_{9/2}$. The calculations, carried out by the Oslo and Strasbourg groups, used effective interactions defined for two different cores, namely ^{100}Sn and ^{90}Zr , but using the same nucleon-nucleon interaction. Details on how to derive the effective

TABLE I. The second and third rows give the intensities for the Doppler-corrected Coulomb excitation peaks of ^{58}Ni and ^{110}Sn from the sum of hits per bin with corresponding background subtraction and from fitting a Gaussian with linear background. The last row gives the $B(E2; 0^+ \rightarrow 2^+)$ in $e^2 b^2$ for ^{110}Sn using these numbers, respectively.

	Energy (keV)	Bin area	Fitted area
^{58}Ni	1454.4	237 ± 15	222 ± 15
^{110}Sn	1211.9	579 ± 24	588 ± 24
$B(E2)e^2 b^2$		0.220 ± 0.022	0.238 ± 0.024

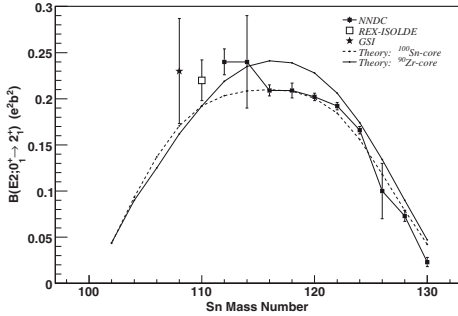


FIG. 3. Current status of measured $B(E2)$ values for the first 2^+ state in even-even Sn isotopes. Note the shift in $B(E2)$ in ^{114}Sn as the $g_{7/2}$ and $d_{5/2}$ orbits start to dominate the configuration. The χ^2 , taken per degree of freedom, for the deviation between the experimental values and the theoretical predictions for the mass number sequences $A_1 = \{114, 112, 110, 108\}$, $A_2 = \{114, 112, 108\}$, and $A_3 = \{114, 112, 110\}$ is $\chi_1^2 = 1.6$, $\chi_2^2 = 1.7$, and $\chi_3^2 = 1.9$ for the ^{90}Zr core. The corresponding values for the ^{100}Sn core is $\chi_1^2 = 3.3$, $\chi_2^2 = 4.2$, and $\chi_3^2 = 4.4$, respectively. Consequently, due to the rather small error the current measurement is statistically a more significant test of the deviation from theory than the previous measurement of ^{108}Sn .

interactions are given in [17]. The ^{90}Zr case includes protons in the $1d_{5/2}$, $0g_{7/2}$, $0g_{9/2}$, $1d_{3/2}$, and $2s_{1/2}$ and neutrons in the $1d_{5/2}$, $0g_{7/2}$, $1d_{3/2}$, $2s_{1/2}$, and $0h_{11/2}$ single-particle orbits. For a ^{100}Sn core, neutrons confined to the $1d_{5/2}$, $0g_{7/2}$, $1d_{3/2}$, $2s_{1/2}$, and $0h_{11/2}$ single-particle orbits define the shell-model space. In the calculation of the $B(E2)$ systematics, an effective neutron charge of $0.5e$ and proton charge $1.5e$ were used for the ^{90}Zr core while an effective neutron charge of $1.0e$ was used for the ^{100}Sn case. The results are displayed in Fig. 3. In the case of a ^{100}Sn core, the experimental $B(E2)$ values are reproduced for all isotopes down to ^{116}Sn . Starting with ^{114}Sn , the theoretical results display the expected parabolic behavior but are at skance with the experimental result for ^{110}Sn and the result for ^{108}Sn [2]. Similar results have emerged for $^{110,108,106}\text{Sn}$ [3] from intermediate-energy experiments during the preparation of this Letter. To reproduce the experimental values one needs a larger effective charge. Furthermore, the experimental values seem to deviate from a good seniority picture for the lighter Sn isotopes. The transition rates are almost independent of the mass number A . Thus the effective charges for the lighter Sn isotopes show stronger renormalization effects. This implies larger core polarization due to particle-hole excitations and a different character of core excitations in the $N = Z$ and $N \gg Z$ regions of the Sn isotopic chain. To further investigate the variation and intrinsic ph structure of the polarization charge in the pure neutron space, Ref. [2] included

a calculation with ^{90}Zr as core with up to four-particle-four-hole proton excitations (current computational limit). In this way, one can reproduce the same trend as for the ^{100}Sn core but with an effective charge for neutrons of $0.5e$ and protons of $1.5e$. These nonrenormalized charges are discussed by, e.g., Bohr and Mottelson [18]. However, still the enlarged calculations deviate from the new experimental data for lighter Sn isotopes. We note that the current result indicates that further core-polarization effects may be needed and/or a better effective interaction introduced. Here the proton-neutron interaction plays an essential role. In particular, the $\pi(0g_{9/2}) - \nu(0g_{7/2}1d_{5/2}1d_{3/2}2s_{1/2})$ monopoles, responsible for the evolution of the spectroscopy between ^{91}Zr and ^{101}Sn , govern the evolution of the proton $Z = 50$ gap with the neutron filling. These monopoles were fitted to reproduce the experimental spectra of nuclei around $A \sim 100$. Here the $\pi(0g_{9/2}) - \nu(1h_{11/2})$ monopole, in particular, suffer from experimental uncertainties. In conclusion, we note the present experimental result, using safe energy Coulomb excitation deviates from current theoretical descriptions of the $Z = 50$ shell gap. Further experiments investigating the reduced transition probability of the corresponding states in lighter even-even Sn isotopes are clearly of importance to further illuminate this question.

This work was supported by the European Union through RII3-EURONS (Contract No. 506065).

- [1] M. Gorska *et al.*, Phys. Rev. Lett. **79**, 2415 (1997); M. Lipoglavsek *et al.* Phys. Lett. B **440**, 246 (1998).
- [2] A. Banu *et al.*, Phys. Rev. C **72**, 061305(R) (2005).
- [3] C. Vaman *et al.*, nucl-ex/0612011.
- [4] M. Goeppert Mayer, Phys. Rev. **75**, 1969 (1949); O. Haxel, J.H.D. Jensen, and H.E. Suess, Phys. Rev. **75**, 1766 (1949).
- [5] D.R. Inglis, Phys. Rev. **50**, 783 (1936); S. Dancoff and D.R. Inglis, Phys. Rev. **50**, 784 (1936).
- [6] W.H. Furry, Phys. Rev. **50**, 784 (1936).
- [7] D.R. Inglis, Phys. Rev. **75**, 1767 (1949).
- [8] A.L. Goodman, Adv. Nucl. Phys. **11**, 263 (1979).
- [9] T. Otsuka *et al.*, Phys. Rev. Lett. **87**, 082502 (2001).
- [10] P. Federman and S. Pittel, Phys. Rev. C **20**, 820 (1979).
- [11] D. Habs *et al.*, Nucl. Instrum. Methods Phys. Res., Sect. B **139**, 128 (1998).
- [12] P. Reiter *et al.*, Nucl. Phys. A **701**, 209 (2002).
- [13] H. Ower, computer program CLX.
- [14] O. Niedermaier *et al.*, Phys. Rev. Lett. **94**, 172501 (2005), and references therein.
- [15] A.M. Hurst *et al.*, Phys. Rev. Lett. **98**, 072501 (2007).
- [16] P. Doornenbal *et al.* (to be published).
- [17] M. Hjorth-Jensen, T.T.S. Kuo, and E. Osnes, Phys. Rep. **261**, 125 (1995).
- [18] Aa. Bohr and B. Mottelson, *Nuclear Structure* (Benjamin, New York, 1969), Vol. 1.

II

$0_{\text{GS}}^+ \rightarrow 2_1^+$ TRANSITION STRENGTHS IN ^{106}Sn AND ^{108}Sn

PAPER II

$0_{gs}^+ \rightarrow 2_1^+$ Transition Strengths in ^{106}Sn and ^{108}Sn

A. Ekström,¹ J. Cederkäll,^{2,1} C. Fahlander,¹ M. Hjorth-Jensen,³ F. Ames,⁴ P. A. Butler,⁵ T. Davinson,⁶ J. Eberth,⁷ F. Fincke,⁷ A. Görgen,⁸ M. Górski,⁹ D. Habs,¹⁰ A. M. Hurst,⁵ M. Huyse,¹¹ O. Ivanov,¹¹ J. Iwanicki,¹² O. Kester,⁹ U. Köster,^{2,13} B. A. Marsh,^{14,15} J. Mierzejewski,^{12,16} P. Reiter,⁷ H. Scheit,¹⁷ D. Schwalm,¹⁷ S. Siem,¹⁸ G. Sletten,¹⁹ I. Stefanescu,¹¹ G. M. Tveten,^{2,18} J. Van de Walle,¹¹ P. Van Duppen,¹¹ D. Voulot,¹⁵ N. Warr,⁷ D. Weisshaar,⁷ F. Wenander,¹⁵ and M. Zielińska^{8,12}

¹Physics Department, University of Lund, Box 118, SE-221 00 Lund, Sweden

²PH Department, CERN 1211, Geneva 23, Switzerland

³Physics Department and Center of Mathematics for Applications, University of Oslo, Oslo, Norway

⁴TRIUMF, Vancouver, Canada

⁵Oliver Lodge Laboratory, University of Liverpool, Liverpool, United Kingdom

⁶Department of Physics and Astronomy, University of Edinburgh, Edinburgh, United Kingdom

⁷Institute of Nuclear Physics, University of Cologne, Cologne, Germany

⁸CEA Saclay, Service de Physique Nucléaire, Gif-sur-Yvette, France

⁹Gesellschaft für Schwerionenforschung, Darmstadt, Germany

¹⁰Physics Department, Ludwig-Maximilian University, Munich, Germany

¹¹Instituut voor Kern- en Stralingsfysica, K. U. Leuven, Leuven, Belgium

¹²Heavy Ion Laboratory, University of Warsaw, Warsaw, Poland

¹³Institut Laue Langevin, 6 rue Jules Horowitz, 38042 Grenoble, France

¹⁴Department of Physics, University of Manchester, Manchester, United Kingdom

¹⁵AB Department, CERN 1211, Geneva 23, Switzerland

¹⁶Institute of Experimental Physics, University of Warsaw, Warsaw, Poland

¹⁷Max-Planck Institute of Nuclear Physics, Heidelberg, Germany

¹⁸Department of Physics, University of Oslo, Oslo, Norway

¹⁹Physics Department, University of Copenhagen, Copenhagen, Denmark

(Received 21 February 2008; published 2 July 2008)

The reduced transition probabilities, $B(E2; 0_{gs}^+ \rightarrow 2_1^+)$, have been measured in the radioactive isotopes $^{108,106}\text{Sn}$ using subbarrier Coulomb excitation at the REX-ISOLDE facility at CERN. Deexcitation γ rays were detected by the highly segmented MINIBALL Ge-detector array. The results, $B(E2; 0_{gs}^+ \rightarrow 2_1^+) = 0.222(19)e^2b^2$ for ^{108}Sn and $B(E2; 0_{gs}^+ \rightarrow 2_1^+) = 0.195(39)e^2b^2$ for ^{106}Sn were determined relative to a stable ^{58}Ni target. The resulting $B(E2)$ values are $\sim 30\%$ larger than shell-model predictions and deviate from the generalized seniority model. This experimental result may point towards a weakening of the $N = Z = 50$ shell closure.

DOI: 10.1103/PhysRevLett.101.012502

PACS numbers: 23.20.Js, 21.60.Cs, 25.70.De, 27.60.+j

Precision measurements in unstable nuclei together with recently developed models of the nucleon-nucleon interaction, stemming from many-body techniques and QCD, show promise to improve our understanding of the finer aspects of the dynamics of the atomic nucleus. One approach to this question is to measure reduced transition probabilities— $B(E2; 0_{gs}^+ \rightarrow 2_1^+)$ —for specific nuclei in the vicinity of a shell closure and to compare these results with calculations based on such models. In particular, one of the pressing questions in nuclear physics today is whether the shell closures, that are well established close to β stability, remain so also for isotopes with a more extreme proton-to-neutron ratio. Intuitive models, such as the generalized seniority scheme [1], predict that these $B(E2)$ values follow a parabolic trend, that peaks at midshell, for a sequence of isotopes between two shell closures. In the following we address the ^{100}Sn shell closure and consequently present results from measurements in the sequence of neutron-deficient even-mass Sn isotopes. This approach

has been made possible by newly developed facilities that produce high-quality radioactive ion beams. Recent measurements in $^{110,108}\text{Sn}$ [2–4] consistently deviate from the broken-pair model as given by the generalized seniority scheme and from current large-scale shell-model calculations [2]. Parallel work [4], using intermediate energy Coulomb excitation, suggests a constant trend of the reduced transition probabilities extending to ^{106}Sn . In this Letter we report results from the first measurements of $^{108,106}\text{Sn}$ using subbarrier Coulomb excitation. This is the only experiment so far for ^{106}Sn that has permitted for complete control of the scattering process and thus explicitly fulfills the conditions for safe Coulomb excitation. Our result still deviates significantly from theoretical predictions but indicates a decreasing trend of the $B(E2)$ with a decreasing number of valence particles outside of the ^{100}Sn core. Note that with this Letter three different isotopes have been used for normalization as ^{112}Sn [2] and ^{197}Au [4] have been used previously. All three experiments yield similar

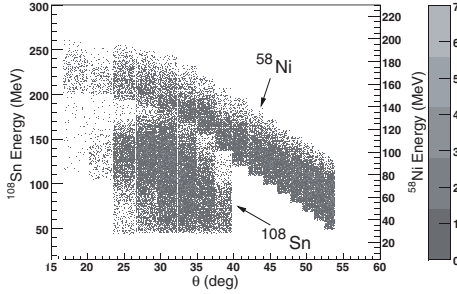


FIG. 1. Energy and angle of the scattered beam and target particles as detected by the DSSSD. The kinematic cuts used to distinguish between ejectiles and recoils have been applied to the data. The corresponding plot for the ^{106}Sn case is similar.

results for $^{110,108}\text{Sn}$. Thus, it appears that the difference between theory and observation is of physical origin. Our result for ^{106}Sn now clearly shows that the seniority model describes the structural evolution of the neutron-rich Sn isotopes well, but for the light Sn isotopes this interpretation appears to break down.

The experiment was carried out at the REX-ISOLDE [5] facility at CERN. The radioactive beams were produced by bombarding a 27 g/cm^2 LaC_x primary target by 1.4 GeV protons delivered by the CERN PS Booster. Atomic Sn was singly ionized using a resonant three-step laser scheme and extracted by an electric potential. Beams with mass numbers $A = 108$ or $A = 106$ were selected by electromagnetic separation. The half-lives of ^{108}Sn and ^{106}Sn are $10.30(8)\text{ min}$ and $115(5)\text{ s}$ [6], respectively. The beam was charge bred for 67 ms in an electron beam ion source [7] in order to reach the 26^+ charge state used for post-acceleration. The final energy was 2.82 and 2.83 MeV/u for the $A = 108$ and $A = 106$ beams, respectively. This is well below the safe bombarding energy [8] of $\sim 3.6\text{ MeV/u}$, corresponding to a 5 fm separation of the

nuclear surfaces. The 2 mg/cm^2 ^{58}Ni target was isotopically enriched to 99.9%. The first excited 2^+ state in ^{58}Ni , used for normalization, is located at 1454 keV , and has an adopted $B(E2; 0^+_{\text{gs}} \rightarrow 2^+_1) = 0.0705(18)e^2b^2$ [6]. Emitted γ rays were registered in the MINIBALL [9] detector array which surrounds the target in a close to 4π configuration. Energy and scattering angle of ejectiles and recoils were detected by a circular double sided silicon strip detector (DSSSD) [10] placed 30 mm downstream from the target (see Fig. 1). Data were recorded using two trigger conditions. The first one was generated by particle- γ coincidence events with a time window of 800 ns and the second one by events arising from one or more particles detected in the DSSSD. The latter trigger was downscaled by a factor of 2^6 . Ejectiles and recoils were easily separated offline due to the kinematics. In brief, the results presented in this Letter were obtained with the following conditions on the data: (a) coincident particle- γ events; (b) kinematic separation of ejectiles and recoils; (c) selection of two-particle ($2p$) events and kinematic reconstruction using one-particle ($1p$) events.

Figure 2 shows the Coulomb excitation γ -ray peaks after imposing the analysis conditions and correcting for Doppler broadening. The lasers were switched on and off with 14.4 s intervals for 1 h every 3 h throughout the experiments in order to measure the composition of the scattered beam over time. Using this information, in combination with the constant cross section for the Coulomb excitation of the contaminants, the respective Sn fractions could be determined over the full duration of the experiments and were $59.0(27)\%$ and $29.2(42)\%$ for the ^{108}Sn and ^{106}Sn beams, respectively. Further details will be published in a forthcoming paper [11]. The $B(E2)$ values were extracted from the experimental data using the coupled-channels Coulomb excitation code GOSIA2 [12]. Note that the static quadrupole moment $Q(2^+_1)$ in ^{112}Sn is consistently $0b$ [13]. For this reason a $Q(2^+_1) = 0b$ was used also in the current analysis. Input parameters and results are displayed in Table 1 and in Figs. 2 and 3. As can be seen in Fig. 3 the results deviate from the theoretical prediction by

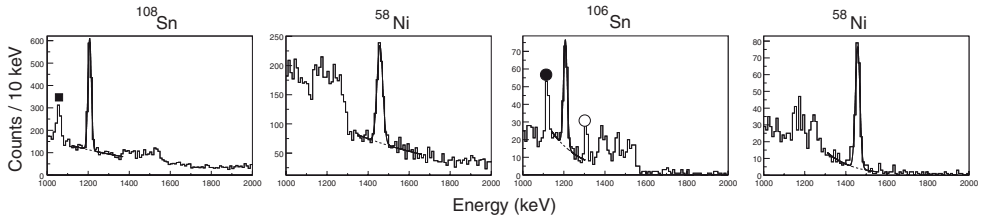


FIG. 2. $2p + 1p$ Doppler corrected γ -ray spectra from the ^{108}Sn and ^{106}Sn experiments. The peak indicated by ■ comes from two closely located ^{108}In decay γ rays that merge due to Doppler correction. The γ ray marked with ● is the deexcitation from the 8^+ state at 1118 keV to the 7^+ ground state in ^{106}In [24]. Similarly the γ ray marked with ○ is the deexcitation from the 9^+ state at 1307 keV to the ground state in the same nucleus.

TABLE I. The two rightmost columns give background information as well as results for the two cases discussed in the text. The last row gives the $B(E2)$ values.

Data	$A = 108^a$	$A = 106^b$
$E(2^+)$ (keV)	1206	1206
γ -ray yield (Ni)	577 (34)	207(15)
γ -ray yield (Sn)	994(38)	133(14)
FWHM (Sn) (keV)	19.3(8)	22.5(26)
FWHM (Ni) (keV)	33.1(18)	26.5(24)
$B(E2; \uparrow)$ (e^2b^2)	0.222(19)	0.195(39)

^a2.82 MeV/u ^{108}Sn on 2.0 mg/cm² ^{58}Ni .

^b2.83 MeV/u ^{106}Sn on 2.0 mg/cm² ^{58}Ni .

more than 1σ . According to the seniority model the $B(E2)$ values naturally decrease with a decreasing number of particles outside the closed core. This trend can be noted in our data for ^{106}Sn . The precision of our result can be put in perspective in the following way. The relative uncertainty for our ^{108}Sn and ^{106}Sn measurements are 9% and 20%, respectively. The uncertainty for the ^{108}Sn measurement reported in Ref. [2] was 25% whereas the corresponding total uncertainty for the ^{108}Sn and ^{106}Sn measurements in Ref. [4] was 17% and 24%. We again note that the present experiment for ^{106}Sn is currently the only one to explicitly fulfill the safe condition. As stated in Ref. [4], the reported $B(E2; 0_{gs} \rightarrow 2_1^+) = 0.240 \pm 0.050 \pm 0.030 e^2b^2$ value for ^{106}Sn in that study was extracted with a relaxed constraint on the impact parameter. Interestingly, our value for ^{106}Sn measured with safe Coulomb excitation does not render a constant trend.

The relative purity of the low-energy excited states in the even-mass Sn isotopes makes them suitable for a shell-model analysis. The relevant model space for neutrons and protons outside of the ^{100}Sn core consists of the

$1d_{5/2}0g_{7/2}2s_{1/2}1d_{3/2}0h_{11/2}$ orbits. The first orbit below the $N = Z = 50$ shell gap is $0g_{9/2}$. It is natural to assume that the missing $0_{gs}^+ \rightarrow 2_1^+$ transition strength, for the ^{100}Sn core calculation (see Fig. 3), can partly be accounted for by proton core excitations. Similarly, neutron excitations across the shell gap would also increase the $E2$ strength. These excitations would be enhanced by a strong $E2$ coupling between the $0g_{9/2}$ and $1d_{5/2}$ orbits. Since the $0g_{7/2}1d_{5/2}$ orbits start to dominate the configurations with a decreasing number of neutrons outside the core the available phase space for excitations of this kind increases. However, as the experimental $B(E2; 0_{gs}^+ \rightarrow 2_1^+)$ increases already when going from ^{116}Sn to ^{114}Sn , it appears that proton excitations play an important role in the transition. A shell-model calculation based on an extended model space that includes a limited number of $0g_{9/2}$ protons and neutrons is on the verge of computational feasibility. A coupling to orbits outside of the model space is approximately accounted for in many-body theory by the perturbative construction of the effective interaction [14]. Previous calculations based on a ^{100}Sn core indicated the need for an explicitly expanded model space. Banu *et al.* [2] included this effect up to 4p-4h proton core excitations by means of a seniority truncated model space outside of a ^{90}Zr core. Because of the seniority truncation in that calculation the symmetric trend of the $B(E2)$ values was retained. The impact of core excitations on the $0_{gs}^+ \rightarrow 2_1^+$ transition probability depends in part on the $0g_{9/2} - 1d_{5/2}$ energy separation, E_g . In a limited $0g_{9/2}0g_{7/2}1d_{5/2}$ neutron model space a $\sim 50\%$ increase of the $B(E2)$ can be noted with a $\sim 50\%$ reduction of E_g from 6 to 3 MeV. Neither the proton nor the neutron $0g_{9/2}1d_{5/2}$ coupling strength is known from experiment. The so-called monopole drift of the single-particle orbits can play a key role in self-conjugate nuclei.

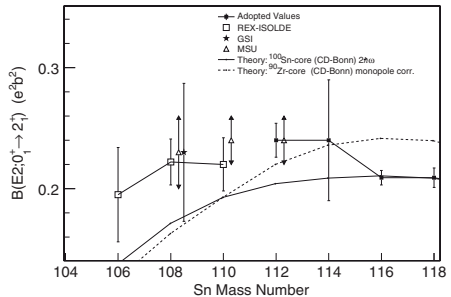
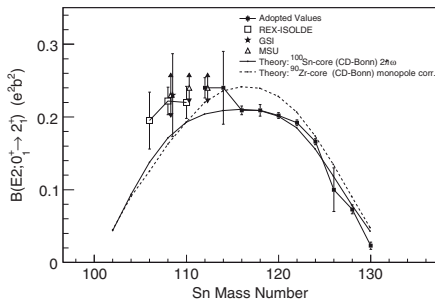


FIG. 3. Left panel: Experimental and theoretical $B(E2)$ values. The dashed curve represents the result from a shell-model calculation using ^{100}Sn as core and a $\nu(g_{7/2}, d, s, h_{11/2})$ model space with a neutron effective charge $e_{\text{eff}}^{\nu} = 1.0e$. The solid line corresponds to using ^{90}Zr as core and a $\pi(g, d, s) - \nu(g_{7/2}, d, s, h_{11/2})$ model space with $e_{\text{eff}}^{\nu} = 0.5e$. Right panel: Enlarged version of the left panel. Only experimental results fulfilling the safe condition are shown in the two panels.

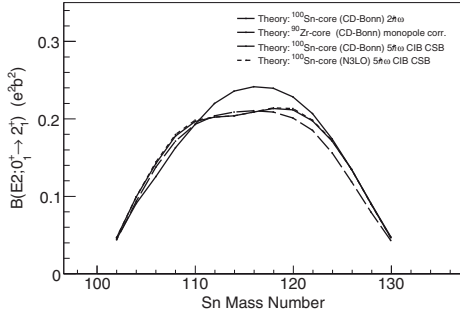


FIG. 4. Theoretical $B(E2)$ values given in $e^2 b^2$ for the even-mass Sn isotopes. The first two calculations are identical to Fig. 3. The ^{90}Zr core calculation was seniority truncated and based on a monopole corrected CD-Bonn interaction [2]. The remaining calculations are based either on the N3LO interaction or a more recent CD-Bonn interaction. The number of excitations allowed in the perturbative scheme is here $5h\omega$. Whether the interaction incorporated charge symmetry breaking (CSB) and charge independence breaking (CIB) is indicated in the legend.

It was shown in Ref. [15] that the interaction between neutrons and protons in $j = \ell \pm 1/2$ orbits modifies the effective single-particle energies, as observed for instance in Ref. [16]. With this line of reasoning, the neutron-deficient Sn isotopes could exhibit a tendency for the proton $0g_{9/2}$ to become less bound as the number of neutrons in $0g_{7/2}$ decreases. This type of single-particle drift was also observed in the Zr isotopes [17]. Further experimental evidence for monopole drift along isotone chains come from (d, p) and (d, t) reactions [18]. Analysis of isomeric core excited states in ^{98}Cd gives a ^{100}Sn shell gap of ~ 6.5 MeV for both neutrons and protons [19]. Also, the energy of the $25/2^+$ level, with a dominating $\nu 0g_{9/2}^{-1}$ component, in ^{99}Cd points towards a shell gap of the same size [20]. However, recent experimental results for the three first excited states in the $N = Z + 2$ nucleus ^{110}Xe instead point towards a possible weakening of the $N = Z = 50$ shell closure [21]. For this Letter we have expanded the shell-model calculations in Ref. [2] by using two more recent nucleon-nucleon interactions (see Fig. 4). One, which is based on chiral effective field theory, N3LO [22], includes pions and nucleons as the only effective degrees of freedom. The other one is a more recent type of charge-dependent (CD)-Bonn interaction [23]. In contrast to the calculations in Ref. [2], we have added here the Coulomb interaction as well and explicitly break the charge symmetry and charge independence between the nucleons. The divergent two-body matrix elements were renormalized using G-matrix theory and tailored to the model space using many-body perturbation techniques

[14]. Interaction terms of two-body matrix elements up to third order were included in this treatment and the maximum energy of intermediate excitations was increased to a limit of $5h\omega$. As can be seen in Fig. 4 the trend of the $B(E2)$ values is sensitive to the coupling to orbits outside of the model space. With these new microscopic interactions the calculations show a deviation from the symmetry expected in the seniority model. Further progress involves using these interactions in an explicitly expanded model space which relies on parallelized calculations carried out on a computational cluster. Work towards this end has recently been initiated.

In this Letter we have reported on Coulomb excitation experiments using $^{108,106}\text{Sn}$ beams at REX-ISOLDE. With this the $B(E2)$ systematics from safe Coulomb excitation now extend down to ^{106}Sn . Calculations using the N3LO nucleon-nucleon interaction and a recent CD-Bonn interaction show an interesting deviation from the symmetric trend predicted by the seniority model but still do not reproduce the experimental data. This observed increase in transition strength clearly shows the need for further theoretical investigations of the nucleon-nucleon interaction as applied to the ^{100}Sn shell closure.

This work was supported by the European Union through RII3-EURONS (Contract No. 506065) and the German BMBF through Grant No. 06 KY 205 I.

- [1] I. Talmi, Nucl. Phys. **A172**, 1 (1971).
- [2] A. Banu *et al.*, Phys. Rev. C **72**, 061305(R) (2005).
- [3] J. Cederkall *et al.*, Phys. Rev. Lett. **98**, 172501 (2007).
- [4] C. Vaman *et al.*, Phys. Rev. Lett. **99**, 162501 (2007).
- [5] O. Kester *et al.*, Nucl. Instrum. Methods Phys. Res., Sect. B **204**, 20 (2003).
- [6] BNL Evaluated Nuclear Structure Data File (ENSDF), <http://www.nndc.bnl.gov>.
- [7] F. Wenander, Nucl. Phys. **A701**, 528 (2002).
- [8] D. Cline, Bull. Am. Phys. Soc. **14**, 726 (1969).
- [9] P. Reiter *et al.*, Nucl. Phys. **A701**, 209 (2002).
- [10] A. N. Ostrowski *et al.*, Nucl. Instrum. Methods Phys. Res., Sect. A **480**, 448 (2002).
- [11] A. Ekström *et al.* (to be published).
- [12] T. Czosnyka *et al.*, Bull. Am. Phys. Soc. **28**, 745 (1983).
- [13] R. Graetzer *et al.*, Phys. Rev. C **12**, 1462 (1975).
- [14] M. Hjorth-Jensen *et al.*, Phys. Rep. **261**, 125 (1995).
- [15] T. Otsuka *et al.*, Phys. Rev. Lett. **95**, 232502 (2005).
- [16] L. Gaudefroy *et al.*, Phys. Rev. Lett. **97**, 092501 (2006).
- [17] P. Federman and S. Pittel, Phys. Rev. C **20**, 820 (1979).
- [18] B. L. Cohen *et al.*, Phys. Rev. **127**, 1678 (1962).
- [19] A. Blazhev *et al.*, Phys. Rev. C **69**, 064304 (2004).
- [20] D. J. Dean *et al.*, Prog. Part. Nucl. Phys. **53**, 419 (2004).
- [21] M. Sandzelius *et al.*, Phys. Rev. Lett. **99**, 022501 (2007).
- [22] D. R. Entem *et al.*, Phys. Rev. C **68**, 041001 (2003).
- [23] R. Machleidt *et al.*, Phys. Rev. C **63**, 024001 (2001).
- [24] D. Seweryniak *et al.*, Nucl. Phys. **A589**, 175 (1995).

III

ELECTRIC QUADRUPOLE MOMENTS OF THE 2_1^+ STATES
IN $^{100,102,104}\text{Cd}$

PAPER III

Electric quadrupole moments of the 2_1^+ states in $^{100,102,104}\text{Cd}$

A. Ekström,¹ J. Cederkäll,^{1,2} D. D. DiJulio,¹ C. Fahlander,¹ M. Hjorth-Jensen,³ A. Blazhev,⁴ B. Bruyneel,⁴ P. A. Butler,⁵ T. Davinson,⁶ J. Eberth,⁴ C. Fransen,⁴ K. Geibel,⁴ H. Hess,⁴ O. Ivanov,⁷ J. Iwanicki,⁸ O. Kester,⁹ J. Kownacki,⁸ U. Köster,^{2,10} B. A. Marsh,^{11,12} P. Reiter,⁴ M. Scheck,⁵ B. Siebeck,⁴ S. Siem,¹³ I. Stefanescu,⁷ H. K. Toft,¹³ G. M. Tveten,^{2,13} J. Van de Walle,² D. Voulot,¹² N. Warr,⁴ D. Weisshaar,⁴ F. Wenander,¹² K. Wrzosek,⁸ and M. Zielińska^{8,14}

¹Physics Department, University of Lund, Box 118, SE-221 00 Lund, Sweden

²PH Department, CERN 1211, Geneva 23, Switzerland

³Physics Department and Center of Mathematics for Applications, University of Oslo, Norway

⁴Institute of Nuclear Physics, University of Cologne, Germany

⁵Oliver Lodge Laboratory, University of Liverpool, United Kingdom

⁶Department of Physics and Astronomy, University of Edinburgh, United Kingdom

⁷Instituut voor Kern- en Stralingsfysica, K. U. Leuven, Celestijnenlaan 200D B-3001, Belgium

⁸Heavy Ion Laboratory, University of Warsaw, Poland

⁹Gesellschaft für Schwerionenforschung, Darmstadt, Germany

¹⁰Institut Laue Langevin, 6 rue Jules Horowitz, F-38042 Grenoble, France

¹¹Department of Physics, University of Manchester, United Kingdom

¹²AB Department, CERN 1211, Geneva 23, Switzerland

¹³Department of Physics, University of Oslo, Norway

¹⁴CEA Saclay, Service de Physique Nucléaire, Gif-sur-Yvette, France

(Received 20 May 2009; revised manuscript received 5 October 2009; published 3 November 2009)

Using the REX-ISOLDE facility at CERN the Coulomb excitation cross sections for the $0_{gs}^+ \rightarrow 2_1^+$ transition in the β -unstable isotopes $^{100,102,104}\text{Cd}$ have been measured for the first time. Two different targets were used, which allows for the first extraction of the static electric quadrupole moments $Q(2_1^+)$ in $^{102,104}\text{Cd}$. In addition to the $B(E2)$ values in $^{102,104}\text{Cd}$, a first experimental limit for the $B(E2)$ value in ^{100}Cd is presented. The data was analyzed using the maximum likelihood method. The provided probability distributions impose a test for theoretical predictions of the static and dynamic moments. The data are interpreted within the shell-model using realistic matrix elements obtained from a G -matrix renormalized CD-Bonn interaction. In view of recent results for the light Sn isotopes the data are discussed in the context of a renormalization of the neutron effective charge. This study is the first to use the reorientation effect for post-accelerated short-lived radioactive isotopes to simultaneously determine the $B(E2)$ and the $Q(2_1^+)$ values.

DOI: 10.1103/PhysRevC.80.054302

PACS number(s): 23.20.Js, 21.60.Cs, 25.70.De, 27.60.+j

I. INTRODUCTION

The isotopes ^{100}Cd , ^{102}Cd , and ^{104}Cd belong to a region of the Segrè chart where excited states at low energy evolve from being governed by single-particle effects to be dominated by collective motion. The gradual alignment of the angular momentum vectors of the two proton holes in ^{98}Cd [1,2] describes the principal part of its wave function up the first 8^+ state. In contrast, vibrational and rotational behavior develop in the surrounding isotopes. At $N \sim 60$ the Cd isotopes are weakly deformed with $\beta_2 \sim 0.1$ [3] and exhibit a low-energy structure of vibrational character [4,5] manifested by a $0_2^+, 2_1^+, 4_1^+$ triplet at nearly twice the energy of the 2_1^+ state. As a consequence, several previous studies of the Cd isotopes [6–10] have focused on interpretations within a multiphonon picture with excitations of quadrupole and quadrupole-octupole type.

Theoretically, the spectra of $^{98-106}\text{Cd}$ have been described in the spherical shell model and in a variety of interacting boson models [11,12]. In a recent series of measurements several groups [13–16] report reduced excitation probabilities for the $0_{gs}^+ \rightarrow 2_1^+$ transition in $^{106,108,110}\text{Sn}$, which deviate

from predictions based on realistic effective nucleon-nucleon interactions. The observed $B(E2)$ discrepancy in the light Sn isotopes appears to originate from an incomplete description of the residual nucleon-nucleon interaction outside the ^{100}Sn core. As a complement to a study of the interaction as a function of the neutron degree of freedom, the neutron-deficient Cd isotopes lend themselves to a similar study where the proton degree of freedom is invoked as well. This aspect is the principal motivation for the work presented here. We also present the results from shell-model calculations based on a realistic effective interaction.

In general, the reduced transition probability for electromagnetic de-excitations between nuclear states is a very sensitive probe of the nuclear wave function. The lifetimes of the low-lying states in $^{102,104}\text{Cd}$ were recently visited employing a plunger device in a recoil distance Doppler-shift (RDDS) measurement, see Refs. [17,18]. In sub-barrier Coulomb excitation the 2_1^+ state can be populated via a direct transition from the ground state, circumventing issues related to feeding through higher lying states. However, the extracted $B(E2)$ value is connected to the sign and magnitude of

the static quadrupole moment $Q(2_1^+)$ via the total Coulomb excitation cross section. Therefore, this study and the lifetime-based investigations are complementary.

In this article we present the results from the first sub-barrier Coulomb excitation measurements of the $0_{gs}^+ \rightarrow 2_1^+$ cross section in $^{100,102,104}\text{Cd}$. From these measurements the $B(E2; 0_{gs}^+ \rightarrow 2_1^+)$ value in $^{100,102,104}\text{Cd}$ was determined and the $Q(2_1^+)$ in $^{102,104}\text{Cd}$ was extracted using the reorientation effect [19,20]. The technique of combined cross-section measurements was explored for the first time using a short-lived radioactive ion beam thus providing a test of the intensity limit for this method for future radioactive beam measurements.

II. RADIOACTIVE ION BEAM PRODUCTION AND DETECTOR EQUIPMENT

The first excited state in $^{100,102,104}\text{Cd}$ was populated by bombarding the respective Cd isotope onto target foils of either 1.8 mg/cm² ^{64}Zn or 1.9 mg/cm² ^{109}Ag . The experiment was carried out at the ISOLDE facility at CERN. The methods of production, postacceleration, and data collection are similar to that of Ref. [21]. The radioactive ion beams were produced by impinging a 1.4 GeV proton beam delivered by the CERN PS-Booster on a 27 g/cm²-thick LaC_x target. The Cd atoms were ionized using a resonant laser ionization scheme providing Cd^+ ions for subsequent electrostatic extraction. The isotope mass was selected using the high-resolution separator of the facility. Contaminating In isobars were suppressed using a primary target with a temperature controlled quartz transfer line [22]. Due to the different vapor pressures of In and Cd at the chosen target temperature a relative reduction of the contaminant of two orders of magnitude was reached. The intensity of the contaminant was determined from the number of elastically scattered particles at the secondary target during laser on/off measurements [15,16,21]. Postacceleration in the REX-LINAC requires a mass-to-charge ratio less than 4.5 that was fulfilled after approximately 62 ms of charge breeding in the REX-EBIS [23]. At the final beam energy of 2.87 MeV/u the scattering occurs below the Coulomb barrier for any combination of projectiles and targets used here [19].

Ejectiles and recoils were detected by a circular double-sided silicon strip detector (DSSSD) placed 32.5 mm downstream of the secondary target covering laboratory angles $\theta \in [15^\circ, 52^\circ]$. The 16 annular strips covering each quadrant of the detector have a pitch per strip of 1.9 mm, whereas, for the current experiment, the 24 radial strips were coupled

pairwise, resulting in a 6.8° radial pitch. For further details see Ref. [24]. The γ rays were detected by the Miniball detector array that comprised 21 sixfold segmented germanium crystals at the time of the experiment. The absolute efficiency was 6% at a γ -ray energy of 1 MeV. Data collection was triggered by a particle- γ coincidence condition. An overview of the experimental parameters is given in Table I. The magnitude of the isobaric contamination of the ^{100}Cd beam was found to be consistent with zero within an experimental uncertainty of less than 10%. The upper limit is motivated by the systematics of the other measurements shown in Table I and by similar measurements in Refs. [15,16]. The intensity of the Cd beams fell with decreasing mass of the isotope. This in combination with the increasing excitation energy of the 2_1^+ state and the expected decrease of the corresponding $B(E2)$ value required longer measuring times for isotopes closer to the proton drip line.

III. EVENT STRUCTURE AND DATA REDUCTION

Time-coincident particle- γ data were collected with an 800 ns coincidence window. A pure particle trigger, down-scaled by a factor of 64 to reduce the amount of surplus data and acquisition dead time, was used outside of this gate. Prompt coincidences were selected offline using a 125 ns gate in the particle- γ time spectrum; see Fig. 1. The γ -ray detection efficiency was increased (10% gain at $E_\gamma = 1$ MeV) by using an offline add-back scheme [15,16]. The angular position of the germanium detectors was fine tuned in the offline analysis with the condition of minimizing the full width at half maximum (FWHM) of the Doppler corrected peaks. The DSSSD was energy calibrated based on the known target thickness and theoretical energy loss curves calculated by SRIM [25]. Assuming the particle interaction point to be in the center of the target resulted in a good Doppler correction of the detected γ rays. The physics events stored on disk are of two types: (i) a 1p event, which is ejectile *or* recoil detected, and (ii) a 2p event, which is ejectile *and* recoil detected.

A discussion related to the 2p and 1p event structure in REX-ISOLDE experiments can be found in Refs. [15,16,26]. In brief, the probability that the ejectile and the recoil simultaneously scatter into a given annular range of the DSSSD is limited by kinematics and by the distance between the secondary target and the DSSSD. A 2p event is constructed when two particles are detected in diametrically opposite quadrants within 100 ns. A 1p event occurs when one of

TABLE I. The experimental parameters for each of the measurements in this work. The measurements were carried out in the order they appear below. It should be noted that the ^{104}Cd beam intensity had to be reduced to avoid damage to the particle detector.

Beam	Target	Beam energy (MeV)	Beam intensity (pps)	Isobaric contamination (%)
^{104}Cd	^{109}Ag	298.5	1×10^6	0.8 ± 0.1
^{102}Cd	^{109}Ag	292.7	5×10^5	0.4 ± 0.1
^{102}Cd	^{64}Zn	292.7	5×10^4	2.7 ± 0.3
^{104}Cd	^{64}Zn	298.5	6×10^5	0.4 ± 0.1
^{100}Cd	^{109}Ag	287.0	3×10^3	0.0 ± 10.0

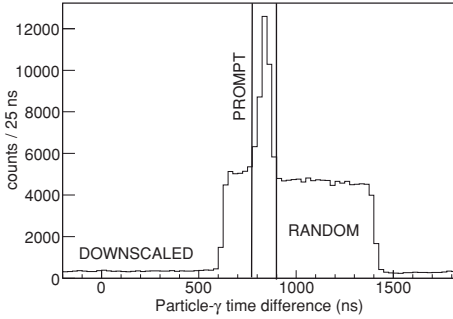


FIG. 1. Particle- γ time-difference spectrum. The prompt particle- γ coincidence window is indicated with vertical lines.

the particles either scatters outside of the annular range of the detector or when it penetrates the DSSSD undetected due to dead-time effects. Given the two-body kinematics of the scattering process, the missing particle in a 1p event can be reconstructed.

IV. DATA ANALYSIS

The spin and parity sequence of the first two excited states in $^{100,102,104}\text{Cd}$ are given in Fig. 2. The $2_1^+ \rightarrow 0_1^+$ transitions treated in this work have energies of 1004, 777, and 658 keV, respectively. A reorientation measurement of the reduced transition probability and the static quadrupole moment requires at least two measurements under different conditions. This was accomplished here by adopting two different target materials, ^{64}Zn and ^{109}Ag , as well as different angular ranges for detection. In ^{64}Zn the 2_1^+ state is located 991 keV above the 0^+ ground state. The 2_2^+ state at 1799 keV is at a too-high energy to be visible in the data under the current experimental conditions. The ^{109}Ag nucleus exhibits a more complicated level structure; see Fig. 2. The $(\frac{5}{2}^-)_1 \rightarrow (\frac{1}{2}^-)_{\text{gs}}$ and $(\frac{3}{2}^-)_1 \rightarrow (\frac{1}{2}^-)_{\text{gs}}$ transitions at 415 and 311 keV were observed in the present data set. A summary of the $E2$ matrix elements for the ^{64}Zn target is given in Table II and similarly for the ^{109}Ag target in Table III. For an extended discussion of the adopted values see below. The experimentally determined γ -ray yields are presented in Table IV. In the following sections the method used in the analysis is expanded on followed by the specific results for different measurements.

TABLE II. The level index, spin, parity, level energy, and reduced matrix elements $\langle i||E2||j\rangle = M_{ij}$, in units of $e b$, for ^{64}Zn , used in the analysis Refs. [27–30].

Level	I^π	Energy (MeV)	1	2	3
1	0^+	0	0.0	0.400(19)	0.043(2)
2	2^+	0.991		$-0.420(79)^a$	0.545(28)
3	2^+	1.799			0.0

^aPositive $M_{12}M_{23}M_{13}$ interference value.

A. Method

1. The Coulomb excitation cross section

The $0_1^+ \rightarrow 2_1^+$ Coulomb excitation cross section is given by

$$\sigma_{E2} = \sigma_R [\kappa_1(\theta_{c.m.}, \xi) B(E2)(1 + \kappa_2(\theta_{c.m.}, \xi) Q(2_1^+))] \quad (1)$$

in second-order perturbation theory. It depends on the Rutherford cross section, σ_R , the reduced transition probability,

$$B(E2; 0_1^+ \rightarrow 2_1^+) = |(0_1^+||E2||2_1^+)|^2 \equiv M_{12}^2, \quad (2)$$

and the spectroscopic quadrupole moment,

$$Q(2_1^+) = \frac{4}{5} \sqrt{\frac{2\pi}{7}} (2_1^+||E2||2_1^+) \equiv 0.75793 M_{22}. \quad (3)$$

The product of the $B(E2)$ and $Q(2_1^+)$ terms describes the reorientation effect. The positive definite coefficients κ_1 and κ_2 are known from perturbation theory [19] and depend on the center-of-mass scattering angle, $\theta_{c.m.}$, and the adiabaticity parameter, ξ . Generally, this dependence leads to an increase in the excitation cross section with increasing beam energy, atomic number, and scattering angle. However, at small $\theta_{c.m.}$, the cross section becomes less sensitive to the sign and magnitude of the static moment. For the ^{104}Cd and ^{102}Cd measurements relative to the ^{64}Zn target the statistics made it possible to extract the cross section also for very small scattering angles, i.e., corresponding to the first two or three of the innermost annular strips of the DSSSD. This provides a third set of data in addition to the ^{109}Ag data and the ^{64}Zn data measured at larger scattering angles.

As mentioned above, lifetime data exist for the 2_1^+ state in $^{104,102}\text{Cd}$ [18,30]. The $B(E2)$ value is, however, still not well established as the number of measurements remains small. The approach adopted here provides two options. The measurements for the two targets can be used independently of previous lifetime measurements to extract a new $B(E2)$ value and a static moment, or the measurements can be combined with previous lifetime measurements to improve the accuracy of the static moment, $Q(2_1^+)$, see e.g., Ref. [33]. We present results using both these approaches.

The projectile excitation cross section, σ^P , is determined by normalization against the corresponding known cross section for a given target, σ^T . The introduction of the two measured γ -ray yields for projectile and target, N_γ^P and N_γ^T , gives;

$$\sigma^P(B, Q) = \frac{N_\gamma^P \varepsilon_\gamma^T W(\theta)^T}{N_\gamma^T \varepsilon_\gamma^P W(\theta)^P} \frac{1}{1 - q} \sigma^T. \quad (4)$$

In practice this procedure provides a measure of the incoming beam intensity. The relative γ -ray detection efficiencies, ε_γ , were obtained using a known ^{152}Eu calibration source. $W(\theta)$ represents the integrated angular distribution of de-excitation γ rays and q represents the fraction of isobaric contamination present in the beam. The cross sections were calculated using the computer code CLX [34] and included effects of energy loss in the target.

TABLE III. The level index, spin, parity, level energy, and reduced matrix elements $\langle i||E2||j\rangle = M_{ij}$, in units of $e b$, for ^{109}Ag , used in the analysis Refs. [30–32].

Level	I^π	Energy (MeV)	1	2	3	4	5	6
1	$\frac{1}{2}^-$	0.0	0.0	0.0	0.0	0.666(27)	0.800(33)	0.042(5)
2	$\frac{7}{2}^+$	0.088		0.0	3.046(15)	0.0	0.0	0.0
3	$\frac{9}{2}^+$	0.133			0.0	0.0	0.0	0.0
4	$\frac{3}{2}^-$	0.311				−0.905(388)	0.219(112)	0.0
5	$\frac{5}{2}^-$	0.415					−0.423(423)	0.0
6	$\frac{3}{2}^-$	0.702						0.0

2. The maximum likelihood estimator

The projectile matrix elements $\langle 0_{\text{gs}}^+||E2||2_1^+ \rangle$ and $\langle 2_1^+||E2||2_1^+ \rangle$ are extracted using a maximum likelihood approach. This method has the advantage that all data are treated on an equal footing and are weighted only by their uncertainties. The likelihood, \mathcal{L} , is a function of the nuclear parameters $B(E2)$ and $Q(2_1^+)$. It is defined as a product of probability distributions, P_k , one for each measurement.

$$\mathcal{L}(B, Q) = \prod_{k \in [Zn, Ag, \tau]} P_k(B, Q). \quad (5)$$

In the numerical analysis, P_k is approximated by a Gaussian probability distribution along the gradient of the contour curve of the k -th measurement. The statistical errors in the γ -ray yield measurements and the known uncertainties in the target matrix elements can be propagated to give the uncertainty in the total cross section. The standard deviation

TABLE IV. Experimental γ -ray yields as extracted from the data analysis.

Measurement	Transition	γ -ray yield
$^{104}\text{Cd} + ^{64}\text{Zn}$		
	$^{104}\text{Cd}: 2_1^+ \rightarrow 0_{\text{gs}}^+$	1487(59)
	$^{64}\text{Zn}: 2_1^+ \rightarrow 0_{\text{gs}}^+$	471(28)
$^{104}\text{Cd} + ^{109}\text{Ag}$		
	$^{104}\text{Cd}: 2_1^+ \rightarrow 0_{\text{gs}}^+$	1028(47)
	$^{109}\text{Ag}: \frac{3}{2}_1^- \rightarrow \frac{1}{2}_{\text{gs}}^-$	2753(95)
	$^{109}\text{Ag}: \frac{5}{2}_1^- \rightarrow \frac{1}{2}_{\text{gs}}^-$	2289(84)
$^{102}\text{Cd} + ^{64}\text{Zn}$		
	$^{102}\text{Cd}: 2_1^+ \rightarrow 0_{\text{gs}}^+$	308(28)
	$^{64}\text{Zn}: 2_1^+ \rightarrow 0_{\text{gs}}^+$	156(23)
$^{102}\text{Cd} + ^{109}\text{Ag}$		
	$^{102}\text{Cd}: 2_1^+ \rightarrow 0_{\text{gs}}^+$	486(34)
	$^{109}\text{Ag}: \frac{3}{2}_1^- \rightarrow \frac{1}{2}_{\text{gs}}^-$	2249(83)
	$^{109}\text{Ag}: \frac{5}{2}_1^- \rightarrow \frac{1}{2}_{\text{gs}}^-$	1985(65)
$^{100}\text{Cd} + ^{109}\text{Ag}$		
	$^{100}\text{Cd}: 2_1^+ \rightarrow 0_{\text{gs}}^+$	$\leq 6.0(24)$
	$^{109}\text{Ag}: \frac{3}{2}_1^- \rightarrow \frac{1}{2}_{\text{gs}}^-$	101(17)
	$^{109}\text{Ag}: \frac{5}{2}_1^- \rightarrow \frac{1}{2}_{\text{gs}}^-$	75(14)

of the cross section in turn provides a $1\text{-}\sigma$ band in the $B(E2) - Q(2_1^+)$ plane. In short, the likelihood function for the Cd isotope of interest represents the total probability of (B, Q) being the pair of parameters that best reproduces the experimental projectile cross sections and the lifetime $\tau(2_1^+)$. The \mathcal{L} is evaluated for $B \in [0, 1]e^2b^2$ and $Q \in [-2, 2]eb$. This corresponds to static and dynamic quadrupole moments that are in line with existing data in the Cd isotopic chain. The final $B(E2)$ and $Q(2_1^+)$ values, \hat{B} and \hat{Q} , maximize the normalized likelihood function, i.e., $\mathcal{L}(\hat{B}, \hat{Q}) = 1.0$. The corresponding uncertainties are extracted from the contour curve $\mathcal{L}(B, Q) = 0.682$ projected on the respective axis.

B. γ -ray yields and transitions

1. $^{102,104}\text{Cd}$ measurements

With the ^{64}Zn target it is possible to identify the scattered projectile and target nuclei directly; see Fig. 3. Typical Doppler corrected γ -ray spectra, for the $^{102}\text{Cd} + ^{64}\text{Zn}$ case, are shown in Fig. 4. The satellite peak next to the $2_1^+ \rightarrow 0_{\text{gs}}^+$ target transition comes from two γ -ray transitions at 1025.0 and 1036.6 keV in the $^{102}\text{Cd} \rightarrow ^{102}\text{Ag} \rightarrow ^{102}\text{Pd}$ decay chain. Exactly the same satellite peak is present in the data from the $^{104}\text{Cd} + ^{64}\text{Zn}$ measurement and is due to remnant radioactive ^{102}Cd isotopes in the target chamber. The analyses of the $^{104}\text{Cd} + ^{109}\text{Ag}$ and $^{102}\text{Cd} + ^{109}\text{Ag}$ measurements are more elaborate. Given the approximately equal masses of these nuclei the kinematic distributions of the scattered particles overlap as can be seen in Fig. 3. This in turn eliminates the possibility of direct particle identification. As an example, simulations using the Rutherford cross section, σ_R , for the ^{104}Cd case show that 97% of the particles scattered into the DSSSD are ^{104}Cd nuclei. Thus a significant number of ^{109}Ag γ rays will be Doppler corrected using the experimental kinematics of a detected ^{104}Cd nucleus. Correspondingly, Doppler correcting all experimental 1p events using the respective masses gives the γ -ray spectra shown in Figs. 5(a) and 5(b). The broad structure present at the bottom part of the Doppler corrected γ -ray peaks arises from the effect mentioned above. The magnitude of this pedestal is proportional to the number of target γ rays detected in coincidence with scattered beam nuclei and vice versa. This effect was analyzed further by simulating the Coulomb excitation cross section $\sigma_{E2} = \sigma_R \cdot P(\theta)$, where

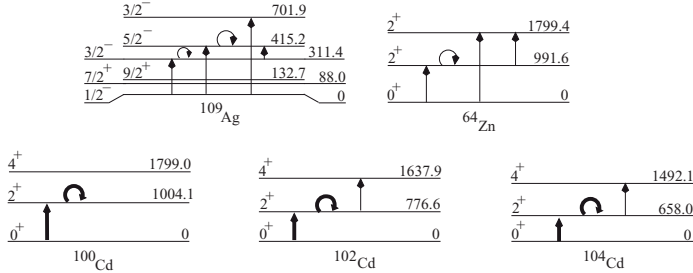


FIG. 2. Experimental level schemes for the projectile and target isotopes. The relevant diagonal and nondiagonal $E2$ transitions are indicated with arrows. Transitions marked with a bold arrow are fitted in the analysis.

$P(\theta)$ is the known Coulomb excitation probability [19] for the ^{109}Ag target nuclei. The following effects were taken into account in the simulation: the energy loss of the particles as they traversed the target foil, the adiabaticity parameter ξ , the angular distributions $W(\theta)$, the Doppler shift of emitted γ rays, the experimental γ -ray detection efficiency, and the

exact DSSSD geometry. Furthermore, a Gaussian distributed beam spot with a standard deviation of 1 mm was used. The simulated γ -ray energy spectrum is shown in Fig. 5(c). The simulation agrees with the experimental data. In detail, the γ rays from the 415 keV $(\frac{3}{2})_1^- \rightarrow (\frac{1}{2})_0^-$ transition are registered in coincidence with a projectile particle in 76%

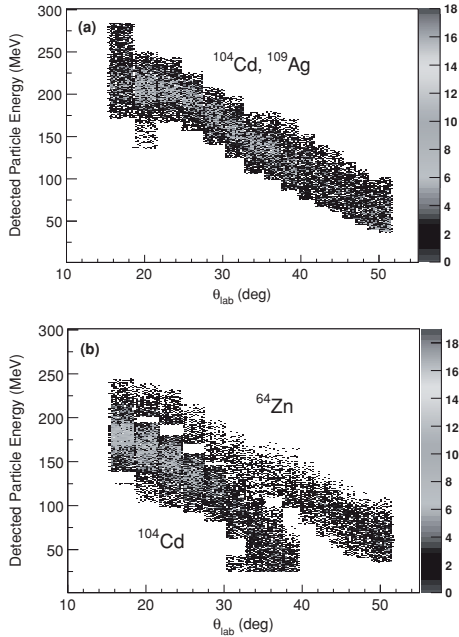


FIG. 3. Energy versus angle of the scattered beam and target particles detected by the DSSSD in the (a) $^{104}\text{Cd} + ^{109}\text{Ag}$ measurement and (b) $^{104}\text{Cd} + ^{64}\text{Zn}$ measurement.

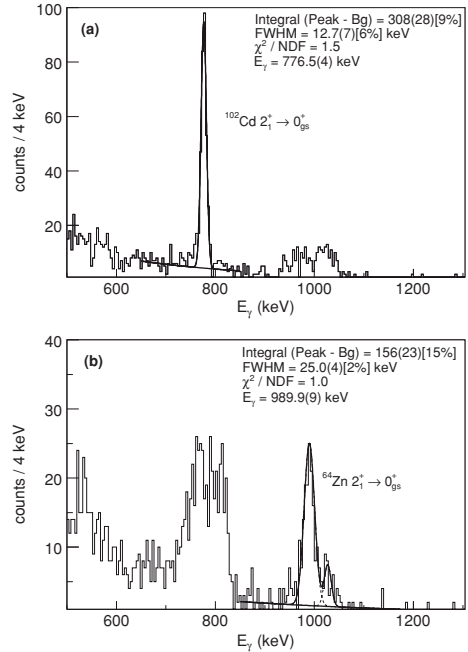


FIG. 4. The Doppler corrected γ -ray energy spectra from the $^{102}\text{Cd} + ^{64}\text{Zn}$ measurement. (a) The ^{102}Cd projectile de-excitation peak and (b) the ^{64}Zn target de-excitation peak.

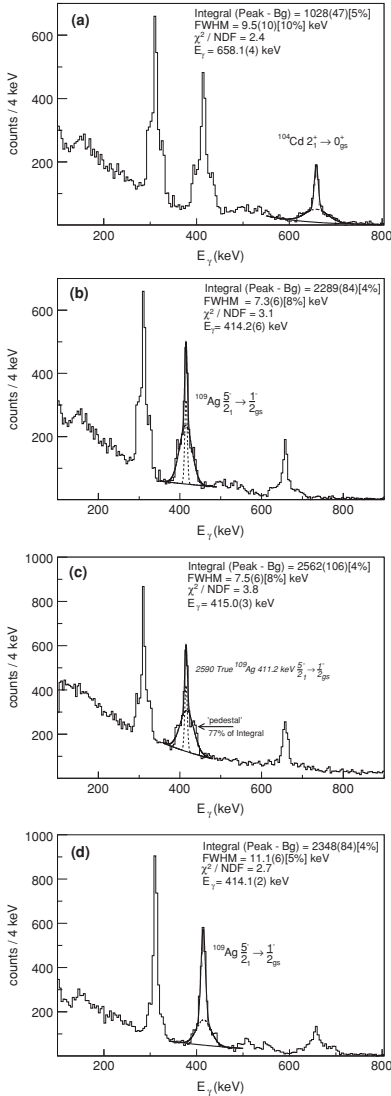


FIG. 5. [(a) and (b)] The Doppler-corrected γ -ray energy spectra from the $^{104}\text{Cd} + ^{109}\text{Ag}$ measurement. The pedestal comes from the ambiguity in the particle identification process. (c) Monte Carlo simulation of the effects of incomplete particle identification in the Doppler correction process. (d) Doppler-corrected γ rays from the ^{109}Ag target using the reconstructed momentum vectors of these particles.

of the Monte Carlo events. According to the fit in Fig. 5(c), the size of the corresponding simulated pedestal is 77(5)%. The experimental pedestal is 78(4)%. Furthermore, it can be verified that the total number of events estimated by the fit routine is accurate within one standard deviation.

Turning to the experimental data set again, it is possible to Doppler correct the transitions in ^{109}Ag using reconstructed momentum vectors of these particles. As expected, this reduces the pedestal of the corresponding peaks, see Fig. 5(d). However, note that the integrated γ -ray yields remain unchanged within one standard deviation. The reconstructed data thus shows consistency but was not used further in the analysis.

2. The $^{100}\text{Cd} + ^{109}\text{Ag}$ measurement

Within the time constraint of the experiment, a few ^{100}Cd events were detected. In this measurement the ^{109}Ag target was chosen over the ^{64}Zn target due to the higher Z of the former. As mentioned, the particle count rate in the DSSSD vanished when the laser ionization was switched off. The Doppler corrected spectrum, Fig. 6, is virtually free from any radioactive background due to the limited beam intensity. However, with the available statistics, only an upper limit on the number of $2_1^+ \rightarrow 0_{gs}^+$ transitions in ^{100}Cd can be extracted. For this analysis all events within $E(2_1^+) = 1004 \pm 100$ keV in the Doppler corrected γ -ray spectrum in Fig. 6 are assigned to the projectile transition of interest. This energy region is defined from the maximum Doppler shift of the projectile γ -ray energy.

3. Matrix elements and transitions in the targets

The adopted value of the diagonal matrix element, $M_{22} = -0.42(8)e b$, in ^{64}Zn [29] depends on the sign of the second-order interference term, $\langle 0_{gs}^+ || E2 || 2_1^+ \rangle \langle 2_1^+ || E2 || 2_2^+ \rangle \langle 0_{gs}^+ || E2 || 2_2^+ \rangle$. However, this ambiguity affects only the $^{102,104}\text{Cd}$ cross sections on the level of 3%, which

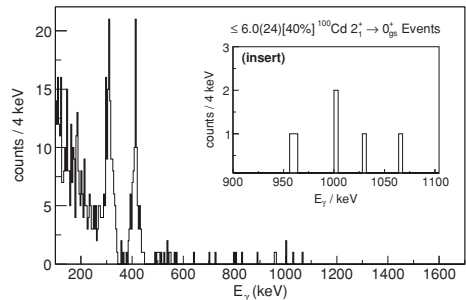


FIG. 6. Doppler-corrected γ -ray energy spectrum from the $^{100}\text{Cd} + ^{109}\text{Ag}$ measurement. All events present in the insert are assigned to the $2_1^+ \rightarrow 0_{gs}^+$ transition in ^{100}Cd . This leads to an upper limit of the corresponding $B(E2)$.

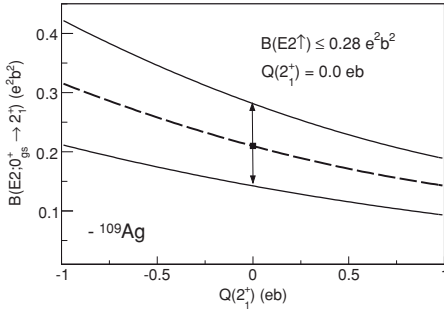


FIG. 7. The dashed line indicates the contour curve of the measured cross section of ^{100}Cd relative to ^{109}Ag . The $B(E2)$ value is extracted under the assumption that the $Q(2_1^+) = 0.0 \text{ eb}$. This is in line with the observed experimental trend seen in the light Cd isotopes. The arrows indicate the extracted uncertainty.

is below the experimental precision. The positive interference term is used in this work due to its lower relative uncertainty.

In ^{109}Ag there exists an $8(1)\%$ γ -decay branch from the 415.2 keV $5/2^-$ state to the 311.4 keV $3/2^-$ state [30]. This feeding of the 311.4 keV γ -ray yield is corrected for in the extraction of the Coulomb excitation cross sections when using ^{109}Ag as target.

V. RESULTS

In this section we present the contour curves, Fig. 7, Fig. 8(a), and Fig. 9(a), that result from the measured cross sections. The measurements relative to ^{64}Zn and ^{109}Ag are given by the black and red curves, respectively. The range of possible $B(E2)$ values is clearly limited by the ^{64}Zn cross section for small center-of-mass angles, $\theta_{\text{c.m.}}$, given by the blue curve in the same figure. The resulting likelihood distributions for $^{102,104}\text{Cd}$ are given in Fig. 8(b) and Fig. 9(b). The correlation between the static and dynamic moments is clear from these figures. The maximum likelihood estimator for the

dynamic moments are $B(E2; \uparrow) = 0.33 \pm 0.01 \pm 0.02 \text{ e}^2 \text{ b}^2$ and $B(E2; \uparrow) = 0.28 \pm 0.02 \pm 0.02 \text{ e}^2 \text{ b}^2$ for ^{104}Cd and ^{102}Cd , respectively. The uncertainties are evaluated at the point of maximum likelihood in the (B, Q) plane. They are separated into statistical and systematic components. The primary source of the systematic error is the precision with which the $B(E2)$ values are known for the target isotopes. For ^{100}Cd a $B(E2) \leq 0.21 \pm 0.07 \text{ e}^2 \text{ b}^2$ is extracted for a $Q(2_1^+) = 0.0 \text{ eb}$. The basis for this assumption is discussed further below. Note that the error in this case includes statistic and systematic effects. The results are summarized in Table V. A higher-lying second 2^+ state has not been observed experimentally in the present Cd isotopes. However, assuming that its energy is equal to that of the second 2^+ state in ^{106}Cd , a direct calculation shows that virtual quadrupole excitations via this state has an impact of $<2\%$ on the cross section. This will not affect the $B(E2)$ values. The resulting effect on the static quadrupole moments in the present Cd isotopes is $<0.05 \text{ eb}$. Thus this systematic effect of a 2_2^+ state was not included in this work. In this investigation the $\langle 0_1^+ || E2 || 2_2^+ \rangle$ and $\langle 2_1^+ || E2 || 2_2^+ \rangle$ matrix elements were taken from ^{106}Cd [35].

VI. SHELL-MODEL INTERPRETATION AND DISCUSSION

The first reorientation measurement was made in ^{114}Cd by J. de Boer *et al.* [36] and the finding of a large negative $Q(2_1^+)$ in that nucleus stimulated much discussion, see, e.g., Ref. [37–39] and references therein. One aim of the current work is to independently establish the trend of $B(E2)$ values for the light Cd isotopes using Coulomb excitation to compare this to the corresponding trend in the light Sn isotopes. The experimental trend of $B(E2)$ values in the Cd isotopic chain that results from this work shows a gradual, almost linear, increase starting with a $B(E2) = 0.28 \text{ e}^2 \text{ b}^2$ in ^{102}Cd toward a $B(E2) = 0.57 \text{ e}^2 \text{ b}^2$ in ^{118}Cd , see Fig. 10. The data on the neutron-rich side of stability remains scarce. The first measurements of the $B(E2)$ value have recently been carried out in $^{122,124}\text{Cd}$ [40] but the $Q(2_1^+)$ remains unknown in those isotopes. Current results seem to indicate a somewhat more rapid decrease in the $B(E2)$ values on the neutron-rich side. Still, it is not yet possible to draw a firm conclusion based

TABLE V. The experimental results obtained in this work as extracted from the maximum likelihood point. The uncertainties are statistical and systematic in origin. If only one uncertainty is quoted this corresponds to the total error. The second column indicates whether the lifetimes from Ref. [18] were included in the likelihood function. The correlation between the $B(E2)$ and the $Q(2_1^+)$ values is shown in Figs. 8(b) and 9(b).

Projectile	Incl.	$\tau(2_1^+)$	$B(E2; 0_1^+ \rightarrow 2_1^+) (\text{e}^2 \text{ b}^2)$	$Q(2_1^+) (\text{eb})$	Target	Projectile σ_{E2} (mb)
^{104}Cd	No		$0.33 \pm 0.01 \pm 0.02$	$0.06 \pm 0.10 \pm 0.11$	^{64}Zn	307(39)
	Yes		0.39 ± 0.01	-0.52 ± 0.19	^{109}Ag	1013(61)
^{102}Cd	No		$0.28 \pm 0.02 \pm 0.02$	$0.22 \pm 0.11 \pm 0.15$	^{64}Zn	202(43)
	Yes		0.28 ± 0.04	0.20 ± 0.43	^{109}Ag	596(48)
^{100}Cd	No		$\leq 0.28^a$	0.0^b	^{109}Ag	201(64)

^aThe precision of this value is 33%.

^bFixed in the analysis to extract the corresponding $B(E2)$; see Fig. 7.

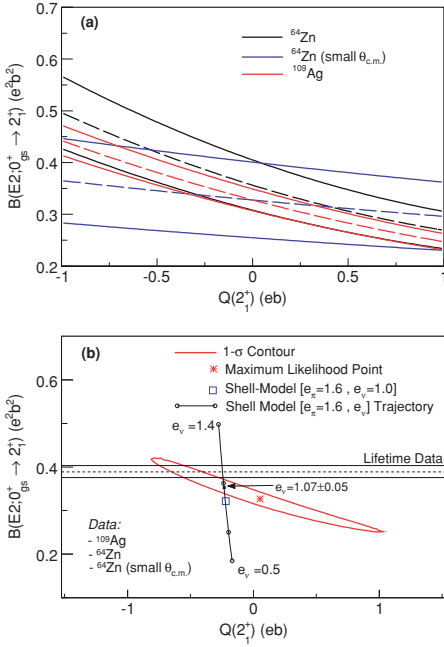


FIG. 8. (Color online) The final likelihood-interpreted results for ^{104}Cd based on the cross-section measurements presented here. (a) The contour curves in the $B(E2) - Q(2^+)$ plane for each measurement. The dashed curves indicate measured values and the solid curves the corresponding uncertainties. (b) The 1- σ contour of the likelihood function. The point of maximum likelihood is indicated with a red star together with horizontal and vertical lines for the corresponding uncertainty. The shell-model prediction with $e_\pi = 1.6e$ and $e_v = 1.0e$ for the location of the $B(E2 \uparrow)$ and $Q(2^+)$ values is indicated with a blue square. The black curve marks the calculated trajectory of the $B(E2 \uparrow)$ and $Q(2^+)$ values as a function of e_v keeping $e_\pi = 1.6e$. The point of maximum likelihood along this trajectory gives the shell-model interpreted values presented in Table VI. The horizontal lines, marked with “Lifetime Data,” indicate the $B(E2)$ value (dashed line) with uncertainties (solid lines) as extracted from the lifetime presented in Ref. [18].

on existing data for the neutron-rich isotopes. An interesting contrast between the Sn and Cd chains is that the apparent onset of collectivity observed in $^{106,108,110}\text{Sn}$ is not reproduced in an obvious way in $^{102,104,106}\text{Cd}$. The reported high-precision measurement in Ref. [18] does indicate an increase in the $B(E2)$ value in ^{104}Cd but this appears not to be maintained for the lighter isotopes. However, this increase is not observed in our measurement.

In the following we discuss our results starting from a shell-model calculation based on a realistic interaction, i.e., without any phenomenological modifications, derived from a

G -matrix-renormalized CD-Bonn nucleon-nucleon potential. This interaction reproduces fairly well the high spin states in $^{101,102}\text{In}$ and ^{99}Cd [6,7]. The nucleus ^{88}Sr is used as an inert core and the location of the single-particle energies were taken from Ref. [41]: $\varepsilon(\pi 1p_{1/2}) = 0.00$, $\varepsilon(\pi 0g_{9/2}) = 0.90$, $\varepsilon(\nu 1d_{5/2}) = 0.00$, $\varepsilon(\nu 2s_{1/2}) = 1.26$, $\varepsilon(\nu 1d_{3/2}) = 2.23$, $\varepsilon(\nu 0g_{7/2}) = 2.63$, and $\varepsilon(0h_{11/2}) = 3.50$ in units of MeV. The calculated $E(2^+)$ and $E(4^+)$ are almost identical to experimental values. Further, the theoretical $B(E2)$ and $Q(2^+)$ values for ^{106}Cd are well within the experimental uncertainties of the adopted values; see Table VI and Fig. 10.

One may now test the predictive power of the shell-model calculation using the probability distributions shown in Fig. 8(b) and Fig. 9(b). One approach to this issue is to keep either the proton effective charge (e_π) or the neutron effective charge (e_v) constant while varying the other. For the present case the magnitude of the relevant diagonal and nondiagonal matrix elements results in a three times larger sensitivity of the predicted $B(E2)$ to a variation in e_v compared to an equal variation in e_π . To facilitate a comparison with the light Sn isotopes it is primarily interesting to investigate renormalization effects in e_v keeping e_π fixed. As a starting point one needs to select a pair of neutron and proton effective charges. The proton effective charge has been extracted from a previous lifetime measurement in ^{98}Cd [1]. However, a recent study [2] of a core-excited isomer in that nucleus indicates that systematic effects might have influenced the value of the extracted proton effective charge. Similarly new measurements of the de-excitation strength of the 6^+ isomer in ^{102}Sn [43] may lead to an improved neutron effective charge. Thus, awaiting further data for the lightest isotopes in the vicinity of ^{100}Sn we instead take ^{106}Cd as the starting point for our investigation. As can be seen in Fig. 10 the effective charges $e_\pi = 1.6e$ and $e_v = 1.0e$ reproduces the $B(E2)$ value in this nucleus. These values are also well in line with those used in previous calculations in this mass region [41,44,45]. The shell-model prediction for $^{102,104}\text{Cd}$ using these effective charges are indicated with squares in Fig. 8(b) and Fig. 9(b). For the ^{104}Cd case the prediction borders the 1- σ contour of the probability

TABLE VI. Shell-model interpretation (SM+exp) of the measured $B(E2; 0^+_{gs} \rightarrow 2^+)$ and $Q(2^+)$ values in units of $e^2 b^2$ and eb, respectively. The energies of the first two excited states, $E(2^+)$ and $E(4^+)$, are also given in units of MeV. The effective proton and neutron charges of the shell-model (SM) values are $e_\pi = 1.6e$ and $e_v = 1.0$. See text for details.

	^{102}Cd	^{104}Cd	^{106}Cd
$E(2^+)_{\text{SM}}$	0.773	0.626	0.566
$E(2^+)_{\text{exp}}$	0.777	0.658	0.633
$E(4^+)_{\text{SM}}$	1.541	1.446	1.409
$E(4^+)_{\text{exp}}$	1.638	1.492	1.494
$B(E2)_{\text{SM}}$	0.24	0.32	0.38
$Q(2^+)_{\text{SM}}$	-0.18	-0.22	-0.24
$B(E2)_{\text{SM+exp}}$	0.32 ± 0.03	0.35 ± 0.02	0.384 ± 0.004^a
$Q(2^+)_{\text{SM+exp}}$	-0.20 ± 0.01	-0.23 ± 0.01	-0.28 ± 0.08^a

^aAdopted experimental value, see Ref. [30].

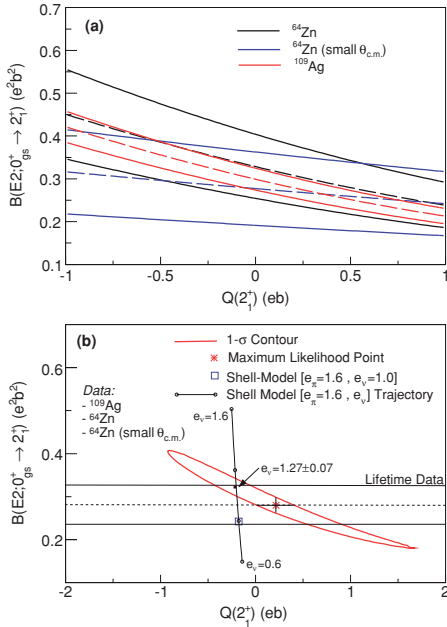


FIG. 9. (Color online) The final likelihood-interpreted results for ^{102}Cd based on the cross-section measurements presented here. The two plots (a) and (b) are identical to the ones shown for the ^{104}Cd case; see the caption of Fig. 8.

distribution while for the ^{102}Cd case the deviation is larger. A variation of e_v will trace out a trajectory in the (B, Q) plane. The point of maximum likelihood along this trajectory gives the neutron effective charge that reproduces the experimental result with highest probability within the model. Consequently, tracing this trajectory, keeping $e_\pi = 1.6e$ fixed, gives a direct measure of the renormalization required for the shell-model to reproduce the data in $^{102,104}\text{Cd}$. For ^{104}Cd the maximum likelihood is reached for $e_v = 1.07 \pm 0.05$ while for ^{102}Cd the corresponding number is $e_v = 1.27 \pm 0.07$. Thus, for the latter case the renormalization of the neutron effective charge amounts to 27% within 3σ . Repeating this investigation with the proton effective charges $e_\pi = 1.4$ and $e_\pi = 1.8e$ requires $e_v = 1.07e$ and $e_v = 0.93e$ to reproduce the experimental $B(E2)$ value in ^{106}Cd . For ^{102}Cd the maximum likelihood is then reached for $e_v = 1.37 \pm 0.07e$ and $e_v = 1.17 \pm 0.07e$. In total, this investigation indicates a $\sim 25\%$ renormalization of the neutron effective charge when moving from ^{106}Cd to ^{102}Cd . The corresponding $B(E2)$ values extracted with maximum likelihood are given in Table VI and with blue dots in Fig. 10(b). It is interesting to note that the predicted $Q(2_1^+)$ are limited to a very narrow range. It is therefore clear from the picture that the presented values are close to

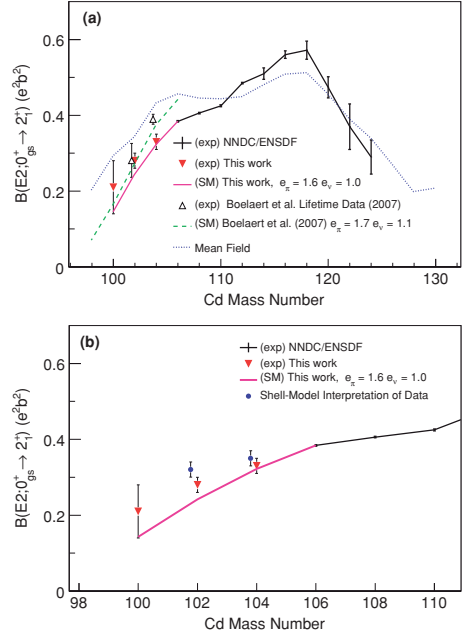


FIG. 10. (Color online) (a) Experimental and theoretical $B(E2; 0_1^+ \rightarrow 2_1^+)$ and values in the Cd isotopes. The “REX-ISOLDE” values (red triangles) are the maximum likelihood estimators extracted in this work. The Boelaert *et al.* lifetime data is Ref. [18], the Boelaert *et al.* shell-model calculation is Ref. [11], and the mean-field calculation is Ref. [42]. (b) Same figure expanded around the neutron-deficient region. The blue dots represent the $B(E2)$ values obtained using the shell-model interpretation of the measured data. See text for details.

the ones that would be obtained from an interpretation based on a fix $Q(2_1^+)$ value from the shell-model. In conclusion, a renormalization of the neutron effective charge in the light Cd isotopes appears necessary although the effect on the observed $B(E2)$ values is not as conspicuous as suggested in the light Sn isotopes [13–16].

It should be mentioned that theoretical predictions for the light Cd isotopes have also been presented in two recent works [11,42]. The shell-model calculations in Ref. [11] were carried out with a valence space consisting of the proton $\pi(1p_{1/2}, 0g_{9/2})$ and neutron $\nu(1d_{5/2}, 2s_{1/2}, 1d_{3/2}, 0g_{7/2}, 0h_{11/2})$ orbits outside an inert $^{88}_{38}\text{Sr}_{50}$ core. For further details see Ref. [11]. The results from this calculation are shown in Fig. 10 where the results from a beyond mean-field calculation [42] using the Gogny force is also plotted. Earlier theoretical models [12] of the neutron-deficient Cd isotopes include taking ^{100}Sn as a core and using a neutron-proton interaction of quadrupole-quadrupole type.

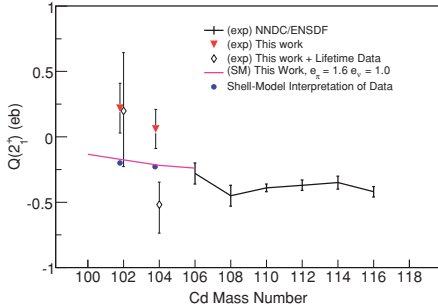


FIG. 11. (Color online) The experimentally known $Q(2_1^+)$ values in the even-mass Cd isotopes. The results of the shell-model calculation carried out in this work are indicated with a magenta line. Invoking the previously published lifetime data [18] in the likelihood function gives the $Q(2_1^+)$ values marked with diamonds. The numerical values for these are given in Table V. See text for details.

As can be seen in Fig. 11 the experimental $Q(2_1^+)$ in ^{104}Cd is lower than that in ^{106}Cd when invoking the previously published lifetime data [18]. While the value from our likelihood analysis lies closer to zero for ^{104}Cd and also somewhat closer to the shell-model prediction the values extracted using both methods almost identical for ^{102}Cd . This may be a further

indication of a slightly too-large $B(E2)$ value extracted from the lifetime measurement in Ref. [18]. The shell-model calculation also indicates a $Q(2_1^+) \approx 0$ e.b. in ^{100}Cd and therefore strengthens the grounds on which the $B(E2)$ value in ^{100}Cd is extracted.

In a spherical harmonic vibrator model the static quadrupole moment is also predicted to be identical to zero [46]. In a article by Alaga [47], the particle-vibrator model was shown to give a $Q(2_1^+) = -0.33$ b for the Cd isotopes in the midshell region, which is in agreement with the later adopted experimental value, see Fig. 11 and Refs. [37,38]. Within that model the quadrupole moment in vibration-like nuclei is a consequence of the interaction between the proton degree of freedom and the vibrator here given by the neutrons. Moreover, energy-weighted sum-rule calculations [48] and investigations [49] using the interacting boson approximation are in agreement with the experimental $Q(2_1^+)$ values in $^{106-116}\text{Cd}$.

Evidently, experimental transition probabilities in the two proton-hole, $N = 50$, nucleus ^{98}Cd are of importance in the investigation of the nucleon-nucleon interaction in the ^{100}Sn region. Expanded theoretical investigations and shell-model calculations relating to this question have been initiated [50].

ACKNOWLEDGMENTS

This work was supported by the Swedish Research Council, the German Federal Ministry of Education and Research under Grant 06KY2051, and the European Union under Contract RII3-EURONS 506065.

- [1] M. Górska *et al.*, Phys. Rev. Lett. **79**, 2415 (1997).
- [2] A. Blazhev *et al.*, Phys. Rev. C **69**, 064304 (2004).
- [3] N. Redon, J. Meyer, M. Meyer, P. Quentin, P. Bonche, H. Floard, and P. H. Heenen, Phys. Rev. C **38**, 550 (1988).
- [4] K. Heyde, P. Van Isacker, M. Waroquier, G. Wenes, and M. Sambataro, Phys. Rev. C **25**, 3160 (1982).
- [5] A. Pandoh, R. Devi, and S. K. Khosa, Phys. Rev. C **60**, 047302 (1999).
- [6] M. Lipoglavsek *et al.*, Phys. Rev. C **65**, 021302(R) (2002).
- [7] M. Lipoglavsek *et al.*, Phys. Rev. C **66**, 011302(R) (2002).
- [8] J. Persson *et al.*, Nucl. Phys. **A627**, 101 (1997).
- [9] M. Palacz *et al.*, Nucl. Phys. **A624**, 210 (1997).
- [10] M. Palacz *et al.*, Nucl. Phys. **A608**, 227 (1996).
- [11] N. Boelaert, N. Smirnova, K. Heyde, and J. Jolie, Phys. Rev. C **75**, 014316 (2007).
- [12] J. Sau *et al.*, Nucl. Phys. **A410**, 14 (1983).
- [13] A. Banu *et al.*, Phys. Rev. C **72**, 061305(R) (2005).
- [14] C. Vaman *et al.*, Phys. Rev. Lett. **99**, 162501 (2007).
- [15] J. Cederkäll *et al.*, Phys. Rev. Lett. **98**, 172501 (2007).
- [16] A. Ekström *et al.*, Phys. Rev. Lett. **101**, 012502 (2008).
- [17] G. Müller *et al.*, Phys. Rev. C **64**, 014305 (2001).
- [18] N. Boelaert *et al.*, Phys. Rev. C **75**, 054311 (2007).
- [19] K. Alder and A. Winther, *Electromagnetic Excitation* (North-Holland, Amsterdam, 1975).
- [20] G. Breit *et al.*, Phys. Rev. **103**, 727 (1956).
- [21] J. V. de Walle *et al.*, Phys. Rev. C **79**, 014309 (2009).
- [22] U. Köster *et al.*, Nucl. Instrum. Methods B **266**, 4229 (2008).
- [23] F. Wenander, Nucl. Phys. **A701**, 528 (2002).
- [24] A. N. Ostrowski *et al.*, Nucl. Instrum. Methods A **480**, 448 (2002).
- [25] J. F. Ziegler, Nucl. Instrum. Methods B **219-220**, 1027 (2004).
- [26] N. Bree *et al.*, Phys. Rev. C **78**, 047301 (2008).
- [27] S. Raman *et al.*, At. Data Nucl. Data Tables **78**, 1 (2001).
- [28] N. Stone, At. Data Nucl. Data Tables **90**, 75 (2005).
- [29] S. Salém-Vasconcelos, M. J. Bechara, J. H. Hirata, and O. Dietzsch, Phys. Rev. C **38**, 2439 (1988).
- [30] ENSDF, <http://www.nndc.bnl.gov/ensdf/>.
- [31] P. Raghavan, At. Data Nucl. Data Tables **42**, 189 (1989).
- [32] M. J. Throop *et al.*, Phys. Lett. **B41**, 585 (1972).
- [33] J. Ljungvall *et al.*, Phys. Rev. Lett. **100**, 102502 (2008).
- [34] H. Ower, computer code CLX.
- [35] W. Milner *et al.*, Nucl. Phys. **A129**, 687 (1969).
- [36] J. de Boer *et al.*, Phys. Rev. Lett. **14**, 564 (1965).
- [37] M. T. Esat *et al.*, Phys. Lett. **B61**, 242 (1976).
- [38] M. T. Esat *et al.*, Nucl. Phys. **A274**, 237 (1976).
- [39] C. Fahlander *et al.*, Nucl. Phys. **A485**, 327 (1988).
- [40] T. Kröll *et al.*, AIP Conf. Proc. **831**, 119 (2006).
- [41] A. Holt, T. Engeland, M. Hjorth-Jensen, and E. Osnes, Phys. Rev. C **61**, 064318 (2000).
- [42] T. R. Rodriguez *et al.*, Phys. Lett. **B668**, 410 (2008).
- [43] M. Górska (private communication).
- [44] B. A. Brown *et al.*, Phys. Rev. C **13**, 1900 (1976).

- [45] K. Sieja, F. Nowacki, K. Langanke, and G. Martinez-Pinedo, Phys. Rev. C **79**, 064310 (2009).
- [46] Aa. Bohr and B. Mottelson, *Nuclear Structure* (Benjamin, New York, 1969), Vol. II.
- [47] G. Alaga *et al.*, Phys. Lett. **B43**, 459 (1973).
- [48] W. Koo *et al.*, Nucl. Phys. **A315**, 21 (1979).
- [49] I. Morrison *et al.*, Nucl. Phys. **A350**, 89 (1980).
- [50] A. Ekström *et al.* (to be published).

IV

COULOMB EXCITATION OF THE ODD-ODD ISOTOPES $^{106,108}\text{In}$

PAPER IV

Coulomb excitation of the odd-odd Isotopes ^{106,108}In

A. Ekström¹, J. Cederkäll^{1,2}, C. Fahlander¹, M. Hjorth-Jensen³, T. Engeland³, A. Blazhev⁴, P. A. Butler⁵, T. Davinson⁶, J. Eberth⁴, F. Finke⁴, A. Görgen⁷, M. Górski⁸, A. M. Hurst⁵, O. Ivanov⁹, J. Iwanicki¹⁰, U. Köster^{2,11}, B. A. Marsh^{12,13}, J. Mierzejewski^{10,14}, P. Reiter⁴, S. Siem¹⁵, G. Sletten¹⁶, I. Stefanescu⁹, G. M. Tveten^{2,15}, J. Van de Walle^{2,9}, D. Voulot¹³, N. Warr⁴, D. Weisshaar⁴, F. Wenander¹³, and M. Zielińska^{7,10}

¹ Physics Department, University of Lund, Box 118, SE-221 00 Lund, Sweden

² PH Department, CERN 1211, Geneva 23, Switzerland

³ Physics Department and Center of Mathematics for Applications, University of Oslo, Norway

⁴ Institute of Nuclear Physics, University of Cologne, Germany

⁵ Oliver Lodge Laboratory, University of Liverpool, United Kingdom

⁶ Department of Physics and Astronomy, University of Edinburgh, United Kingdom

⁷ CEA Saclay, Service de Physique Nucléaire, Gif-sur-Yvette, France

⁸ Gesellschaft für Schwerionenforschung, Darmstadt, Germany

⁹ Instituut voor Kern- en Stralingsfysica, K.U. Leuven, Belgium

¹⁰ Heavy Ion Laboratory, University of Warsaw, Poland

¹¹ Institut Laue Langevin, 6 rue Jules Horowitz, 38042 Grenoble, France

¹² Department of Physics, University of Manchester, United Kingdom

¹³ AB Department, CERN 1211, Geneva 23, Switzerland

¹⁴ Institute of Experimental Physics, University of Warsaw, Poland

¹⁵ Department of Physics, University of Oslo, Norway

¹⁶ Physics Department, University of Copenhagen, Denmark

Received: date / Revised version: date

Abstract. The low-lying states in the odd-odd and unstable isotopes ^{106,108}In have been Coulomb excited from the ground state and the first excited isomeric state at the REX-ISOLDE facility at CERN. With the additional data provided here the $\pi g_{9/2}^{-1} \otimes \nu d_{5/2}$ and $\pi g_{9/2}^{-1} \otimes \nu g_{7/2}$ multiplets have been reanalyzed and are modified compared to previous results. The observed γ -ray de-excitation patterns were interpreted within a shell-model calculation based on a realistic effective interaction. The agreement between theory and experiment is satisfactory and the calculations reproduce the observed differences in the excitation pattern of the two isotopes. The calculations exclude a 6^+ ground state in ¹⁰⁶In. This is in agreement with the conclusions drawn using other techniques. Furthermore, based on the experimental results, it is also concluded that the ordering of the isomeric and ground state in ¹⁰⁸In is inverted compared to the shell-model prediction. Limits on $B(E2)$ values have been extracted where possible. A previously unknown low-lying state at 367 keV in ¹⁰⁶In is also reported.

PACS. 23.20.Js Multipole matrix elements – 21.60.Cs Shell model – 25.70.De Coulomb excitation – 27.60.+j 90≤A≤149

1 Introduction

The low-lying states in ^{106,108}In can be interpreted as the coupling of a proton (π) hole in the $g_{9/2}$ orbit to the neutron (ν) states in the corresponding ^{107,109}Sn isotopes [1, 2]. Here we aim to expand the knowledge of the low-lying energy spectrum in ^{106,108}In using Coulomb excitation for the first time. According to measurements of the magnetic dipole moment in ¹⁰⁸In [3–5], the 7^+ ground state and the $T_{1/2} = 39.6$ min isomeric 2^+ state are dominated by the $\pi g_{9/2}^{-1} \otimes \nu d_{5/2}$ configuration. The higher lying states have previously been identified in terms of the $\pi g_{9/2}^{-1} \otimes \nu d_{5/2}$

and $\pi g_{9/2}^{-1} \otimes \nu g_{7/2}$ multiplets [5] based on the observed decay-pattern following the ¹⁰⁸Cd(p,n γ)¹⁰⁸In reaction. In ¹⁰⁶In the identification of the states is less clear. According to Refs. [3,4,6] the 7^+ ground state has a dominating $\pi g_{9/2}^{-1} \otimes \nu d_{5/2}$ configuration. The first excited state in ¹⁰⁶In is also isomeric with $T_{1/2} = 5.2$ min. However, the spin measurements are inconsistent. For instance, (p,n γ) measurements report this state as a 3^+ state [7], while decay studies suggest a spin and parity of 2^+ [8,9]. It is well known that the γ -ray decay pattern following e.g. a compound reaction is largely governed by the yrast sequence, whereas for β -decay it depends on the nature of

Table 1. Yields and relative intensities of the observed γ -ray transitions in ^{108}In .

Transition	E_γ (keV)	γ -ray Yield	Intensity
$7^+ \rightarrow 7^+_{\text{gs}}$	151	377(66)	23(4)
$3^+ \rightarrow 2^+$	169	1536(64)	100(4)
$(5^+) \rightarrow 7^+_{\text{gs}}$	248	631(50)	50(5)
$(5^+) \rightarrow (6, 7, 8)$	151	79(14)	5(1)
$3^+ \rightarrow 2^+$	236	1106(67)	86(6)
$4^+ \rightarrow 3^+$	283	192(60)	17(5)
$4^+ \rightarrow 3^+$	216	150(50)	11(4)

Table 2. Yields and relative intensities of the observed γ -ray transitions in ^{106}In . The two yields given for the 123 keV doublet transition correspond to the yield of the observed γ -ray peak.

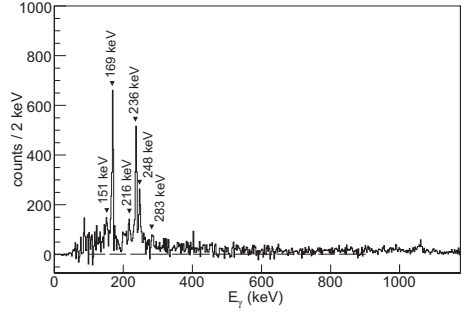
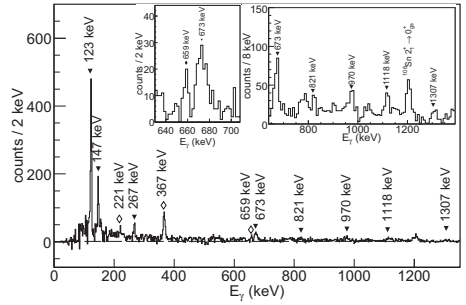
Transition	E_γ (keV)	γ -ray Yield	Intensity
$(6^+ 7^+ 8^+ 9^+) \rightarrow 7^+_{\text{gs}}$	123	897(41)	100(5)
$(7^+) \rightarrow 7^+_{\text{gs}}$	147	566(61)	68(8)
$(2^+) \rightarrow (2^+)_{\text{gs}}$	123	897(41)	100(5)
$(6^+) \rightarrow 7^+_{\text{gs}}$	367.1(2)	321(29)	64(6)
$(6^+) \rightarrow (7^+)_{\text{gs}}$	221.1(14)	38(14)	6(2)
$6 \rightarrow (6^+ 7^+ 8^+ 9^+)_{\text{gs}}$	267	105(21)	17(4)
$(8^+) \rightarrow 7^+_{\text{gs}}$	821	59(16)	18(5)
$(8^+) \rightarrow (7^+)_{\text{gs}}$	673	128(24)	36(7)
$(8^+) \rightarrow 7^+_{\text{gs}}$	1118	66(23)	25(9)
$(8^+) \rightarrow (7^+)_{\text{gs}}$	970	81(21)	28(7)
$(9^+) \rightarrow 7^+_{\text{gs}}$	1307	40(12)	17(5)
not placed	658.7(4)	42(11)	12(3)

the initial state of the parent nucleus. In Coulomb excitation the excited states are populated from below. The probability to populate a state is determined by the reduced transition matrix element for the initial and final states. Therefore, for the case at hand, this method offers the possibility to investigate the $\pi^{-1} \otimes \nu$ multiplets starting from a specific initial state that couples to the higher lying excited states in a manner different from the techniques used before.

In the following the data is interpreted using a two-step approach. First, the spectrum of the low-energy states in the two isotopes was calculated in the shell-model. The results of this calculation, including the transition probabilities, were used as input to the coupled-channels Coulomb-excitation code GOSIA [10]. Secondly, the de-excitation patterns simulated in this way were compared to the corresponding experimental observations. From this, the $\pi^{-1} \otimes \nu$ multiplet character of some of the excited states could be inferred. It should be noted that the shell-model interaction used here reproduces the energy spectrum of ^{106}In and ^{108}In well.

2 Experimental technique

The measurements were carried out at the REX-ISOLDE facility using RIBs consisting of both Sn and In isotopes.

**Fig. 1.** Doppler corrected γ -ray energy spectrum for ^{108}In showing the decay of the levels populated in Coulomb excitation.**Fig. 2.** Doppler corrected γ -ray energy spectrum for ^{106}In showing the decay of the levels populated in Coulomb excitation. The transitions indicated with empty diamonds were detected for the first time in this work.

The results for the Sn isotopes have been published, see Ref. [11]. The definition of the physical events and the offline data analysis for the present case is identical to that of the Sn experiment and therefore treated very briefly here. The In isotopes were produced by bombarding a LaC_x target with 1.4 GeV protons. The produced species effused into an ion-cavity where the In isotopes were singly ionized through surface ionization against the cavity walls. Singly charged isotopes were subsequently extracted from the cavity by an applied electric field and the mass of interest was selected using electromagnetic separation. The low-energy RIB was post-accelerated to a final energy of 2.8 MeV/u and bombarded onto a 2.0 mg/cm² thick ^{58}Ni target. At this beam energy the inelastic collision process was safe in the meaning that the target and the projectile nuclei did not penetrate their mutual Coulomb barrier. Scattered beam and target particles were detected in a double sided silicon strip detector (DSSSD) [12]. The γ -

rays were detected by the MINIBALL spectrometer [13] which consists of 24 highly segmented Ge-detectors surrounding the secondary ^{58}Ni target in a spherical configuration. Particle- γ events were time-correlated by a 100 ns gate applied in the particle- γ coincidence spectrum.

3 The observed γ -ray de-excitation patterns

The Doppler corrected γ -ray energy spectra and the extracted γ -ray yields for ^{108}In and ^{106}In are shown in Figs. 1-2 and Tables 1-2. All but three γ -ray transitions observed in ^{106}In could be assigned to known levels in this nucleus whereas all of the observed γ -ray transitions in ^{108}In are known from before, see Fig. 3. The 151 keV γ -ray yield in ^{108}In is the sum of the yields from the $(5)^+ \rightarrow (6, 7, 8)$ and $7^+ \rightarrow 7^+_{\text{gs}}$ transitions. One of the 151 keV transitions originates from a $(5)^+$ state with a known 248 keV $(5)^+ \rightarrow 7^+_{\text{gs}}$ branch. From this, the 151 keV doublet was resolved, see Table 1. The yield of the 123 keV γ -ray transition in ^{106}In is also a doublet. It is the sum of the $(2)^+ \rightarrow (2)^+$ and $(6^+, 7^+, 8^+, 9^+) \rightarrow 7^+_{\text{gs}}$ transitions. However, a separation similar to that in ^{108}In was not possible. Three previously unknown γ -ray transitions at 221.1(14), 367.1(2) and 658.7(4) keV were detected in ^{106}In . The 367 keV γ -ray peak is rather prominent, see Fig. 2. The low probability for multiple Coulomb excitation favors a direct excitation from the 7^+_{gs} state to a $(5^+, 6^+, 7^+, 8^+, 9^+)$ state at 367.1(2) keV. According to the shell-model calculations, see Sec. 3.1, this state likely has spin and parity 6^+ . From the energy sums, the 221.1(14) keV γ -ray peak was placed as an 9(3)% decay-branch from the 367 keV state to the (7^+) state at 147.2 keV. This further strengthens the existence of a state at 367 keV. The weak 658.7 keV transition, see Table 2, could not be placed.

3.1 Shell-model based GOSIA simulations

From inspection of the experimental de-excitation patterns of ^{106}In and ^{108}In shown in Fig. 3, one can conclude that the states at higher energy couple more strongly to the 7^+ ground state in ^{106}In than in ^{108}In . In order to investigate this further a set of theoretical E2 and M1 transition matrix elements were derived using a realistic effective interaction [14] based on a G-matrix renormalized CD-Bonn nucleon-nucleon potential [15]. The model space included the orbits $\nu(1g_{7/2}, 2d_{5/2}, 3s_{1/2}, 2d_{3/2})$ and $\pi(1g_{9/2}, 2p_{1/2})$ outside the ^{88}Sr core. The single particle energies were taken from Ref. [16], the effective charges were set to $e_\pi = 1.5$ e and $e_\nu = 1.0$ e, and the standard gyromagnetic ratios were used. The negative parity orbit $\nu(1h_{11/2})$ was excluded for computational gain since it has a very small amplitude in the wave functions that describe the low-energy positive-parity states. The transition matrix element were then used to simulate the γ -ray yield using the coupled-channels code GOSIA [10]. The simulation included the geometry of the setup, the thickness of the target foil, and the theoretical internal conversion

coefficients [17].

The shell-model calculation for ^{106}In predicts a 6^+ ground state instead of the previously experimentally assigned 7^+ ground state. In addition, in order for the GOSIA simulations to reproduce the coupling to the higher lying states the 6^+ ground state must be replaced by the theoretical first excited 7^+_{gs} state. Indeed, a GOSIA simulation based on a 6^+ ground state leads to an intense $8^+_{\text{gs}} \rightarrow 7^+_{\text{gs}}$ transition and only one transition to the ground state, namely from the 7^+_{gs} state. However, experimentally other transitions are observed as well which corroborates the 7^+_{gs} shell-model state as the ground state. The 1307 keV state was tentatively assigned as 9^+ in Ref. [18]. Most likely, it corresponds to the 9^+ state at 1271 keV in the shell-model calculation. The observed decay of the (8^+) state at 821 keV has two branches, one to the 7^+ ground state and the other to the (7^+) state at 147 keV. The shell-model calculation predicts a similar transition between an 8^+ state and the 7^+ ground state. However, the branch to the second 7^+ state is not reproduced. Nevertheless, the tentative 8^+ assignment seems plausible.

The simulated γ -ray intensities for transitions to the isomeric 2^+ state and the 7^+ ground state in ^{108}In are consistent with data if the isomeric fraction of the indium component of the RIB is 50%, see Fig. 4. However, the current analysis is independent of the exact beam composition although the isomeric fraction of the RIB can be resolved using the γ -rays following the decay of the beam particles implanted at the experimental setup [21]. In order to reproduce the adopted data in ^{108}In , the 2^+ ground state and first excited 7^+ state of the shell model has to be interchanged. This conclusion is based on the intensity of the transition between the 3^+ state at 198 keV and the isomeric 2^+ state at 30 keV. The 3^+ state can be identified as the 262 keV state in the shell-model. The shell-model correctly describes the feeding of this state from above by a 4^+ state at 482 keV, corresponding to the 4^+ state at 796.4 keV in the calculation. Furthermore, both the shell-model state and the experimental counterpart have a decay branch to a lower lying second 3^+ state which then decays to the first excited isomeric 2^+ state. We stress that the coupled decay-pattern of these four states is, apart from the energies of the involved states, very well reproduced in the shell-model calculation. Therefore, the experimental 3^+ state at 266 keV most likely corresponds to the 501 keV state in the shell-model calculation. As mentioned, the $(6,7)^+$ at 248 keV has a 91.2% decay branch directly to the 7^+ ground state. The only similar transition in the shell-model calculation is from the 5^+ state at 392 keV. Therefore the 248 keV state is here tentatively assigned as having spin and parity 5^+ , see Fig. 3. It should be pointed out that the 97 keV transition from the low-lying $(6, 7, 8)$ state to the 7^+ ground state was not observed since at this energy the de-excitation is dominated by internal conversion and the detection threshold of the MINIBALL Ge-detectors was ~ 100 keV.

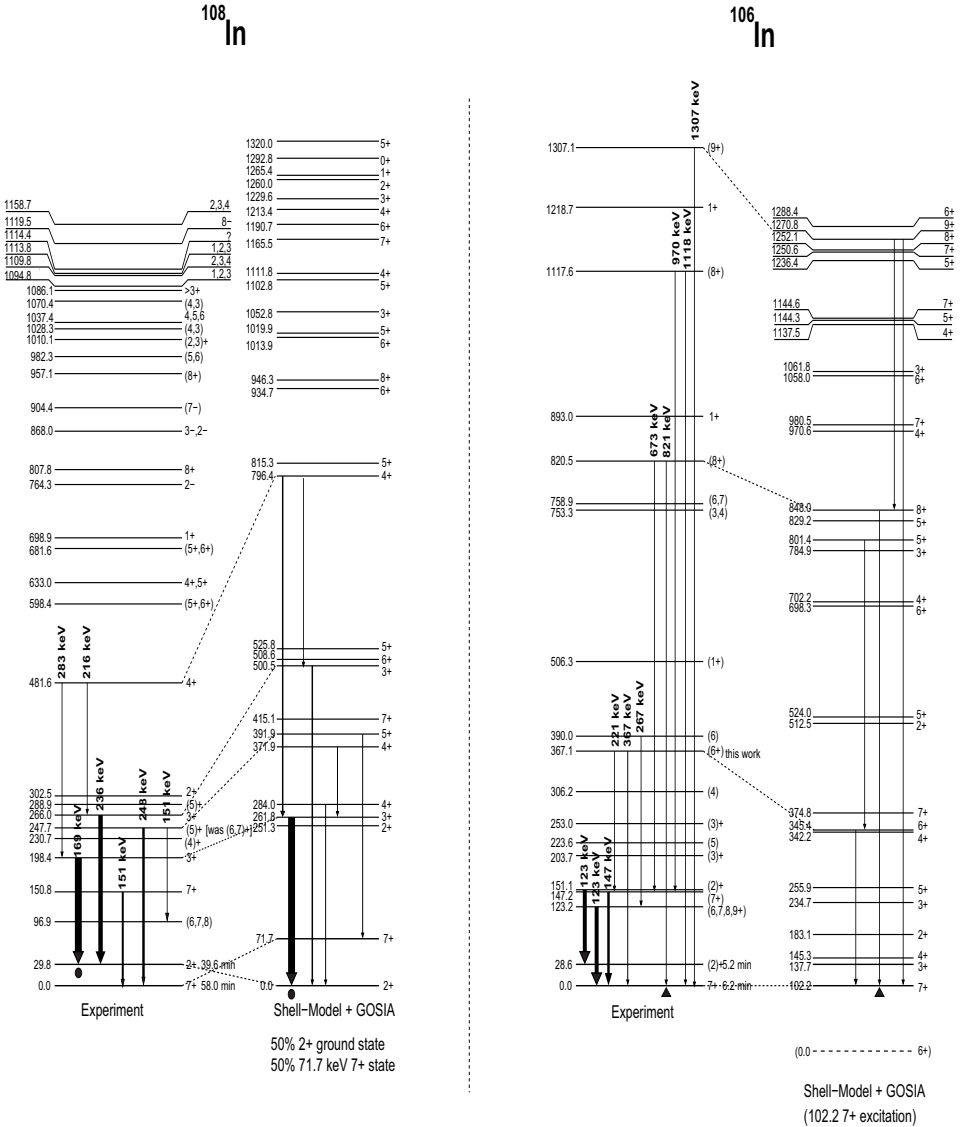


Fig. 3. Experimental and theoretical levels in $^{106,108}\text{In}$. The width of the arrows reflect the observed γ -ray yields. The theoretical γ -ray de-excitation patterns were obtained from a GOSIA simulation based on the E2 and M1 transition matrix elements derived from a shell-model calculation. The theoretical γ -ray yields were normalized to the experimental transition indicated with a triangle or a circle. The shell-model calculation for ^{106}In predicts a 6^+ ground state and a first excited 7^+ state. In order to reproduce the experimentally observed spin sequence, the 6^+ ground state was excluded and the first excited 7^+ state was assigned as the ground state. The level at 367 keV in ^{106}In was observed in this work and the tentative spin assignment is indicated. Also, the experimental levels and their theoretical counterparts, where identified, are connected with a dashed line.

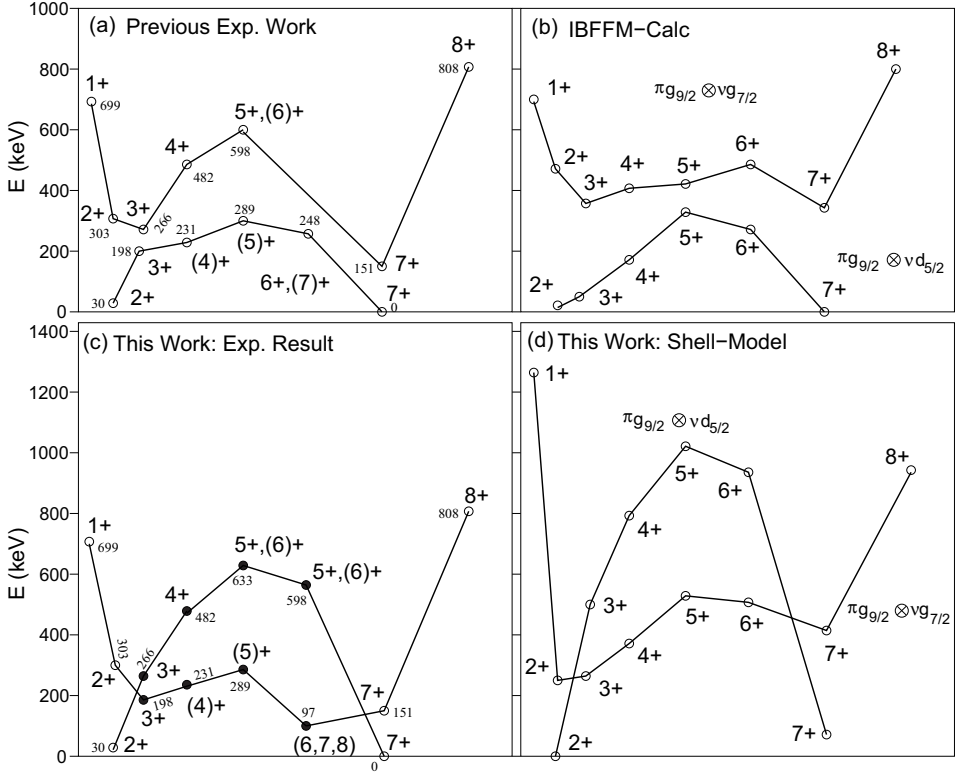


Fig. 4. The four panels show the experimental and theoretical $\pi g_{9/2}^{-1} \otimes \nu g_{7/2}$ and $\pi g_{9/2}^{-1} \otimes \nu d_{5/2}$ multiplets in ^{108}In . Empty circles (○) represent previous data or theory. Filled circles (●) represent levels re-assigned based on this work. The W-shape of the $\pi g_{9/2}^{-1} \otimes \nu g_{7/2}$ multiplet arises when the occupation probability $v_{g_{7/2}}^2 \sim 0.5$ [19]. (a) Summary of the two previous efforts [5, 20] based on reaction and high-spin studies. (b) The result of the interacting-boson-fermion-fermion calculation presented in Ref. [5] (c) Multiplet interpretation of this work (d) The multiplet structures of the shell-model calculation.

3.2 Multiplet interpretation

In two previous efforts [5, 20], the excited states of ^{108}In have been interpreted in terms of the $\pi g_{9/2}^{-1} \otimes \nu g_{7/2}$ and $\pi g_{9/2}^{-1} \otimes \nu d_{5/2}$ multiplets, see Fig. 4(a). However, the previous measurements were not directly sensitive to the transition matrix elements but had to rely on branching and mixing ratios. These were based on decay data, angular distributions from a (p,n γ) reaction, and from a high-spin study of ^{108}In . The results were compared [5] with an interacting boson-fermion-fermion calculation (IBFFM) [19], see Fig. 4(b). The residual interaction of the corresponding Hamiltonian was fitted to reproduce the energy spectrum of ^{108}In . Here, we interpret parts of the experimental en-

ergy spectrum of ^{108}In starting from a realistic shell-model interaction without phenomenological modifications, see Fig. 4(c)-(d). The theoretical multiplets were extracted in the following way. Between neighboring $I \rightarrow I+1$ states of the same $\pi^{-1} \otimes \nu$ multiplet one can expect a large M1 matrix element, which we in the following refer to as the M1-overlap. Starting with the 2^+ ground state of the shell-model calculation, which has a dominating $\nu d_{5/2}$ component, a sequence of states belonging to the $\pi g_{9/2}^{-1} \otimes \nu d_{5/2}$ multiplet can be identified by following the strongest M1 matrix elements. Similarly, the theoretical $\pi g_{9/2}^{-1} \otimes \nu g_{7/2}$ multiplet was traced out by starting with the only 1^+ state in the shell-model calculation. In detail, the 2^+ ground state of the calculation has a large M1-overlap with the

3^+ shell-model state at 501 keV. Invoking the similarities in the simulated and observed de-excitation patterns, it is concluded that the experimental 3^+ state at 266 keV also belongs to this multiplet, see Fig. 4(c). This assumption is strengthened by this state being fed by the 4^+ state at 482 keV. This assignment differs from the one in Ref. [5] and Fig. 4(a). We suggest that the experimental 3^+ state at 198 keV does not belong to the $\pi g_{9/2}^{-1} \otimes \nu d_{5/2}$ multiplet.

The reason is that the corresponding shell-model state at 262 keV has an M1-overlap with respect to the 2^+ shell-model ground state which is 20% smaller than the overlap with the 3^+ shell-model state at 501 keV. In the previous section, the observed 4^+ state at 482 keV was identified as the calculated 4^+ state at 796 keV. The M1-overlap of this state with the 3^+ shell-model state at 501 keV is twice that of the overlap with the 3^+ state at 262 keV. This makes a $\pi g_{9/2}^{-1} \otimes \nu d_{5/2}$ assignment of the 4^+ state at 482 keV plausible. Continuing, the 5^+ and 6^+ states of this multiplet would correspond to the shell-model states at 1020 keV and 935 keV. In the shell-model, these states are the fourth and the second states with these spins and parities. Therefore, assuming an equivalent sequence of the spins and parities in the experimental spectrum, the states at 633 keV and 598 keV are suggested to belong to the $\pi g_{9/2}^{-1} \otimes \nu d_{5/2}$ multiplet. In the shell-model, the 6^+ state at 935 keV has the largest M1 overlap with the 7^+ shell-model state that corresponds to the experimental ground state.

Regarding the $\pi g_{9/2}^{-1} \otimes \nu g_{7/2}$ multiplet, the only low-lying 1^+ state in the experimental spectrum is located at 699 keV. In the shell-model calculation, the 1^+ state has the largest M1-overlap with the low-lying 2^+ state at 251 keV. The only experimental low-lying 2^+ state, apart from the isomeric state at 30 keV, is located at 303 keV. Therefore, it is reasonable to assign this state to the $\pi g_{9/2}^{-1} \otimes \nu g_{7/2}$ multiplet. From the discussion above, we assign the experimental 3^+ state at 198 keV to the $\pi g_{9/2}^{-1} \otimes \nu g_{7/2}$ multiplet. The $(4)^+$ state of this multiplet is according to the shell-model the second state with this spin and parity. Therefore, the next non-assigned $(4)^+$ state at 231 keV is tentatively assigned to the $\pi g_{9/2}^{-1} \otimes \nu g_{7/2}$ multiplet. Similarly, the 5^+ and 6^+ states of the shell-model correspond to the experimental $(5)^+$ state at 289 keV and the $(6, 7, 8)$ state at 97 keV. It is noteworthy that the $3^+ - (4)^+ - (5)^+$ sequence of states of the $\pi g_{9/2}^{-1} \otimes \nu g_{7/2}$ multiplet were all assigned to belong to the $\pi g_{9/2}^{-1} \otimes \nu d_{5/2}$ multiplet in earlier efforts, see Fig. 4(a). The lowest 7^+ and 8^+ states in the shell-model calculation can be assumed to correspond to the experimental 7^+ and 8^+ states at 151 keV and 808 keV.

The $\pi^{-1} \otimes \nu$ multiplets cover the same energy range. This could be interpreted as originating in the nearly degenerate $5/2^+$ ground state and first excited $7/2^+$ state in ^{109}Sn , with an energy difference of only 13 keV [1,2]. The IBFFM calculations and the $^{108}\text{Cd}(p,n\gamma)^{108}\text{In}$ reaction data in Ref. [5] predict a larger energy splitting between the $\pi g_{9/2}^{-1} \otimes \nu g_{7/2}$ and $\pi g_{9/2}^{-1} \otimes \nu d_{5/2}$ configurations

than the one deduced in this work. It is worth pointing out that the parameters for the neutron-core coupling in the IBFFM calculations of Ref. [5] were fitted to the energies of the experimentally determined $\pi^{-1} \otimes \nu$ multiplet.

4 Coulomb excitation analysis

For completeness we present upper limits of three $B(E2)$ values extracted from the ^{108}In data using the computer code GOSIA [10]. The E2 and M1 couplings between the states shown in Fig. 3 were included in the analysis as well as the small set of known branching ratios and mixing ratios from Ref. [5]. For the cases where several tentative spin assignments exist, the lowest spin was chosen. However, the solution was not sensitive to any variation of tentative spin assignments for the present case. The properties of the χ^2 -minimum were tested by initiating the minimization routine with a wide range of starting conditions using randomization and rescaling of the matrix elements. The statistical uncertainties of the γ -ray yields and the large number of free parameters rendered final matrix elements with large correlated uncertainties. However, the extremes of the uncertainties for three of the E2 matrix elements in ^{108}In were reasonable, see Table 3. They provide a first estimate of the lower limits of the lifetimes of two of the excited states in ^{108}In . Furthermore, the flight time between the secondary target and the DSSSD was ~ 2 ns. This provides an upper limit of the lifetimes of all the states observed in $^{106,108}\text{In}$ since the de-excitation γ -ray peaks appear only in the Doppler corrected spectra. These values can be compared to the lifetimes of some of the low-lying states in ^{110}In , determined from the $^{107}\text{Ag}(\alpha, n\gamma)^{110}\text{In}$ reaction [22], which are in the order of $\gtrsim 5$ -10 ps.

5 Conclusions

In conclusion, the radioactive isotopes $^{106,108}\text{In}$ have been Coulomb excited from their ground states and first excited isomeric states. The multiplet structure of ^{108}In has been reanalyzed in view of the de-excitation patterns observed here. The realistic residual interaction based on the CD-Bonn potential does not predict the correct ground state spins of $^{106,108}\text{In}$ but it reproduces the observed transition patterns in general. Further Coulomb excitation studies accompanied with high-statistics decay- and reaction-studies are needed in order to improve the precision of the transition matrix elements in $^{106,108}\text{In}$. This information will provide a good benchmark for studies of the nucleon-nucleon interaction in the vicinity of ^{100}Sn , and the π - ν two-body matrix-elements in particular.

This work was supported by the Swedish Research Council, the European Union through RII3-EURONS (Contract No. 506065), and the German BMBF through Grant No. 06 KY 205 I.

Table 3. Observed γ -ray transitions in ^{108}In and the deduced limits on the transition probabilities where possible.

Transition	E_i (keV)	E_f (keV)	E_γ (keV)	Lifetime τ_m (ps)	B(E2) (Wu)
$7^+ \rightarrow 7_{\text{gs}}^+$	150.8	0.0	150.8	$4 < \tau_m \lesssim 2000$	< 196
$5^+ \rightarrow 7_{\text{gs}}^+$	247.7	0.0	247.7	$4 < \tau_m \lesssim 2000$	< 222
$5^+ \rightarrow (6)$	247.7	96.9	150.8	$4 < \tau_m \lesssim 2000$	< 93

References

1. L. Kaubler *et al.*, Z. Phys. A **351**, 123 (1995).
2. J. J. Ressler *et al.*, Phys. Rev. C **65**, 044330 (2002).
3. D. Vandeplasseche *et al.*, Phys. Rev. Lett. **57**, 2641 (1986).
4. J. Eberz *et al.*, Z. Phys. A **323**, 119 (1986).
5. A. Krasznahorkay *et al.*, Nucl. Phys. A **499**, 453 (1989).
6. J. Gulyas *et al.*, Nucl. Phys. A **506**, 196 (1990).
7. B. W. Filippone *et al.*, Phys. Rev. C **29**, 2118 (1984).
8. B. Roussire *et al.*, Nucl. Phys. A **419**, 61 (1984).
9. R. Barden *et al.*, Z. Phys. A **329**, 319 (1988).
10. T. Czosnyka *et al.*, *GOSIA*, Heavy Ion Laboratory, Warsaw University.
11. A. Ekstrom *et al.*, Phys. Rev. Lett. **101**, 012502 (2008).
12. A. N. Ostrowski *et al.*, Nucl. Instr. and Meth. A **480**, 448 (2002).
13. P. Reiter *et al.*, Nucl. Phys. A **701**, 209 (2002).
14. M. Hjorth-Jensen *et al.*, Phys. Rep. **261**, 125 (1995).
15. R. Machleidt *et al.*, Phys. Rev. C **53**, R1483 (1996).
16. A. Holt *et al.*, Phys. Rev. C **61**, 064318 (2000).
17. T. Kibdi *et al.*, Nucl. Instr. and Meth. A **589**, 202 (2008).
18. D. Seweryniak *et al.*, Nucl. Phys. A **589**, 175 (1995).
19. S. Brant *et al.*, Z. Phys. A **329**, 151 (1988).
20. C. J. Chiara *et al.*, Phys. Rev. C **64**, 054314 (2001).
21. A. Ekstrom *et al.*, Nucl. Instr. and Meth. A (submitted) .
22. A. Krasznahorkay *et al.*, Nucl. Phys. A **503**, 113 (1989).

V

DETERMINATION OF THE ISOMERIC FRACTION IN A POSTACCELERATED RADIOACTIVE ION BEAM USING THE COUPLED DECAY-CHAIN EQUATIONS

PAPER V

Determination of the isomeric fraction in a postaccelerated radioactive ion beam using the coupled decay-chain equations

A. Ekström, J. Cederkäll, D. D. DiJulio, C. Fahlander

Physics Department, University of Lund, Box 118, SE-221 00 Lund, Sweden

J. Van de Walle

PH Department, CERN 1211, Geneva 23, Switzerland

Abstract

A method based on the coupled decay-chain equations for extracting the isotopic and the isomeric composition of a postaccelerated radioactive ion beam is presented and demonstrated on a data set from a Coulomb excitation experiment. This is the first attempt of analyzing the content of a postaccelerated radioactive ion beam using this technique. The beam composition is required for an absolute normalization of the measurement. The strength of the method, as compared to present online-based methods, lies in the determination of the isomeric fraction of a partially isomeric beam using all data accumulated during the experiment. We discuss the limitations and sensitivity of the method with respect to the γ -ray detection efficiency and the accumulated flux.

Keywords: Postaccelerated radioactive ion beam, Isomeric beam, Decay-chain analysis, GEANT4

PACS: 29.38.Gj, 29.85.Fj, 29.30.Kv

1. Introduction

Technical advances in the postacceleration of radioactive ion beams (RIBs) produced in ISOL-facilities enable high-precision studies of many exotic isotopes using well-known techniques such as Coulomb excitation or transfer reactions. Still, even though significant advances are being made in targetry and separation techniques, the incident RIBs very often contain additional isobaric species apart from the one under study. Consequently, in many experiments a time-varying beam composition must be investigated for the purpose of normalization. A variety of techniques based on lasers [1] or ionization chamber methods are in use to extract this information. Such measurements are usually carried out several times during an experiment and provide an instantaneous measure of the isobaric composition of the beam. We will concentrate on an offline method that uses the γ -rays detected following the decay of the unstable components of the RIB. In particular, this method allows for the extraction of the isomeric to ground state fraction of a partially isomeric beam. See Fig. 1 for the case under study here. This approach also serves as a valuable consistency check for the methods mentioned

above. The sensitivity with respect to the uncertainties in the γ -ray detection efficiencies and branching ratios is investigated using a data set from a Coulomb excitation experiment that was carried out at the REX-ISOLDE facility.

2. The experiment and the production of the RIB

The method has been tested in parallel with the analysis of Coulomb excitation data taken at the REX-ISOLDE facility at CERN. In this experiment a 2.82 MeV/u RIB consisting of ^{108}Sn ($T_{1/2} = 10.30(8)$ min), ^{108}In in the ground state ($T_{1/2} = 58.0(12)$ min), and ^{108}In in the first isomeric 2^+ state ($T_{1/2} = 39.6(7)$ min) was Coulomb excited against a stable 2.0 mg/cm² thick ^{58}Ni target. The primary aim of this experiment was to investigate the low-lying collective properties of ^{108}Sn . The main results from the data analysis can be found in Ref. [2] and is independent of the method investigated here. The scattered particles were detected by a circular double-sided silicon-strip detector (DSSSD) placed 3 cm downstream of the ^{58}Ni target and positioned in a spherical target chamber. The γ -rays were detected by the 8 MINIBALL HPGe triple-clusters [3] surrounding

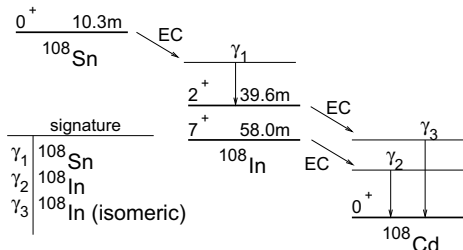


Figure 1: This figure schematically shows the different types of γ -rays, $\gamma_1, \gamma_2, \gamma_3$, that were used as a signature for identifying the Sn, In^{gs}, and In^m parts of the beam. The decay branches of ^{108}Sn only populate states in ^{108}In that feeds the 2^+ isomeric state. The $^{108}\text{In } 7^+$ ground state decays into certain states in ^{108}Cd and comes from the beam component only.

No.	E_γ (keV)	I_γ (%)	Exp. Yield Y_γ	Parent
1	272.75	45.5(6)	6801282(6229)	^{108}Sn
2	396.43	64.3(6)	9788686(5212)	^{108}Sn
3	669.11	22.6(4)	2383319(3667)	^{108}Sn
4	730.87	9.3(10)	467648(2737)	^{108}In
5	1032.92	35(3)	1017867(2096)	^{108}In
6	1056.79	29(3)	1309156(2076)	^{108}In
7	1529.72	7.3(4)	802648(1596)	$^{108}\text{In}^m$

Table 1: The most intense observed γ -ray yields from the different decay chains of the beam components. Their γ -ray intensities I_γ [5] are normalized to the decay of the parent nucleus.

the target chamber in a spherical configuration. Each triple-cluster consisted of three individual Ge-crystals. The RIB was produced by bombarding a thick primary target consisting of LaC_x with 1.4 GeV protons provided by the PS Booster of the CERN accelerator complex. The isotopes produced in the induced fission, spallation, and fragmentation reactions effused into an ionization cavity where the Sn isotopes were singly ionized using resonant laser ionization [4]. The In and In^m isotopes were singly ionized from surface ionization on the walls of the cavity. The A=108 isotopes of the extracted 1+ ions were subsequently separated in the high resolution mass-separator of the facility. After initial cooling, trapping, and charge breeding the RIB was postaccelerated by the REX-linac to its final energy.

3. Method: Coupled decay-chain analysis

After passing the target the unstable beam particles are stopped in the target chamber and the downstream

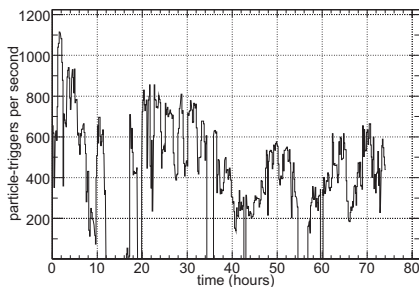


Figure 2: (color online) The particle-trigger rate provides a measure of the variation in the incident beam flux. For several periods of time the beam was switched off. However, with the method presented here this is taken into account.

beam dump where they decay and populate excited states in the daughter nuclei. The composition of the beam is reflected in the total number of detected γ -rays from transitions that can be uniquely coupled to a certain isotopic/isomeric component of the beam. See Fig. 1 for a schematic illustration of this concept. For this particular case it was possible to identify at least one individual decay-path for each component, see Table. 1. Here one should note that postacceleration of a RIB typically requires several orders of magnitude higher intensity than is required to establish the decay scheme. Consequently, isotopes studied using postaccelerated RIBs have well-known decay schemes. The data presented in Table 1 were collected over the 75 hours in which the experiment was running. The coupled-decay chain method makes it possible to analyze the γ -ray yields using different half-lives of the components and time-periods without any incident beam. The content of the RIB can be written as;

$$\mathcal{P} \cdot ^{108}\text{Sn} + \mathcal{Q} \cdot ^{108}\text{In}^{\text{gs}} + \mathcal{R} \cdot ^{108}\text{In}^m \quad (1)$$

where $0 \leq \mathcal{P}, \mathcal{Q}, \mathcal{R} \leq 1$ represent the magnitude of each component. The primary aim of the analysis is to extract \mathcal{Q} and \mathcal{R} . The time-dependence of the Sn-fraction $\mathcal{P}(t)$ can be removed by introducing a time-average $\langle \mathcal{P} \rangle$ according to;

$$\langle \mathcal{P} \rangle = \frac{\int \mathcal{P}(t) \mathcal{F}(t) dt}{\int \mathcal{F}(t) dt} \quad (2)$$

In the following the time-averaged value is referred to as \mathcal{P} . The fluctuations of the incident beam flux $\mathcal{F}(t)$ is provided by the number of particles detected in the

DSSSD, see Fig. 2. The ratio α of indium in the meta-stable state ($^{108}\text{In}^m$) to the total indium fraction of the beam ($^{108}\text{In}^{gs} + ^{108}\text{In}^m$), i.e. $\alpha \equiv \mathcal{R}/(\mathcal{Q} + \mathcal{R})$, was assumed to be constant. This assumption is reasonable since the heating and the chemical properties of the primary target does not change during the experiment in any respect that would influence this ratio. It should be pointed out that the variations of \mathcal{P} originates in fluctuations of the ionization efficiency, caused by e.g. a drift in the positions of the laser beams. The activity of the beam components that were deposited in the experimental setup over time is described by the following set of differential equations;

$$\begin{aligned}\dot{\text{Sn}} &= -\lambda_{\text{Sn}}\text{Sn}(t) + \mathcal{P}\mathcal{F}(t) \\ \dot{\text{In}}^m &= +\lambda_{\text{Sn}}\text{Sn}(t) - \lambda_{\text{In}^m}\text{In}^m(t) + (1 - \mathcal{P})\alpha\mathcal{F}(t) \\ \dot{\text{In}}^{gs} &= -\lambda_{\text{In}^{gs}}\text{In}^{gs}(t) + (1 - \mathcal{P})(1 - \alpha)\mathcal{F}(t)\end{aligned}\quad (3)$$

where the amount of each isotope is denoted by $\text{Sn}(t)$ etc., and the dot indicates the time-derivative. The coupled differential equations in Eq. 3 were solved by a fourth-order Runge-Kutta routine with a step-length of 100 seconds and with the initial conditions;

$$\text{Sn}(t = 0) = \text{In}^{gs}(t = 0) = \text{In}^m(t = 0) = 0 \quad (4)$$

The equations were integrated over the entire experiment and took into account the periods when the data acquisition system was switched off. The final number of deposited isotopes of a certain kind depends on the values of \mathcal{P} and α . For each combination of these, the expected γ -ray yield Y_γ was calculated from the known γ -ray intensities in Table 1, the known decay constants, and the γ -ray detection efficiency, see Sec. 3.1. The overall normalization constant was removed by forming ratios R_i of the type

$$\frac{Y_\gamma(\text{In}^{gs})}{Y_\gamma(\text{Sn})}, \frac{Y_\gamma(\text{In}^m)}{Y_\gamma(\text{Sn})}, \frac{Y_\gamma(\text{In}^m)}{Y_\gamma(\text{In}^{gs})} \quad (5)$$

and were subsequently compared to its experimental counterparts using a χ^2 -type penalty function given as;

$$\chi^2/\nu = \frac{1}{\nu} \sum_i \left(\frac{R_i^{\text{exp}} - R_i^{\text{calc}}}{\sigma_i} \right)^2 \quad (6)$$

where ν represents the total number of degrees of freedom. In total, the 2 parameters of the model and the 15 ratios that could be formed from Table 1 gives $\nu = 13$. The uncertainty σ_i of each ratio comes from the uncertainties in the γ -ray intensities, the detection efficiencies, the decay constants, and the experimental γ -ray yields. These errors were propagated using Gaussian error propagation.

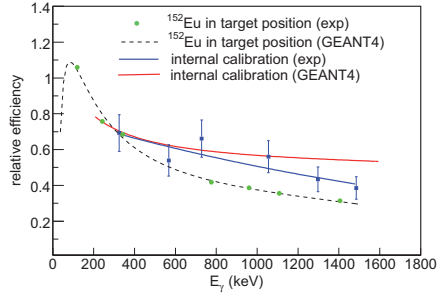


Figure 3: (color online) Simulated (GEANT4) and experimental relative γ -ray detection efficiencies. The blue curve is obtained from an internal calibration of the observed yields from the $^{108}\text{In}^{gs} \rightarrow ^{108}\text{Cd}$ decay. The green solid dots represent the result from a measurement with a ^{152}Eu source placed in the target position, i.e. nearly the center of the target chamber. The black dashed curve represents the corresponding simulation. The red dashed curve shows the simulated result when using a scattered beam. See the text for details.

3.1. The γ -ray detection efficiency of a scattered particle source

The γ -rays that are listed in Table 1 were detected by the MINIBALL spectrometer. The corresponding activity was distributed over the scattering chamber, the downstream beam dump, and on the inside of the beam pipes. The implementation of the collected γ -ray yields in the decay-chain model requires the knowledge of the detection efficiency of the MINIBALL to radiation emitted from the Rutherford-distributed particle source. This is provided by an internal calibration that is based on the observed γ -rays from the $^{108}\text{In}^{gs} \rightarrow ^{108}\text{Cd}$ decay of the scattered beam. Note that additional and less intense γ -rays, not included in Table 1, were used for this purpose in order to expand the interval of detected energies as much as possible. Most of the corresponding intensities were known to a precision of $\sim 10\%$. Therefore, the uncertainty of the internal calibration is of the same size. The data points were fitted to an exponential function and the result is shown as the blue solid curve in Fig. 3. Compared to the experimental efficiency obtained from a ^{152}Eu source placed in the center of the chamber, represented by the green solid dots in Fig. 3, the internal calibration indicates a stronger attenuation of low energy γ -rays. This appears to be consistent with the intuitive reasoning that the γ -rays emitted from particles that were stopped in the beam dump, ~ 1.4 meters downstream, have to penetrate more material before reaching any of the MINIBALL Ge-detectors.

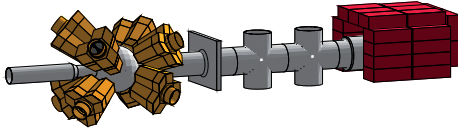


Figure 4: (color online) GEANT4 geometry of the setup showing the 8 MINIBALL triple-clusters (yellow). The spherically shaped target chamber was located in the center and consisted of 2 mm thick aluminum. The beam dump was 1.4 m further downstream and covered by shielding bricks made of lead (red). The γ -ray detection efficiency was simulated for a source of ^{108}In particles Rutherford scattered against a 2.0 mg/cm^2 thick ^{58}Ni target. A transverse beam emittance of 0.3 mm-mrad was included as well as the energy loss dE/dx of the ^{108}In particles as they traversed the target. See the text for details.

However, given the uncertainty of the internal calibration, the form of the internal efficiency-curve was investigated further using a GEANT4 simulation. The eight MINIBALL triple-clusters were positioned around the target chamber according to the experimental configuration, see Fig. 4. A ^{108}In beam with an energy of 2.82 MeV/u was Rutherford scattered against a 2.0 mg/cm^2 thick ^{58}Ni target inside the target chamber in the simulation. The energy loss of the projectiles as they traversed the target foil was also included. According to measurements and simulations [6] the transverse phase space properties of the beam can be adequately described by an emittance of $0.3\pi \cdot \text{mm} \cdot \text{mrad}$ (normalized at 3.0 MeV/u) and a Gaussian distributed diameter of 4 mm . From the Rutherford cross section it is clear that 99.9% of the scattered beam continues towards the beam dump. The particles in the center of the beam that scatter at an angle $\theta_{lab} > 9.5^\circ$ do not pass through the hole of the particle detector placed 3 cm downstream in the target chamber. However, due to the Gaussian width distribution of the beam, 17% of the particles that scatter with $\theta_{lab} > 9.5^\circ$ will pass through the hole and be stopped within 3 cm behind the target chamber. Nearly all, 99.7% , of the beam particles that Rutherford scatter $\theta_{lab} < 9.5^\circ$ will end up in the beam dump, the remaining 0.3% are stopped along the path towards the beam dump. The simulations show that the absolute detection efficiency for a γ -ray emitted from this region is on the order of 0.02% , which is $1/500$ of the detection efficiency of a γ -ray emitted from inside or in the immediate vicinity of the target chamber, see Fig. 5. Still, the fraction of the detected γ -rays that originate from the beam dump is comparable to the fraction that was emitted from the target chamber since the particle density in the beam dump is ~ 1000 times higher.

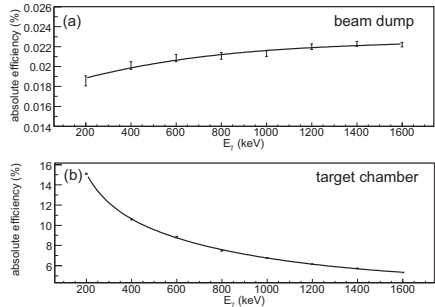


Figure 5: Simulated (GEANT4) γ -ray detection efficiency of the MINIBALL spectrometer for (a) γ -rays that were emitted from the beam dump and (b) γ -rays that were emitted from inside the target chamber.

Furthermore, the efficiency curve belonging to the beam dump increases with increasing γ -ray energy, a component which is also present in the experimental internal calibration-curve of Fig. 3. Therefore the experimental internal calibration-curve can be understood from the properly weighted linear combination of the simulated absolute efficiency curves of the beam dump and the target chamber in Fig. 5. This linear combination is represented by the red solid curve in Fig. 3. In this model, the scattered particle fraction residing on the inner surface of the beam pipes between the target chamber and the beam dump is neglected. The exact amount depends on the spatial width of the beam and the transverse emittance. The agreement between the simulated and the experimental versions of the internal calibration-curve was improved if the efficiency component of the target chamber was shifted from 0.1% to 0.2% . Effectively, this can be interpreted as incorporating the particles that were stopped between the target chamber and the beam dump. This shift has been included in Fig. 3. Given that the shape of the internal calibration curve can be understood from the effects described above it was used in the current application of the coupled decay-chain model.

4. Results

The χ^2 value per degrees of freedom depends on α and \mathcal{P} . A variation of these generates a two-dimensional distribution in the \mathcal{R} - \mathcal{P} plane. The location of the global minimum of the χ^2/ν -statistic determines the isomeric fraction as well as the Sn-fraction of the beam that best fits the data. The extent of the $\chi^2_{min}/\nu + 1$ contour, which

defines the uncertainty of the result, is governed by the precision of the terms in Eq. 6. A dominating systematic effect comes from the γ -ray intensities I_γ in Table 1. This is seen when the X^2/ν expression is truncated such that only one signature transition per beam component is included. For the present case, this reduces the number of degrees of freedom to $\nu = 1$. The result of using e.g. the transitions of Table 1 with indices 3, 5, and 7 is shown in Fig. 6(a). The global minimum $X^2 = 0$ indicates a perfect fit to the data. However, the choice of transitions introduces a bias in the result due to the fluctuating precision of the previously reported γ -ray intensities. Indeed the X^2/ν -surface based on all the data listed in Table 1, see Fig. 6(b), gives a wider minimum with a X^2/ν statistic closer to one. Clearly, circumventing the fluctuations in the γ -ray intensities comes at the expense of the precision in the final result. One can note that the linear dependence between \mathcal{R} and \mathcal{P} present in Fig. 6(a) remains when the uncertainties of the efficiency calibration are set to zero. However, the extent of the X^2 -minimum in the linear direction shrinks with a factor of two and covers $54\% \leq \mathcal{P} \leq 64\%$ and $18\% \leq \mathcal{R} \leq 28\%$.

The $X^2_{\min}/\nu + 1$ region in Fig. 6(b), i.e. the green area, delimits the optimal set of values of \mathcal{R} and \mathcal{P} to $0\% \lesssim \mathcal{R} \lesssim 30\%$ and $50 \lesssim \mathcal{P} \lesssim 80\%$. This is consistent with the value obtained using the online laser method $\mathcal{P}_{\text{laser}} = 59 \pm 3\%$ [2], which is also indicated in Fig. 6(c). For the present case the precision of \mathcal{R} is improved when the decay-method is used in conjunction with the laser on/off technique, as shown in Fig. 6(b). Along the $\mathcal{P}_{\text{laser}} = 0.590$ path in the $\mathcal{R} - \mathcal{P}$ plane the lowest X^2/ν value is 1.18 and occurs for $\mathcal{R} = 0.20$. The uncertainty of this value can be estimated from the $X^2/\nu + 1$ intersections of the $\mathcal{P}_{\text{laser}} = 0.590 \pm 0.027$ paths, leading to an isomeric fraction $\mathcal{R} = 0.20^{+0.07}_{-0.09}$. The uncertainties in the efficiency curve are propagated to the final result in a standard fashion. Typically the efficiency can be determined to a level below $\sim 1\%$. For the present case the uncertainty of the internal calibration is 10-20% and therefore impacts the final result accordingly. However, this uncertainty is comparable to the overall precision of the γ -ray intensity ratios. The interplay of these two quantities will determine the precision of the final result for the case under study. The impact of the uncertainties $\delta\lambda_i$ of the decay constants λ_i in Eq. 3 is negligible in the present context. This was investigated numerically by solving the equations for the two combinations of $\lambda_i \pm \delta\lambda_i$ that maximally perturb the position of the X^2 minimum in the $\mathcal{R} - \mathcal{P}$ plane, see Fig. 7. The effect of the uncertainties of the decay constants in Eq. 3 can easily be included in a maximum likelihood

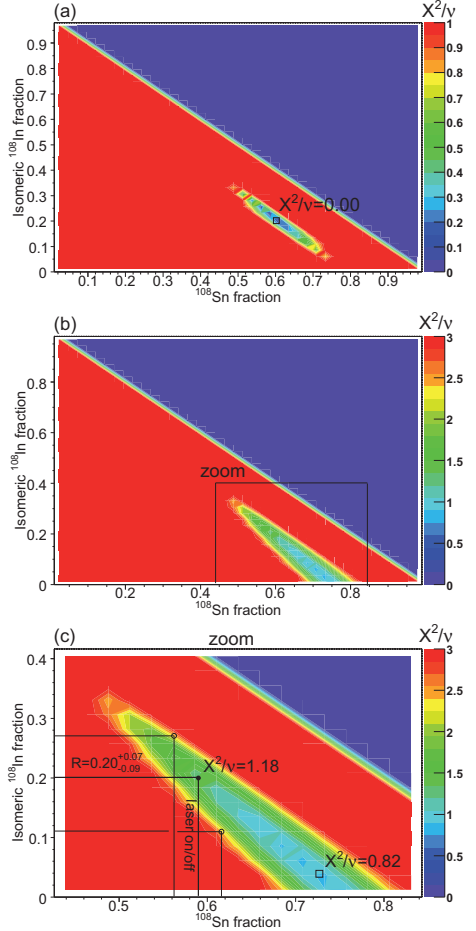


Figure 6: (color online) (a) The X^2/ν -surface based on one transition per beam component. Here, transitions 3,5, and 7 of Table 1 were used. The number of degrees of freedom for this case is $\nu = 1$. The one-sigma contour for this case is defined by the $X^2/\nu + 1 (= 0.0 + 1)$ contour, i.e. where the red region begins. This panel shows that the extent of the total $X^2_{\min}/\nu + 1$ surface depends on the precision of the quoted γ -ray intensities. In panels (b) and (c) the X^2/ν distribution per number of degrees of freedom (ν) for varying ^{108}Sn and $^{108}\text{In}^m$ fractions of the beam. The input data are shown in Table 1 and the γ -ray efficiencies were obtained from the internal calibration curve in Fig. 3. The obtained valley of optimal X^2/ν is consistent with the laser on/off value 0.590 ± 0.027 for the ^{108}Sn fraction [2]. The one-sigma contour for this case is defined by the $X^2_{\min}/\nu + 1 (= 0.82 + 1)$ value. Along the path $\mathcal{P}_{\text{laser}} = 0.590$, the optimal $^{108}\text{In}^m$ fraction is $0.20^{+0.07}_{-0.09}$.

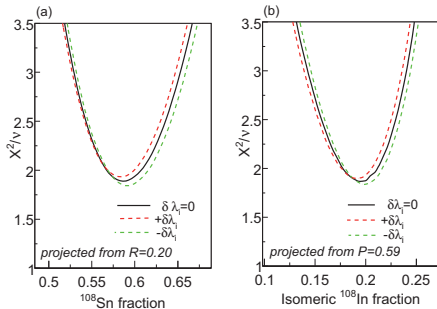


Figure 7: (color online) The panels show the χ^2 curves for a given (a) \mathcal{R} and (b) \mathcal{P} value. The impact of the uncertainties in the decay constants of Eq. 3 are indicated by the dashed curves. See the text for details.

method or in a conservative approach using the resulting extreme positions of the of the $\chi^2_{min} + 1$ values.

5. Conclusion

A method for deducing the isotopic and isomeric composition of a postaccelerated radioactive ion beam was presented. The strength of this method lies in its ability to determine the isomeric as well as the isotopic ratios of the beam in an offline analysis using all the accumulated data. This is an improvement over methods that e.g. determine the isotopic ratio using instantaneous online measurements and consequently influence the beam flux. The method was successfully applied to a real case. The optimal scenario for this type of analysis would be if the scattered beam particles were deposited in a simple, small, and well-defined geometry. Naturally, the outcome of the analysis depends on the availability of at least one well-known decay transition that is completely independent from the other components of the beam. Also, the half-lives of the beam components must be short enough that the investigated species have had time to decay within the duration of the measurement, i.e. the measurement time should be at least three times the half-life.

References

- [1] J. V. de Walle, et al., Phys. Rev. C 79 (2009) 014309.
- [2] A. Ekström, et al., Phys. Rev. Lett. 101 (2008) 012502.
- [3] J. Eberth, et al., Prog. in Part. and Nucl. Phys. 46 (2001) 389.
- [4] V. Fedosseev, et al., Nucl. Instr. and Meth. B 266 (2008) 4378.
- [5] J. Blachot, Nucl. Data Sheets 91 (2000) 135.
- [6] D. Voulot, priv. comm.